Computational Modeling of Hard Tissue Response and Fracture in the Lower Cervical Spine under Compression Including Age Effects

by

Fiona Khor

A thesis

presented to the University of Waterloo

in fulfillment of the

thesis requirement for the degree of

Master of Applied Science

in

Mechanical and Mechatronics Engineering

Waterloo, Ontario, Canada, 2018

Author's Declaration

I hereby declare that I am the sole author of this thesis. This is a true copy of the thesis, including any required final revisions, as accepted by my examiners.

I understand that my thesis may be made electronically available to the public.

Abstract

Almost half of motor vehicle accident (MVAs) victims experience traumatic spinal cord injuries (SCI), which are often associated with rollover accidents. Specifically, rollovers have the highest incidence rate of AIS2+ cervical spine injuries and more than half of the patients with SCIs demonstrated spine fractures with the majority being burst fractures. Detailed finite element human body models (HBMs) have been utilized to assess the safety of occupants and pedestrians in crash scenarios, augmenting the results from crash test dummies in physical tests. HBMs can predict the potential for injury and provide data such as fracture initiation and propagation that is not possible to collect experimentally. Biofidelic HBMs capable of predicting tissue-level injury require representative material properties and tissue level failure criteria. However, current HBMs use simplified constitutive models and are not capable of predicting the fracture threshold and fracture pattern for complex scenarios, such as the vertebrae in the neck. The objective of this study was to investigate constitutive models with age effect that are representative of cortical and trabecular hard tissues and assess the failure response of a C57 (C5-C6-C7) segment model under compression loading.

Two sets of material properties were identified that corresponded to the lower age of the experimental test samples (younger than 50 years old (YO)) and the higher age of the test samples (older than 70 YO). The available constitutive models in a commercial finite element code (LS-DYNA) were reviewed and the constitutive models that best represent the cortical and trabecular bone responses were analyzed. As there were no single constitutive model available that included all the key properties of hard tissues, asymmetric and anisotropic elastic-plastic (cortical) and crushable foam (trabecular) models were evaluated. Single element simulations were performed to verify the constitutive models. A functional spinal unit (FSU) model was extracted from a detailed 50th percentile HBM (Global Human Body Models Consortium (GHBMC) M50-O v4.3) and a centric compression simulation was performed to identify the best performing constitutive model compared to experimental data. Various eccentricity cases of the compression experiments were simulated as well such as anterior, posterior and lateral.

The anisotropic model predicted failure values and fracture patterns in better agreement with experimental data compared to an asymmetric or isotropic and symmetric model. This study showed the importance of including age effects that correspond to the age of experimental test subjects. This study also showed that simulations could provide additional insight regarding fracture initiation and progression, which is challenging to measure in dynamic experiments. Gender, segment level, and strain rate effect were not included in this work, which are limitations of the current study. In addition, the lack of human cervical spine experimental data for improved model validation is another limitation of this study. In conclusion, this study successfully utilized uncalibrated material properties of cortical and trabecular bone tissue from literature and accurately predicted failure outcomes of compression experiments with the implemented constitutive models.

Acknowledgements

I would first like to thank my supervisor, Dr. Duane Cronin for his guidance and mentorship. He had provided me with an opportunity to conduct research at the University of Waterloo, funding to attend conferences and opportunity to publish a journal paper. He had always been active in ensuring that I am doing well.

I am also pleased to thank the Global Human Body Models Consortium (GHBMC) for their financial support, leadership and feedback throughout the project.

Additionally, I would also like to thank Dr. Van Toen and Dr. Carter for providing me with additional experimental data such as high-speed videos and X-ray imaging for comparing my simulation results with.

I would also like to thank my coworkers and fellow students in the GHBMC project, especially Jeffrey Barker, Brock Watson, Donata Gierczycka, and Dilaver Singh who had helped troubleshoot LS-DYNA and Hypermesh problems that I had encountered along the way and their guidance and support throughout my graduate student career.

Lastly, I would like to thank my family for their unconditional support of my education and work. My parents especially have provided me an opportunity for a better future and had always made sure that I am receiving the best education I can possibly get.

Table of Contents

List of Figures

x

List of Tables

List of Equations

Chapter 1: Introduction

1.1 Motivation for Research

Almost half of the victims from motor vehicle accidents (MVAs) experience traumatic spinal cord injuries (SCI) (43% occurrences in Australia and 45% in USA) [O'Connor, 2002]. Rollovers comprise only 2.2% of MVAs [Digges, 2002; El-Hennaway et al., 2014] but approximately 80% of vehicle-related SCI [Wigglesworth, 1991; Thurman et al., 1995] is associated with rollovers [O'Connor, 2002]. In addition, falls and violence have always been one of the leading causes of traumatic SCIs [Ge et al., 2018]. There is an increase in SCI cases in the aged population (age of 65 and above) than younger population (below age of 65) [Chen et al., 2016] and SCI cases from falls in the aged population of above 46 years old had been increasing from 2010 to 2014 [Chen et al., 2016]. Majority (64%) of patients with SCIs reported spine fractures and 48% of that are burst fractures [Pickett et al., 2006]. In rollover accidents, the cervical spine is often subjected to axial compression loading [Raddin et al., 2009; Foster, 2016], which may lead to a fracture of the hard tissues in the cervical spine [Argenson et al., 1997]. The injury mechanism for burst fractures is compression [Myers and Winkelstein, 1995]. The lower cervical spine, particularly the C5 and C6 vertebrae were found to be one of the highest injured zones in cervical spine injuries among survivors of MVAs [Yoganandan et al., 1989; De Wit et al., 2012]. Lower cervical spine injuries had the highest level of complete and incomplete quadriplegia [Yoganandan et al., 1989; De Wit et al., 2012].

Detailed finite element human body models (HBMs) can help advance our understanding of the mechanics of various injuries and provide data that is not possible to collect experimentally. However, for these models to be biofidelic, accurate material properties and tissue level failure criteria are required. At present, trabecular and cortical bones are often represented in computational models using linear isotropic material properties and this simplification is also included in two of the most widely used current HBMs (THUMS and GHBMC) [Asgharpour et al., 2014; De Wit et al., 2012]. Besides that, the mechanical properties in these studies were retrieved from experiments and the specimens are usually aged (above 50 years old) [Asgharpour et al., 2014] or mixed of young and old over a range of ages [De Wit et al., 2012]. In general, no studies took into account the effects of age on the mechanical properties. For HBMs to be biofidelic, they must be assessed with modes of loading and loading rates that are representative of the application scenarios for the model. An importance aspect of model validation against experiment data is the requirement of accurate material properties and constitutive models. This research work contributes to the validation of cortical and trabecular bones in the lower cervical spine segment under compression loading with various eccentricities (posterior, anterior, and lateral) with the effect of age taken into account. Failure and fracture responses would be evaluated against experimental data to validate the models

1.2 Research Objectives and Approach

The first objective of this thesis was to conduct a literature survey on available mechanical properties of both trabecular and cortical bone. The structure of trabecular and cortical bone are quite distinct from one another. The trabecular bone has a porous foam-like structure and the cortical bone has a dense structure with canals. The differences seen in their mechanical properties are due to their structure. The second objective was to investigate constitutive models that could best represent the trabecular and cortical bone material response. In this thesis, the constitutive models were selected from a wide range of models available in a commercial explicit finite element analysis code (LS-DYNA, LSTC, Livermore, CA) and material properties from literature review were applied to the selected constitutive models. The sets of mechanical properties of both trabecular and cortical bones in both "young" and "aged" donor populations representing the age of the compression experiment subjects' were retrieved from various literature sources. The young donor populations were assumed to be less than 50 years old (50YO) and aged being older than 70 years old (70YO) as bone loss accelerates after age 50 [Wishart et al., 1995]. Asymmetric and anisotropic material properties were investigated and single element simulations were performed to verify the constitutive models. The best constitutive model that could represent these properties and provide results agreeable with experimental data was selected. The third objective was to simulate a C57 segment model in four compression cases (centric compression, posterior eccentricity compression, anterior eccentricity compression and lateral eccentricity compression with high and low eccentricity) [Carter, 2002; Van Toen et al., 2014]. A sensitivity study on load position and a mesh refinement study were also performed to further validate the model. The simulation results were compared with experimental results in terms of failure values and fracture patterns.

1.3 Thesis Organization

The second chapter of this thesis reviews the general microstructure and mechanical properties of cortical and trabecular bone. This chapter also discusses the factors affecting the bone properties and the structure of bone and properties of bones, specifically in the cervical spine that pertains to the area of interest of this thesis. In addition, this chapter also reviews the fracture patterns in the cervical spine and experimental methods involving hard tissue failure in the cervical spine. Lastly, this chapter provides a background on existing computational models of the cervical spine and the Global Human Body Models Consortium (GHBMC) cervical spine model.

Chapter three of this thesis describes the methodology. The first section looks at the literature review to identify the mechanical properties for trabecular and cortical bones, for both young and aged donor populations. The constitutive model identification process and corresponding single element simulation cases for verification are described. The model setup and simulation boundary conditions that were applied to closely represent the experimental FSU testing are described. Finally, this chapter discusses the methodology performed for a mesh refinement study and assessment of element size on the computational outcome.

Chapter four discusses the results of the simulations for the single element simulations, the compression simulations and the mesh refinement study.

Chapter five investigates a discussion of the results such as the effects of filtering, model sensitivity to load position, specimen orientation and boundary conditions, the strain-based element erosion approach, and mesh refinement.

Chapter six summarizes the research findings and presents recommendations that should be addressed in future research.

Chapter 2: Background on Bone Properties, Experiments and Finite Element Models

2.1 Bone Composition and the Structure of Cortical and Trabecular Bone

Bones provide a framework for the body and offer support for tissues and muscle attachments. Bones also protect our organs and assist us in our movement by acting as levers. In addition, bones also store minerals, fat, and the bone marrow, which synthesizes blood cells. At the macroscopic level, the two main types of bones are cortical and trabecular bone (Figure 1).
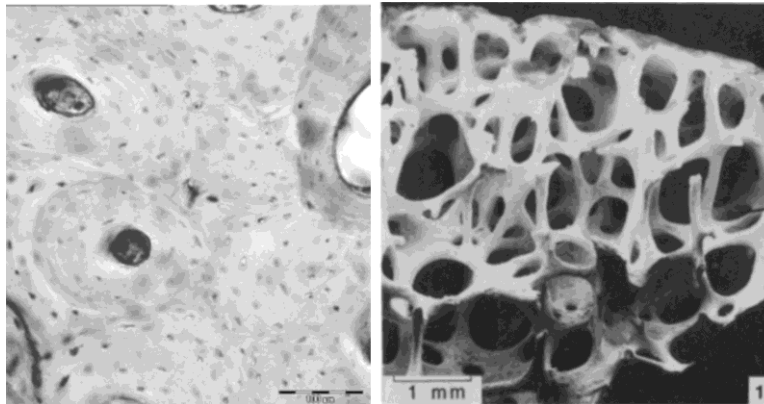
(Reprinted with permission from Oxford University Press, Augat, 2006 (left) and Elsevier, Gibson, 1985 (right))

Figure 1: Microstructure comparison of cortical and trabecular bone

Cortical bone with its dense solid structure containing microscopic channels comprises 80% of the skeletal bone mass [Cowin, 2001]. On the other hand, the remaining 20% of the skeletal mass is composed of a porous lattice structure of plate- or rod-like struts called the trabecular bone [Cowin, 2001]. Cortical bone is typically found in long bones and as a cortex or thin shell formed around vertebral bodies and other trabecular bones [Martin et al., 1998]. Trabecular bone, on the other hand, is found in the vertebra, flat bones, and ends of long bones [Martin et al., 1998].

The constituents of bone include collagen, water, hydroxyapatite mineral, small amounts of proteoglycans, and non-collagenous proteins [Martin et al., 1998]. The hydroxyapatite minerals are small crystals located within and between collagen fibers [Cowin, 2001] that contain many structural substitutions [Martin et al., 1998] and provides hardness to bone. The organic matrix of bones consists 90% of collagen and 10% of non-collagenous proteins [Cowin, 2001]. Collagen is a structural protein and provides bone flexibility, tensile strength, rigidity and compressive strength [Martin et al., 1998]. The ground substance of bone contains proteoglycans. Osteocalcin, secreted by osteoblasts comprises the non-collagenous proteins and is important in mineralization of new bone [Martin et al., 1998].

At the microstructural level, the primary composition of bone is mineralized collagen fibers organized in structures known as lamellae. The three major patterns of lamellae are concentric, circumferential, and interstitial. Concentric lamellae are typically found in cortical bone,

arranged in concentric layers with alternating angles between the primary directions of the fibers in each layer. The circumferential lamellae form a few layers surrounding the outer circumference of the trabecular bone region that is enclosed by the cortical bone region. The interstitial lamellae are fragments of former concentric or circumferential lamellae and fill the gaps between the Haversian canals [Cowin, 2001].

Within cortical bone, approximately 10 to 15 concentric lamellae form circular rings of 70 to 100µm thick around a longitudinally oriented vascular channel called the osteon or the Haversian system, which is the main structural unit of cortical bone [Cowin, 2001] (Figure 2).

(Image from: https://pubs.geoscienceworld.org/rimg/article-lookup/64/1/223)
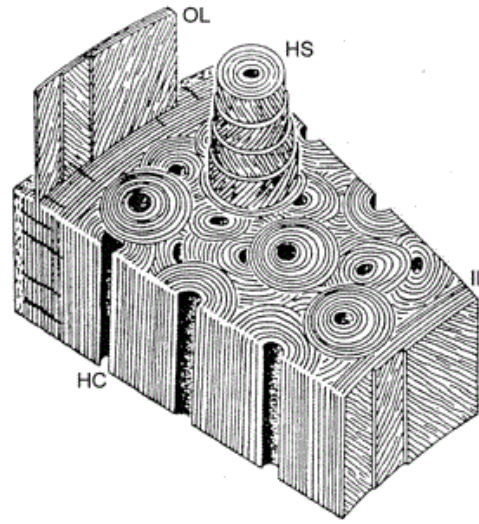
Figure 2: Microscopic view of the cortical bone featuring the osteons (OL: outer circumferential layer, IL: inner circumferential layer, HS: Haversian system, HC: Haversian canal)

The Haversian canal contains blood vessels, lymphatic nerves, and loose connective tissue that connect to the bone marrow and periosteum. These canals are interconnected with transverse Volkmann's canals that branch out to form an interconnected network providing blood flow in radial paths.

The microstructure of bones affects their mechanical properties. In cortical bones, theoretically, the packing of the local Haversian system makes the cortical bone transversely isotropic [Katz, 1980; Ashman et al., 1984]. However, ideal packing (Figure 3a) is rarely achieved in Haversian bones as they are typically arranged randomly (Figure 3b) and cortical bones in humans usually have a mixture between two histological types: Haversian or lamellar which are transversely isotropic and orthotropic respectively [Ashman et al., 1984].
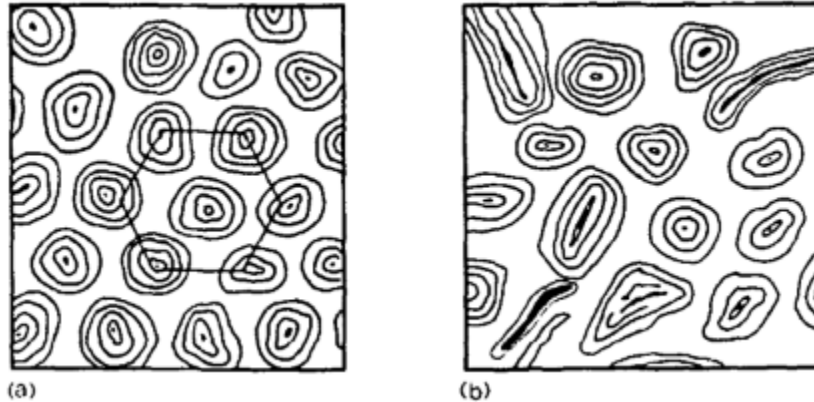
Figure 3: (a): Ideal hexagonal close-packed Haversian systems for transverse isotropy assumption of cortical bone (b) Typical orientation of Haversian systems

Nevertheless, several researchers [Van Buskirk & Ashman, 1981; Yoon & Katz, 1976; Hoffmeister, 2000] have shown that there is little difference between the fully orthotropic or transversely isotropic assumption used for elastic moduli in stress analysis, especially at an apparent level. The difference is significant in the physiological sense, as the lower elastic modulus in the radial direction is associated with greater permeability for blood flow from the medullary canal to the periosteum (outward radial direction in long bone) [Yanson, 1974].

In trabecular bones, the plate- or rod-like structures that form the lattice structure of the trabecular bone are known as trabeculae and are approximately 200 µm thick [Martin et al., 1998]. The two types of trabeculae are trabecular packets and interstitial lamellae. The main structural units of trabecular bone are trabecular packets or hemiosteons (half osteons), which are shallow crescent shape angular groupings of lamellae [Cowin, 2001]. They are separated by the cement line [Cowin, 2001] formed from bone remodeling events. The lamellae in trabecular bone are arranged parallel to the trabecular surface [Burr et al., 2013].

2.2 Mechanical Properties of Cortical Bone

Many studies on bone tissue that involves experimental testing had been reported. There are various methods for measuring the mechanical properties of cortical bone. The common modes of loading in experimental tests reported for cortical bone are tension, compression, and shear. Tension and compression testing were typically performed to measure the elastic constants and strength of cortical bone in the longitudinal (osteon) direction or transverse direction [Reilly and Burstein, 1974]. Due to the small displacements, an extensometer is often used to diminish errors due to testing machines and grip compliances. In tension and compression mechanical testing, the sample sizes are usually dogbone samples with dimensions of 15mm in length and 2mm in width [Reilly and Burstein, 1974]. For shear modulus and strength, torsional tests were typically performed [Reilly and Burstein, 1975].

Based on the transversely isotropic or orthotropic assumption as discussed in Section 2.1, it is well established in literature that cortical bone has a higher elastic modulus and strength in the longitudinal or osteonal direction [Reilly & Burstein, 1975; Bayraktar, 2004; Turner et al., 1999; Rho, 1997; Ashman, 1984; Hoffmeister, 2000). The longitudinal direction is oriented along the

direction of osteons and the transverse direction is perpendicular to the osteon direction as shown in Figure 4 below.
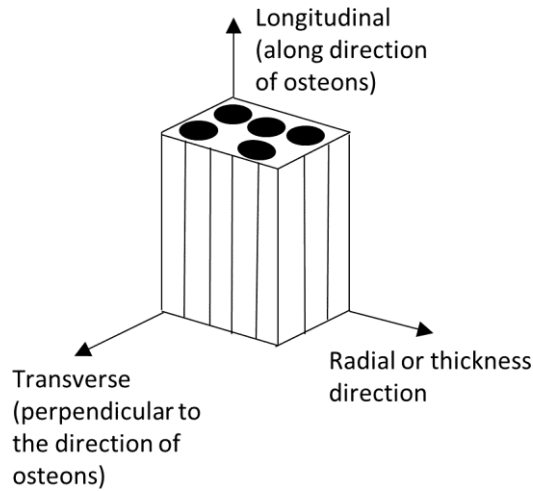
Figure 4: Longitudinal and transverse directions in bone

Similarly, cortical bone is also known to be asymmetric in nature in failure or ultimate properties [Reilly & Burstein, 1975] (Figure 5) such that the ultimate strength is higher in compression than in tension in both the longitudinal and transverse directions.
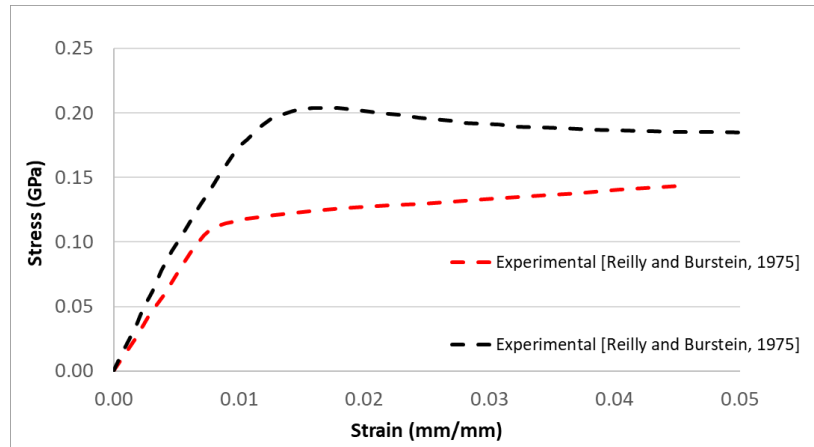
Figure 5: Asymmetry cortical bone stress-strain curves

In contrast, the ultimate strain is higher in tension than compression in the longitudinal direction but vice versa in the transverse direction [Reilly & Burstein, 1975]. The stress-strain response in tension was found to be bi-linear elastic-plastic with a well-defined yield point whereas, in compression, the response was elastic-plastic with material softening [Reilly &Burstein, 1975]. For the shear response of cortical bone, it had been found that the ultimate shear stress and strain occurred when the specimens were loaded in shear across the fiber direction transversely compared to in the longitudinal direction [Tang, 2015].

In this work, a full literature review of the mechanical properties of cortical bone was conducted. The elastic and ultimate properties of human cortical bone were reported in various studies using different experimental methods such as standard uniaxial mechanical testing [Reilly and Burstein, 1975; Bayraktar et al., 2004], nanoindentation [Turner et al., 1999; Zysset et al., 1999],

ultrasonic [Rho et al., 1996; Ashman et al., 1984; Hoffmeister et al., 2000] and pendulum type tensile impact test [Saha et al., 1976]. The cortical bone mechanical properties were retrieved from compression and tension experiments [Reilly and Burstein, 1974; Reilly and Burstein, 1975] and shear experiment [Tang, 2015]. The study by Reilly and Burstein (1974 and 1975) was chosen as they had an extensive number of samples (36) in their experiment with a wide age range (20 to 86 years old) which would be ideal in this work which looked into the age effects of mechanical properties. Their study also measured both asymmetric and anisotropic properties of cortical bone, which is another important aspect of this work. The shear experiment by Tang et al. (2015) was chosen for the shear mechanical properties of cortical bone as this study had extensively looked into shear deformation and fracture of human cortical bone using Iosipescu shear tests.

2.3 Mechanical Properties of Trabecular Bone

The mechanical properties of trabecular bone vary due to apparent density and arrangement of trabeculae with respect to the loading direction [Turner, 2002]. Anisotropy of a trabecular bone sample is due to the distinct porous structure and arrangement of rod and plate trabeculae [Kabel, 1999; Cowin, 2001]. Unlike cortical bone, the apparent elastic of modulus of a trabecular bone sample is not significantly different in tension and compression loading [Kopperdahl et al., 1993; Morgan et al., 2003]. The modulus does however depend on anatomic site and structural density Kopperdahl et al., 1998; Cowin, 2001]. Bones are generally heterogeneous and have different microstructural properties depending on the anatomical region, differing between anterior, posterior, medial and lateral locations at the harvest site and therefore, the anatomical region [Sanborn, 2016; Li, 2013; Abdel-Wahab, 2010; Shore et al., 2013]. Due to the large variations in architecture of the trabecular bone across different anatomic sites, there is no single universal modulus-density relationship [Morgan et al., 2003] and therefore the modulus-density relationship varies between linear or power law types [Kopperdahl et al., 1998; Cowin, 2001]. In addition, trabecular bone has intra-site variation such that within the vertebrae, there are morphological differences between the posterior, anterior, inferior and superior regions [Hulme et al., 2007]. The morphological differences and bone functional remodeling causes the elastic modulus in the anterior, posterior, medial and lateral regions within a trabecular bone sample to vary [Goldstein et al., 1983]. Due to this variation, equations to convert the modulus of the trabeculae tissue to the apparent modulus using volume fraction or apparent density were developed [Yang, 1999]. Apparent density in trabecular bone samples is usually defined as the division of the hydrated bone specimen mass with its marrow or dried bone specimen mass without marrow by specimen volume. The anisotropic apparent elastic moduli are a function of the axial tissue elastic moduli and solid volume fraction, which considers the porosity of the specimen. To convert apparent density to volume fraction, the volume fraction is multiplied by the density of the actual solid matrix material, which is approximately 1.9g/cm^3 for human bone [Yang, 1999]. The apparent yield strain of a trabecular bone sample is uniform within a specific bone but different across anatomical regions and is higher in compression than in tension [Morgan and Keaveny, 2001]. The yield strain, unlike the modulus exhibits a weak dependency on apparent density [Morgan and Keaveny, 2001]. The ultimate strain on the other hand is higher in tension than in compression [Kopperdahl and Keaveny 1998]. It had been discovered that the elastic modulus is an excellent predictor of yield strength for all sites and loading modes [Morgan and Keaveny, 2001]. Unlike cortical bone, the yield strength and ultimate strength for trabecular bone do not exhibit significant asymmetry [Kopperdahl and Keaveny, 1998]. Another

study; however, did find the compression yield strain (0.0077) to be slightly higher than the tensile yield strain (0.0070) although anatomical variation was found to be higher [Morgan and Keaveny, 2001]. Trabecular bone generally has lower strength in shear than in compression at the apparent level [Sanyal, 2012]. The ratio of shear to compressive strength depends on the trabecular microarchitecture especially at low bone volume fraction where the bone volume fraction (bone volume divided by total volume) is less than 0.20 [Sanyal et al., 2012]. The ratio of shear to compressive strengths is approximately 0.58 as predicted by traditional von Mises criterion for specimens with low bone volume fraction [Sanyal et al., 2012]. Amongst their specimens, the vertebral body specimen (average age of 66) has the lowest bone volume fraction of 0.09 whereas the highest (0.25) was found in the femoral neck specimen (average age of 70) [Sanyal et al., 2012]. The mode of tissue-level trabeculae failure in shear was predominantly tensile yielding whereas under compression, it was predominantly tensile yielding at low bone volume fraction specimens (such as the vertebra) but compression otherwise in high bone volume fraction specimens. In shear loading, the tensile yielding occurs along load paths oriented at approximately 45 degrees with respect to the main trabecular orientation but for compression, tensile failure occurs in horizontal trabeculae for low bone volume fraction specimens and compression failure in longitudinal trabeculae for high bone volume fraction specimens [Sanyal, 2012]. The tensile failure in horizontal trabeculae in low density specimens occurred due to bending of vertical trabeculae causing the interconnecting horizontal trabeculae to elongate in tension [Sanyal, 2012]. The architecture of trabecular bone is highly dependent on density. Higher density specimens such as samples from the femoral head or bovine trabecular bones have more of a plate-like structures whereas lower density specimens such as samples from the cervical vertebral bodies have more of a rod-like structures [Gibson et al.,2005; Keaveny et al., 2001, Amling et al., 1996]. This may lead to the different failure mode seen in low density and high density trabecular specimens in which the low density rod-like structure trabecular specimens are more susceptible to bending than the high density plate-like structure trabecular specimens under compression loading.

Unlike the tensile stress-strain curve (Figure 6), the compressive curve is different with a much higher energy absorption capacity due to its porous lattice structure of trabeculae rods and plates.
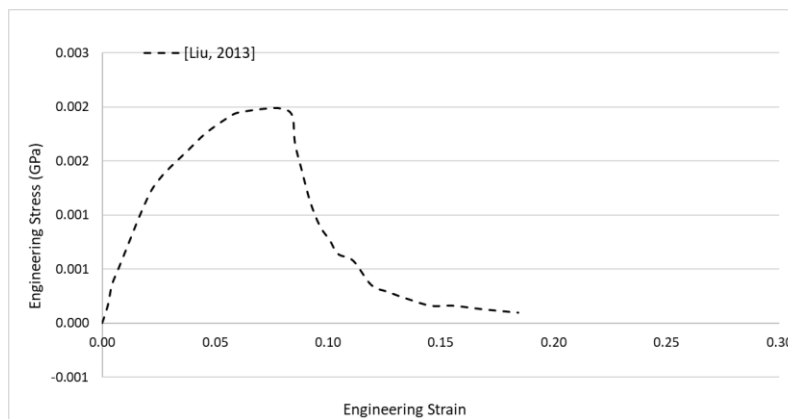
(Image adapted from Liu, 2013)

Figure 6: Tensile curve of a typical trabecular bone specimen [Liu, 2013]

9

The compressive curve generally initiates with a linear elastic regime until an ultimate failure point, dropped in force before extending as a stress plateau towards a strain of more than 50% [Hayes and Carter 1976; Gibson, 1985; Liu, 2013, Halgrin, 2012] (Figure 7).
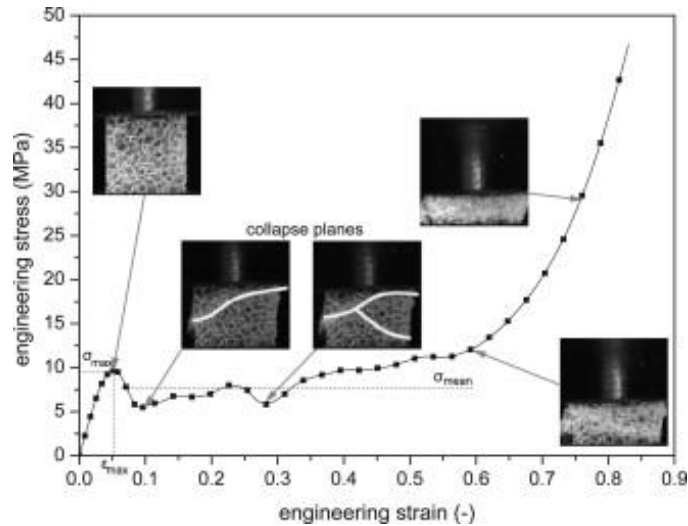
Figure 7: Compressive curve of trabecular bone [Halgrin et al., 2012]

The plateau is due to a pore collapse regime in which the fracture and buckling of trabeculae occur, absorbing energy [Hayes and Carter, 1976]. The buckling of the trabecular could be initiated from the collagen struts (organic phase) based a study that demineralised bovine trabecular bones to evaluate the asymmetry mechanical behavior of the organic collagen fibers [Xie et al., 2018]. Once the pore closure begins, consolidation or densification occurs in which the stiffness of the specimen increases greatly [Hayes and Carter, 1976; Liu, 2013]. This is due to the trabeculae failing and contacting one another, providing more resistance to load [Gibson, 1985]. This mechanical response is similar to that of cellular materials [Gibson, Ashby, 1988]. As the density of trabecular bone increases, the thicker and more plate-like trabeculae cause an increase in Young's modulus and compressive strength but reduce the strain at which the trabeculae contact and initiate the consolidation region at an earlier strain with a shorter plateau region [Gibson,1985]. This theory was demonstrated by Hayes and Carter [1976], in which the consolidation strain was approximately 20% for a specimen with a density of 962 g/cc whereas the consolidation strain was approximately 60% for a specimen with a density of 559 g/cc (Figure 8).
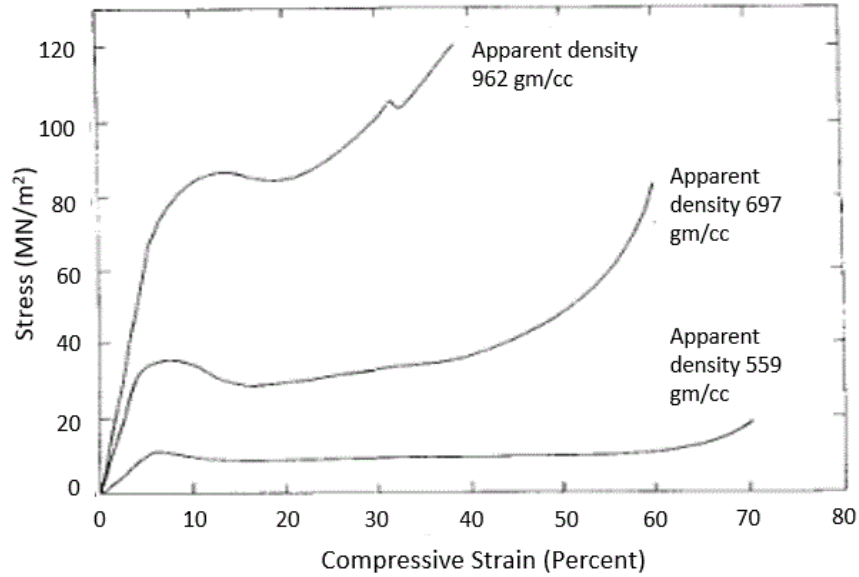
Figure 8: Compressive stress-strain curve of typical specimens of bovine subchondral trabecular bone with different apparent densities

Trabecular bones are challenging to measure, especially the trabeculae struts due to the small scale of the specimens. End artifact errors are known to occur in mechanical testing in which the trabecular bones are compressed by two platens [Odgaard and Linde, 1991] (Figure 9).
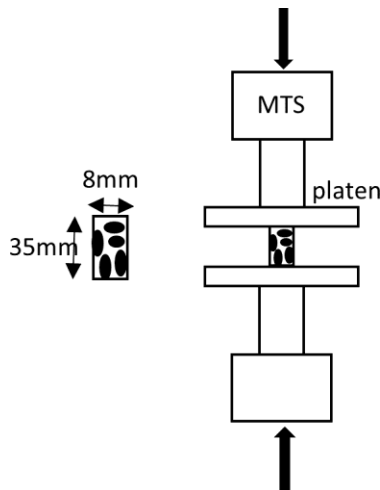
Figure 9: Platen technique [Keaveny et al., 1997]

Due to their porous structure, the cut out trabecular bones will have their mutual support lessened near the cutout surfaces leading to higher deformations in this region adjacent to the platen in axial loading underestimating the elastic modulus. Also, the higher friction near the platen-bone surface interface will overestimate the elastic modulus as the central region is strained less than the bottom and top surfaces and so higher compressive forces are needed to deform the specimen. The net effect of the overestimation due to friction and underestimation due to

11

structural end phenomenon gives an underestimated modulus of approximately 20% [Odgaard and Linde, 1991]. To diminish this end artifact error, 4-extensometer and endcap techniques were implemented [Keaveny, 1997]. In the 4-extensometer technique, specimens were press-fitted into brass endcaps with an extensometer attached to the surface to eliminate end-artifacts of deformations measured around the specimen. In the endcap techniques, the extensometers were attached to the end of the endcaps. Both methods were more accurate as the non-linear toe region in the modulus curve from the compressive platens technique were mitigated [Keaveny, 1997]. The ultrasonic method is able to measure properties in the three principal directions without end-artifact errors or errors induced due to irregular machine shaped of the specimens [Cowin, 2001]. However, one of the limitations of the ultrasonic method is that the actual length of the ultrasonic wave is unknown and the calculation of velocity is based on the overall length of each specimen, which is probably shorter than the actual pathway length that the ultrasonic wave traveled in the specimen [Cowin, 2001]. The ultrasonic method measures the average in the entire specimen, which does not take into account the heterogeneity of trabecular bone [Cowin, 2001]. In addition, the tissue density of the microspecimen cannot be measured accurately using the ultrasonic method and therefore micro- and continuum level of specimens had similar modulus reported [Cowin, 2001]. The nanoindentation method, on the other hand, is usually used to measure tissue level properties as this method allows measurement at the microscopic level [Cowin, 2001] such as trabeculae. However, in this work, the trabecular bone computational model required properties at a continuum level (whole vertebra) as the trabecular bone structure is porous and therefore the architecture and structure of the trabecular bone affect the properties at a continuum level.

The trabecular bone properties utilized in this work are from a study that performed quasi-static compressive and tensile tests of trabecular bone from human cervical spines [Liu, 2013]. This experiment was utilized as they have specifically utilized trabecular bone samples from the human cervical spine and there is a lack of data involving experimentation of these samples. Most data of human vertebrae involves specimens from the thoracic spine [Kopperdahl and Keaveny, 1998] or lumbar spine [Lindahl, 1976].

2.4 Factors Affecting Bone Mechanical Properties: Strain Rate, Age, and Gender Effects

2.4.1 Strain Rate

Hard tissues have been reported to be viscoelastic or rate-dependent [Sanborn, 2016, McElhaney, 1965, Shim, 2005]. McElhaney (1965) predicted that under compression with increasing strain rate from 0.001 to 1500 s^{-1}, human cortical bone specimens exhibit increasing modulus, have a higher failure stress, but demonstrate a lower failure strain. Sanborn (2016) tested cortical bone over a strain rate range from 0.0001 to 26 s^{-1} and found similar results to McElhaney (1965). In contrast, Hansen (2008) found that under compression with strain rates ranging from 0.14 to 29 s^{-1}, the failure stress for cortical bone in human specimens increased from low to intermediate strain rate, reaching a peak at approximately 20 s^{-1} and then decreased after. Hansen (2008) found that as the strain rate increased from 0.08 to 17 s^{-1} in tension, the peak force and displacement decreased and the Young's modulus increased. In contrast, according to another study by Melnis and Knets (1982), the ultimate strength increased with strain rate from 10^{-5} to 1s^{-1} but the initial Young's modulus remained constant. Therefore, the results of these studies

regarding the effect of strain rate are inconsistent. It had been discussed that the results of these studies may vary depending on the specimen moisture content [Sanborn, 2016; Yamashita, 2000] as the mechanical behavior of collagen in bones is hydration dependent. Furthermore, embalmed specimens used in a few experiments may alter the measured mechanical properties. Although short-term preservation did not cause any changes, there was a significant difference when specimens were preserved long-term in formalin concentration [Sanborn, 2016; Ohman, 2008]. By keeping the specimen moist in a saline water bath rather than embalming fluid, the ductile to brittle transition was found to be delayed [Hansen et al., 2008]. Besides that, different test methods as well as different ranges of strain rates over which the experiments were performed may contribute to differences in the results. Furthermore, although the literature examples listed in the studies in this section all use human specimens, due to the small amount of experimental data involving human specimens, results in several studies were often compared with other studies that use equine, porcine, or bovine specimens [Hansen et al., 2008]. The differences in results found may also be confounded by variations in the microstructure of bones between species.

Apart from that, the mechanical properties of trabecular bone are affected by the presence of the marrow or interstitial fluid [Hayes and Carter, 1977] but the contribution of this material is difficult to quantify as it depends on the experimental conditions [Halgrin et al., 2012]. Previous non-destructive testing on unconfined specimens (opened cells) [Chaari et al., 2007; Carter and Hayes, 1977] or confined specimens (closed cells) [Chaari et al., 2007; Charlebois et al., 2010] were performed in compression. In the unconfined compression experimental testing simulating the boundary conditions of flat bones, the maximum compressive stress, the elastic modulus and the maximum strain decreased with the presence of marrow [Halgrin et al., 2012]. The mechanical softening confirms the fluid flow pressure effect hypothesis in which the transverse stress or pressure created in the sample by the marrow flow increases the transverse strain applied on the trabecula, causing the premature collapse of the trabecula [Halgrin et al., 2012]. In unconfined compression tests with the presence of marrow, it was found that the fluid effects were only observed for strain rates higher than 10 s^{-1} [Carter and Hayes, 1977]. This confirmed that the marrow effect only affected the viscoelastic behavior of trabecular bone in traumatic compressive loading and the trabecular bone was not hydraulically strengthened by the presence of marrow under moderate, physiological loading conditions [Carter and Hayes, 1977]. Under confined conditions, the fluid flow is prevented and therefore the fluid and marrow that were expelled in the unconfined tests remained within the specimen and contributed to the increase in stiffness and strength after the collapse of the trabeculae [Chaari et al., 2007; Charlebois, 2010]. In a compressive strain rate study within 100 s^{-1} and 1200 s^{-1}, utilizing fresh human cervical spine trabecular bone [Shim et al., 2005], it had been found that the ultimate stress and strain, and Young's modulus increased with strain rate, agreeing with the data from Carter and Hayes (1977). However, due to the variability in data, it was discussed that the influence of strain rate was as important as the composition of the bone tissue and trabeculae orientation. It was concluded that apparent density was a more important factor than strain rate.

In summary, studies regarding the effect of strain rate of the mechanical properties of cortical and trabecular bone demonstrated inconsistencies in results. In tension, for cortical bones, the specimens demonstrated higher ultimate stress in tension and in compression with increasing strain rates [Sanborn, 2016; McElhaney, 1965]. However, another study found contradicting results in which the specimens had lower peak force in tension with increasing strain rate

13

[Hansen et al., 2008]. One author has suggested that this variability may be due to the biological differences in the bone between specimens such as the mineral content, microstructural flaws, and variation in the osteon size or the orientation relative to the loading direction [Sanborn, 2016]. However, due to the lack of data in strain rate effect on the asymmetry and anisotropy mechanical properties of both cortical and trabecular bone (cervical), strain rate effect was not included in this study.

2.4.2 Bone Density, Age and Gender Effects

An important factor related to variations in the mechanical properties of bone is the apparent bone density. The apparent bone density is the mass per unit volume of a region of bulk bone [Martin et al., 1998]. It is necessary to be cautious of the various bone density measurement techniques utilized in different studies. One invasive method would be to measure the mass of defatted bone after testing and divide by the total initial specimen volume [Shim, 2005]. Non-invasive methods include X-ray, calibrated computer tomography (CT) imaging or the dual energy x-ray absorptiometry (DEXA or DXA) methods. Ash density is the ash weight per unit total sample in which the samples are incinerated and has been found to provide results similar to apparent density [Mosekilde, 1987].

Considering the vertebrae of 57 subjects with the average age of 25, it was found that bone mineral density (BMD) varied between vertebra levels [Yoganandan, 2006] such that the BMD was highest in C2 ($274.0mg/cm^3$) and lowest in L3 ($169.7 mg/cm^3$). In terms of cervical spine, the BMD of C2 ($274.0mg/cm^3$), C4 ($270.1mg/cm^3$), and C5 ($268.3mg/cm^3$) were significantly greater than BMD of C3 ($256.2mg/cm^3$) and C6 ($242.6mg/cm^3$) [Yoganandan, 2006]. The BMD of C3 ($256.2mg/cm^3$) was significantly greater than BMD of C6 ($242.6mg/cm^3$) [Yoganandan, 2006]. In comparison with another study [Zink et al., 1997] in which the average subject age of the specimens was 57.6 years for females and 54.4 years for males, the mean BMD of the C4 to C7 specimens were $200.7 mg/cm^3$, agreeing that BMD decreases with increasing age [Yoganandan, 2006].

The microstructure of bone defines its mechanical properties and it had been found that the percentage osteonal or channel area in cortical bone increased with age [McCalden, 1993]. In cortical bones, in general, both tensile and compressive mechanical properties showed a decline with age [Burstein, 1976; McCalden, 1993] as porosity increases. The ultimate tensile strength was reported to decrease at a rate of approximately 2.1% per decade [Burstein et al., 1976] and 5% per decade in a subsequent study [McCalden et al., 1993]. The ultimate tensile strain was reported to decrease by approximately 9% per decade [McCalden et al., 1993] and 5.1% per decade in a prior study [Burstein, 1976]. The decreasing fracture energy (12% per decade) or toughness with age had been linked to the brittleness of aged cortical bone [McCalden et al., 1993]. There is controversy concerning the elastic modulus such that, one study found the elastic modulus to decrease by 1.5% per decade [Burstein et al., 1976], whereas another found that the elastic modulus did not change with increasing age [McCalden et al., 1993]. For compression, the elastic modulus, and ultimate stress decreased by approximately 2.2% and 2.5% per decade respectively [Burstein et al., 1976].

For vertebral trabecular bone, it had been found that there was a decline in ash density of about 50% from the age 20 to 80 years and subsequent declination in energy absorption capacity, ultimate strength and elastic modulus [Mosekilde, 1987]. The ultimate strain, on the other hand, appeared to increase in vertebral trabecular bone with increasing age [Mosekilde, 1987].

However, in trabecular bones, the age-related changes depend not only on changes in density but also on the trabecular architecture [McCalden, 1997; Mosekilde, 1993]. In vertebral bodies, with age, changes in internal architecture due to remodeling, dimensions and cortical thickness affect the bone strength [Mosekilde, 1993]. As a person ages, the osteoclastic perforation of horizontal trabeculae in the vertebral trabecular lattice structure showed no signs of re-establishment [Mosekilde, 1993] and led to a discontinuous lattice structure that compromised the structural integrity. This disappearance of the horizontal struts increased the anisotropy of trabecular bone in vertebral bodies [Mosekilde et al., 1985]. The disappearance of these struts caused the slenderness ratio of the remaining vertical trabeculae to reach a critical size of about 100: 1 resulting in elastic buckling and bending which decreased the strength [Mosekilde et al., 1985]. It had also been found that the bone loss in men accelerated from the age 50 due to the decrease in free androgen causing a decrease in bone formation [Wishart et al.,1995].

Age effects on the strength of the whole cervical spine had also been studied. The compressive failure load of the cervical spine was found to be the highest (418kg) in the 20 to 39 age group and least (190 kg) in the 60 to 79 age group [Yamada, 1970]. A scaling factor of 1.2 to 1.3 had been suggested in a study by Myers [Myers et al., 1995] based on the aforementioned studies such that the cervical spine tolerance for the young human cervical spine is 3.44±0.881 kN [Myers et al., 1995]. Pintar et al. (1998) found that the compressive tolerance for a human cervical spine varied from 7 kN in the young (30 years old) to 2 kN in the aged (90 years old). However, this study found that there were considerable interactions between the effects of loading rate, age, and gender [Pintar et al., 1998].

In terms of gender effects, the estimated vertebral strength was 22% greater in young men (22 to 29 years old) than young women (22 to 29 years old) due to their larger cross-sectional area and the vertebral strength declined more in women than men with age (-43% versus -31% from 20 to 90 years old) [Bouxsein et al., 2006]. Females tend to lose more BMD than males (-55% versus -39% from 20 to 90 years old) [Bouxsein et al., 2006] which would lead to the greater loss of strength at a higher rate [Yeni et al., 2011; Bouxsein et al., 2006]. The accelerated bone loss in women is caused by the onset of menopause, which causes a decrease in estrogen level [Leboff, et al.,1999]. The lower tensile and compression failure load in females is approximately 83% that of male due to size [Yamada, 1970]. A subsequent study however determined the effect of gender to be a constant 600 N difference between men and women [Pintar et al., 1998] and the female mean was 75% that of the male. The differences seen could be due to the fact that the latter study utilized majority of their samples from the 50 to 95 year old age group [Pintar et al., 1998] and so the increased effect of osteoporosis resulted in lower values than prior study [Yamada, 1970].

Lifestyle, nutrition, and genetics also contribute to variability in bone density, and therefore variation in mechanical properties. However, in general, bone density decreases with age and gender which results in a decrease in mechanical properties with age. Although gender influences the mechanical properties and strength of the vertebra, it is not as significant as age. This study also found that there is an interactive effect between age and loading rates such that loading rate has a greater effect on younger age groups than older [Pintar et al., 1998]. Burst fractures occur at high rates of loading due to the build-up for marrow fluid pressure and the viscosity of the marrow fluid is affected during aging [Pintar et al., 1998]. The lack of interactive effect between age and loading rates in older age groups could be explained due to the decreased mineralization and increase bone marrow fat content with age that might affect the viscosity

[Pintar et al., 1998]. Therefore, in this work, only the effect of age on mechanical properties is taken into account as it is more significant than gender and the effect of strain rate is inconclusive.

2.5 Anatomy and Structure of the Human Cervical Spine

2.5.1. Anatomical Terms

Anatomy is the study of the structure of the human body. The anatomical position that has been adopted globally refers to the body position as if the person was standing upright with the head, gaze and toes directed forward, arms adjacent to the sides with the palms facing forward and lower limbs close together with the feet parallel [Moore et al., 2018] (Figure 10).

There are four anatomical references planes within a body: median, frontal, transverse, and sagittal plane. The median plane or median sagittal plane passes longitudinally through the midlines of the head, neck, and trunk, dividing the body into left and right [Moore et al., 2018] (Figure 10). The frontal plane is a vertical plane that intersects the body in the front and back, the transverse plane is a horizontal plane at right angles to the median and frontal planes that divides the body into top and bottom and the sagittal plane divides the body into right and left [Moore et al., 2018] (Figure 10). The main use of planes is to describe sections such as longitudinal, transverse, and oblique sections. Longitudinal sections are parallel to the long axis of the body whereas transverse sections are cross sections that are perpendicular to the longitudinal axis. Oblique sections on the other hand are slices that are cut at an angle away from the sagittal, frontal, or transverse planes.

Anatomical terms are used to describe the directions within the body with respect to reference planes and regions. The anatomical terms are usually in pairs of opposites. For examples, superior refers to the structure that is near the topmost point of the cranium called the vertex whereas inferior refers to the structure that is near the sole of the feet [Moore et al., 2018] (Figure 10). Similarly, cranial and caudal refers to the top most point in the specimen and bottom most respectively (Figure 10). Posterior or dorsal refers to the back surface of the body whereas anterior or ventral refers to the front (Figure 10). Medial denotes a structure that is nearer to the median plane of the body whereas lateral denotes a structure that is moving further away from the median plane along the frontal plane [Moore et al., 2018] (Figure 10).
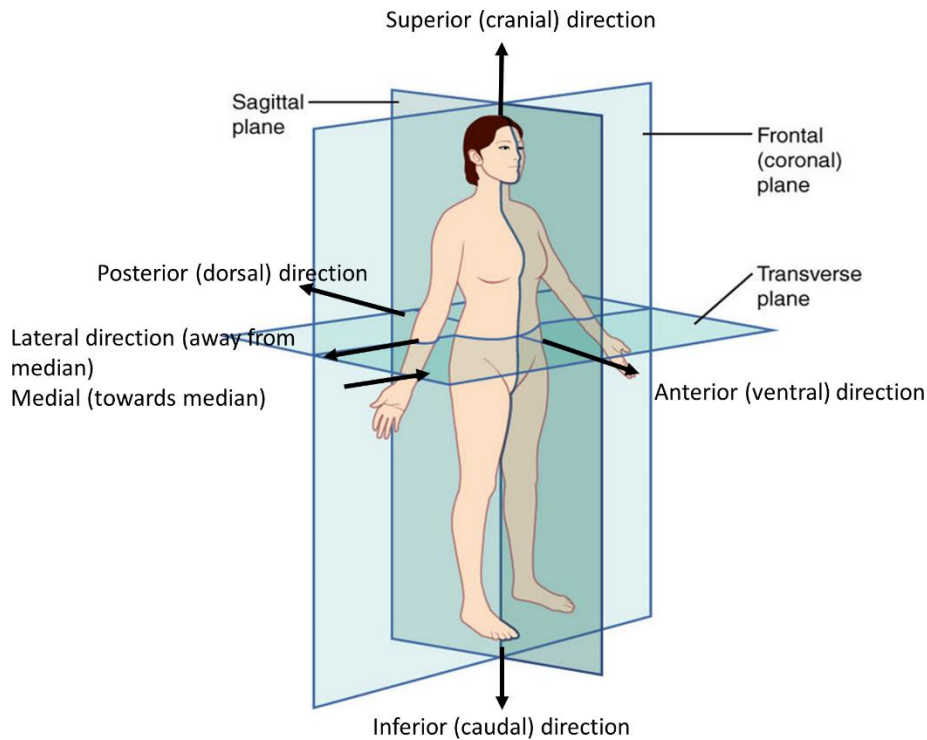
(Image adapted from https://commons.wikimedia.org/wiki/File:Planes_of_Body.jpg)

Figure 10: Anatomical terms for planes and direction

The anatomical terms for the movement of the head and neck are flexion, extension, lateral, and rotation. Flexion denotes bending towards the anterior direction whereas extension is bending towards the posterior direction (Figure 11). Lateral flexion or bending denotes bending movement of the head or neck to the right or left around the antero-posterior axis in the front plane (Figure 11). Axial rotation involves turning the head around its longitudinal axis [Moore et al., 2018] (Figure 11).
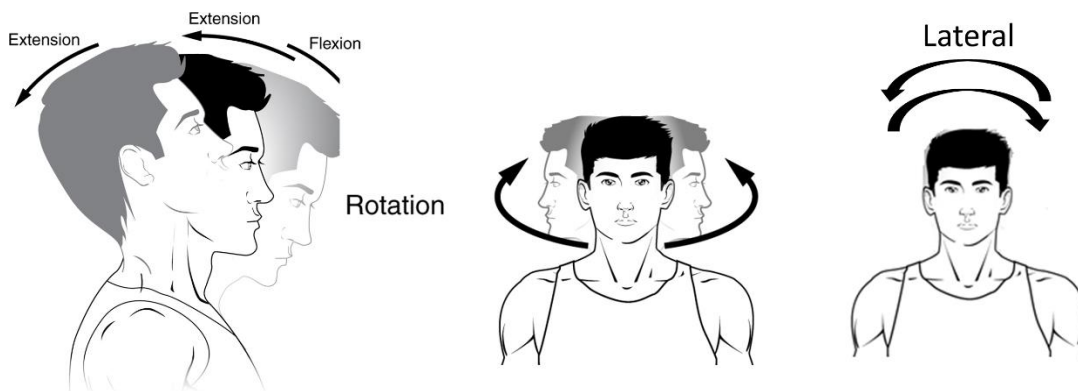
(Image adapted from: https://en.wikipedia.org/wiki/Anatomical_terms_of_motion)

Figure 11: Anatomical terms of motion

2.5.2. Anatomy, Structure of the Cervical Vertebrae

The cervical spine comprises seven vertebrae that form eight motion segments between the occiput (C0), which is the base of the skull, and the first thoracic vertebra (T1) [Myers and Winkelstein, 1995] (Figure 12). The cervical spine is generally divided into two regions, the upper and lower cervical spine regions. The first cervical vertebra (atlas or C1) and second cervical vertebra (axis or C2), form the upper cervical spine region. The third to seventh cervical vertebrae (C3 to C7) constitute the lower cervical spine [Singh, A.P., 2017].
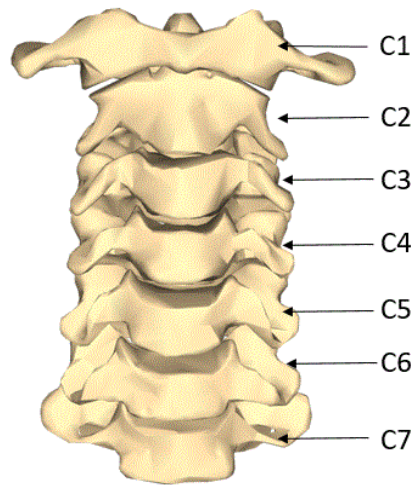
(Adapted from https://commons.wikimedia.org/wiki/File:Cervical_vertebrae_-_close-up_-_anterior_view.png)

Figure 12: Cervical spine column

There is a distinct difference in the shape and function of the axis and atlas in comparison to the lower cervical spine. The atlas is composed of a bony ring that is divided into an anterior and posterior arch and lateral masses (Figure 13). The lateral masses of the ring are enlarged facet articular surfaces that articulate with the occipital condyles of the skull.
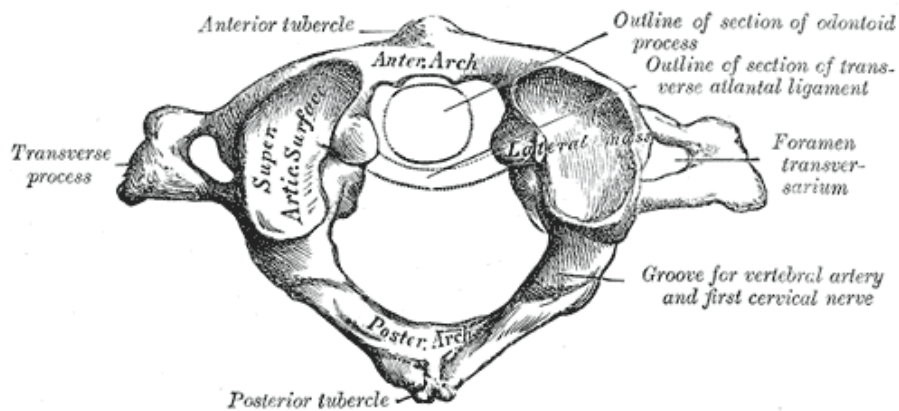
(Image from Gray, 1918)

Figure 13: Structure of the atlas

The axis is composed of a cylindrical vertebral body and a bony posterior arch, similar to the lower cervical vertebrae but including the dens or odontoid process (Figure 14). The odontoid process projects superiorly from the axis between the lateral masses of the atlas and forms a synovial articulation with the posterior surface of the anterior arch of the atlas.
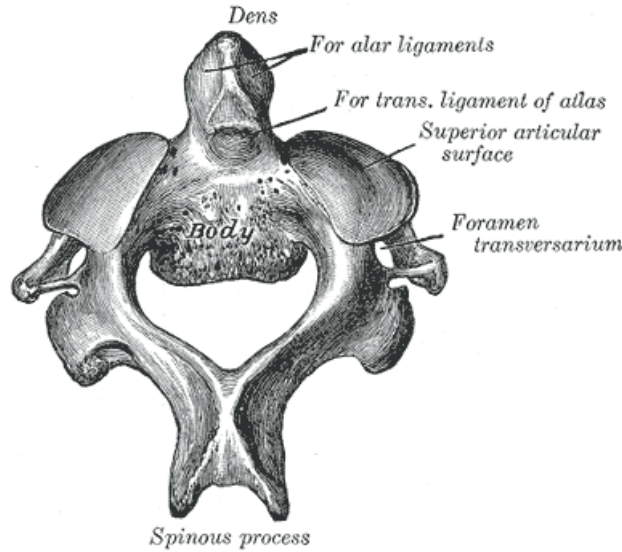
(Image from Gray, 1918)

Figure 14: Structure of the axis

The posterior arch or elements of the lower cervical vertebrae (Figure 15) consist of the pedicles, laminae, spinous process, transverse processes and superior and inferior facet surfaces.
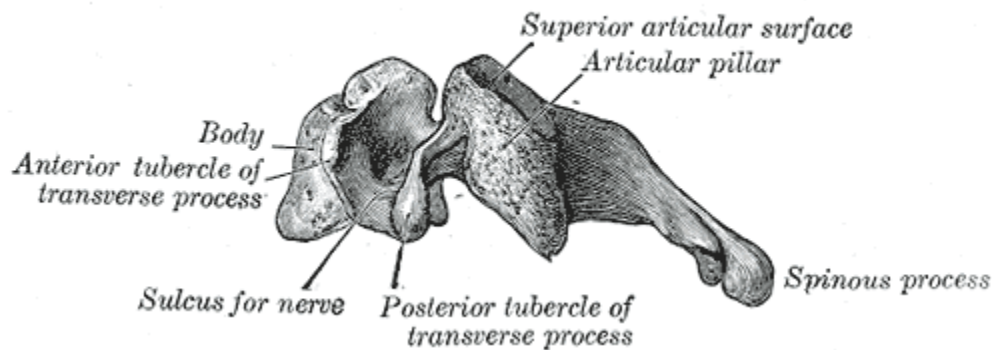
(Image from Gray, 1918)

Figure 15: Lateral view of a lower cervical spine vertebra

These structures contribute to the range of motion of the spine, protect the spinal cord from direct trauma, and provide spinal musculature attachment sites [Myers and Winkelstein, 1995]. The pedicles form a connection between the postero-lateral surfaces of the vertebral bodies and the articular process (Figure 16).
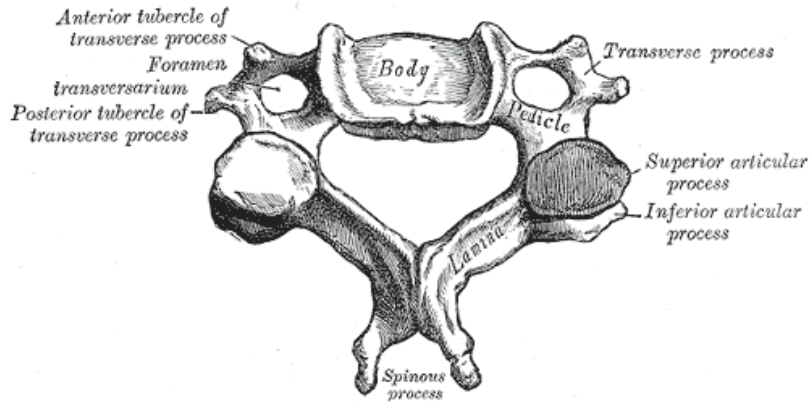
Figure 16: Top view of a lower cervical spine vertebra

The facet surfaces are flat and obliquely oriented structures on the superior and inferior surface of the articular process. In addition, the transverse processes project laterally from the pars interarticularis which is the part between the inferior and superior articular process of the facet joint and connect to the vertebral body. The laminae are posterior bony plates, enclosing the spinal cord whereas the spinous process is the posterior midline fusion of the two laminae [Myers and Winkelstein, 1995].

The lower cervical spine vertebrae are similar in shape but progressively increase in size towards the inferior location of the spine (Figure 20). The lowest cervical vertebra segment, C7 changes slightly in shape such that it has a long spinous process and the transverse processes are larger in size [Singh, 2017]. The vertebral canal encloses the spinal cord, which is enclosed anteriorly by the vertebral body and posteriorly by the neural arch, which is the posterior bony structures of the vertebra. A FSU consists of two adjacent vertebrae, intervertebral disc, and ligaments (Figure 17). In this work, a model of the C567 segment comprising of two functional spinal units (FSUs) was utilized.
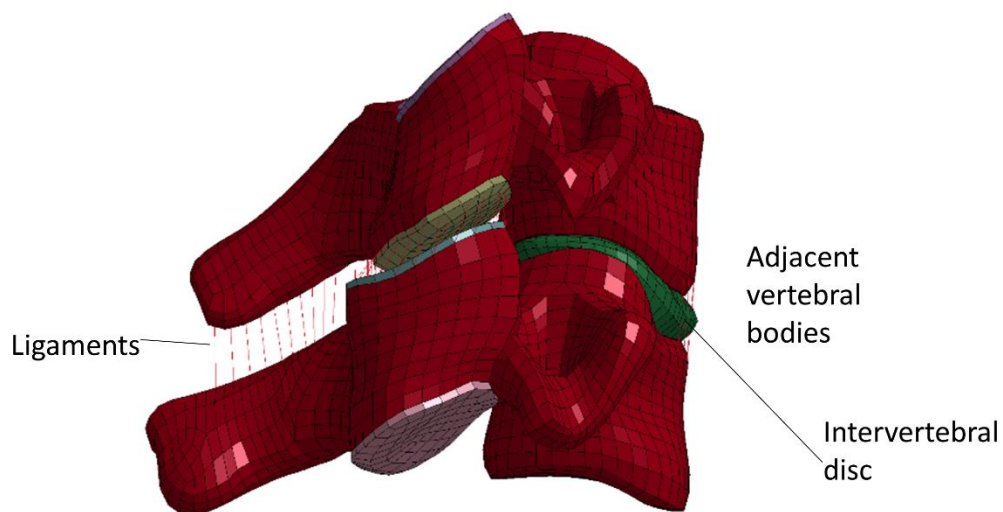
Figure 17: A functional spinal unit (FSU) Finite Element Model [GHBMC]

20

In between adjacent vertebral bodies are the intervertebral discs (IVD). The IVD consists of three components: the nucleus pulposus, the annulus fibrosus and the ground or annulus matrix (Figure 18). The nucleus pulposus is an enclosed fluid constituting of water in a matrix of proteoglycans, collagen, and other matrix proteins [Iatridis et al., 1996]. The nucleus exhibits a solid-like behavior under dynamic conditions but fluid-like at slow deformation rate and this transition from "fluid" to "solid" is also seen with aging and degeneration [Iatridis et al., 1996; Iatridis et al., 1997].
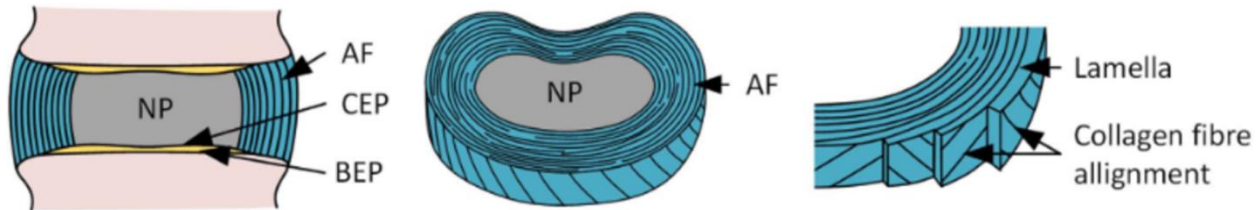
(Image from Newell et al., 2017)

Figure 18: Components of the intervertebral disc with the collagen fibre alignment in each lamella layer (NP: nucleus pulposus, AF: annulus fibrosus, CEP: cartilaginous endplate, BEP: bony endplate) [Newell et al., 2017]

The annulus fibrosus are laminae of collagen fibers. The outer layer consists of Type I collagen fibers and gradually changes to Type II as the layer progresses closer to the nucleus pulposus. An important characteristic of the annulus fibrosus is that the successive lamellae consist of collagen fibers that are oriented alternately at approximately 30 degrees and 150 degrees to the transverse plane (Figure 18) [Skaggs et al., 1994].

In the lower cervical spine, the main ligaments are the anterior longitudinal ligament (ALL), posterior longitudinal ligament (PLL), interspinous ligament (ISL), ligamentum flavum (LF) and the capsular ligament (CL) (Figure 19). The ALL is a long and wide band of fibers that is attached from the atlas and runs down to the sacrum anteriorly [Moore et al., 1999]. The ALL is firmly attached to the anterior edges of the intervertebral discs and vertebral bodies whereas it is more loosely attached at the middle region of the vertebral bodies when it is concaved inwards [Gray, 1918]. The PLL on the other hand begins at the C2 and runs to the sacrum along the posterior region of the vertebral bodies in the vertebral canal. The PLL is narrower than the ALL but is widest and most firmly attached at the intervertebral discs [Moore et al., 1999].
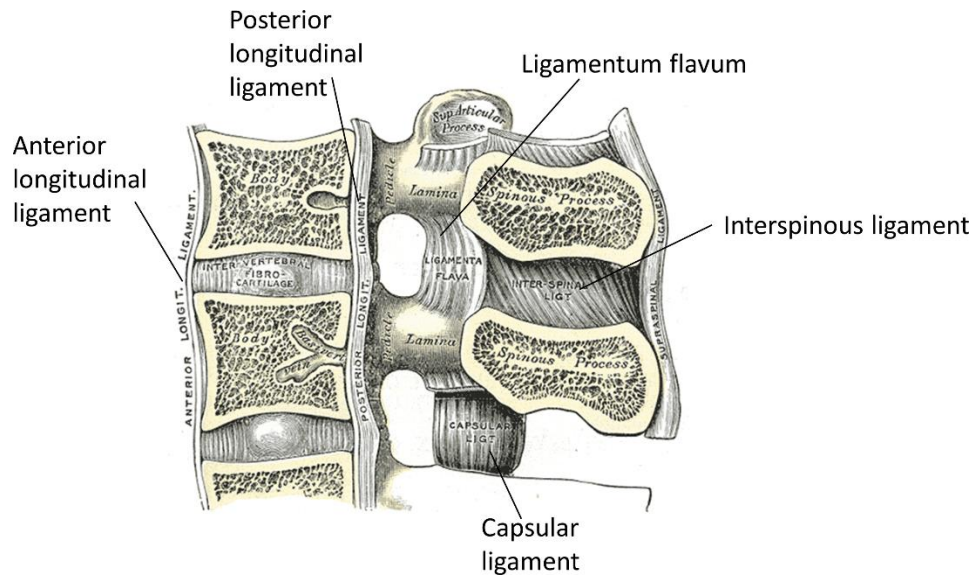
Figure 19: Ligaments in the lower cervical spine

The ligamentum flavum (LF) is found between the adjacent laminae, within the vertebral canal and posterior to the spinal cord. These elastic ligaments exist between vertebrae from the C2 to the sacrum [White et al., 1990]. The capsular ligaments (CL) attached adjacent articular processes, surrounding the facet joints. These ligaments fully enclose the joint to contain the synovial fluid. The interspinous ligament (ISL) attaches adjacent spinous processes, and ligaments are found from the root to the tip of each process [Moore et al., 1999; Gray et al., 1918]. This thin and weak ligament is in contact anteriorly with the LF whereas its posterior edge is in contact with the supraspinous ligament which is a strong ligament running along the posterior region of the spine that are more present from the C7 to the sacrum and underdeveloped in the cervical spine [Moore et al., 1999; Mattucci, 2011].
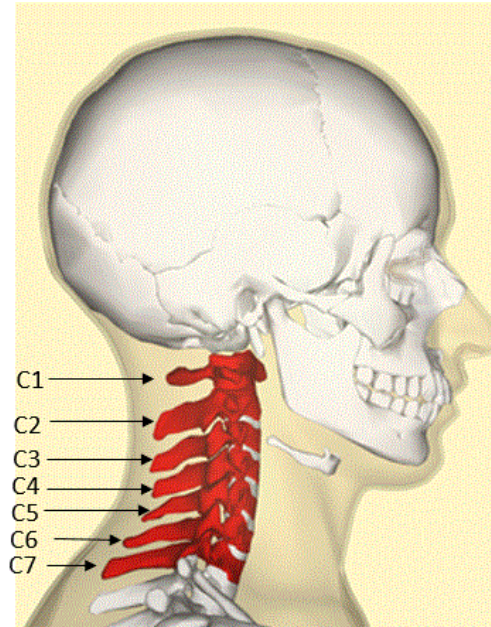
Figure 20: Lateral view of the cervical spine column

The structure and architecture of bones differ between anatomical regions. For example, in long bones, the epiphysis or ends composes of trabecular bone surrounded by a thin layer of cortical bone whereas the diaphysis or shaft has a thick layer of cortical bone surrounding a hollow bone marrow tube. As this research is focused on the cervical spine, the structure of the vertebra will be explained in detail. The vertebrae are composed mostly of low density trabecular bone with a thin layer of stiff, high density cortical shell (Figure 21).
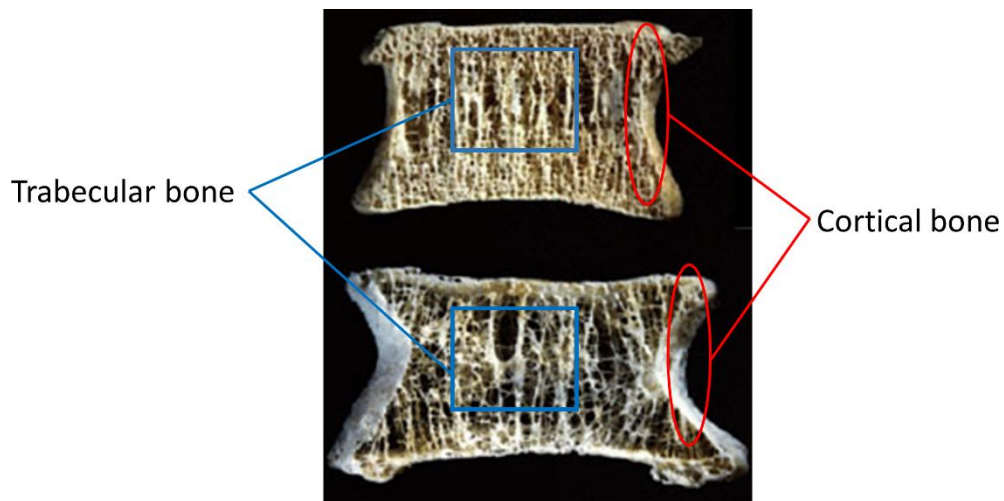
Figure 21: Structure of cervical vertebral column with the dense cortical bone surrounding the porous trabecular bone. The top image shows a high-density specimen whereas bottom image shows that of a low-density vertebra.

Based on studies on the role of cortical shell and trabecular bone in the vertebra, the maximum fraction of load supported by the cortical shell is at the midsection of the vertebra whereas the maximum load fraction taken by the trabecular bone is at the endplates [Eswaran et al., 2006; Cao et al.,2001]. The nucleus pulposus induces a quasi-static stress concentration that transfers the force directly to the trabecular bone underneath the endplate when the vertebra encounters axial loading. Due to the stiffness of the cortical shell, the endplate deflects more into the soft trabecular body upon axial loading, which increases the stress in the trabecular bone. However, as the load progresses towards the mid-transverse plane, the load-carrying role of the cortical shell increases [Cao et al., 2001].

According to Mosekilde et al. [1993] and Silva et al. [1994], the cortical shell and endplates around the vertebra resemble condensed and fused trabecular bone rather than a typical cortical bone structure. Scanning electro microscope (SEM) micrographs have shown that the outer layer of the cortical shell is more chaotic and canal filled than the trabecular bone structure whereas the inner layer was less mineralized and more lamellar-like, similar to a trabecular bone structure. A study by Arnold [1970] reported the inner third of the cortical shell to be lamellar (trabecular) and the remainder to be Haversian (cortical). However, although microstructurally different, Roy et al. [1999] had measured the elastic modulus of the cortical shell to be approximately 18GPa longitudinally and 16GPa transversely, which is similar to cortical bones from other anatomic regions. There are no experimental studies on the mechanical properties of cortical shell of the vertebra, probably due to the thin structure and difficulty in extracting the cortical shell from the samples and conducting mechanical tests on them. Therefore, the properties of the cortical bone of the vertebral body in this work were retrieved from experimental studies that measured cortical bone mechanical properties from long bones [Reilly and Burstein, 1974].

As mentioned in Section 2.3, the architecture is highly dependent on density and higher density specimens from the femoral head or bovine trabecular bones have more of a plate-like structure whereas lower density specimens from the cervical vertebral body have more of a rod-like structure [Gibson et al., 2005; Keaveny et al., 2001, Amling et al., 1996]. The tensile stress-strain curve of the trabecular bone in human vertebra specimen presented a nonlinear increase in slope up until an ultimate failure point before material softening is seen [Liu, 2013] (Figure 22).
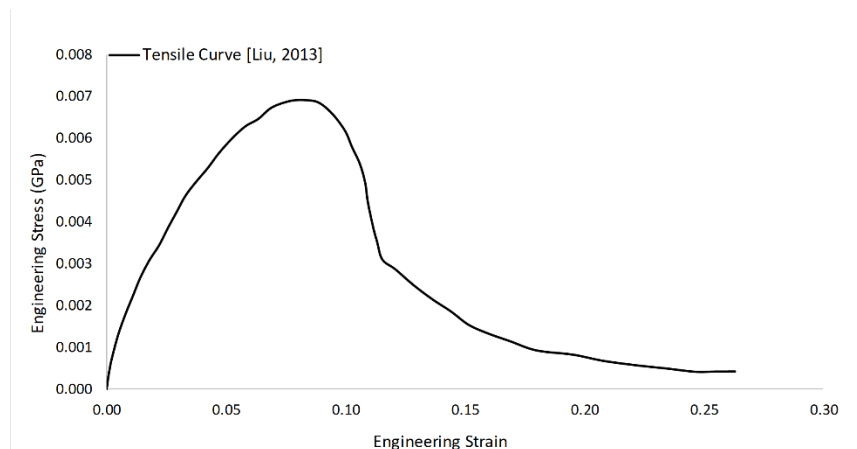
Figure 22: Typical tensile curve of trabecular bone sample from human vertebral body [Liu, 2013]

24

2.6 Epidemiology

Traumatic SCI resulting from impact and fracture of the vertebra can cause complete or incomplete paralysis leading to permanent or temporary disabilities. Depending on the injury severity, persons with SCI face high lifelong healthcare expenses and a decrease quality of life [Ge et al., 2018]. Almost half of the MVA cases (43% in Australia [O'Connor, 2002] and 45% in USA [Go et al., 1995]) resulted in traumatic SCI. A high percentage (85%) of vehicle rollovers resulted in SCI [Thurman et al., 1995] although approximately only 3% of MVAs [Foster, 2013] are related to rollovers. In USA from 2003 to 2014, the leading cause of traumatic SCIs are falls (22%), followed by MVAs (12.7%) and violence (6.1%) [Ge et al., 2018]. Most of the patients (31% of 685 subjects) who experience SCI were diagnosed to be due to falls [Ge et al., 2018]. A high proportion of SCI patients from falling (21.7%) are of the aged population (65 years or older), whereas 8.5% of aged SCI patients are from motor vehicle accidents [Ge et al., 2018]. In terms of the young SCI patients below the age of 35, most (27.7%) are diagnosed with SCI from MVAs followed by violence (25.2%) [Ge et al., 2018]. In another study on the traumatic SCI in the USA between 1972 to 2014, MVAs were found to be the leading cause of SCI although there is a decrease in percentage from the 1970s (47.0%) to between 2010 to 2014 (38.1%) [Chen et al., 2016]. Besides that, SCI due to falls increased especially in patients of the age 46 and above [Chen et al., 2016]. There has also been a higher incidence rate of SCI cases (87.7 new cases per million in 2009) amongst aged patients above the age of 65 than younger patients below the age of 65 (49.9 new cases per million) which would agree with the findings that the percentage of new SCI cases in aged victims above 65 years has increased from 3.1% in the 1970s to 13.2% in 2010 to 2014 [Chen et al., 2016].

The injury patterns of the spinal column that causes SCI are dislocation (45-58%) and burst fracture (9-35%) [Mattucci et al., 2018]. Burst fractures are typically due to compression of the vertebra whereas dislocation is due to shear. When burst fractures occur, fragments of bone may break off and cause spinal canal occlusion whereas when dislocation occurs, there is a significant amount of translation or sliding between two vertebrae. In rollover MVAs, axial compression is the usual loading mode on the cervical spine [Foster, 2013; Raddin, 2009] which may induce spine fracture [Argenson et al., 1997]. More than half (64%) of MVA patients with SCI experience fractures and burst fractures are reportedly the most common fracture type (48%) [Pickett et al., 2006]. Although controversy exists, it has been shown that injury is most common between the C4 and C6 vertebrae [Myers and Winkelstein, 1995]. The C5 and C6 vertebrae were found to be one of the highest injured zones in cervical spine injuries among survivors of MVA [Yoganandan et al., 1989]. In terms of fatal spinal injuries from MVA, the occiput, C1 and C2 vertebrae are the most common trauma sites [Yoganandan, 1989; Myers and Winkelstein, 2005]. In addition, in a study including fatal and nonfatal MVA injuries, the uppermost cervical spine segment, C1 was the most common with the lower cervical spine segment (C5-C7) being the next most common [Myers and Winkelstein, 1995]. This work focuses on the lower cervical spine segment, C57 due to available experimental data [Carter et al., 2003; Van Toen et al., 2014] to simulate.

2.7 Hard Tissue Injuries of the Cervical Spine

The Allen-Ferguson classification [Allen et al., 1982] is the most comprehensive system that classifies injury patterns based on the position of the spine at the time of injury allowing one to deduce the mechanism of injury. The mechanism of cervical spine injuries involves compression,

tension, or shear with a combined load state such as flexion, extension or lateral bending [Myers and Winkelstein, 1995]. As this thesis focuses on hard tissue failure or fractures due to compression loads, injuries from compression loadings are discussed.

According to Allen et al. [1982], there are six mechanistic classifications of lower cervical spine injuries: vertical compression, compressive flexion, compressive extension, distractive extension, distractive flexion, and lateral flexion (Figure 23). The vertical compression, compressive flexion, compressive extension, and lateral flexion were identified as loading classifications that involve hard tissue fracture [Allen, 1982].
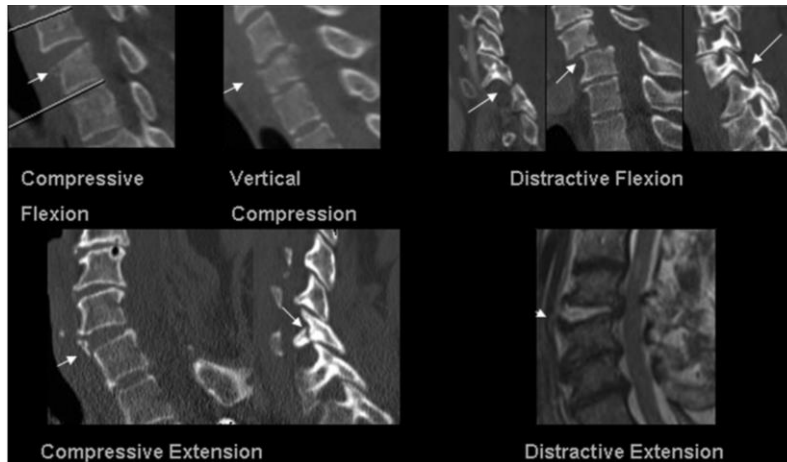
(Reprinted by permission from Oxford University Press, Aarabi, 2013)

Figure 23: Five of the Allen Ferguson classifications for lower cervical spine injuries

Lower cervical spine injuries are usually due to compression in which Allen et al. [1982] reported a peak occurrence at the C6-C7 and C7-T1 segments. When the lower cervical spine is compressed axially, the intervertebral disc bulges, the nucleus pulposus presses into the vertebral body and fractures it [Maiman et al., 1983]. Further compression would result in the disc and vertebral body fragments being pushed anteriorly or posteriorly into the spinal canal [Maiman et al., 1983].]. Burst fractures arise from the failure of vertebral body endplate due to the increased intervertebral disc pressure upon compression which forces the nucleus pulposus into the adjacent vertebral body [Mattucci, 2018]. This would lead to the comminution of fractures with fragments protruding into the vertebral canal. Burst fractures (Figure 24) were seen in specimens that had a slight flexion [McElhney et al., 1983] or straight configuration [McElhaney et al., 1983; Carter et al., 2000; Pintar et al., 1995] within the eccentricity of approximately 1.0 cm.

Figure 24: Burst fracture

Compression-flexion fractures were the most common MVA injuries in the lower cervical spine amongst survivors [Yoganandan, 1989], particularly in the C56 motion segment or functional spinal unit (FSU) whereas Allen found C45 to be the most frequently injured segment [Allen et al. 1982]. Under compression-flexion, the fractures are usually teardrop, burst, Clay-Shoveler's or wedge compression [Myers and Winkelstein, 1995; McElhaney, 1982; David et al, 2013]. Anterior wedge compression fractures occur in compression loading with approximately an anterior eccentricity value of 1.0 cm [McElhaney et al., 1983]. Wedge fractures are similar to the burst fractures, but only occur at the anterior region of the vertebral body whereas burst fractures occur within the entire vertebral body. The teardrop fracture is a triangular shaped fragment seen in the anterior inferior corner of the lower cervical vertebral [Kazarian, 1981; Babcock, 1976] (Figure 25). Clay Shoveler's fracture is an oblique fracture of the spinous process from the abrupt tension of the interspinous ligaments [David et al, 2013; Edeiken-Monroe et al., 1986].
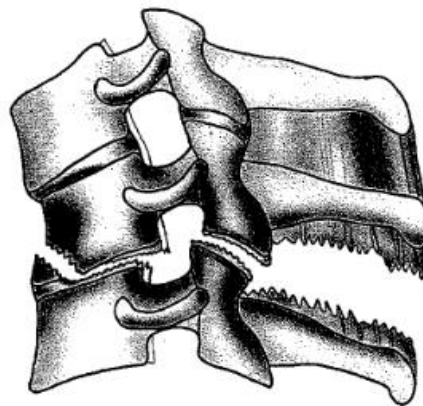
Figure 25: Teardrop fracture

Compression-extension fractures on the other hand would cause rupture of the ALL and compression of the posterior spinal column causing fractures in the lamina or facet [Kazarian, 1981]. Fractures in the vertebral arch, posterior vertebral body, pedicles, facets, lamina, spinous process, and articular process were also noted in a compression-extension loading [Allen et al., 1982; Kazarian, 1981; Babcock, 1976; Forsyth 1964; David et al., 2013].

27

Upper cervical spine compression injuries usually occur at the atlas. Jefferson and multipart atlas fractures involves fractures in the posterior and anterior arches of the C1 vertebra (Figure 26) [Myers and Winkelstein, 1995; Foster, 2013]. Under compression-extension loading, fracture of the pedicles or the pars interarticularis (part between the inferior and superior articular process) of the axis or C2 vertebra [Myers and Winkelstein, 1995] called Hangman's fracture can occur. Other upper cervical spine fractures that involve the C2 vertebra are Type I and Type II odontoid fracture in which Type 1 has only the tip of the odontoid process or the den fractured whereas Type II is at the base of the odontoid process. The injury mechanism for these fracture are hyperextension or hyperflexion of the neck. When the entire cervical spine is compressed in experiment, the upper cervical spine segments may undergo hyperextension or hyperflexion.
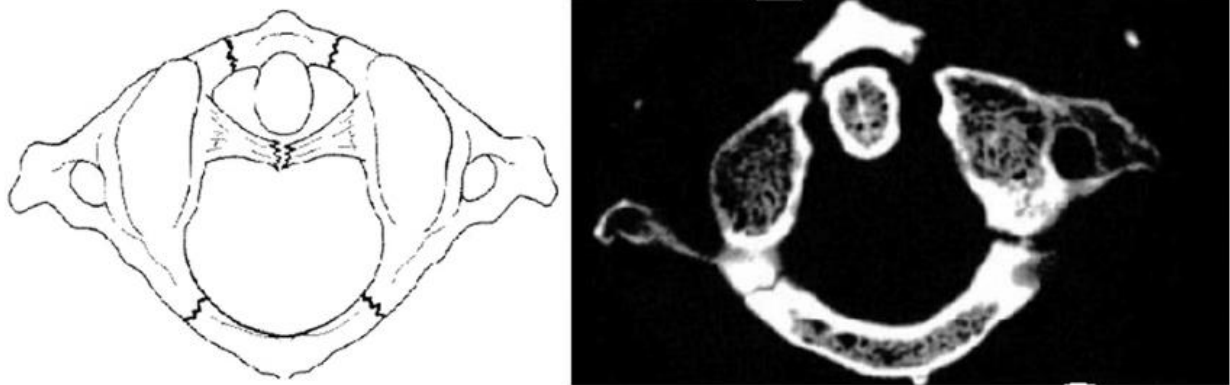
(Reprinted with permission from Elsevier, Kalantar, 2013)

Figure 26: Image and computer tomography scan of a multipart atlas or Jefferson fracture

2.8. Compression Experimental Methods on Cervical Spine for Hard Tissue Failure

Historically, compressive loading experiments to assess the mechanisms of injury of spinal fractures have been done on whole-cadavers, isolated cadaveric spines, functional spinal units (FSU), as well as single vertebrae. The current data and finding of studies at each scale are discussed below.

2.8.1 Whole-cadaver

A study by Yoganandan (1986) involved vertically dropping full cadavers headfirst in an unrestrained and a restrained condition using a special fixture to simulate muscle forces from a height of 0.9 to 1.5 m onto a force plate [Yoganandan et al., 1986]. The restrained cadavers were mostly impacted first on the vertex or highest point of their skull whereas in the unrestrained cadavers, the impact occurred at either the occiput (base of the skull) or the vertex [Yoganandan et al., 1986]. Force gauges were implanted into the C5-C6 vertebral bodies and peak forces on the head and cervical transducer were recorded. In general, in the unrestrained cadavers, the peak forces on the cervical transducer in the C5-C6 were between a range of 1.1 kN to 2.6 kN and 1.1 kN to 1.8 kN for the restrained cadavers [Yoganandan et al., 1986]. The peak forces on the head of the unrestrained cadavers ranged from 3.0 kN to 7.1 kN whereas, in restrained cadavers, they range from 9.7 kN to 14.0 kN [Yoganandan et al., 1986]. In a subsequent study on the effects of head, neck inertia, and impact surfaces during dynamic impact of cadaver heads with

intact spines, head impact forces (5.8 ±2.5kN) were also measured to be higher than the neck forces (1.9±0.7kN) as the neck force is reduced by the product of the head mass and head acceleration [Nightingale et al., 1997]. The type of fractures seen in the unrestrained subjects was compression fracture of the C3 vertebra and Type II odontoid fractures whereas Jefferson fracture at the C1, C6 spinous process fractures, fractures in the C2 vertebral body, lamina, skull and thoracic vertebrae were seen the restrained subjects [Yoganandan et al., 1986]. A subsequent intact cadaver study by Yoganandan (1989) assessed the biomechanical responses of intact cadaver torsos when compressed axially at a dynamic rate of 112 to 142 cm/s [Yoganandan et al., 1989]. A neck failure load range of 1.51 kN to 2.94 kN were measured from the load cell in the loading head of the MTS device in the unrestrained cadaver [Yoganandan et al., 1989]. Spinous process fracture of the C6, C5-C6 endplate failure, avulsion of anterior inferior body of C4, rupture of the anterior longitudinal ligament (ALL) and posterior atlanto-occipital ligament and disruption of C1-C2 capsular ligaments and nuchal ligaments were also reported [Yoganandan et al., 1989].

Although whole cadaveric studies are the best replication of real scenarios, it is difficult to determine the injury mechanism of spinal fractures as it usually involves combined modes of loading due to the lordosis or curvature of the spine. A lot of complexity is involved in full cadaveric tests which makes it difficult to isolate the effects with the failure response seen.

2.8.2 Isolated Cadaveric Spine

To fully characterize the mechanisms of injury and injury tolerance of the cervical spine, using isolated spines and segments allowed for a more controlled loading and visualization of injury production [Myers and Winkelstein, 1995]. However, limitations were the small sample sizes and quality as surgically removing the segments and potting them may affect their structural integrity. In addition, there is a wide range of failure forces seen due to boundary condition sensitivity. As for the lack of muscle effects, although it may be a limitation, under compression scenarios, they were assumed to have a small effect [Myers and Winkelstein, 1995; Nightingale et al., 1997]. In contrast however, a recent computational study by Nightingale assessed the factors that influenced the cervical spine loads during compression and found that the simulations with muscle had 32% larger peak compressive forces (771±738 N) across all flexion angles although the effect on moment was not as significant (average increase of 6±13 Nm) [Nightingale et al., 2016]. The explanation for this is that muscles added structural stability that maintained the spine in an upright posture for a longer duration and the added muscle mass provided an inertial constraint to buckling [Nightingale et al., 2016].

In a study by Maiman et al. (1983), the mean failure force of the isolated spine C1 to T3 under axial load was 7.4 kN (only one sample) whereas in specimens with intact torsos and heads the average axial load was 2.7 kN. The average failure load was 3.6 kN for all specimens (isolated spine, intact torsos and heads) that were loaded axially. In addition, burst fractures of the C5 and compression fractures of posterior elements with disruption of the posterior ligaments were mostly seen in specimens when the base of the skull to T3 complexes that were impacted axially [Maiman et al., 1983]. Upper cervical spine fractures such as teardrop and arch fractures of C2 were seen when the specimens were impacted in flexion and odontoid fracture when the specimens were impacted in extension (with disruption of ALL and annulus) [Maiman et al., 1983]. In the whole torso specimens, the failure mode was in flexion and disruption of the posterior ligaments at the C1 was observed [Maiman et al., 1983]. This showed the importance

of the boundary conditions and the experimental preparation of the test samples. In a study involving straightened isolated spine complexes (from the base of the skull to C5, C6, C7 or T1), a mean failure force of 3.9 kN [McElhaney et al., 1983] was measured. Injuries such as Jefferson fractures, burst fractures, anterior wedge compression fractures and posterior element fractures were observed [McElhaney et al., 1983].

In a subsequent study by Yoganandan et al. (1989) involving intact head-cervical spine and ligamentous cervical columns (C2-T2) at a rate of 2.54 mm/s, the load range was between 0.5 kN to 1.1 kN and 0.67 kN to 1.1 kN respectively. Pintar et al. (1990) on the other hand reported the mean neck load to be 3.5 kN ± 1.95 kN in head-T2 complexes at a rate of 2.95 to 8.13 m/s and 3.3 kN in a subsequent study using head to T1-T2 complexes at a rate of 2.5 to 8 m/s [Pintar et al., 1995]. A dynamic compression impact experiment that involved un-embalmed human heads and intact spines, the resting lordosis of the spine was preserved by orienting the C7 to T1 intervertebral disc at 25 degrees to horizontal [Nightingale et al., 1997]. The specimens were dropped from a height of 0.53 m that were less than that required to cause a skull fracture but sufficient to cause cervical spine injuries [Nightingale et al., 1997]. The impact velocity was 3.2 m/s and the axial neck force to fracture was approximately 1.9 kN ± 0.7 kN [Nightingale et al., 1997]. Fractures produced were a multipart atlas, lower cervical compression fractures, lower cervical bilateral facet dislocations and posterior-element fractures [Nightingale et al., 1997]. The mixed types of fractures were attributed to buckling deformation in the cervical spine upon impact, which caused the extension to occur around mid-cervical vertebra section and flexion at the lower cervical vertebra section.

It was observed that studies with the lordosis of the spine removed in pre-alignment [Pintar et al., 1990; McElhaney et al., 1983] reported larger failure forces than neutrally positioned spines with curvature because of bending stresses [Nightingale et al., 1997].

2.8.3 Limitations in Whole Head and Spine Experiments

The effect of inertial loading from the head or the impactor leads to a scatter in tolerance data and this was seen in a study by Yoganandan (1986) in which the force measured on the head was approximately 3.5 times higher than on the neck. The degree of constraint influenced the variation in failure loads such that more constraint led to a greater value of failure force [Myers et al., 1991; McElhaney et al., 1983]. In an experiment involving constrained and unconstrained heads [Yoganandan et al., 1986], 4.5 kN failure load was measured in the constrained heads whereas in a prior experiment [McElhaney; 1983], a mean failure load of 3.9 kN was measured in constrained straightened spine. Similarly, for the fully constrained lower cervical spine, a failure load of 4.8kN was achieved [Myers et al., 1991]. From various experiments involving full cadavers, head-neck complexes or isolated neck complexes, a failure load range of 0.3 to 14.7 kN [Myers & Winkelstein, 1995] was reported, which suggest that a compressive failure force tolerance does not exist as these values include all data with varying specimen types. The scatter in these data however can be reduced when effects of head inertia and data from experiments with end conditions that are more representative of those occurring in real-world accidents are taken into account [Myers & Winkelstein, 1995]. As the head or impactor force data are larger than the resulting neck force due to inertial effects, using only measured neck load data would be a better measure of cervical spine tolerance [Myers & Winkelstein, 1995].

Furthermore, the effect of age was identified as important. McElhaney et al. (1970) suggested that the vertebral cancellous bone from 20-year-old donors was 45% stronger than that of 50-

year old donors, and that cortical bone was 10% stronger [Keaveny and Hayes, 1993] between these two age groups [Myers and Winkelstein, 1995]. The suggested cervical spine tolerance range for young human cervical spines was 3.64 kN to 3.94 kN [Myers and Winkelstein, 1995; Nightingale et al., 1997]. A recent study had proven age to be a significant covariate in compression-related injuries [Yoganandan et al., 2017]. The gender effect was also identified as important due to size differences and the average means of the failure loads of two studies have reported 1.68 kN for female specimens and 3.03 kN for male specimens [Pintar et al., 1995; Nightingale et al., 1997].

2.8.4 Functional Spinal Units and Single Vertebra

The true injury mechanism and resulting structural damage and fracture patterns are defined by the loading environment at the site of injury [Carter et al., 2002]. Therefore, with isolated segments or specimens, factors such as curvature of the spine or inertial loading from head or impactor could be reduced. These studies can focus on specific variables affecting the outcome without other factors. In the study that involved axial compression with anteroposterior eccentricity, multiple two FSUs from various lower cervical spine levels were utilized to measure load near the injury site and minimize inertial effect errors [Carter et al., 2002]. Although preference was given to selecting the C57 segment, due to variability in specimen quality and limited availability, the segments ranged from C24 to C6T1 [Carter et al., 2002]. The inferior and superior vertebrae in each two FSU segment were potted and to produce an axial (centric) compression injury mechanism, the axial force vector was within the boundaries of the vertebral body [Carter et al., 2002]. Thus, a fixed-fixed end condition scheme was implemented by placing the superior and inferior potting molds in a custom compression fixture that prevented the specimen from rotating or translating horizontally [Carter et al., 2002]. In order to produce the compression-flexion and compression-extension injury mechanisms, the axial load vector was moved beyond the boundaries of the vertebral body by an initial eccentricity equivalent to the anterior-posterior depth of the middle vertebral body from the inferior IVD centroid [Carter et al., 2002]. This configuration utilized a fixed-free loading scheme in which the inferior potting mold was fixed but the superior potting mold was allowed to translate and rotate in the midsagittal plane using a bending fixture with an aluminum yoke and roller bearings to apply the eccentricity [Carter et al., 2002]. The axial displacement applied to the specimens varied between specimens (4 mm to 20 mm) with a 45 N compressive preload (head weight) [Carter et al., 2002]. This study found that different failure responses were seen with centric compression, flexion- or extension-compression scenarios such that larger amounts of hard tissue failure with higher failure forces were seen in centric compression than in flexion-compression scenarios [Carter et al., 2002]. The mean failure loads in these two cases were in the 3 kN range, which fell within the range of other similar experimental data [Van Toen et al., 2014; Zhu et al, 1999].

Another compression experimental test was performed on isolated single specimens of bone vertebra (C3 to T2) with the cranial and caudal-most aspects of the bone potted [Van Toen et al., 2012]. This study differentiated failures of spinal ligaments and vertebral bodes using acoustic emission signals [Van Toen et al., 2012]. A subsequent study by Van Toen (2014, 2015) utilized a similar test set up as Carter (2002) but focused on compression with lateral eccentricity cases [Carter et al., 2002; Van Toen et al., 2014; Van Toen et al., 2015] with multiple two FSUs. Similar to the prior study, an acoustic emission signal method to detect and differentiate injuries of ligaments and hard tissues [Van Toen et al., 2014]. This study had two lateral eccentricity configurations: low (0.3 mm or 1% of the average lateral dimension of the cranial and caudal

vertebral bodies) and high (150% of the average lateral dimension of the cranial and caudal vertebral bodies) [Van Toen et al., 2014]. Two FSUs from C35 to C6T1 were utilized, similar to a prior study [Carter et al., 2002], and applied an axial displacement boundary condition at a rate of 0.5 m/s [Van Toen et al., 2014]. This study found that the low lateral eccentricity compression case produced more hard tissue failure (vertebral bodies, endplate, laminae and spinous process fractures) and higher failure forces than the high lateral eccentricity compression case which showed more soft tissue failure (ALL, intertransverse ligament, facet capsule, intervertebral disc, and ligamentum flavum) [Van Toen et al., 2014; Van Toen et al., 2015].

Apart from that, in a study by Zhu et al. [1999], high-speed axial loading to failure was performed on FSUs (C24) from young cadavers and hard tissue injuries were found in a 50 J high impact energy trauma with instabilities in flexion, extension, and axial rotation with a peak impact force of 4.89 ± 0.38 kN. This study highlighted the spinal instability in a traumatic injury of the cervical spine. The spinal instability allowed for a combination mode of loadings on the cervical spine, complicating the characterization of injury mechanisms.

2.9 Existing Computational Models of the Spine and Methods to Model Fracture

Computational modeling as an injury prediction tool had been on the rise over the last decade, especially in the automotive industry for safety assessment and virtual crash testing. In this study, the axial impact of the lower cervical spine segment (C57) was performed computationally and validated with available experimental data. An important aspect of hard tissue modeling is predicting fracture propagation which would potentially able a HBM to predict post-fracture response. This is acknowledged to present challenges in existing HBM [De Wit et al, 2012]. The HBMs that are currently widely used and commercially available for use are the Global Human Body Models Consortium (GHBMC) and the Total Human Model for Safety (THUMS) models, although several neck models exist.

Current computational models of the vertebra and their outcomes and limitations were reviewed. One of the methods to retrieve geometry of the vertebral body for modelling is based on bulk measurements as a representation of an average vertebra and another is based on converting image voxels of CT scanned vertebra to hexahedral mesh elements to achieve a subject-specific geometry [Jones et al., 2008]. The material properties for most image-based models are homogeneous with no distinction between the cortical shell and cancellous bone. The material property for the subject-specific trabecular bone is usually based on density and image data [Buckley et al., 2007, Crawford et al, 2003]. The cortical shell, on the other hand, is usually given isotropic and elastic material properties [Idkaidek et al., 2016].

On the other hand, for the average geometry-based models, homogeneity, anisotropy, and porosity had been considered. Most often, the trabecular and cortical bone in computational models were given linear elastic-plastic isotropic material properties [Kumaresan, 1999; Yoganandan, 1999; Hong-Wan et al.,2006; Laville et al., 2009; Panzer et al., 2009; Kallemeyen et al.,2010, Erbulut et al.,2014; Zhang et al., 2010; Teo et al.,2001; Marta, 2010]. Computationally, bone had been investigated at the micro-scale [Abdel-Wahab et al., 2012; Ural et al., 2011; Feerick et al., 2013; Idkaidek et al., 2016], macro-scale at the coupon level [Garica et al., 2009; Li et al., 2013], and macro-scale at the whole bone level [Antonio et al., 2012; Ariza et al., 2015; Asgharpour et al., 2014; Iwamoto et al., 2005; Zysset et al., 2013].

No studies have been done extensively on the constitutive models for cortical and trabecular bones in the current computational spine models. Whyne et al. (2001) developed a two-dimensional, axisymmetric finite element model of the L1 vertebral body and both elastic and poroelastic material properties were investigated [Whyne et al., 2001]. Transversely isotropic elastic and poroelastic properties were given for the trabecular bone whereas isotropic elastic and poroelastic for the cortical shell. In terms of axial impact investigation using finite element model of the lower cervical spine, a study focused on the C46 segment models, particularly using geometric and contact non-linearity but still with linear elastic material characteristics [Hong-Wan et al., 2006]. This study was based on a prior work involving compression of a C46 model but with linear geometric and contact [Yoganandan et al., 1996]. Similarly, a study investigated the force-displacement responses and motion of a C46 segment model with experimental study utilizing linear isotropic material properties for the bone [Teo et al., 2001]. Other axial impacts have been done on the lumbar vertebra models due to extensive experimental data in this area (Buckley et al., 2007; El-Rich et al., 2009; Zeinali et al., 2010, Oschia et al., 2003].

Bone fracture modelling had been investigated by various methods such as the cohesive finite element method [Ural et al., 2006; Ural et al., 2011], reduced stiffness approach [Hambli, 2013], QCT/X-FEM analysis [Giambini et al., 2016; Li et al., 2013; Abdel-Wahab et al.,2012; Feerick et al., 2013] and the element deletion approach [Harrison et al, 2012; Hambli et al., 2012],. Cohesive finite element method is a non-linear fracture mechanics approach that predicts crack propagation by a simplified traction-crack opening displacement relationship [Ural et al., 2011]. The traction-crack opening displacement relationship includes material softening and nonlinearity and isolates the fracture process from the surrounding continuum constitutive model [Ural et al., 2011]. This method is able to represent the nonlinear behavior of the process zone that is unable to be captured by linear elastic fracture mechanics analysis [Ural et al., 2011]. The parameters involved in this method are the material critical strength, a characteristic crack opening displacement at fracture and the energy needed to open the crack [Ural et al., 2011]. Therefore, the main limitation of the cohesive element approach is that the fracture path must be pre-defined for the analysis [Ali et al., 2014; Feerick et al., 2013; Li et al., 2013].

With the X-FEM approach, the crack propagation was successfully modelled based on a solution-dependent criterion without requiring a predefined path [Li et al., 2013]. Li (2013) had modeled the variability and anisotropy of the non-linear fracture process of cortical bone under three point bending with a bone specimen model of 2D quadrilateral elements [Li et al., 2013]. However, it is computationally costly and is currently mostly used in 2D models [Hambli et al., 2013; Li et al., 2013; Abdel-Wahab, 2012; Feerick, 2013]. In addition, most of the models are at the micro-scale level [Budyn et al., 2010; Feerick et al., 2013' Abdel-Wahab et al., 2012; Idkaidek et al., 2016]. It was found that simulation convergence was the main issue reported where a smaller mesh size with small or large simulation increment size, predicted multiple, mutually intersecting cracks over a small region, causing numerical instability in the 2D cortical bone model with the X-FEM approach [Idkaidek et al., 2016]. Therefore, for accuracy of results, optimization of analysis increment size and mesh density were required [Idkaidek et al., 2016]. The X-FEM approach in 3D models had been investigated in limited studies [Ali et al., 2014;

Giambini et al., 2016] and is currently not widely available. One study involving the analysis of compression fracture in a vertebra FEM [Giambini et al., 2016] managed to overcome the element size dependency problem that is the limitation of other methods (cohesive FEM, reduced stiffness, and element deletion) and predicted fracture patterns that agreed with experimental results using the QCT or X-FEM approach in a 3D model with density-dependent linear elastic properties and user-defined density dependent compressive strain failure criterion. However, the failure loads (41-44%) and stiffness were over-predicted due to the density-dependent linear elastic material property relations that were based on formerly published empirical equations. Besides that, the reduction in failure load was due to the failure of elements from noncontact interface between the newly formed surfaces of the models.

In the reduced stiffness approach, upon reaching a failure criterion, the elements stiffness was reduced with an experimental damage law [Hambli et al., 2013]. The stiffness matrix of the element was set to zero when the damage parameter of the element reached the critical damage value which would redistribute the stress state in the vicinity of the damaged zone [Hambli et al., 2013]. With reduced stiffness, the element was still able to withstand forces and distortion [Giambini et al., 2016]. However, the fracture location, pattern, or propagation was not consistently accurately using a user-defined failure criterion [Giambini et al., 2016]. Due to the additional amount of distortion that the elements withstand, in order to avoid convergence issues and numerical instability, a finer mesh was required with the expense of larger computational time [Giambini et al., 2016]. With a finer mesh, the damage growth prediction was more accurate and the predicted critical damage at fracture was faster leading to a faster crack propagation [Hambli et al., 2013].

With the element deletion approach, when an element reaches a failure strain or stress criterion, the failed element stresses and response in the model becomes zero, and the element is deleted from the model. This deletion of the element represents the cracks [Giambini et al., 2016]. One of the limitations of using an element deletion approach is that crack initiation and propagation both occur due to the failure of an element [Hambli et al.,2013; Hambli et al.,2012]. The fracture pattern is thus determined by the deleted elements of the mesh. In a more geometrically complex scenario, a study with a cervical spine segment model demonstrated that an isotropic metal plasticity model with element erosion based on maximum plastic strain criterion predicted the failure initiation location but failed to predict the fracture pattern [De Wit et al., 2012]. There were other studies that had utilized this method to predict fracture patterns at the whole bone level for some modes of loading [Schileo et al., 2008; Niebur et al., 2000]. The advantages of the strain-based criterion are that the simulation is numerically stable [De Wit et al., 2012] and the results predicted generally agree with experimental data [Schileo et al., 2009; Ford et al., 1996; Keaveny et al., 1994; Pankaj et al., 2012]. It had also been found that the failure of bone is controlled by strain [Niebur et al., 2000; Hambli et al., 2013; Nalla et al., 2003] and an experimental study had been performed showing that the local fracture criterion for human cortical bone is consistent with strain-based criterion which validated the assumption of strain-

based criterion that had been widely used in theoretical models [Nalla et al., 2003]. Therefore, in this work, an element deletion approach based on a failure strain criterion was utilized.

2.10 The GHBMC Model

The GHBMC is one of the most recent and fully validated HBM at present. Various body regions are developed, validated and integrated into the full HBM. The cervical spine in the GHBMC model was validated with approximately 60 load cases from segment level to the full cervical spine in flexion, extension, axial rotation and lateral bending [Barker et al., 2017]. Examples of loadings include flexion, extension, compression, tension, and mixed-modes. Research in hard tissue failure is still at its preliminary stage in which basic mechanical properties of trabecular and cortical bones were utilized in linear isotropic material models [De Wit et al., 2012]. This research was based on a previously developed hard tissue cervical spine segment model [De Wit et al., 2012] that used elastic-plastic material properties for cortical and trabecular bone with an effective plastic strain failure criterion.

The M50 GHBMC model is a representative of a 50th percentile male (26 years old, 78.6kg, 174.9cm height) [Gayzik et al., 2011]. The C57 cervical spine segment model used in this thesis was extracted from the full neck M50 GHBMC model (Version 4.4) (Figure 27). Simulations of the model were ran using a commercial finite element code (LS-DYNA, R7.1.2). The full neck model with skull and skin has 354,841 nodes and 293,264 elements (81,939 shell, 4402 beam, 206,684 solid, 59 discrete). The extracted segment model used in this thesis included the vertebrae, the intervertebral discs, and ligaments with a total of 41,920 elements.
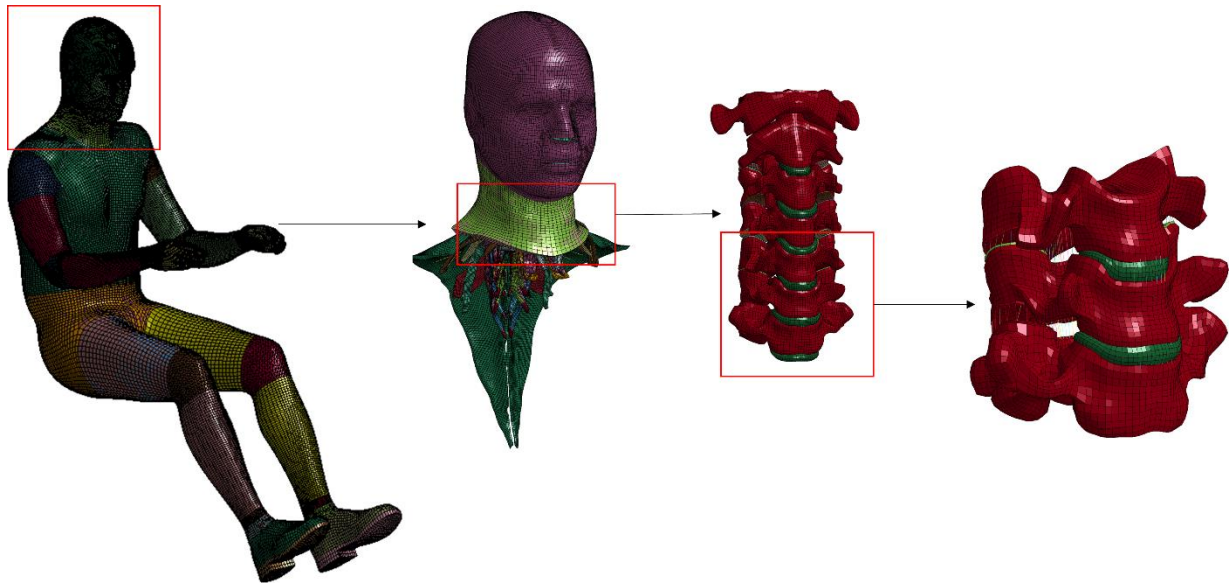
Figure 27: GHBMC full body model, GHBMC full neck model, full cervical spine model, extracted C57 segment model (left to right)

The cortical bone was represented by shell elements whereas the trabecular bone was represented by solid elements (Figure 28). The constitutive model utilized in both cortical and trabecular bone in the neck model was plastic kinematic with compressive mechanical properties shown in Table 1.

Trabecular bone
solid elements

Cortical bone shell
elements
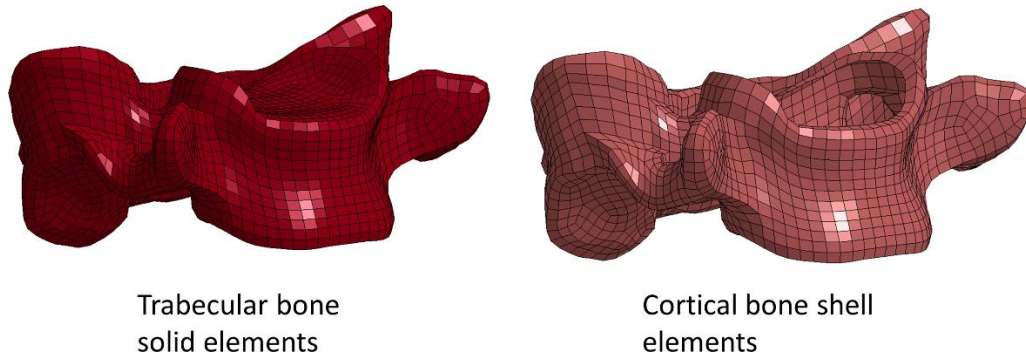
Figure 28: Trabecular and cortical bone models

Table 1: Trabecular and cortical bone mechanical properties in the GHBMC model

	Cortical Bone	Trabecular Bone
Density (kg/mm^3)	2E-6	1.1E-6
Young's Modulus (GPa)	18.44	0.442
Poisson's Ratio	0.28	0.3
Yield Stress (GPa)	0.1898	0.00283
Tangent modulus (GPa)	1.2489	0.0301
Failure strain	0.0178	0.095

The plastic kinematic model was a typical linear elastic-plastic model with the plastic response determined by the yield strength and a tangent or hardening modulus. The hard tissue elements in the GHBMC neck model were eroded when the failure strain shown in Table 1 was reached. In the vertebra, the superior and inferior endplates and articular cartilage were defined as shown in Figure 29. The articular cartilage was modeled with 3D solid elements whereas the superior and inferior endplates were modeled with 2D shell elements. The endplates were a continuation of the cortical shell covering the inferior and superior surfaces of the vertebral body and was assigned a plastic kinematic constitutive model as well similar to the hard tissues in the model. The articular cartilage was modeled with a quasi-linear viscoelastic material model.

36
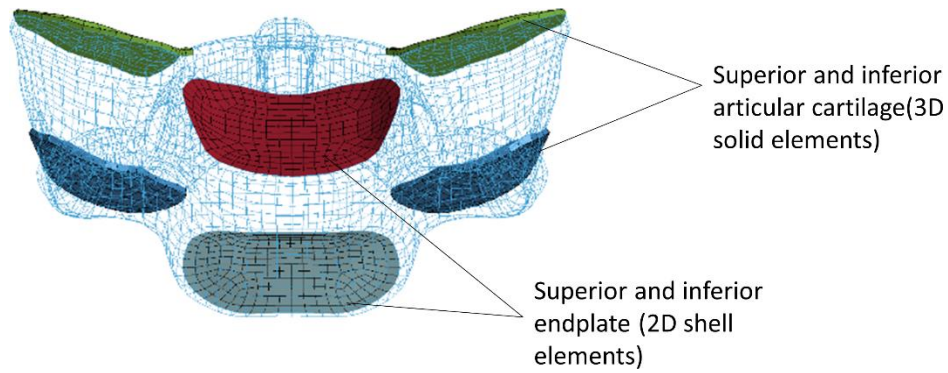
Figure 29: Articular cartilage and endplate in the vertebra model

The IVD model consisted of the annulus fibrous, nucleus matrix, and nucleus pulposus (Figure 30). Five pairs of concentric rings of shell elements represented the annulus fibrosus whereas the annulus matrix and nucleus pulposus were modeled as 3D solid elements. Each pair of the annulus fibrosus concentric ring had similar material properties except that one of the rings would have an element direction that was negative of the other (For example: 45 degrees and -45 degrees). The material direction was rotated by an angle of 25 degrees for the innermost layer from the transverse axis and the angle was increased by 5 degrees for each layer until the outermost layer attained an element direction that was 45 degrees away from the transverse axis. With the layers of concentric rings, the material properties of the annulus fibrosus were able to be varied radially but not circumferentially. The annulus fibrosus was modeled using a fabric constitutive model with tensile material properties derived from literature [Holzapfel et al., 2005; Ebara et al.; 1996] as under compression, the annulus fibrosus acted in tension to resist the nucleus pressure [Shan et al., 2015]. The non-linear stress-strain curves were assigned to decrease progressively in stiffness and strength from the outermost layer to the innermost layer.
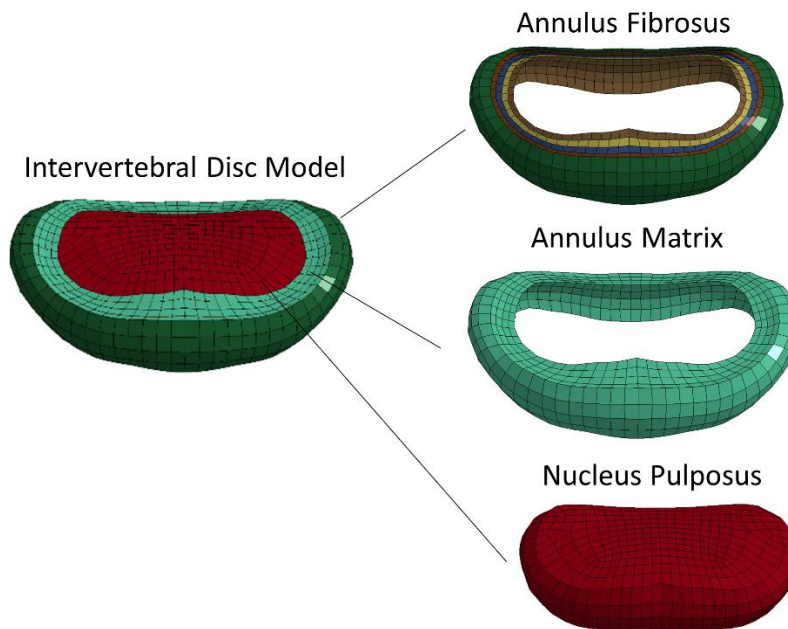
Figure 30: The intervertebral disc model

The annulus matrix covered the annulus fibrosus layers and shared nodes with the annulus fibrosus at each level in the radial direction (Figure 31). The annulus matrix was modeled using a Hill constitutive model and experimental data was fitted to the material model [Panzer et al., 2006]. The nucleus pulposus was modeled as an elastic fluid with a bulk modulus of 1.72 GPa and a density of 1.36 g/cm^3 [Iatridis et al., 1996].

Annulus fibrosus   Annulus matrix covering the annulus fibrosus
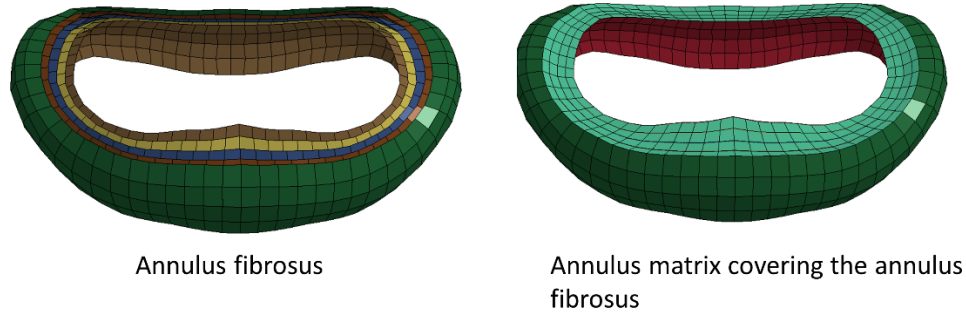
Figure 31: Annulus fibrosus and annulus matrix model

In the lower cervical spine, the five main ligaments were modeled which included the anterior longitudinal ligament (ALL), posterior longitudinal ligament (PLL), interspinous ligament (ISL), ligamentum flavum (LF), and the capsular ligament (CL) were modeled as 1D beam elements.

Anterior Longitudinal
Ligament (ALL)
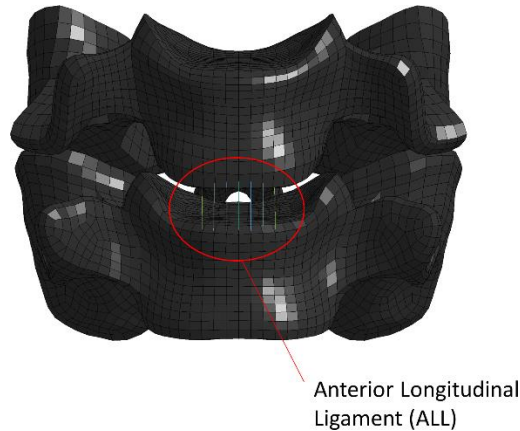
Figure 32: ALL in the model

The ALL (Figure 32) in between the anterior gap of the vertebral body whereas the PLL was in between the posterior gap of the vertebral body (Figure 34). There were a total of 4 sets of beam elements for each ligament such that each set of elements would be given progressively decreasing failure displacement from the center so that the outermost beam elements would fail first before the inner center most beam element (Figure 33) .
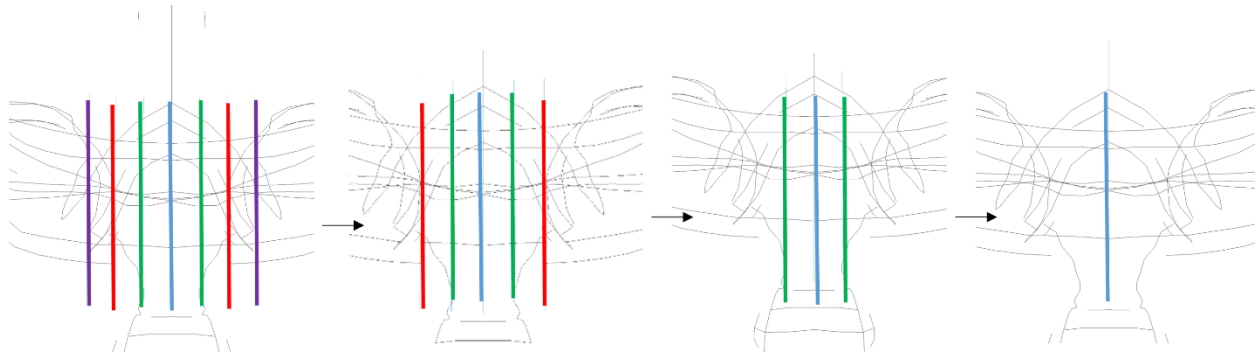
Figure 33: Progressive failure of ligaments modeled as beam elements

For example, the ALL was modeled with 7 beam elements with the middle most beam element being a set and the three subsequent left and right beam element pairs were assigned a set each. The PLL was modeled with 7 beam elements similar to the ALL.

Posterior Longitudinal
Ligament (PLL)
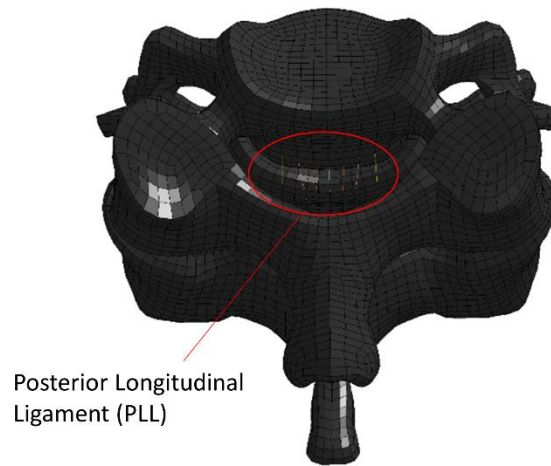
Figure 34: PLL in the model

The ligamentum flavum located between the lamina (Figure 35) was modeled using 15 beam elements and sets of 4 for the purposes of erosion.

Ligamentum Flavum (LF)
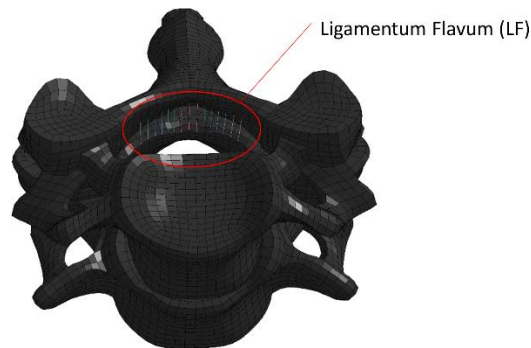
Figure 35: Ligamentum flavum in the model

The interspinous ligament located in between two adjacent spinous process was modeled using 14 beam elements (Figure 36) whereas the capsular ligament was modeled with 26 beam elements for each facet joint (Figure 37).
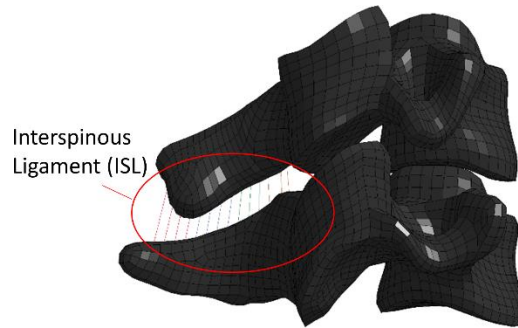
Figure 36: Interspinous ligament in the model

The ligaments were assigned force-displacement response with tensile material properties representing younger population (average age of 44) [Mattucci et al., 2012]. The force-displacement curves input for each ligament were scaled based on spinal level and gender.
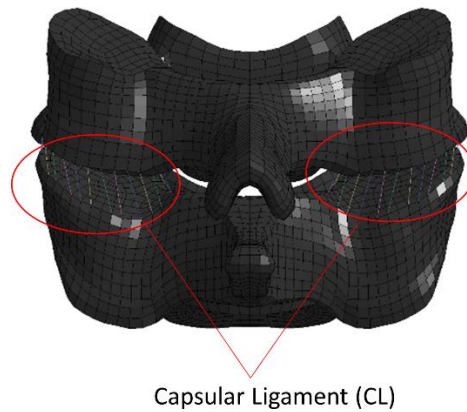
Figure 37: Capsular ligament in the model

In the segment model extracted from the GHBMC HBM, crash induced injuries (CIIs) can be predicted in the bone, the ligaments and the IVD. In the trabecular or cortical bone, once an element reaches failure strain, the element is deleted simulating a fracture. In the ligaments, once the beam element reaches the ultimate force, the force remains at that value linearly until the failure displacement was reached. As mentioned, progressive failure of the ligaments was modeled by varying the failure displacement of each set of the beam elements and once the failure displacement is reached, the beam element is eroded. As for the IVD, the failure of the tiebreak contact between the IVD and the endplate and bone defines the CII. The tiebreak contact ties two surfaces together and has a normal stress failure criterion of 0.01 GPa. Once the nodal stress reaches the failure criterion, the node is released from the tiebreak contact depicting failure in the IVD.

Chapter 3: Methods

3.1 Assessment of Mechanical Properties for Bone from Literature

As mentioned in Chapter 2 and in a recent study [Yoganandan et al., 2017], age is a significant covariate in compression-related injuries to the cervical spine. The material properties of the cortical and trabecular bones in the vertebra in this study were determined for both young and aged specimens. The young specimen mechanical properties were based on data collected for specimens below the age of 50 whereas the aged properties were based specimens above the age of 70. This age group was determined based on the amount of data that could be found in literature and corresponding to the FSU experiments. Besides that, bone loss in men had been found to accelerate from the age of 50 due to the decreased bone formation from the decreasing levels of free androgen [Wishart et al., 1995]. Furthermore, it had been established that females are more prevalent to develop osteoporosis from the age of 50 [Kanis et al., 1994; Vernon-Roberts and Pirie, 1973]. Age effect of the disc and ligaments were not included in this study as age effect of the disc is often masked by degeneration effect, which varies between ages depending on the subjects and affects the mechanical properties greater than age [Adams et al.1996; Acaroglu, 1994]. The ligaments are not important in compression, which is the loading of interest in this work.

The methodology in this work was summarized in a flow chart (Figure 38). First, the material properties of the trabecular and cortical bone were identified based on literature review. The age effect was studied as well and the 'Young' and 'Aged' properties were identified. Constitutive models from LS-DYNA were then identified and the best constitutive models (asymmetry and anisotropy) that could represent the cortical and trabecular bone were selected. Single element simulations were then performed to verify the models. Four possible combinations of trabecular and cortical bone models were validated in a centric compression experiment simulation with the C57 segment model. In this work, simulation with a single vertebra was first investigated before advancing to a C57 segment model. However, the single vertebra was found to be sensitive to the boundary condition and the disc in the C57 segment model provided a more consistent boundary condition by redistributing the load to the C6 vertebra, which induced a more realistic, consistent, and predictable failure scenario. The constitutive model combination that could best predict the experimental outcome was selected and this model combination was subsequently used in the compression simulation with eccentricities (posterior, anterior, and lateral) for further validation and analysis.
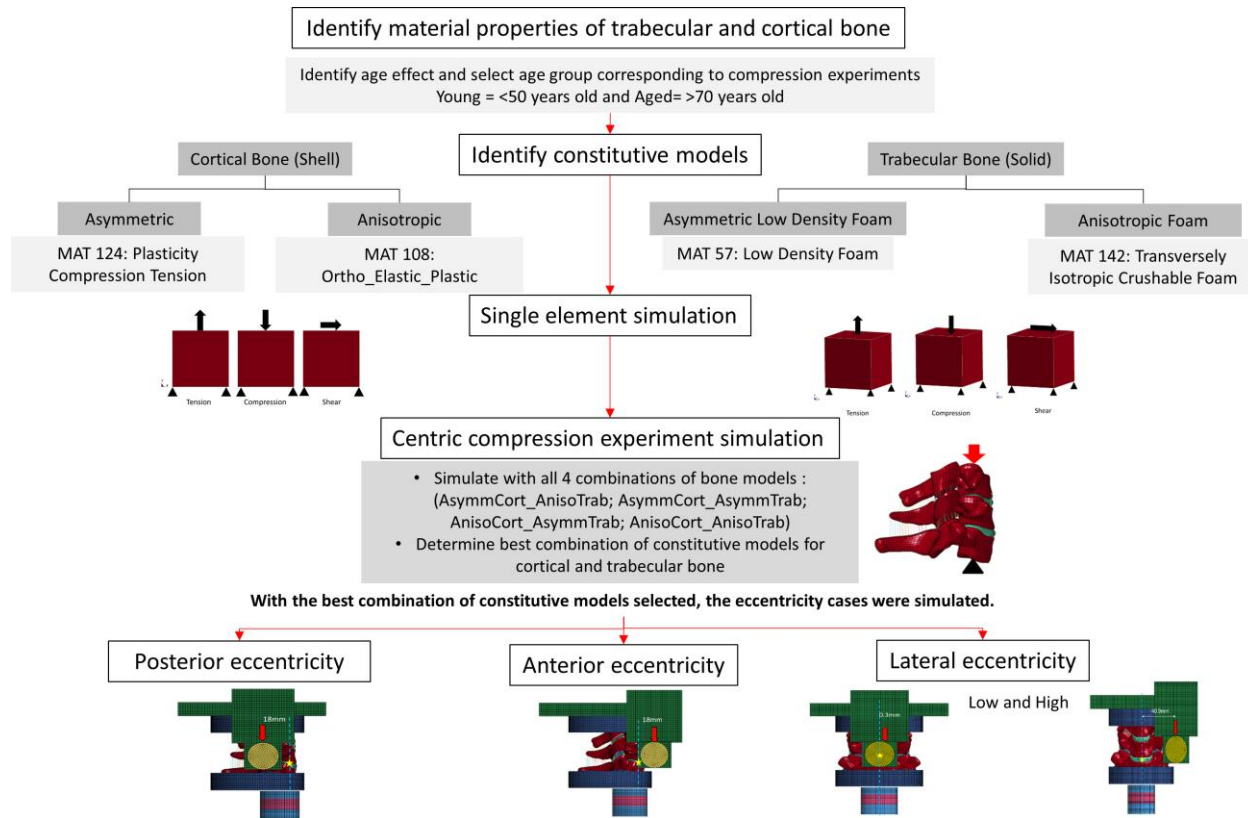
Figure 38: Methodology flow chart

3.1.1. Mechanical Properties of Cortical Bone

The elastic properties of cortical bone were utilized from various studies [Reilly and Burstein, 1974; Reilly and Burstein, 1975; Tang et al., 2015; Ashman et al., 1984] that measured mechanical properties of cortical bone specimens from the long bones. In this work, due to the tight porosity range of cortical bone, its mechanical properties such as the elastic moduli do not differ much between the long bones and the vertebra [Roy, 1999; Reilly et al., 1975]. There is also a lack of measured mechanical properties of cortical bone specimens from specifically the cervical spine due to the small specimen sizes. In addition, the compression loading that the cervical spine experiences is similar to the type of loading that the long bones in the femur and tibia typically experience and therefore, it has been justified that the properties in this case would be fairly similar according to Wolff's law. The Poisson's ratios were achieved by Ashman et al.'s [1984] study in which the elastic constants were calculated based on an orthotropic symmetry assumption. Therefore, only ν_{12} and ν_{31}. and ν_{23} were utilized from his study (Table 2) in which 1 is the longitudinal direction along the osteons and 2 and 3 are in the transverse directions perpendicular to the osteon direction. The bulk modulus was calculated using an isotropic assumption equation, $K=E/(3*(1-2\nu))$ in which ν is the longitudinal Poisson's ratio or ν_{12}.

Table 2: Poisson's ratio of cortical bone (Ashman et al., 1984)

Poisson's ratio (Ashman et al., 1984)	
ν_{12}	0.350
ν_{31}	0.222
ν_{23}	0.422

The cortical bone mechanical properties were retrieved from a study that utilized experimental specimens from cadavers of a wide age range between 20 to 86 years old [Reilly and Burstein, 1974]. The average mechanical properties of their entire sample size for both compression and tension were summarized in Appendix B.

The age did not significantly affect the mechanical properties of cortical bone except for the ultimate strain and strain hardening modulus in tension loading [Reilly and Burstein, 1974]. However, to be as accurate as possible, the mechanical properties used for the aged model were based on the average data recorded for specimens of age 70 and above and for the young model, specimens of age 50 and below. The tension and compression properties for both young and aged models were compiled [Reilly and Burstein, 1974] and the transverse properties were compiled based on the ratio of the average longitudinal properties over averaged transverse properties in a subsequent study by Reilly and Burstein (1975) (Table 3). Although there was a subsequent 1976 study based on aged properties, the ultimate strain data in compression and the other values were similar to those in their prior year studies [Reilly and Burstein,1974; Reilly and Burstein, 1975 (Table 4). Table 5 and Table 6 summarize the properties in the longitudinal and transverse directions under tension, compression and shear loadings for both young and aged cortical bone models.

Table 3: Ratio of longitudinal and transverse properties in tension, compression, and shear

Ratio of Longitudinal/Transverse	Tension [Reilly and Burstein, 1975]	Compression [Reilly and Burstein, 1975]	Shear [Tang, 2015]
Ultimate Stress	2.547	1.565	0.579
Yield Strain	1.750	0.909	0.832
Elastic Modulus	1.372	1.556	0.875
Ultimate Strain	4.429	0.661	0.405

Table 4: Average properties of young cortical bone [Reilly and Burstein, 1974]

Young (Average of specimens < 50 years old)	Longitudinal [Reilly and Burstein, 1974]		Transverse [Reilly and Burstein, 1975]	
Cortical Bone	Tension	Compression	Tension	Compression
Yield Stress (GPa)	0.114		0.048	
Ultimate Stress (GPa)	0.134	0.20	0.053	0.129
Elastic Modulus (GPa)	16.34	17.91	11.92	11.51

Plastic Modulus (GPa)	0.773		1.15	
Ultimate Strain	0.034	0.021	0.008	0.031

Table 5: Average properties of aged cortical bone [Reilly and Burstein, 1974]

Aged (Average of specimens > 70 years old)	Longitudinal [Reilly and Burstein, 1974]		Transverse [Reilly and Burstein, 1975]	
Cortical Bone	Tension	Compression	Tension	Compression
Yield Stress (GPa)	0.106		0.044	
Ultimate Stress (GPa)	0.124	0.188	0.049	0.120
Elastic Modulus (GPa)	15.350	17.325	11.188	11.13
Plastic Modulus (GPa)	1.089		3.28	
Ultimate Strain	0.023	0.021	0.005	0.031

As there were not many shear data on young and aged specimens, the shear properties remained constant between the two models [Tang, 2015] (Table 6).

Table 6: Shear properties in the longitudinal and transverse direction of cortical bone [Tang, 2015]

Shear [Tang, 2015]	Longitudinal	Transverse
Ultimate stress (GPa)	0.029	0.050
Yield strain	0.010	0.012
Elastic modulus (GPa) G12=G13, G23	3.500	4.000
Ultimate strain	0.010	0.025

The GHBMC utilized similar mechanical properties to the young longitudinal compressive properties (Table 7).

Table 7: GHBMC cortical bone mechanical properties

GHBMC cortical bone mechanical properties [De Wit et al., 2012]	
Elastic modulus (GPa)	18.44
Poisson's ratio	0.29
Plastic modulus (GPa)	1.2489
Yield Strength (GPa)	0.1898
Yield strain	0.0103
Ultimate Strength (GPa)	0.212
Ultimate strain	0.028

3.1.2. Mechanical Properties of Trabecular Bone

The mechanical properties of trabecular bone vary based on density due to its porous architecture that varies within anatomical sites. Due to the continuum model of the trabecular bone, it is important that the properties of the trabecular bone model were based on the apparent mechanical properties of a vertebra rather than tissue properties of trabeculae. The tissue mechanical properties of a single trabecula strut are much stronger than the apparent mechanical properties of a vertebral body [Wolfram et al., 2010] and therefore, it is erroneous to consider tissue properties for the constitutive model of an apparent finite element model of a vertebra. The mechanical properties of a young specimen were based on a digitized 47 years old cadaver (fresh bone density= 1.2 g/cc, apparent bone density = 0.65 g/cc) stress-strain curve [Liu et al., 2013]. The cervical spine trabecular bone properties were retrieved from a quasi-static experiment performed by Liu et al., (2013) utilizing unconfined human cervical spine trabecular bone samples. Since the strain rate was only 10^{-3}/s in this experiment, the marrow had sufficient time to flow among cells freely and thus the mechanical resistance was attributed only to the hard tissue in the study by Liu (2013). However, in the vertebra, the trabecular bone is confined by the cortical bone and there may be an increase in strength and stiffness as the marrow is confined within. As this was the only human cervical spine trabecular bone tensile and compression tests with extensive results [Liu et al., 2013] that had been found up to date, these properties were utilized. In addition, it had been found that the fluid influence was observed only in the last compression stage when the strain was higher than 0.3 [Chaari et al., 2007] in a compression experiment using bovine rib samples. In the study by Liu et al. (2013), the specimens were not loaded to failure and therefore the densification region was initiated at a strain of 0.6 [Carter and Hayes, 1976] with the assumption that the properties in the region were that of a dense cortical bone specimen, which would be explained later in this section. This may compensate for the higher stiffness and strength that would be otherwise present in a confined specimen. As this thesis work was based on compression loading, the compression properties were prioritized over the tensile properties. The tensile ultimate strain and stress were recorded based on a high-density specimen [Liu et al., 2013] (Table 8).

Table 8: Tension and compression properties based on a young (high-density) specimen [Liu et al., 2013]

Young Trabecular Bone [Liu, 2013]	Tension	Compression
Yield Strength (GPa)		0.014
Elastic Modulus (GPa)		0.689
Yield Strain		0.033
Ultimate Strain	0.096	0.457 (before densification)

Ultimate Stress (GPa)	0.007	0.014

For the aged model, the young stress-strain compressive curve was scaled to that of approximately age 80 (77 years old) by applying a ratio of 0.616 based on the ultimate stress declining by 12.8% per decade [Mosekilde et al., 1987]. The average low-density specimen (approximately 0.2383 g/cc of apparent bone density) tensile stress-strain curve with an ultimate tensile stress of approximately 0.002 GPa and ultimate strain of 0.077 [Liu et al., 2013] was digitized and utilized for the aged model (Table 9).

Table 9: Tension and compression properties based on an aged (low-density) specimen [Liu et al., 2013; Mosekilde, 1987]

Aged Trabecular Bone [Liu, 2013; Mosekilde, 1987]	Tension	Compression
Yield Stress (GPa)		0.0086
Elastic Modulus (GPa)		0.344
Yield Strain		0.033
Ultimate Strain	0.077	0.6 before densification)
Ultimate Stress (GPa)	0.002	0.0086

As mentioned in Section 2.5, the vertebral body densifies upon compression. The complete stress-strain curve was not shown in the study by Liu et al. [2013] as the experiment was stopped before the densification zone was reached to prevent from over damaging the specimens for density measurement. To incorporate the plateau and the densification zone, it was assumed that the densification zone would consist of a stiffness and density similar to that of cortical bone when the struts were all compacted into a dense and solid structure. Utilizing the apparent density of trabecular bone (0.72 g/cc) and cortical bone (2.00 g/cc) of young samples, and Poisson's ratio (0.2) [Qiu et al.,2005; Hong et al.,2007; Lim et al.,2000] the following calculation (Equation 1) to determine the longitudinal strain (ε_z) of the specimen at the initiation of densification was performed. It was assumed that the mass was constant at 1 g, and the trabecular bone was transversely anisotropic.

Equation 1: Calculation of longitudinal strain at initiation of densification

$$\frac{1g}{0.72\frac{g}{cc}} = 1.389cc\,(Trabecular\ Bone)$$

$$\frac{1g}{2.0\frac{g}{cc}} = 0.5cc \, (Cortical \; Bone)$$

$$Volumetric \; strain = \frac{\delta V}{V} = \frac{1.389cc - 0.5cc}{1.389cc} = 0.64$$

$$Volumetric \; strain = \varepsilon_x + \varepsilon_y + \varepsilon_z$$
$$= 0.2\varepsilon_z + 0.2\varepsilon_z + \varepsilon_z \; (Transversely \; anisotropic \; assumption)$$

$$\varepsilon_z = \frac{0.64}{1.4} = 0.457$$

It was therefore assumed that at the strain of 0.457, densification of the young vertebral segment initiates. The plateau and densification region usually involved a smooth transition [Halgin et al., 2012]. The study showed that all test samples showed a similar trend and so the average curve was used to determine the optimum quadratic curve fit for the shape of the curve. This quadratic curve equation was then implemented to achieve the shape of the densification curve and the complete trabecular compressive stress-strain region up to approximately a strain of 0.8. The plateau length and ultimate strain before densification region increases as the apparent density of the vertebral body decreases [Hayes and Carter, 1976]. This was due to the cell walls being thicker for a higher density specimen and thus, the strain at which the cell walls touch as the vertebra was crushed, decreases, reducing the length of the collapse stress plateau [Gibson, 1985]. Therefore, it was assumed that the strain when densification initiates for the aged trabecular bone was approximately 0.6 [Hayes and Carter, 1976]. The curve, similar to the younger specimen, was extrapolated to an ultimate strain of approximately 0.8 since it was not expected for the compression simulations to surpass a strain of 0.8.

To eliminate errors from mechanical testing such as end artifact and specimen misalignment, apparent elastic constants had been computed through high-resolution finite element analyses [Kabel et al., 1999; Yang, 1999]. Yang (1999) had derived a theoretical relationship between the orthotropic elastic constants, density, and tissue modulus whereas Kabel (1999) had derived the relationship based on the orthotropic elastic constants, density, fabric eigenvalues and tissue modulus. The main difference between these theories is that Kabel (1999) involved specimen-specific architectural information with the fabric eigenvalues whereas Yang (1999) did not [Morgan and Keaveny, 2003]. Both theories were based on Cowin and Yang (1997) and a study by Cowin (1985) had treated the tissue modulus as isotropic and uniform and predict site-specific apparent modulus-density relationships. Due to insufficient experimental data like micro-computational tomography (mCT) scans to determine the mean intercept length (MIL) tensors and fabric eigenvalues, the methodology in a study by Yang (1999) was chosen.

To utilize the relationship in a study by Yang (1999) to determine the apparent off-axis elastic moduli, an individual trabecula tissue modulus and volume fraction of a cervical vertebra were needed. Many experiments to determine the elastic modulus of an individual trabecula exist

[Kim et al., 2002]. However, only a few pertained to vertebra experiments, usually lumbar or thoracic vertebra specimens and none from the cervical due to the small specimen size that induces difficulty in experimental testing. A study by Rho et al. (1997) had reported an elastic modulus of 13.5 GPa for dry thoracic vertebrae trabeculae whereas another study by Hoffler et al. (2000) had determined the modulus to be 8.57 GPa from a moist lumbar trabecular lamellar tissue. The discrepancy with the data in a study by Rho [(997) was discussed to be due to the absence of tissue moisture and anatomical location variation. Other studies that involved other anatomical locations such as the tibia had measured values of 4.59 GPa (range from 3.27 GPa to 10.58 GPa) [Choi et al., 1990] via nanoindentation tests and 8.7 GPa [Runkle and Pugh, 1975] via single trabecular buckling tests. Besides that, the properties also vary between measurement techniques whether it is via ultrasonic or mechanical tests. For example, a study by Ashman and Rho (1988) had determined the elastic modulus of a trabecular strut from a femur to be 13 GPa via ultrasonic test. It had been discussed however that mechanical tests often induce artefact errors that would underestimate the modulus [Kim et al., 2002; Gibson and Ashby, 1997] and a re-examination by Gibson and Ashby (1997) had suggested a value of 12 GPa for the elastic modulus of the individual trabeculae [Kim et al., 2002]. Furthermore, mechanical tests have the probability of inducing misalignment error, especially when the specimen size is small like an individual trabecula. A study by Ashman et al. (1989) had determined the on-axis and off-axis elastic properties from proximal tibia specimens via ultrasonic technique but due to specimen differences such as architecture, sex, and gender, it is preferred to remain consistent with one set of data from one study.

According to Turner and Cowin (1988), the trabecular bone is truly orthotropic and not transversely isotropic as when determining transversely isotropic constants via formulas from Whitehouse (1974), the maximum difference is over 60% for trabecular bone but only 6.4% for cortical bone. However, due to lack of experimental data of strength and shear curves of trabecular bones specifically in a human cervical vertebra in all three directions, a transversely anisotropic assumption was made in this work. For the compression stress-strain curve, a ratio of 0.34 was applied [Mosekilde et al. 1985] to achieve the transverse curve (transverse ultimate stress: 0.00476 GPa for young material model and 0.00292 GPa for aged material model) whereas, a ratio of 0.58 [Sanyal et al., 2012] for the shear curve. The transverse elastic modulus is determined using a ratio of 0.4 [Augat et al. 1998] from the longitudinal elastic modulus. In accordance with the transversely isotropic assumption, Augat et al. (1998) had determined the ratio of the anterior-posterior modulus to the cephalo-caudal (longitudinal) and medial-lateral modulus to the cephalo-caudal modulus of lumbar vertebra specimens to both be 0.4. Formulas to determine transversely isotropic constants from known orthotropic elastic constants using theoretical relationships [Yang, 1999] were utilized [Yoon et al. 2002]. Based on this calculation, the horizontal axis (transverse) moduli were approximately 2.5 lower than the longitudinal axis moduli, therefore agreeing with the ratios in a study by Augat et al. (1998).

Using the effective tissue modulus of 12 GPa [Gibson and Ashby, 1997] and longitudinal apparent elastic modulus [Liu et al., 2013], the volume fraction of the young and aged samples in the study by Liu (2013) was determined. Once the volume fraction was determined, the rest of the elastic properties like shear and bulk modulus were calculated. For the young specimen with an apparent elastic modulus of 689 MPa [Liu et al., 2013] and 12 GPa tissue modulus, the calculated volume fraction was 0.181 and 0.123 [Yang, 1999] for the aged specimen with an apparent elastic modulus of 344 MPa [Liu et al., 2013] (Table 10). The modulus G_{32} therefore was 113 MPa for the young specimen and 53 MPa for the aged specimen, whereas G_{12} was 165 MPa for young specimens and 78 MPa for aged specimens (Table 10). In order to determine the shear (G) and bulk modulus (K), the isotropic elastic relationship (Equation 2) was utilized with the assumption of a Poisson's ratio of 0.3 [Hernandez, 2016; Jaasma et al., 2002; Zysset et al., 1999] (Table 10).

Equation 2: Isotropic elastic relationship

$$E = 2G * (1 + v)$$

$$E = 3K * (1 - 2v)$$

Grote et al. (1995) had measured the volume fraction throughout the cervical spine with respect to age and for young specimens below the age of 45, the average volume fraction was approximately 0.2 for C6 vertebra and 0.16 for aged specimens above the age of 45. Although there were discrepancies with calculated volume fraction, which was probably due to the specimen variations, the discrepancies were not too large in the sense that the volume fraction of cervical spine specimens were around the 0.2 range.

Table 10: Young and aged elastic properties of trabecular bone

Elastic Properties (MPa)	Young	Aged
E1 [Liu, 2013]	689	344
E2=E3 [Yoon et al., 2002]	293	138
G32 [Yoon et al., 2002]	113	53
G21=G31 [Yoon et al., 2002]	165	78
G	265	132
K	574	287

Table 11: GHBMC trabecular bone mechanical properties

GHBMC trabecular bone mechanical properties	
Elastic modulus (GPa)	0.442
Poisson's ratio	0.3
Plastic modulus (GPa)	0.0301
Yield stress (GPa)	0.00283
Yield strain	0.0064
Ultimate stress (GPa)	0.00569
Ultimate strain	0.101

The GHBMC mechanical properties were generally lower than both the young and aged set of properties that were reviewed and proposed for this thesis study (Table 11). The GHBMC model elastic modulus (0.442 GPa) fell between the young and aged elastic moduli and was 29% higher than the aged elastic modulus of 0.344 GPa but 36% lower than the young elastic modulus of 0.689 GPa. In comparison to the yield stress, the yield stress in the GHBMC model (0.00283 GPa) was lower by 67% compared to the aged model (0.0086 GPa) and 80% to the young model (0.014 GPa). Under compression, densification occurs in trabecular bones, which increases the ultimate strength causing it to be higher than the strength that was defined in the GHBMC elastic-plastic models for trabecular bones. The ultimate stress of 0.00569 GPa in the GHBMC model, therefore, would be lower than both young and aged ultimate stress. In general, the GHBMC trabecular bone model was weaker than the proposed young and aged longitudinal trabecular bone material models but stronger than the young and aged transverse trabecular bone material models in this thesis.

3.2. Implementation of Constitutive Models

Following a review of the constitutive models available in LS-DYNA, it was noted that no single material model incorporated all the response characteristics for hard tissues such as asymmetry, anisotropy, strain rate dependency and damage. Therefore, constitutive models that best represented cortical bone and trabecular bone were selected for assessment. As mentioned earlier in the introduction, the key properties of cortical and trabecular bone are asymmetry and anisotropy (Section 2.2 and 2.3). Besides that, owing to its architecture, trabecular bone possesses foam-like properties in which densification occurs upon crushing (Section 2.5). These properties were therefore focused upon in this thesis. Table 12 below shows the material model nomenclature that will be utilized in this work and the material model description from LS-DYNA [LSTC, 2016].

Table 12: Model Nomenclature Summary

Model Nomenclature	Material Model from LS-DYNA	Description
SYMISOCORT and SYMISOTRAB	MAT_019:MAT_PLASTIC_KINEMATIC	Isotropic, symmetric in tension and compression, metals plasticity model
ASYMMCORT	MAT_124: MAT_PLASTICITY_COMPRESSION_TENSION	Isotropic, tension-compression asymmetry metals plasticity model
ANISOCORT	MAT_108: MAT_ORTHO_ELASTIC_PLASTIC	Symmetric metals plasticity model with an anisotropic yield criterion
ASYMMTRAB	MAT_57:MAT_LOW_DENSITY_FOAM	Highly compressible low density foam models
ANISOTRAB	MAT_142:MAT_TRANSVERSELY_ISOTROPIC_CRUSHABLE_FOAM	Transversely isotropic, crushable, and of low density foam models

For cortical bone, an asymmetric elastic-plastic model (AsymmCort) and an orthotropic elastic-plastic model (AnisoCort) were chosen to be evaluated. For trabecular bone, a low-density crushable foam model with asymmetry in failure (AsymmTrab) and a transversely isotropic low-density crushable foam model (AnisoTrab) were selected. As mentioned in Section 3.1, a 'young' and an 'aged' set of properties were defined for each model. With two constitutive models for each bone model, four configurations were evaluated (AnisoTrab_AsymmCort, AnisoTrab_AnisoCort, AsymmTrab_AsymmCort, AsymmTrab, AnisoCort) for the cervical segment models (Table 13). The goal of this work as mentioned was to improve on the current

constitutive models in the GHBMC model, which utilized a linear symmetric isotropic elastic-plastic model. The constitutive models (SymIsoCort_SymIsoTrab) in the GHBMC model with material properties from a prior study [De Wit et al., 2012] will be evaluated with the models in this study with material properties including age affect in compression simulations.

Table 13: Constitutive Model Combinations Nomenclature

Model Nomenclature	Constitutive Model Combinations
SymIsoCort_SymIsoTrab	MAT_019 + MAT_019
AsymmCort_AsymmTrab	MAT_124 + MAT_57
AsymmCort_AnisoTrab	MAT_124 + MAT_142
Aniso_Cort_AsymmTrab	MAT_108 + MAT_57
AnisoCort_AnisoTrab	MAT_108 + MAT_142

AsymmCort allowed tension and compression curves to be both defined. AnisoCort on the other hand, allowed one curve to be defined with curves in other directions calibrated based on defined yield stress ratios. Therefore, based on the ratios tabulated in Section 3.1.1, the transverse ultimate compressive stress was 0.645 of the longitudinal stress [Reilly and Burstein, 1975] and the shear stress was 0.422 [Tang et al., 2015].

AnisoTrab allowed curve definitions for shear stress in both the longitudinal and transverse directions. The ratio mentioned in Section 3.1.2. was utilized such that the transverse compression curve of the trabecular bone was 0.34 of the longitudinal curve [Mosekilde et al., 1985] and both longitudinal and transverse shear curves were 0.58 of the longitudinal compression curve [Sanyal et al., 2012]. As for AsymmTrab, only the longitudinal compression curve was defined. Both trabecular bone models however allowed tension failure to be defined in an elastic-plastic manner such that the ultimate tensile stress was defined and once the linear elastic region reached this stress, the curve became horizontally linear until it reached the failure strain defined through element erosion (MAT_ADD_EROSION).

In off-axis loading, the primary failure mode for the trabecular bone was found to be shear. However, there was a lack of ultimate shear strain values for human vertebra properties. Besides that, under compression loading, the horizontal struts were the first to fracture due to a cantilever-type mode of bending whereas the vertical trabecular would buckle [Fyhrie and Schaffler, 1994]. The effect of the bone marrow contained within the trabeculae struts increased the transverse strain by applying a higher pressure on the struts and thus accelerating the collapse of the trabecula [Halgrin, 2012]. As the failure mechanism was primarily bending and buckling of the struts under compression, the erosion or failure strain was set to be the maximum principal (tensile) strain. A strain-based failure criterion was chosen over a stress-based failure criterion as failure strains are weakly dependent on density and therefore if stress values were used, they would be normalized by density or modulus [Silva et al., 1998]. Furthermore, Ford and Keaveny (1996) had found that failure strains were homogenous and isotropic in bovine tibial trabecular

bone and therefore, a single maximum principal (tensile) strain value was set as a failure criterion. The minimum principal (compression) strain value was not set as a failure criterion because the element erosion method was unable to represent the crushing of the trabeculae and the densification of the specimen. If the minimum principal strain value was set as a failure criterion, elements will be deleted at a set compressive strain although realistically, the fragments will still stay within the specimen, filling into the pores. In general, failure strain in compression, tension, and shear were specified for the cortical bone and only in tension for the trabecular bone.

3.3. Element Orientation for Anisotropic Material Models

When an anisotropic material model is utilized, the material direction must be specified. Generally, it had been found that functional adaption or Wolff's law applies to the human vertebrae [Smit et al., 1997]. This means that the trabeculae are aligned parallel to the load path. Therefore, axial compression is the most significant load case for the vertebral body [Smit et al., 1997]. The pedicles and vertebral body transition region experience large moment because of the transfer of loads from the articular pillars to the vertebral bodies from rotational in the horizontal plane and shearing from the anterior to posterior direction during walking [Cramer and Darby, 2014]. As shown in Figure 39, the trabeculae direction is aligned based on load path in which tensile loading is seen around the pedicles region due to bending and compressive loading in the vertebral body and articular pillars. In the spinous process, bending is also expected and so the stress path is horizontal.
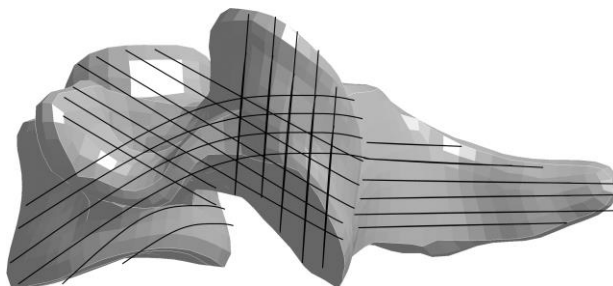
(Image adapted from Cramer and Darby, 2014)

Figure 39: Trabeculae direction in the vertebra is aligned along the load path

Therefore, in this study, in the vertebral body and the articular pillars, which primarily support axial compression, the elements were aligned longitudinally or parallel to the loading direction (axial). The pedicles, lamina, and spinous process protrusions were more susceptible to bending and therefore, the stronger direction of the osteons or trabeculae would be horizontal or parallel to the geometry (Figure 40 and Figure 41). The directions of the element longitudinal (strong) direction (solid black arrows) (Figure 40, Figure 41) are shown to be as described earlier, parallel to the geometry in the spinous process, pedicles and lamina, whereas the directions are along the height of the geometry in the articular pillars and vertebral body.
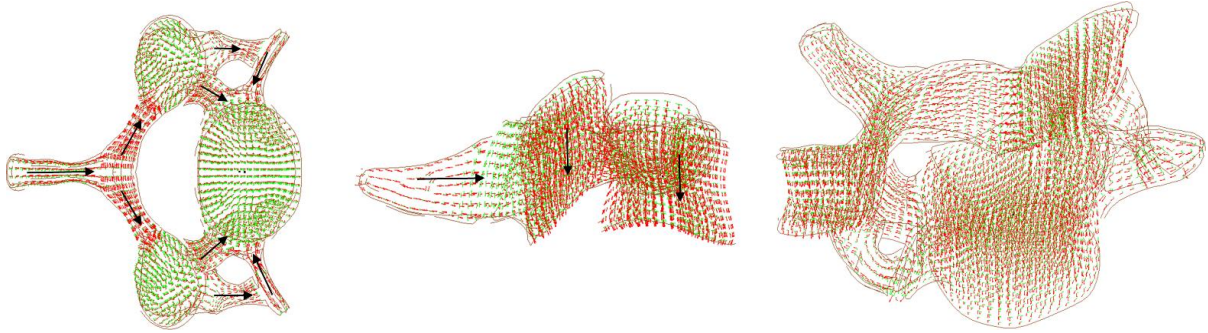
Figure 40: Element orientation in the trabecular bone of the C6 vertebra
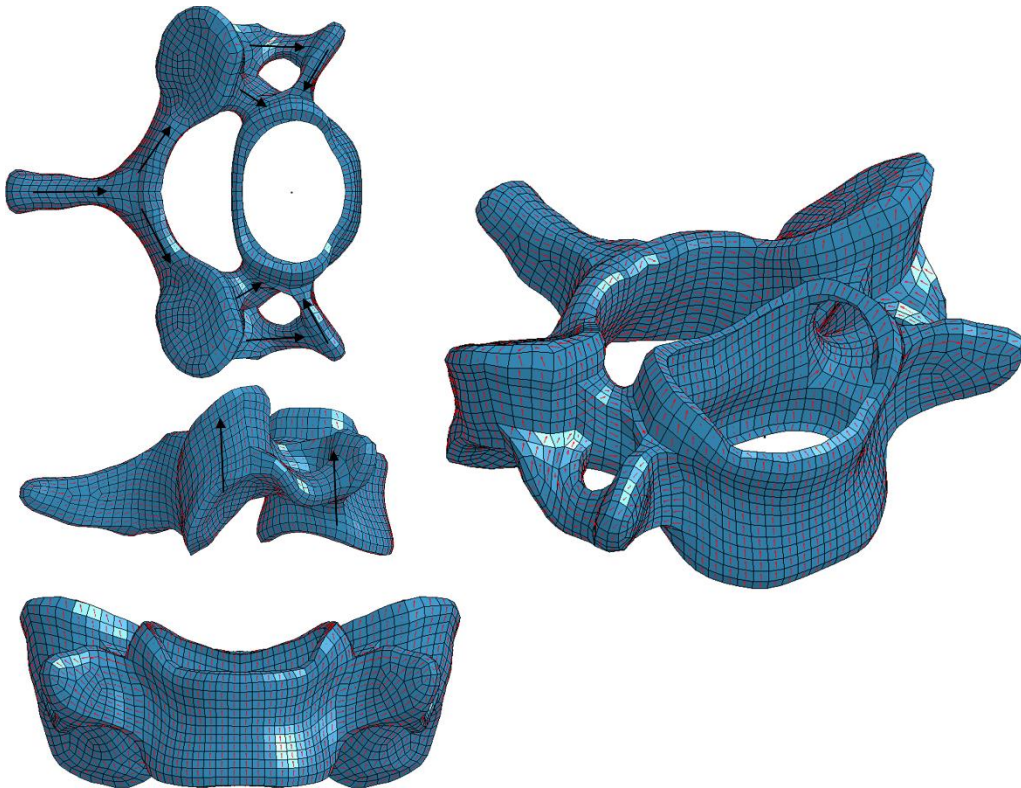
Figure 41: Element orientation in the cortical bone of the C6 vertebra

To orient the elements, the element nodes were numbered such that the direction from node 1 to node 2 was the longitudinal direction [LSTC, 2015]. The nodes for the solid elements in the trabecular bone were defined using a macro Python script (Hyperworks 2013, Altair). For the shell elements in the cortical bones, angles were set to orient the longitudinal direction of the by a given angle away from the direction from node 1 to node 2. This was done in a commercial software (LS-Prepost, LSTC) that also supported aligning selected shell elements based on a generated spline curve that would ensure a smoother transition between components of the vertebra that has conflicting longitudinal direction. In addition, to ensure symmetry, the element and node numbering between the left and right sections of the vertebra were a reflection of one another. Thus, the node numbering and angle values were copied to elements on the adjacent half

keeping in mind that the rotational direction of nodal arrangement in the elements were also being reflected and will have to be considered when numbering the nodes.

3.4. Vertebral Segment Geometry Comparison

In order to compare and analyze the experimental specimens with the GHBMC model, it was important to consider the geometrical and posture (curvature) differences of the cervical spine segments. The GHBMC neck model represented a 26 year old male [De Wit et al., 2012]. The anterior-posterior diameter of the mid-section of the C6 segment was approximately 17.35 mm with a cross-sectional area of 308.5 mm^2. Due to variations between specimens, this discrepancy had to be considered when comparing simulation results with experimental. In order to measure dimensions in X-ray scans, a freely available software (Tracker, Open Source Physics) was utilized as this software allows manual object tracking with position based on a defined scale. The vertebral body anterior-posterior dimensions were estimated using X-ray scans [Carter et al., 2002] and the Tracker software based on the reported mean midsagittal diameter (MSD) (Figure 42). The MSD is measured between the posterior aspect of the vertebral body and the spinolaminar line along a line parallel to the bottom surface of the inferior potting [Carter et al, 2002] (Figure 42).
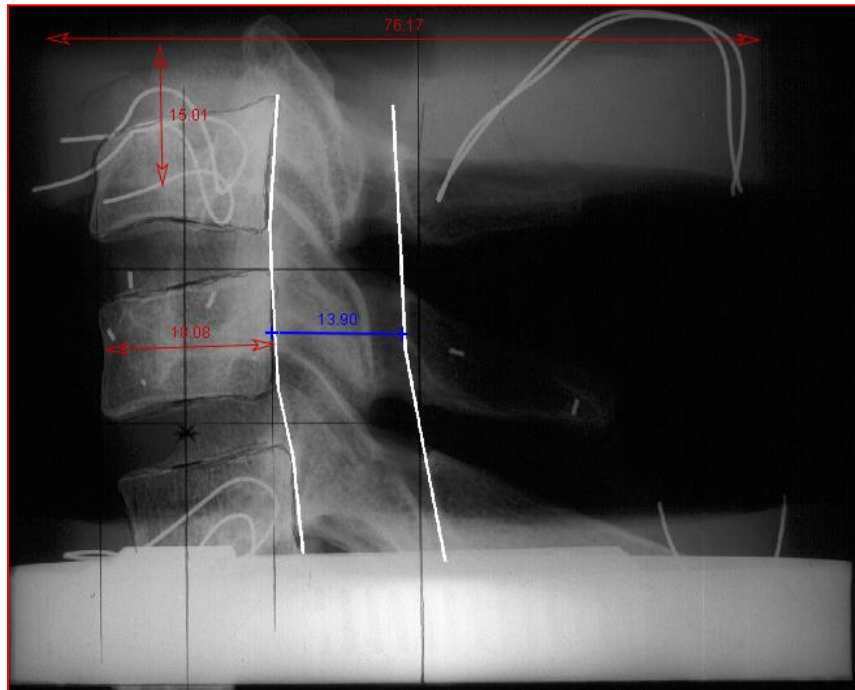
Figure 42: Measurement of potting and vertebral body depth (red) based on the given mean MSD (blue) [Carter, 2002]

Appendix A shows the inferior, superior, anterior and posterior depth of the vertebra, intervertebral disc dimensions and Bezier angle from the X-ray scans provided by Dr. Carter [Carter et al., 2002] in comparison with the GHBMC model. The superior Bezier angle was calculated by drawing a line from the superior posterior corner of the C5 vertebra to the inferior posterior corner of the C7 vertebra and a line from the superior to the inferior posterior corner of the C5 vertebra [Klinich et al., 2004] (Figure 43). The inferior Bezier angle was calculated in a

similar manner but with the C7 vertebra (Figure 43). The anterior and posterior depth of the invertebral disc were measured as well (Figure 43).
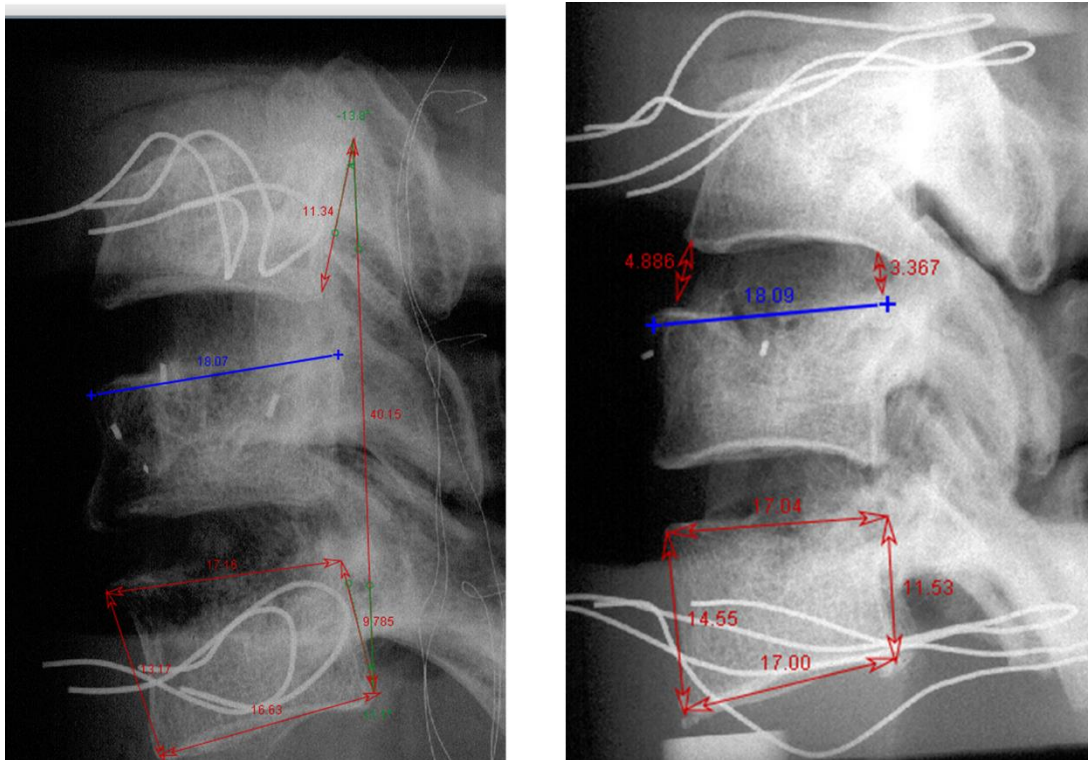
Figure 43: Measurement of Bezier angle (left) and invertebral disc (IVD) depth (right)

For the low lateral eccentricity case [Van Toen et al. 2014], the only C5-6-7 segment extracted was from a female specimen of age 72 with an average vertebral body cross-sectional area of 317 mm^2. The measurement was performed utilizing the dimensions of the ¼-20 socket head screw in the x-ray as a reference scale, with a head diameter of 9.22 mm (Figure 44).
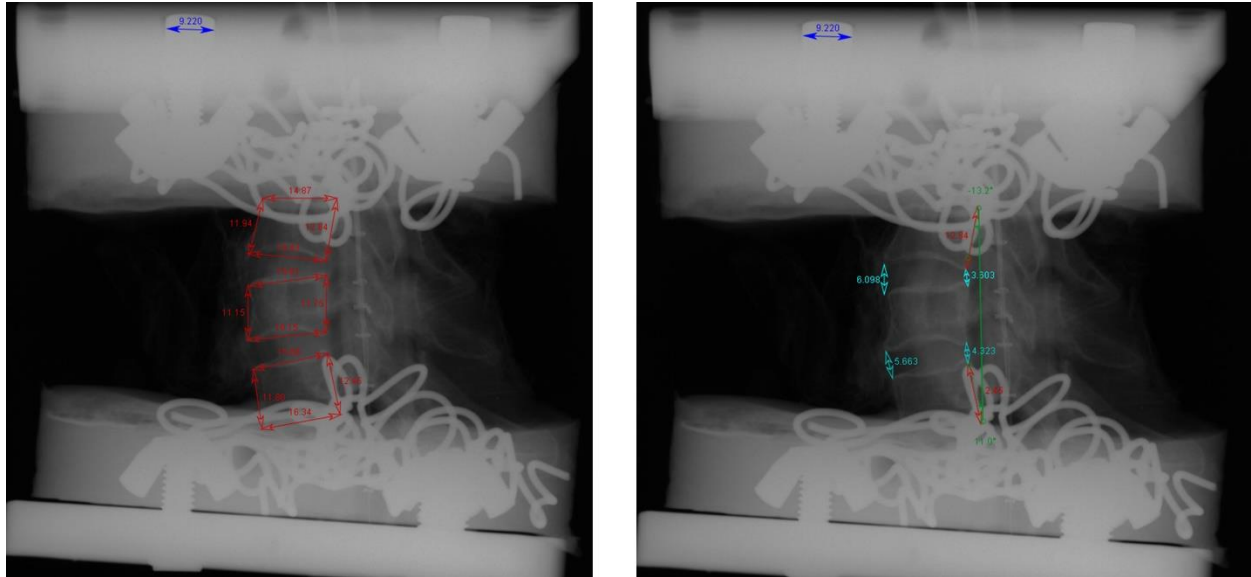
Figure 44: Measurement of vertebral depth(red) (left), IVD (light blue) depth (right), and Bezier angle (green) (right) based on screw dimension (dark blue)

The measurements results are shown in Appendix A. In terms of the specimen depth, as it was from a female specimen, it was smaller in comparison to the GHBMC model. For the intervertebral disc height, the C67 disc was close to the GHBMC dimension but for the C56 disc, the anterior height was slightly higher than the GHBMC model and slightly lower for the posterior height. For the Bezier angle, the lateral eccentricity female specimen (specimen H1318) had a similar angle to that of the aged male specimen (specimen #10) that was utilized in the centric compression experiment. This means that for both these specimens, there was more flexion in the curvature of the spine than the GHBMC model. These geometry differences within each specimen and the model would play a role in the failure responses.

The thickness of the cortical shell varies within the vertebral segment itself [Panjabi et al., 2001; Ritzel et al., 1997; Schmitz et al., 2004]. According to Panjabi et al. (2001), the central region of the inferior endplate is thicker than the central region of the superior endplate although Schmitz et al. (2004) found it to be otherwise (Table 14 and Table 15).

Table 14: Endplate thickness of the C567 (Panjabi et al., 2001)

Cervical Segment Level [Panjabi et al., 2001]	C5	C6	C7
Mean Superior Endplate Thickness (mm)	0.55	0.63	0.60
Mean Inferior Endplate Thickness (mm)	0.62	0.65	0.67

Table 15: Endplate thickness of the C567 (Schmitz et al., 2004)

Cervical Segment Level [Schmitz et al., 2004]	C5	C6	C7
Mean Superior Endplate Thickness (mm)	0.80	0.84	0.82
Mean Inferior Endplate Thickness (mm)	0.76	0.75	0.81

57

Findings in a study by Panjabi et al. (2001) supported a prior study by Denis et al. (1983) in which a higher occurrence (49.2%) of burst fractures was found at the superior endplate and only 6.8% occurred at the inferior endplate. In addition, Schmitz et al. (2004) had also found the medial region of the endplate to be thinner than the lateral right and left region. Both studies found that the superior endplate was thinner towards the anterior region whereas for the inferior endplate, in contrast to Schmitz (2004), Panjabi et al. (2001) found that the inferior endplate became thinner towards the posterior region. This discrepancy was likely due to the in-plane partial volume effect of the CT scans and the automated edge detection algorithm used which had a low threshold for defining the edge between air and bone as bone [Schmitz et al., 2004]. Besides that, variations due to specimens and methodological differences in defining the endplate thickness could induce the differences in results [Panjabi et al., 2001; Schmitz et al., 2004]. Panjabi et al. (2001) defined the endplate thickness perpendicular to a tangent through the inferior endplate whereas Schmitz et al. (2004) defined the endplate thickness perpendicular to the local slope of the endplate, which would consider the different endplate orientations. The thickness values determined by Schmitz (2004) using computed tomography (CT) measurements were higher than Panjabi (2001) who used direct measurement technique (Table 15). This agreed with the findings by Silva et al. (1994) on CT measurements overestimating the thickness by at least a factor of 2 [Panjabi et al., 2001; Silva et al., 1994].

Table 16: Anterior and posterior cortical shell thickness (Panjabi et al., 2001)

Cervical Segment Level [Panjabi et al., 2001]	Anterior	Posterior
C5	0.62mm	0.44mm
C6	0.66mm	0.49mm
C7	0.70mm	0.48mm

In addition, the anterior region of the cortical shell is thicker than the posterior region (Table 16) [Panjabi et al., 2001]. Based on the GHBMC C57 model, the cortical shell was given a uniform thickness using only the anterior thicknesses reported [Panjabi et al., 2001]. As for the endplates, both C6 and C7 segments had the thickness of 0.59 mm at the superior and inferior regions whereas the C5 segment has a 0.58 mm thickness for the superior endplate and 0.59 mm for the inferior endplate. These values were closer to the superior endplate thicknesses reported [Panjabi et al., 2001] than the inferior endplate thickness. The lack of variation of the thickness of the cortical shell and endplate in the simulation as opposed to actual specimens could lead to variation between simulation and experimental results.

3.5. Single Element Verification of Material Properties

Implementation of the mechanical properties and verification of the material models was undertaken using single element test cases in tension, compression and shear loading. A 1 mm^3 solid element and 1 mm^2 shell element were utilized in all simulations with a 1mm/ms rate as shown in Figure 45 and Figure 46 as strain rate effects were not being considered. For the tension case, the element was deformed in the positive z-direction whereas, for compression, the

cube was compressed in the negative z-direction. The element was allowed to expand in tension and contract in compression preserving the Poisson's ratio. For the shear case, a displacement boundary prescribed motion in the x-direction was applied to the top surface of the cube and the bottom surface of the cube was fully constrained in all directions.

Tension   Compression   Shear
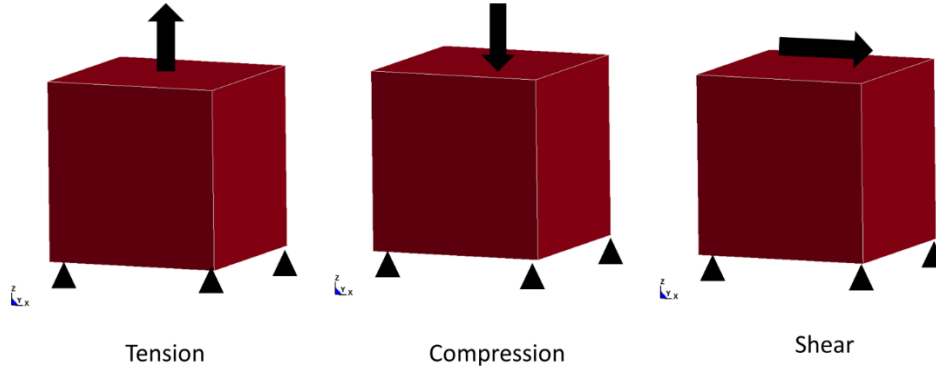
Figure 45: Single element simulation for solid elements

Tension   Compression   Shear
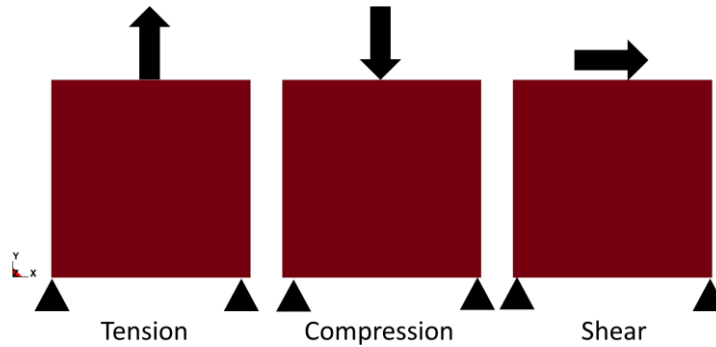
Figure 46: Single element simulation for shell elements

An element failure criterion (MAT_ADD_EROSION) was used to erode the elements in tension, compression, and shear respectively based on their failure strains in each loading. It was noted that these strains were utilized individually in each loading configuration such that only compressive failure strain was set for compression loading and so on. Having multiple failure strains at once would cause the failure strain of individual loadings to differ due to the mixed mode of failure. The failure strain for tension, compression, and shear for the cortical bone were based on Reilly and Burstein (1974) and Tang et al. (2015) (Section 3.1.1). The next step included all three failure strains and to simulate the single element simulation in tension, compression and shear loading. It is worth mentioning that when the maximum shear strain was the only input in the model, LS-DYNA used the tensorial shear strain value. However, when multiple failure strains were in the input of the model, LS-DYNA used the engineering shear strain value, which is twice the tensorial shear strain. Maximum and minimum principal strain and shear strains were set as the failure strains for the cortical bone model and the elements eroded whenever one of the failure strain was reached first.

The failure strain for tension for trabecular bone was based on studies by Liu et al. (2013) and Mosekilde et al. (1987) (Section 3.1.2.). In compression of a foam-like material, the material densifies upon being compressed and therefore, it is technically erroneous to erode an element based on the minimum principal strain. If an element was eroded due to minimum principal strain, the erosion will remove material from the calculation in the computational model whereas, in reality, the broken trabeculae filled in the spaces in the porous structure and increased the strength of the material. There was a lack of data on the shear failure strain in trabecular bones in the human cervical spine as stated in Section 3.2. Due to the lack of data, it was decided that the trabecular bone model was set to only fail due to the maximum principal strain criteria.

3.6. Centric Compression Simulation Boundary Conditions

As the focus of this thesis was on hard tissue failure prediction, the centric compression case was selected to determine the best constitutive models in the FEM as hard tissue fractures were seen predominantly in this case [Carter, 2002]. The boundary conditions were based on the experimental set up [Carter, 2002] in which the custom compression fixture was attached to the upper potting mold, preventing rotation in all directions and only allowing translation downwards.

The upper and lower segments of the functional spinal unit were potted with polymethylmethacrylate (PMMA) [Carter, 2002]. A pre-load of approximately 40 N was applied before the displacement input for load application. The axial displacement profile produced peak displacements of between 8 and 15 mm with a Haversine velocity profile and the desired pulse width of 16 ms [Carter, 2002]. The displacement input curve was differentiated from the experimental MTS ram velocity input curve. Depending on the specimens such as young (below 50 years old) or aged (above 50 years old), the displacement profiles were applied accordingly such that the peak displacement was approximately 14 mm for young specimens and 8mm for aged specimens. For the young simulation, the displacement input curve was based on specimen #10 (male aged 30, segment C5-7) and for the aged simulation, the displacement input curve was based on specimen #12 (male aged 80, segment C5-7) [Carter, 2002].

The C567 segment was extracted from the full neck GHBMC model. Three different methods for replicating the potting boundary condition were performed and evaluated. The first method applied the boundary conditions to the superior C5 and inferior C7 endplate as seen in Figure 47

below.
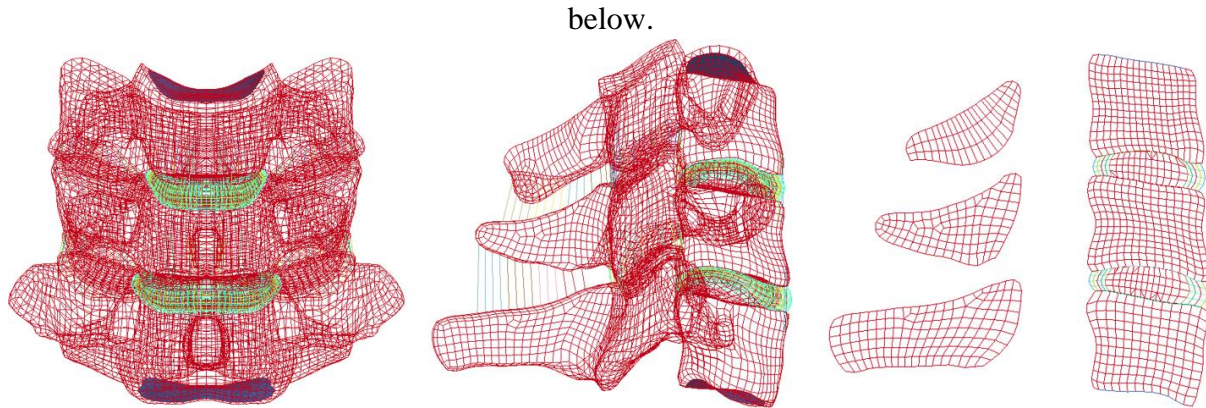
Figure 47: C5-6-7 model with C5 superior and C7 inferior endplates (blue)

The second method involved modeling the potting by estimating the depth of the potting material at the C5 and C7 segments based on CT and X-ray scans shared by Dr. Carter as shown in Figure 48 below. The diameter of the potting material would be approximately 3" (76.2 mm) as the standard potting molds were made from 3" ID X 3.5" OD PVC tubing that was cut into 19 mm long sections [Carter, 2002]. The depth of the potting was not given explicitly but was mentioned that the depth was established such that specimen would be held rigid without interference with the intervertebral joints. The depth of the potting however could be roughly estimated using the X-ray scan and the Tracker software. The X-ray scans were scaled by using the midsagittal diameter (distance between the posterior aspect of the vertebral body and the spinolaminar line along a line parallel to the bottom surface of the inferior potting) [Carter, 2002] of the specimens and from there, the depth of the potting, as well as the geometry of the specimens, were estimated. A standard PMMA material property was assigned to the potting model using an elastic material model. Due to the complexity of the shape of the vertebral body, tetrahedral elements were used to fill the volume of the potting in Hypermesh. A shell layer on the surface of the cylindrical potting was created for boundary condition application.
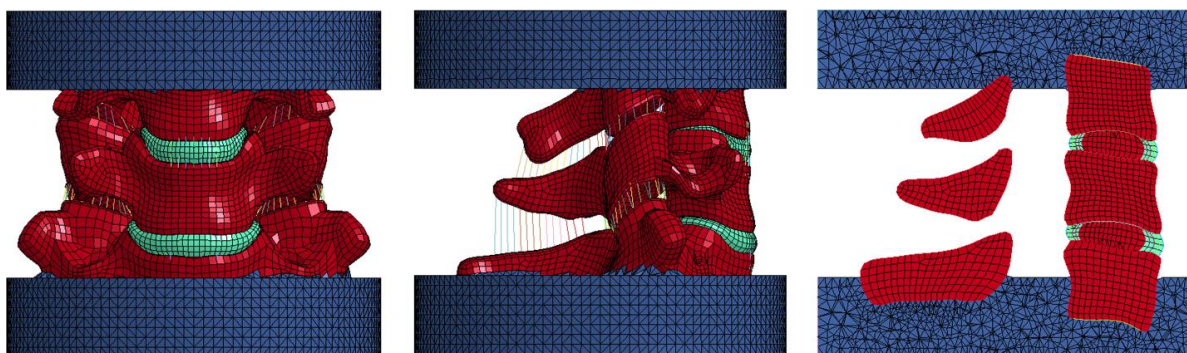
Figure 48: Potting (blue) loading configuration boundary condition

The C5 superior endplate or the top potting was constrained in all rotational directions and in the y and x translational direction. The C7 inferior endplate or bottom potting on the other hand was constrained in all rotational and translation directions.

The compression injury mechanism occurs when the eccentricity was smaller than the distance from the centroid of the inferior intervertebral disc to the anterior and posterior boundaries of the vertebral body [Carter, 2002]. The loading utilizing the fixed-fixed end condition in which the ends were rotationally and anteroposterior translationally constrained demonstrated the axial load vector to remain between the posterior longitudinal ligament (PLL) and the centroid of the inferior intervertebral disc (IVD) [Carter, 2002].

In the simulation, for the endplate methodology, the boundary condition was applied based on the center of gravity of the endplate, which would be between the PLL and the centroid of the inferior IVD (Figure 49). For the potting case, the center of gravity based on the potting was towards the posterior edge of the vertebra (approximately 20 mm away from the center of the endplate) (Figure 49). Therefore, the center of gravity to which the load was applied on should be recalibrated to the center of the endplate. As the center of gravity was recalibrated, the moment of inertia change was calculated based on parallel axes theorem.
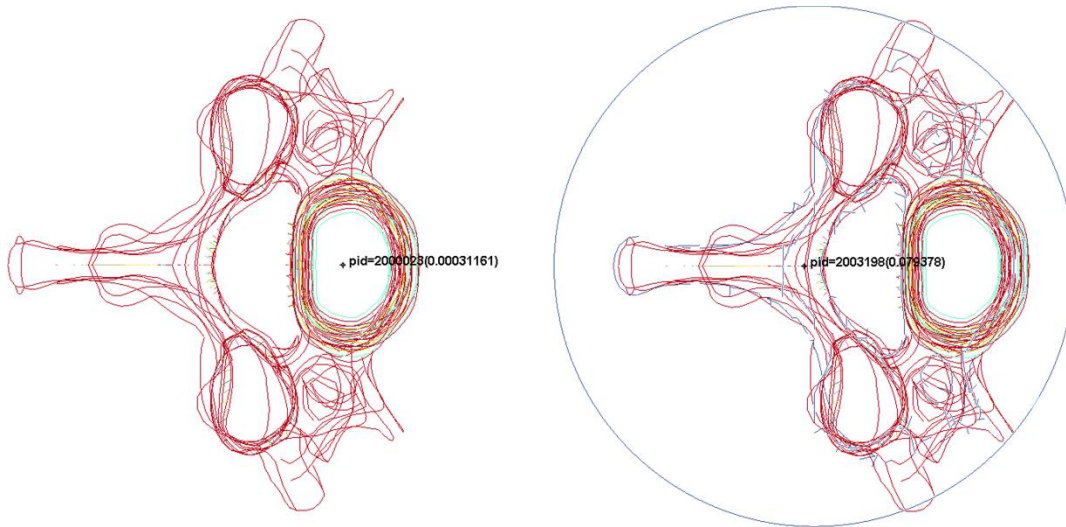
Figure 49: Centre of gravity of the endplate (left) and the potting (right) configuration

To measure forces, the force output from the endplate was retrieved. For moment measurement at the inferior IVD, the X-directional force was retrieved at the endplate and the Y-rotational moment was achieved by multiplying the X force with the distance from the CG of the endplate to the CG of the inferior IVD, which is 37.80 mm.

This endplate simulation methodology was the most simplified simulation version of the centric compression case. This simulation was used to evaluate and identify the best material configuration out of the four. The four combination of constitutive models (Section 3.2) were AsymmCort_AsymmTrab, AsymmCort_AnisoTrab, AnisoCort_AsymmTrab and AnisoCort_AnisoTrab. Once the best material configuration was identified, this material configuration was subsequently used in the potting method for centric compression as well as other loading cases with eccentricity that will be discussed in the next few sections. These models were also compared against the SymIsoCort_SymIsoTrab model for hard tissues in the

GHBMC neck model [De Wit et al., 2012] to identify the importance of asymmetry, anisotropy and age effect.

3.7. Eccentricity Cases Boundary Conditions

Four eccentricity cases (posterior, anterior, low lateral, high lateral) [Carter, 2002; Van Toen, 2014] that reported hard tissue failure were simulated. In the extension compression case with posterior and anterior eccentricities [Carter et al., 2002], hard tissue failure was seen in the posterior and anterior segments of the vertebra respectively.
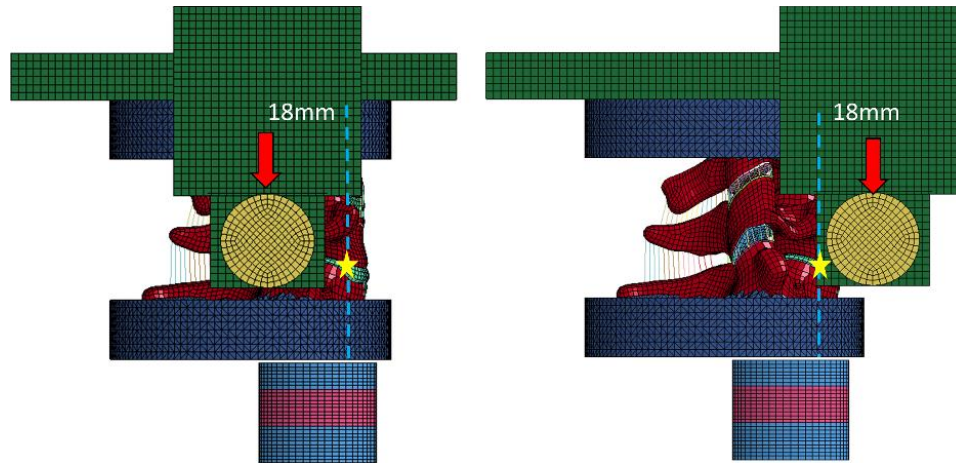
Figure 50: Posterior (left) and anterior (right) eccentricity boundary condition and set up

The eccentricity was the anterior-posterior depth of the middle vertebra body width from the centroid of the inferior intervertebral disc (IVD). The anterior-posterior depth of the C6 vertebral body model was approximately 18 mm and therefore the load was applied 18 mm posteriorly from the centroid of the inferior IVD for the posterior eccentricity case and anteriorly for the anterior eccentricity case (Figure 50). Due to the large eccentricity causing rotation, the best method to simulate the boundary condition was to simulate the experimental set up with the impact being applied on the bearings of the fixture on top of the specimen as this would represent the inertia in the system. In the experiment, the fixture could move anterior-posteriorly which would create the eccentricity. The displacement boundary condition was based on specimen #47 (male aged 94, segment C5-7) for the posterior eccentricity compression case and specimen #17 (male aged 61, segment C5-7) for the anterior eccentricity compression case.

For the lateral case based on Van Toen`s [Van Toen et al., 2014] experiment, the low lateral eccentricity was 1% of the average lateral dimensions of the cranial and caudal vertebral bodies whereas the high lateral eccentricity was 150%. The low lateral eccentricity case predominantly resulted in hard tissue failure whereas the high lateral eccentricity case produced more soft tissue failure [Van Toen, 2014]. The fixture in this experimental set up [Van Toen, 2014] was similar to that of Carter (2002) with the difference being the location of the bearing and impactor. The impactor and bearing were placed on the specimen to provide lateral eccentricity to the loading as seen in Figure 51 by rotating it around the z-axis by 90 degrees. For the low lateral

eccentricity simulation, the location of the bearing was 0.3 mm (1% of the average lateral width of the C5 and C6 vertebral bodies) laterally away (along with the x-axis) from the center of gravity (CG) of the inferior IVD (Figure 51). The high lateral eccentricity simulation, on the other hand, had the bearing 40.9mm (150% of the average lateral width of the C5 and C6 vertebral bodies) away from the CG of the inferior IVD.
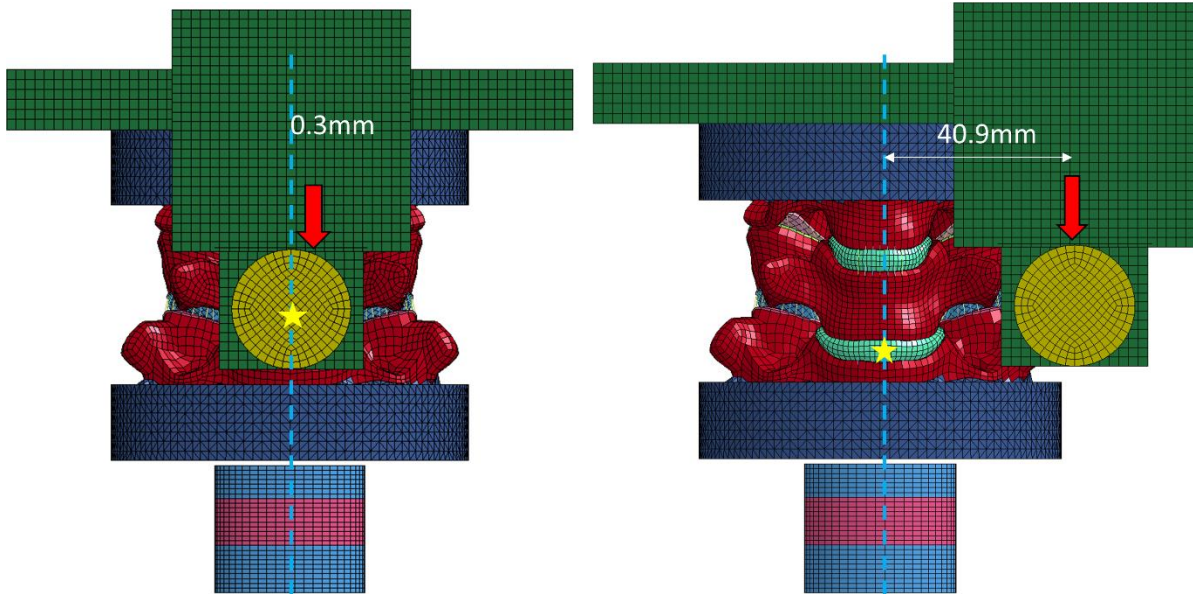
Figure 51: Lateral eccentricity boundary condition and set up (Left: Low eccentricity, Right: High eccentricity)

A preload of 45 N was applied to the set up along the C5 superior endplate center of gravity for approximately 250 ms, which is enough time for the simulation to settle. After which, a displacement boundary condition was applied using the curve retrieved from the MTS ram velocity input similar to the centric loading cases. For the lateral eccentricity case, the boundary condition applied to the C5 superior endplate or superior potting was given a linear displacement profile based on a constant velocity of 0.5 mm/ms [Van Toen, 2014]. For the low and high lateral eccentricity cases, the specimen was compressed by 20% and 40% respectively of the height between the inferior most to superior most aspect of the vertebral bodies in the segment. Therefore, in the simulation case, the segment would be compressed by approximately 12.5 mm (25ms) for the low lateral eccentricity case and 25 mm (50 ms) for the high lateral eccentricity case.

During the preload application, the superior C5 endplate could only move in the z-direction and constrained rotationally. After the preload application and upon loading with eccentricity, the superior C5 endplate was free to translate and rotate. The inferior C7 endplate and bottom of the inferior potting were constrained in all directions both translationally and rotationally.

As a displacement boundary condition was applied based on the experimental MTS ram velocity input, the moment could not be measured from the loaded part directly unless a rotational angle

boundary condition was defined. Therefore, three cylinders were created (Figure 50 and Figure 51) beneath the vertebral body that represented the load cell similar to the experiment. The top and bottom cylinder of the load cell would be defined as rigid material to tie the inferior C7 endplate or inferior potting to the top cylinder of the load cell and have the bottom cylinder of the load cell constrained in all rotational and translational directions. The middle cylinder was given an elastic material model and a splitting plane methodology was utilized in measuring the moment.

To compare the moment results, the moment was resolved from the load cell to the centroid of the inferior IVD of the C6 segment, similar to experiment. The centroid of the load cell and the centroid of the inferior IVD of the C6 segment was determined and this distances were used to resolve the moment from the load cell to the inferior IVD. The difference in length in the x-direction was 5.45 mm, 0.00 mm in the y-direction and 37.42 mm in the z-direction. With the displacements and the moment output from the load cell from the splitting plane method, the moment was then resolved at the inferior IVD. As mentioned in section 3.4, the best material configuration for both cortical and trabecular bone determined in the simplified centric compression simulation was used in these simulations.

3.8. Experimental Data Compilation

For the centric compression, posterior and anterior eccentricity compression cases, the experimentalist, Dr. Carter [Carter, 2002], provided the failure load, displacement, and moment curves. In addition to that, CT scans were provided to determine the fracture pattern of the specimens. 3D Slicer (version 4.6.2), a publicly available and free software was used to analyze the CT scans and determine the location of the fracture. For the lateral eccentricity compression case, Dr. Van Toen [Van Toen et al, 2014], had provided CT scans as well and the failure load and moment was compared with the values that were published in her paper [Van Toen, 2014].

3.9. Mesh Refinement Analysis

Mesh refinement was performed by splitting both solid and shell elements twice in all parts except the disc for model stability purposes. The centric loading simulation is performed for this analysis as it is the most simplified simulation in this study. The original mesh has 41,920 elements, the medium mesh (single split) has 222,660 elements and the fine mesh (double split) has 1,544,880 elements. The mesh size in the original mesh was approximately 1.4 mm, the medium mesh was 0.7 mm and the fine mesh was 0.35 mm (Figure 52). The material directions of the C6 trabecular and cortical bone models were oriented using a similar method performed with the original mesh model (Section 3.3).
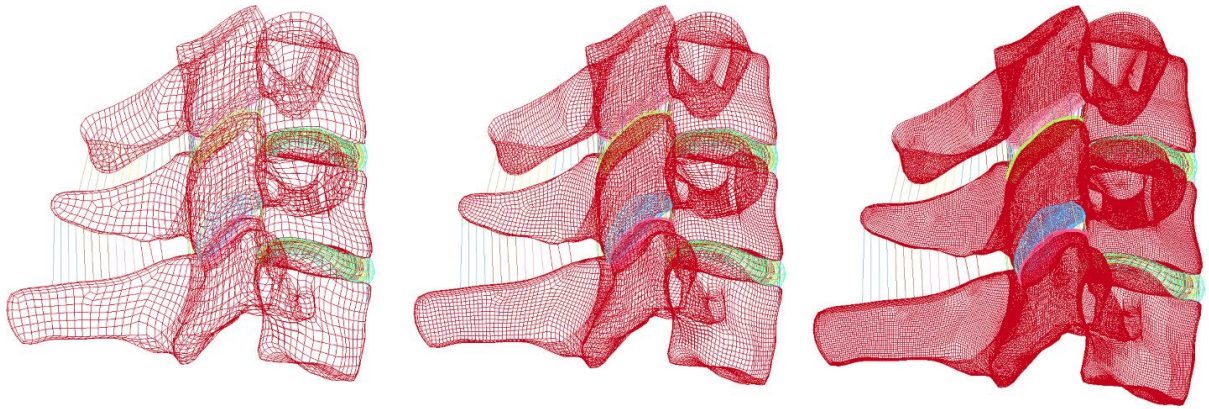
Figure 52: Mesh refinement split set up (left to right: original, medium (single split), fine (double split))

Chapter 4: Results

4.1. Single Element Simulation

4.1.1. Cortical Bone Models

As the goal of this thesis was to improve on the existing isotropic and symmetric bone model (SymIsoCort_SymIsoTrab) that was being used in the GHBMC model, the GHBMC model was set as the baseline model. To measure the capability of the current model, single element simulations utilizing the GHBMC constitutive models for cortical bone were performed in tension, compression, and shear and compared against experimental data. A symmetric and isotropic elastic-plastic model with kinematic hardening was utilized in the SymIsoCort with cortical bone properties that were similar to the young compressive longitudinal cortical bone properties proposed in this study and trabecular bone properties that had lower strength than the aged trabecular bone properties proposed. As shown in Figure 53 below, the yield strength of the SymIsoCort model (0.19 GPa) was similar to the compressive yield strength of the young (0.19 GPa) and aged (0.20 GPa) models of the cortical bone [Reilly and Burstein, 1975], and the ultimate strength (0.21 GPa) was 6% higher than the young ultimate strength (0.20 GPa). Due to the symmetric nature of the model, under tension, a similar curve as the compression was seen and thus the tensile strength values were over-predicted. The ultimate compressive strain in the GHBMC model (0.028) was 37% higher than the young and aged ultimate compressive strain (~0.0205) [Reilly and Burstein, 1975]. Summary of this comparison is shown in Table 17.

Table 17: Summary of comparison of mechanical properties in SymIsoCort with properties used in this study

SymIsoCort (GHBMC)		
Yield Strength (GPa)	0.19	Similar to the young and aged compressive yield strength [Reilly and Burstein, 1975]
Ultimate Strength (GPa)	0.021	6% + of young ultimate compressive strength [Reilly and Burstein, 1975]
Ultimate Strain	0.028	37% + of young and aged ultimate compressive strain [Reilly and Burstein, 1975]

The shear stress, on the other hand, was $\frac{1}{\sqrt{3}}$ of the tensile stress based on von Mises criterion. As this model did not allow shear definition, the element eroded at the given effective plastic strain at failure (0.0178) (Figure 54). The ultimate engineering shear strain at the effective plastic strain at failure was 0.047.
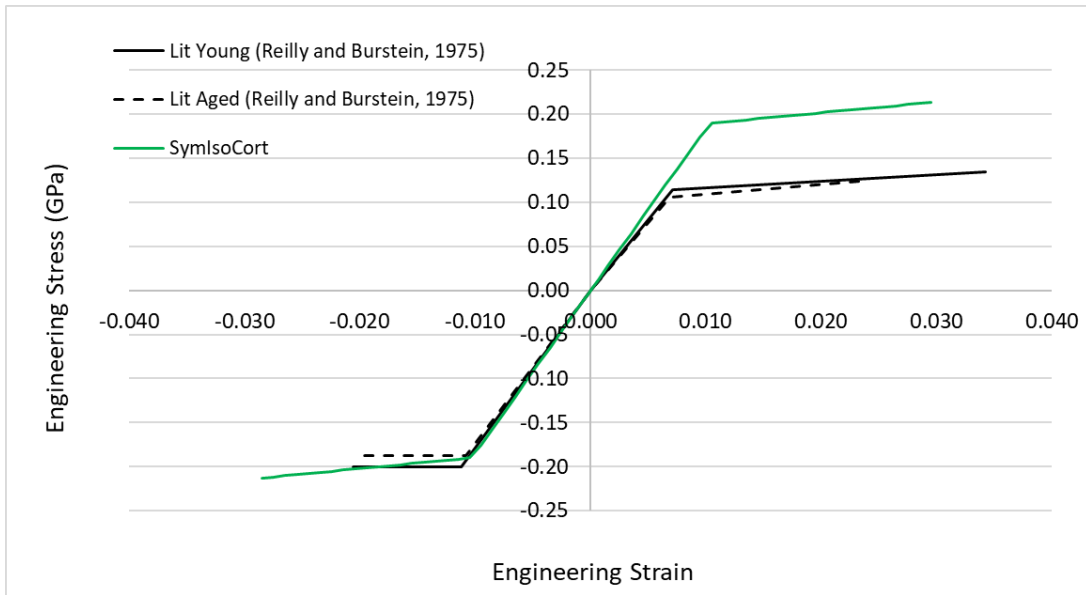
Figure 53: Tension and compression stress-strain curve (green) of the SymIsoCort model against experimental data (solid black: young and dotted black: aged)
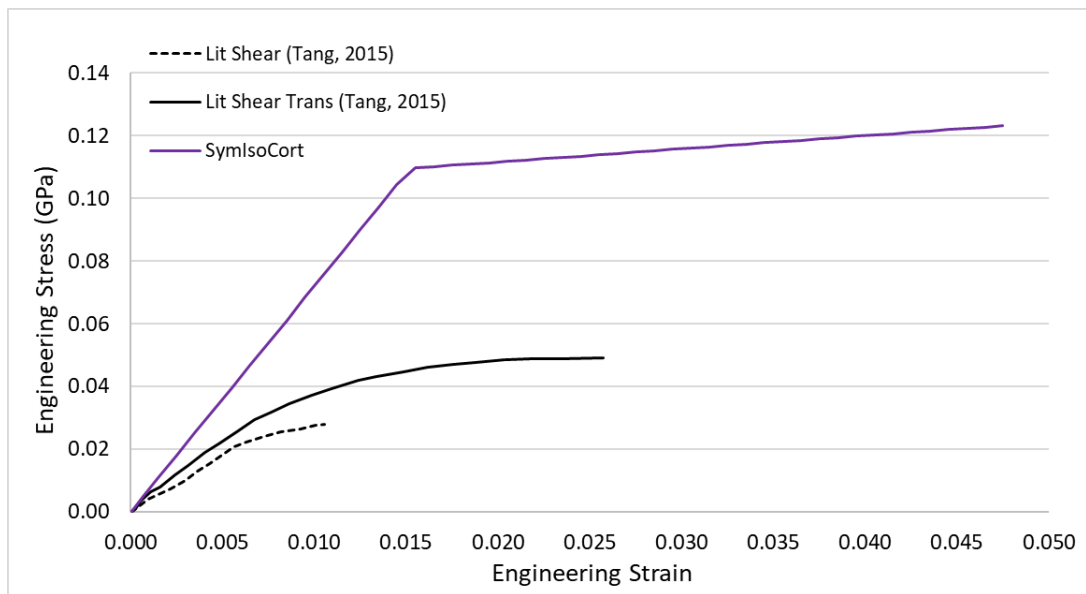
Figure 54: Shear stress-strain curve of the SymIsoCort model (purple) against experimental data (black)

Model Capabilities in Tension, Compression, and Shear Single Element Simulation

The cortical bone was tested with an asymmetric (AsymmCort) and an orthotropic (AnisoCort) elastic-plastic model (See Section 3.2) with each having a set of young and aged mechanical properties (Table 4 and Table 5). An additional failure model by strain (MAT_ADD_EROSION) was utilized that eroded elements using longitudinal compressive and tensile strains [Reilly and Burstein, 1975] and transverse shear strain [Tang et al., 2015].

68

As shown in Figure 55 and Figure 56, the AsymmCort was able to predict the tension and compression stress-strain curves for both young and aged specimens as this model allowed input from both modes of loading. With maximum principal strain at failure defined (0.0337 for young and 0.0230 for aged), the model failed in tension upon reaching the failure strain defined (Figure 55 and Figure 56) predicting the experimental ultimate stress and strain (Young: 0.13 GPa and 0.035; Aged: 0.121 GPa and 0.0225). Similarly, the model failed in compression upon reaching the failure strain defined based on minimum principal strain (-0.0203 for young and -0.0202 for aged) and predicted the experimental ultimate compressive stress and strain (Young: -0.201 GPa and -0.0195; Aged: -0.195 GPa and -00.0195).
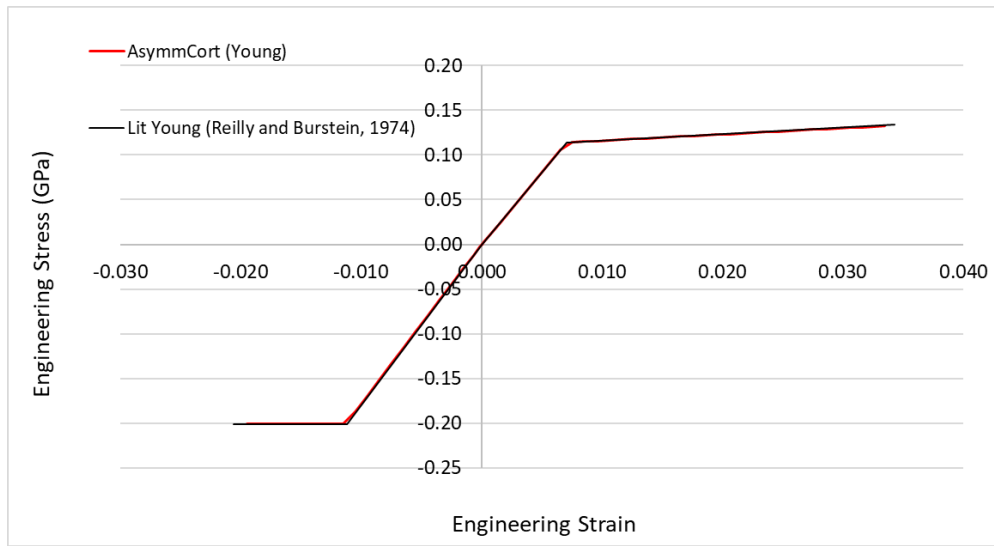
Figure 55: Tension and compression stress-strain curve of AsymmCort model (red) compared against experimental data for young specimens (black)
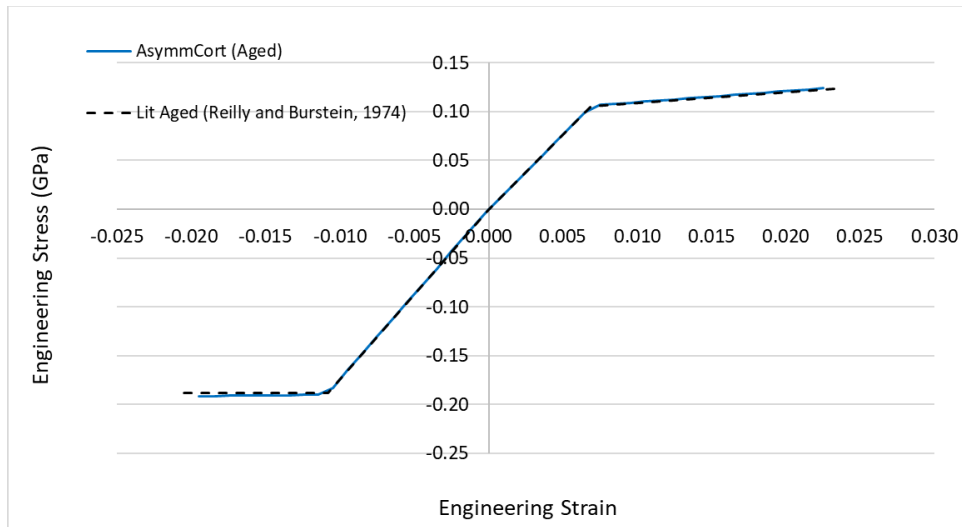
Figure 56: Tension and compression stress-strain curve of AsymmCort model (blue) compared against experimental data for aged specimens (black)

Due to lack of experimental data, the shear mechanical properties in the young and aged model were the same. There was no explicit shear definition in this model and therefore, the shear properties were determined from the von-Mises criterion ($\frac{1}{\sqrt{3}}$ of the compressive stress) (Figure 57) (Young: 0.115 GPa; Aged: 0.11 GPa). This model failed at the given maximum tensorial shear strain value at failure (0.0129) with MAT_ADD_EROSION which corresponded to an engineering shear strain of 0.0257 predicting the experimental longitudinal shear strain value. As this model had no anisotropic properties, there was no difference in the transverse direction. Furthermore, because cortical bone was modeled as shell elements, there was only in-plane shear.
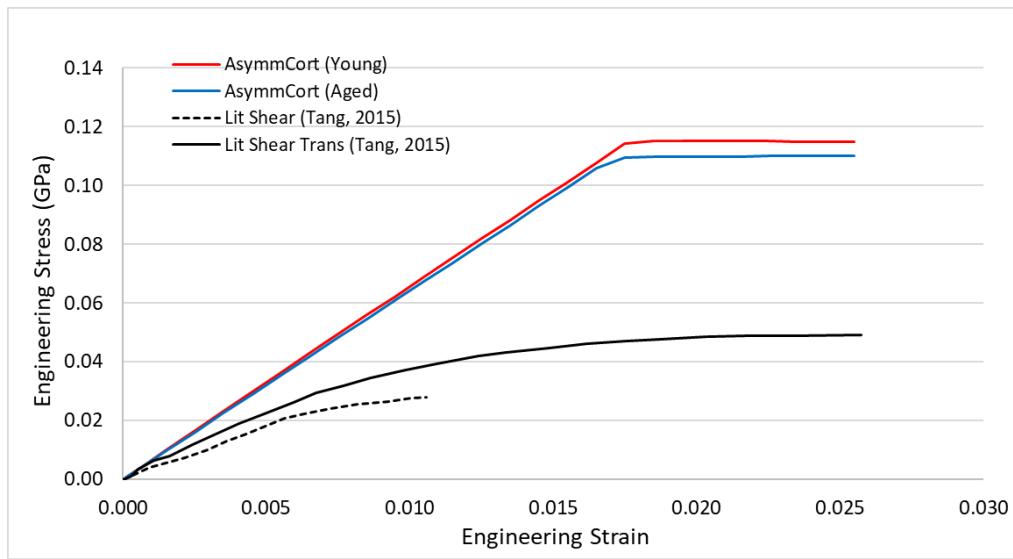
Figure 57: Shear stress-strain curve of the AsymmCort model (young: red and aged: blue) compared against experimental data (black)

For the AnisoCort model, only one curve definition was enabled in the material model and since this thesis work focused on the compression of the cervical spine, the compression curve was utilized. As the AnisoCort model is a symmetric model, the tensile curve was similar to that of the compressive curve. As only one minimum and one maximum principal strain could be defined, the longitudinal minimum and maximum principal strain was utilized instead of the transverse strain as most of the cortical shell was presumed to be in their longitudinal direction when being compressed.
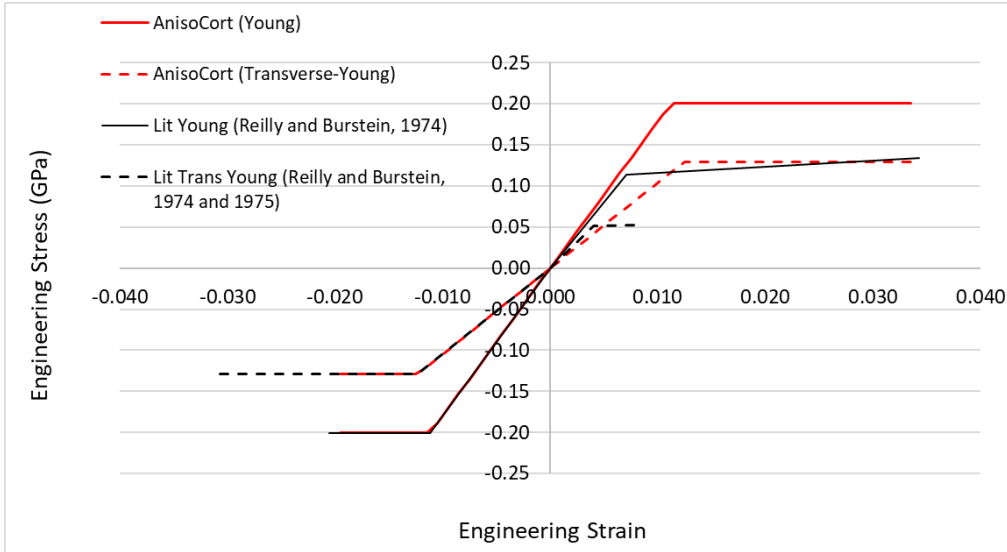
Figure 58: Tension and compression stress-strain curve of AnisoCort model compared against experimental data for young specimens in the longitudinal (solid red and black) and transverse (dotted red and black) directions
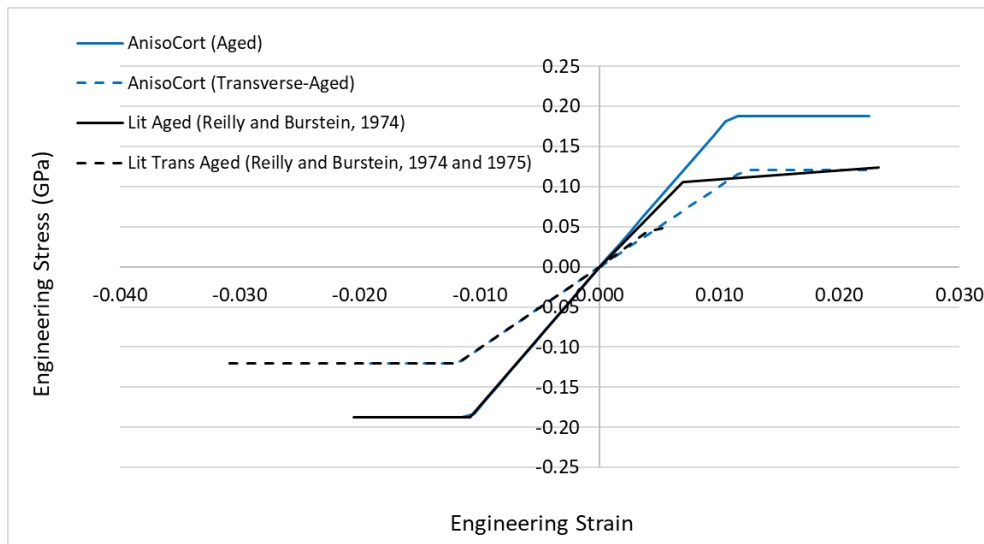
Figure 59: Tension and compression stress-strain curve of AnisoCort model compared against experimental data for aged specimens in the longitudinal (solid blue and black) and transverse (dotted blue and black) directions

In compression, both young and aged AnisoCort models predicted the ultimate compressive stresses in the longitudinal (Young: -0.200GPa; Aged: 0.188GPa) and transverse (Young: 0.129GPa; Aged: 0.120GPa) (Figure 58 and Figure 59). The ultimate compressive strain in the longitudinal direction (Young: 0.02; Aged: 0.02) were accurately predicted but the transverse strain (Young and Aged: 0.031) was over-predicted by approximately 37% (Young and Aged: 0.019) as the elements were defined to fail using the longitudinal minimum principal strain.

71

In tension (Figure 58 and Figure 59), both young and aged AnisoCort models over-predicted the experimental ultimate tensile stresses in both longitudinal (Young: 0.134 GPa; Aged:0.124 GPa) and transverse (Young:0.0525 GPa; Aged:0.0484 GPa) directions by approximately 50% (Young: 0.200 GPa; Aged: 0.188 GPa) and 147% (Young: 0.130 GPa; 0.120 GPa) respectively. This is because the model lacked asymmetry and utilized the compression curve in tensile loading. Similar to the compression loading, as the minimum principal strain at failure was defined to be the longitudinal failure strain, the ultimate compressive strain in the longitudinal direction was accurately predicted (Young: 0.034; Aged: 0.0225) but the transverse strain (Young: 0.008; Aged: 0.005) was over-predicted by approximately 330% (Young: 0.034; Aged: 0.0225).

The shear properties used in the young and aged AnisoCort models were the same, due to lack of experimental data describing shear properties as a function of age. The shear stress-strain curve of the AnisoCort model was based on von-Mises criterion and hence it had been internally coded to be $\frac{1}{\sqrt{3}}$ of the input compressive curve (Figure 60) in the model. In the AnisoCort model, the ratio to achieve the shear stress of 0.05GPa is 0.431 [Tang, 2015] for the young model and 0.461 for the aged model. As the cortical bone was modeled as a shell element, there were only in-plane shear properties.
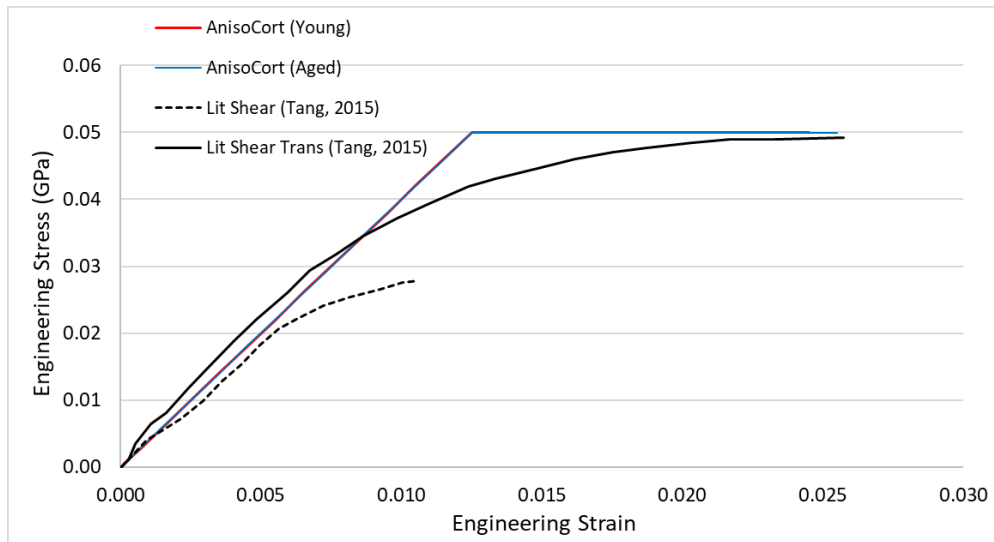
Figure 60: Shear stress-strain curve of AnisoCort model compared against experimental data for young (solid red) and aged (solid blue) specimens in the longitudinal (solid black) and transverse (dotted black) directions

Multi-Failure in Cortical Bone Model

As mentioned in the previous section, MAT_ADD_EROSION is an additional option that can be defined for various types of failure strain. The previous section showed the model capabilities in individual failure strain: maximum principal strain under tension loading, minimum principal strain under compression loading, and maximum shear strain under shear loading. In this section,

all three failure strains were defined in the model and this would be implemented in the segment models.

With all three failure strain defined, in the young and aged AsymmCort models, failure due to the maximum shear strain failure criterion (tensorial: 0.013; engineering:0.026) occurred before the maximum (young:0.0337; aged:0.0232) or minimum (young:-0.0203; aged:-0.0202) principal strain under tension and compression loading (Figure 61 and Figure 62). Due to this, the ultimate tensile stress and strain values for the young AsymmCort model were under-predicted by 9.5% (0.121 GPa) and 49% (0.0175) respectively and by 5.9% (0.116 GPa) and 25% (0.0175) for the aged AsymmCort model. The ultimate compressive stress was accurately predicted in the young AsymmCort model (0.2 GPa) but the strain is under-predicted by 15% (0.0175). In the aged AsymmCort model, the ultimate compressive stress is under-predicted by 6.5% (0.188 GPa) and the strain by 15% (0.0175).
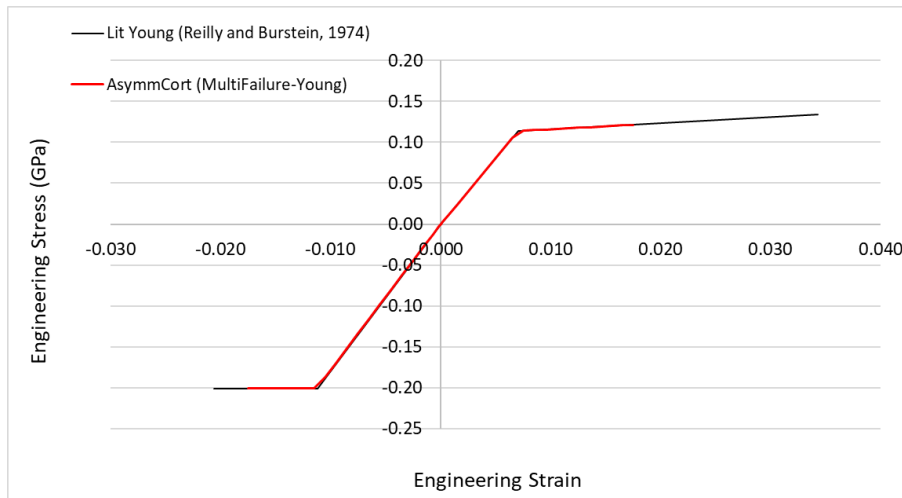
Figure 61: Tension-compression curve of young AsymmCort model with multiple defined failure strain
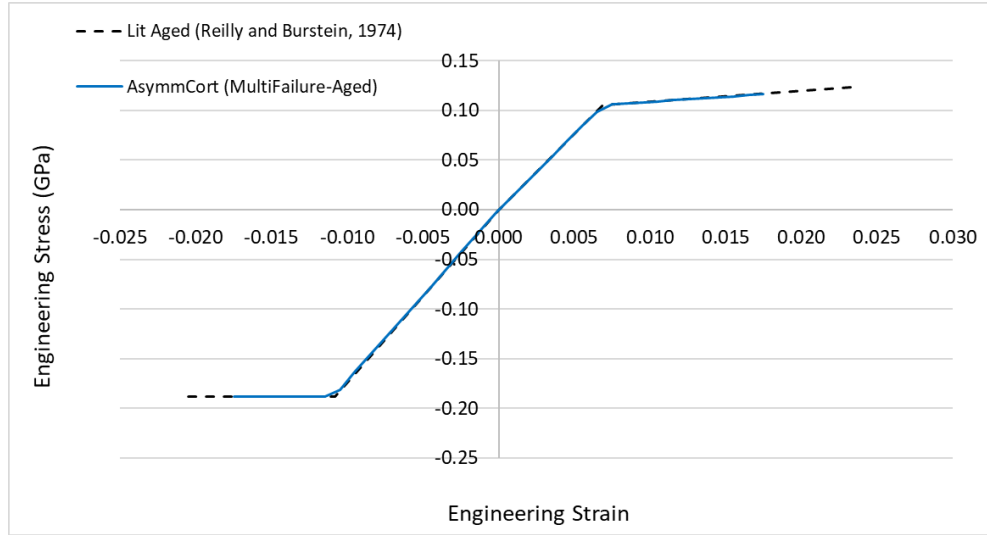
Figure 62: Tension-compression curve of aged AsymmCort model with multiple defined failure strain

For shear loading, as the models failed due to the maximum shear strain criteria, the ultimate engineering shear strain 0.0260 (Figure 63) were predicted accurately by both young and aged AsymmCort models which have no distinction between the shear properties due to lack of experimental data. As mentioned in the previous section, as the ultimate shear stress values were based on the von-Mises criteria of the compressive stress, the ultimate shear stress value (0.05 GPa) were over-predicted in both young and aged AsymmCort models.
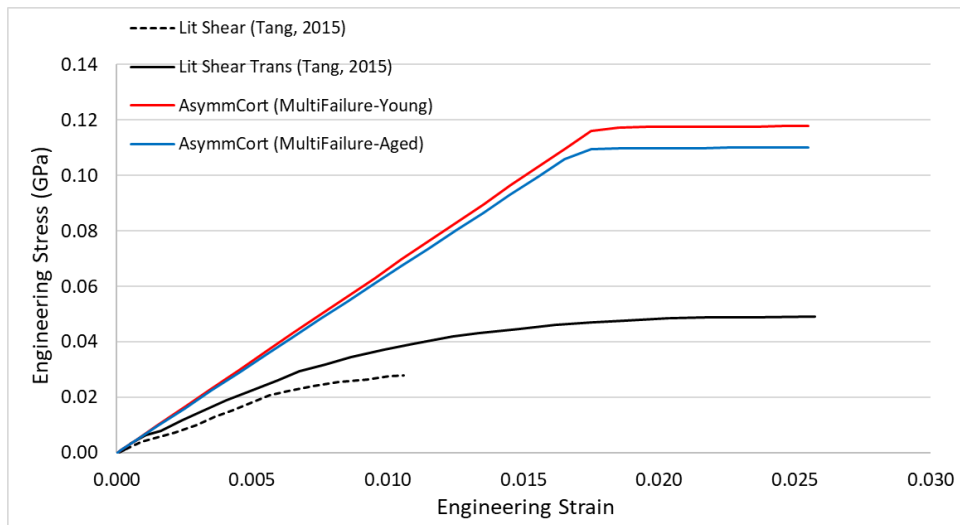
Figure 63: Shear curves of the young and aged AsymmCort model with multiple defined failure strain

For the AnisoCort model, similarly, the maximum shear strain criteria (0.026) defined the failure of the models under longitudinal and transverse tension and compression loadings. The elements reached the maximum shear strain before the maximum and minimum principal strain failure

values. Due to this, in compression, the ultimate strain values in both longitudinal and transverse directions were under-predicted by 15% (0.0175) and 47% (0.0165) respectively in both young and aged AnisoCort models (Figure 64 and Figure 65). The ultimate compressive stresses in the longitudinal and transverse direction were accurately predicted in the young (0.2GPa and 0.129GPa) and aged (0.188GPa and 0.12GPa) AnisoCort models. The ultimate tensile stress values were over-predicted due to the lack of asymmetry in this model. The ultimate longitudinal tensile stress was over-predicted by 50% (0.2GPa) in the young AnisoCort model and 52% (0.188GPa) in the aged AnisoCort model. The ultimate longitudinal tensile strain on the other hand was under-predicted by 49% (0.0175) in the young AnisoCort model and 10% (0.0185) in the aged AnisoCort model. The ultimate longitudinal tensile stress and strain values were over-predicted by 145% (0.129GPa) and 114% (0.016) in the young AnisoCort model and by 149% (0.12GPa) and 214% (0.0165) in the aged AnisoCort model.
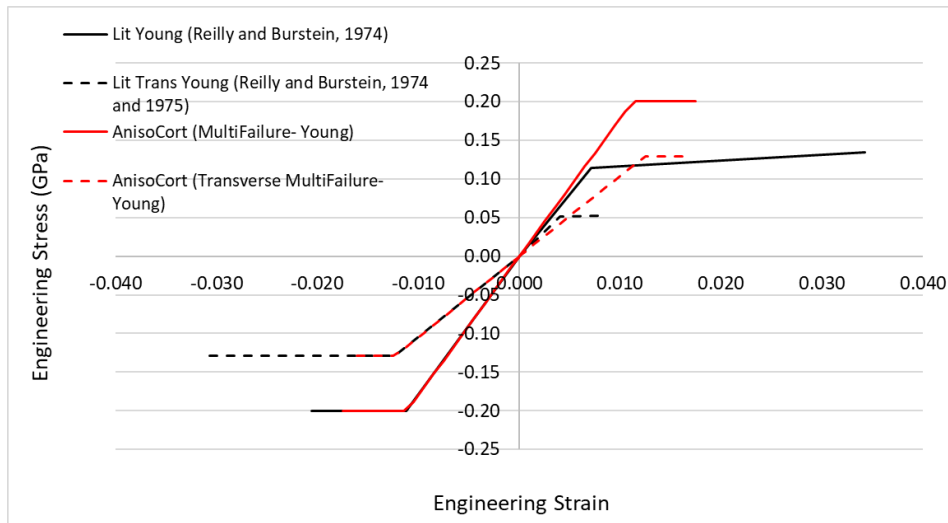
Figure 64: Tension-compression stress-strain curves of the young AnisoCort model in longitudinal and transverse directions with multiple failure strain criteria
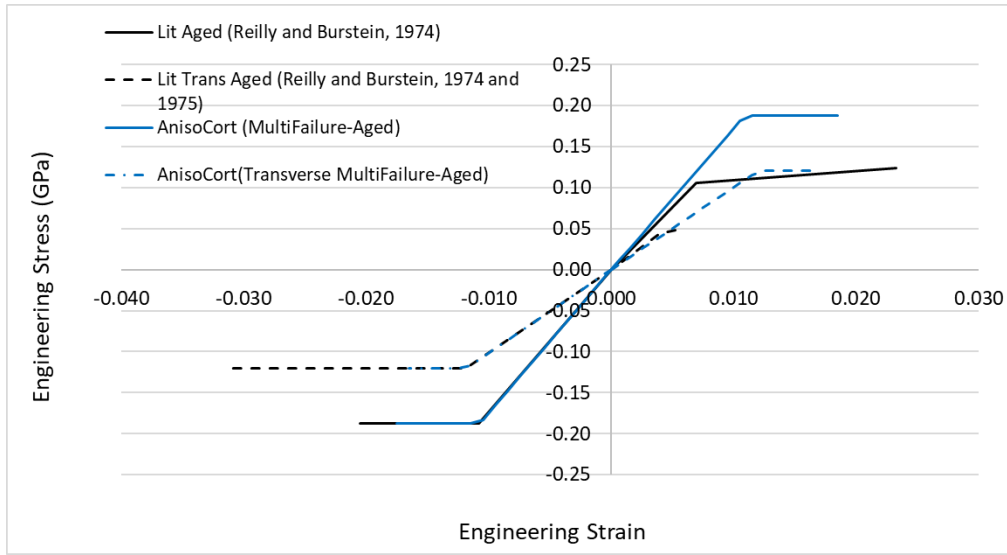
Figure 65: Tension-compression stress-strain curves of the aged AnisoCort model in longitudinal and transverse directions with multiple failure strain criteria
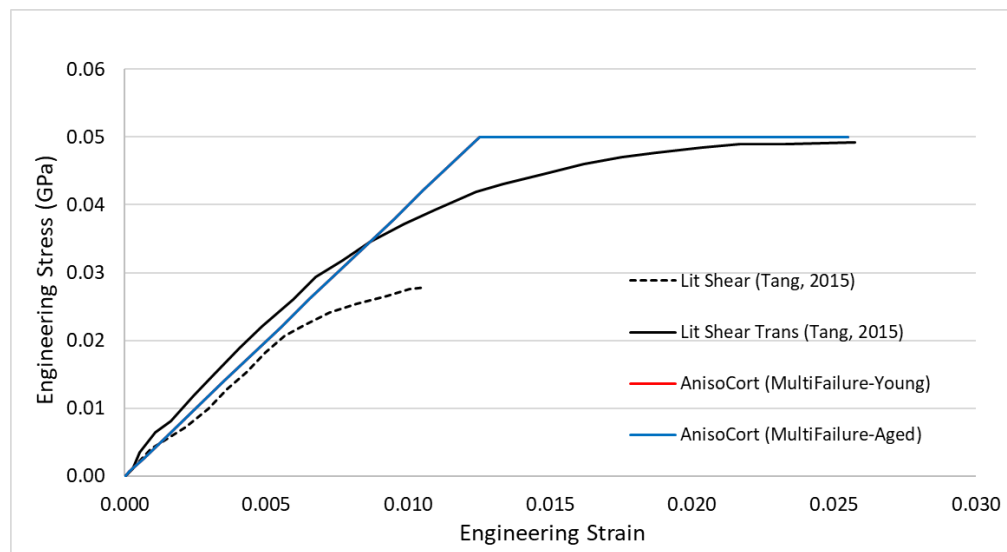
Figure 66: Shear stress-strain curve of the young and aged AnisoCort model with multiple failure strain criteria

As the maximum shear strain failure criteria defined the failure of the model, the ultimate shear strain value of 0.0260 was predicted accurately in both young and aged AnisoCort models (Figure 66). Furthermore, as shear was able to be defined in this model, the ultimate shear stress value of 0.05GPa were accurately predicted as well. Again, it is noted that due to the lack of experimental data, there was no distinction in the shear properties in the young and aged AnisoCort models.

4.1.2. Trabecular Bone Models

For the trabecular bone model, the GHMBC model was set as the baseline similar to the cortical bone model. A similar symmetric isotropic elastic-plastic model was utilized. Trabecular bone however behaves similar to a foam (Section 3.1.2.) due to its architecture. As mentioned in Section 3.1.2, the experiment was stopped prior to densification to prevent damaging the specimen for density measurement and to include the densification region in the constitutive models, the plateau was extended (Section 3.1). Therefore, as shown in Figure 67, the experimental black lines (solid for young and dotted for aged) representing the curves from literature [Liu et al, 2013], stopped to avoid damaging the specimen for density measurement and hence the densification region was never reached. As shown in Figure 67 and Figure 68, the SymIsoTrab model did not predict the experimental curves.
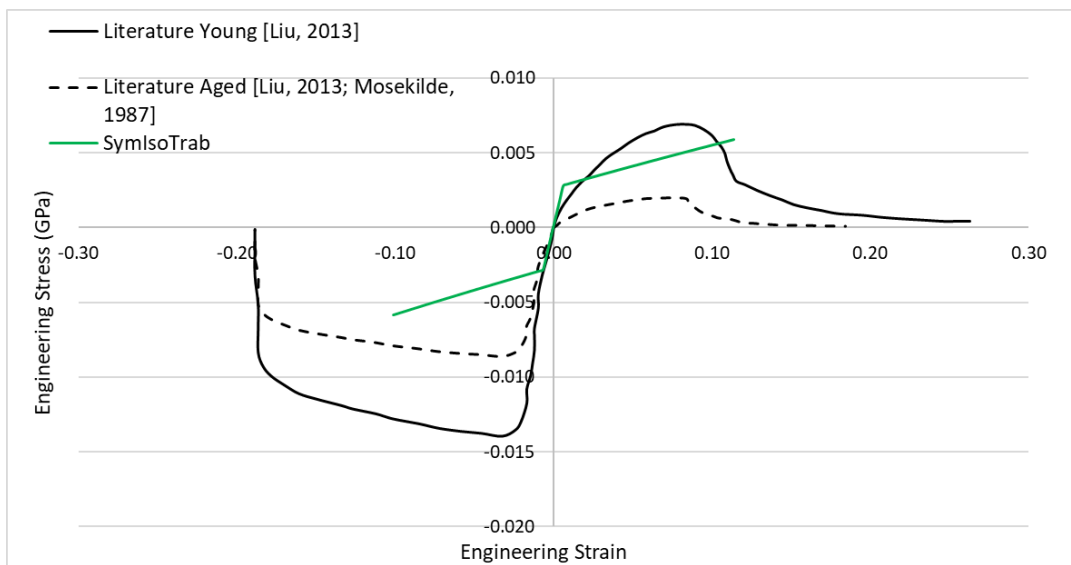
Figure 67: Tension and compression stress-strain curve of SymIsoTrab model (green) compared against experimental data (solid black: young and dotted black: aged)
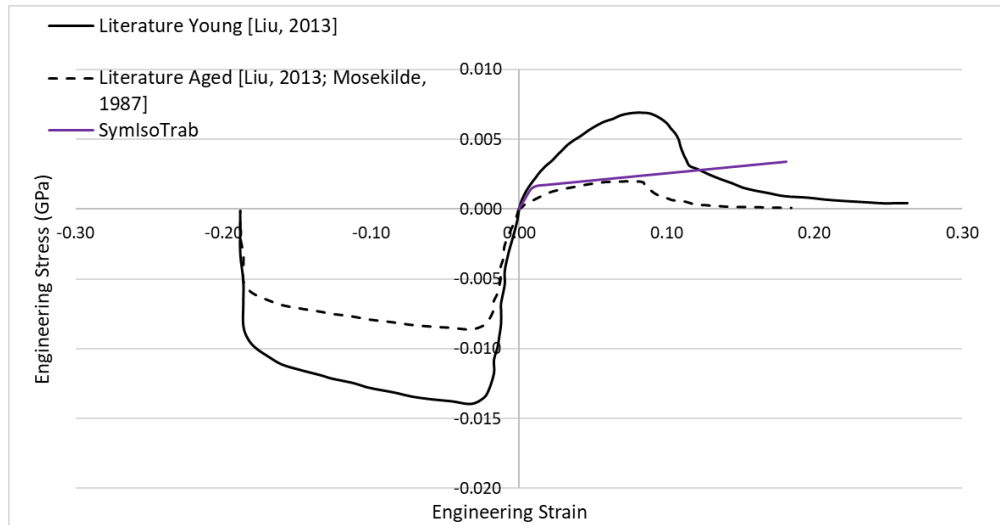
Figure 68: Shear stress-strain curve of SymIsoTrab model (purple) compared against experimental data (solid black: young and dotted black: aged)

For the young trabecular bone material properties, the plateau was extended until approximately 0.456 before densification begins (Section 3.1). As for the aged trabecular bone, as mentioned in Section 3.1, the densification region starts at a higher strain approximately around 0.6 and hence the plateau was extended up to that strain. The aged specimen stress curve was 0.616 of the young specimen stress curve [Liu et al., 2015]. The transverse curve was reduced by approximately 0.34 [Mosekilde et al., 1985] and the shear curve by 0.58 [Sanyal et al., 2012] which was approximately the von-Mises criterion value.

The trabecular bone was tested with two foam constitutive models (AnisoTrab and AsymmTrab) (See Section 3.2). Based on Figure 69 and Figure 70, for both young and aged models, the AnisoTrab model was able to predict experimental stress-strain curves in the longitudinal (young: 0.014 GPa; aged: 0.0086 GPa) and transverse directions (young: 0.0045 GPa and aged: 0.0029 GPa). Although there was no definition of yield stress or strain in the material model, it predicted the ultimate stress before densification accurately. As there was no failure due to minimum principal strain, the model did not fail in compression.

The tension curve was modeled as a linear elastic-plastic curve in the AnisoTrab model without an option to define the curve. Therefore, the ultimate longitudinal stress (0.0069 GPa) was predicted but not the elastic modulus or the yield stress and strain values. The element failed under the maximum principal strain of 0.095, which predicted the experimental ultimate tensile strain value. Similarly, for the aged model, the longitudinal ultimate stress (0.0002 GPa) and strain (0.076) were predicted accurately as the element failed due to the maximum principal strain criteria.

As mentioned the shear curve was based on von-Mises criterion and is $\frac{1}{\sqrt{3}}$ or 0.58 of the compression curve and assumed to be similar in both longitudinal and transverse direction

[Sanyal, 2012]. To achieve this, a ratio of 1.89 of the compressive curve was utilized to obtain an ultimate shear stress of approximately 0.008 GPa, which was 0.58 of the young compressive stress, 0.014 GPa. Similarly, for the aged curve, a ratio of 1.01 of the compressive curve was utilized to achieve a shear stress of approximately 0.0049GPa, which was 0.58 of the aged ultimate compressive stress of 0.0086GPa. The model failed due to the maximum principal strain criteria and at this failure strain, the engineering shear strain was 0.181 for the young model and 0.143 for the aged model.
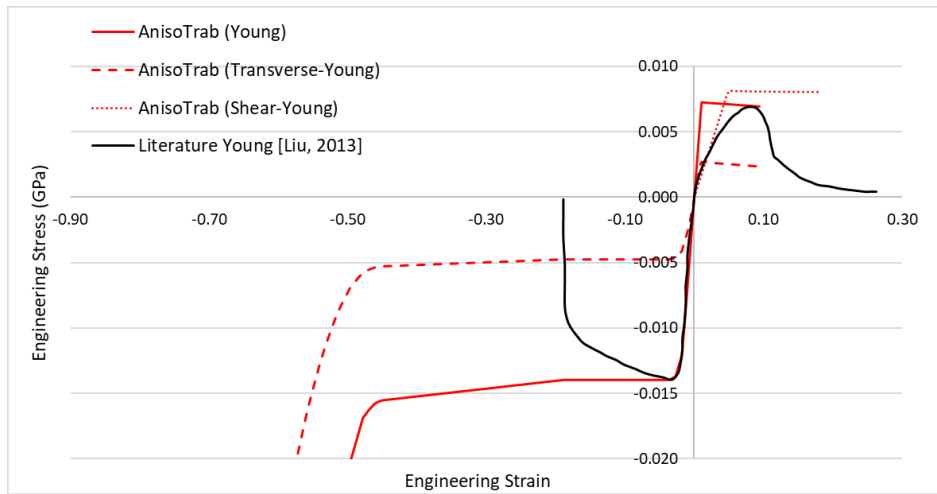
Figure 69: Tension (red), compression (red) and shear (dotted red) stress-strain curves in the longitudinal (solid) and transverse (dashed) directions of the AnisoTrab model compared against experimental data (solid black) for young specimens
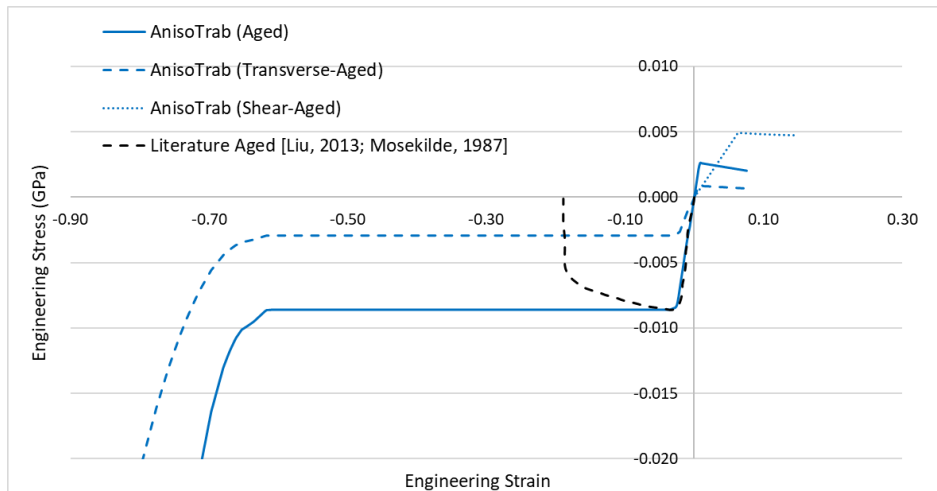
Figure 70: Tension (blue), compression (blue) and shear (dotted blue) stress-strain curves in the longitudinal (solid) and transverse (dashed) directions of the AnisoTrab model compared against experimental data (dotted black)

The AsymmTrab model was able to predict the ultimate compressive stress before densification for both young (0.014 GPa) and aged specimens (0.0086 GPa) (Figure 71 and Figure 72). This

model as mentioned before did not fail in compression. Similar, to the AnisoTrab model, there was no full definition of tensile yield stress and strain and the curve was modeled as linearly elastic-plastic. Due to the maximum principal strain failure criteria, the ultimate tensile stress and strain values were predicted for the young (0.0069 GPa and 0.096) and aged (0.002 GPa and 0.076) models. Unlike the AnisoTrab model, which allowed shear definition, this model did not allow any. The shear stresses (~0.010 GPa for young model and ~0.005 GPa for aged model) were similar to the theoretical shear stress values [Sanyal,2012] (~0.08 GPa for young model and 0.046 GPa for aged model) (Figure 71 and Figure 72) and thus the shear stress values in this model were obtained via the von Mises criterion of the compressive stress. Under shear, the element failed under maximum principal strain failure criterion and at this failure strain, the engineering shear strain was 0.183 for the young model and 0.147 for the aged model.
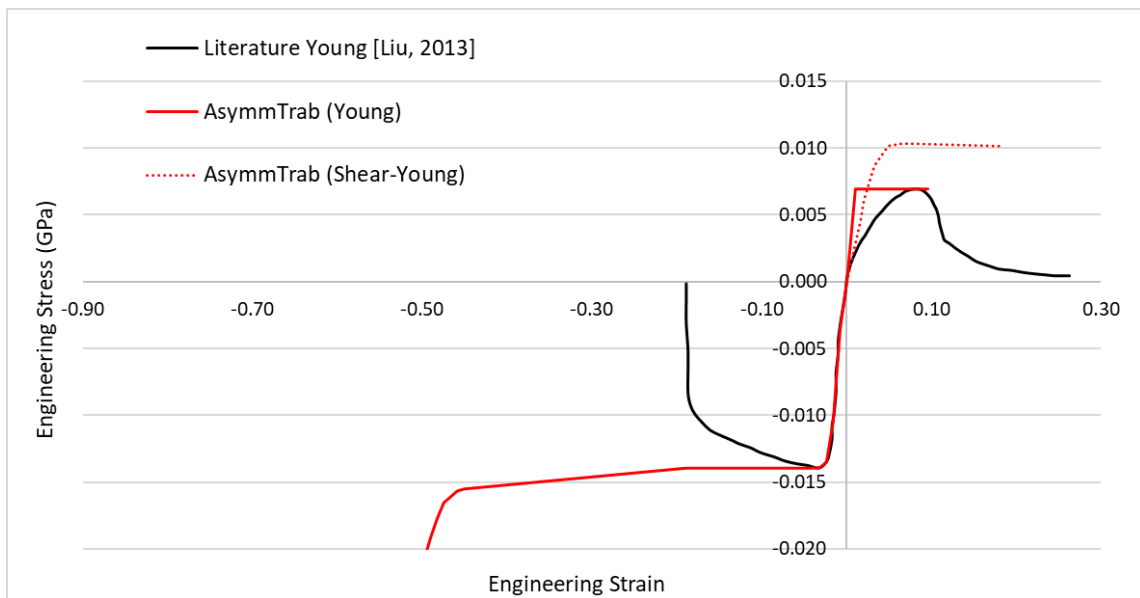
Figure 71: Tension (solid red), compression (solid red) and shear (dotted red) stress-strain curves of the AsymmTrab model compared against experimental data (solid black) for young specimens
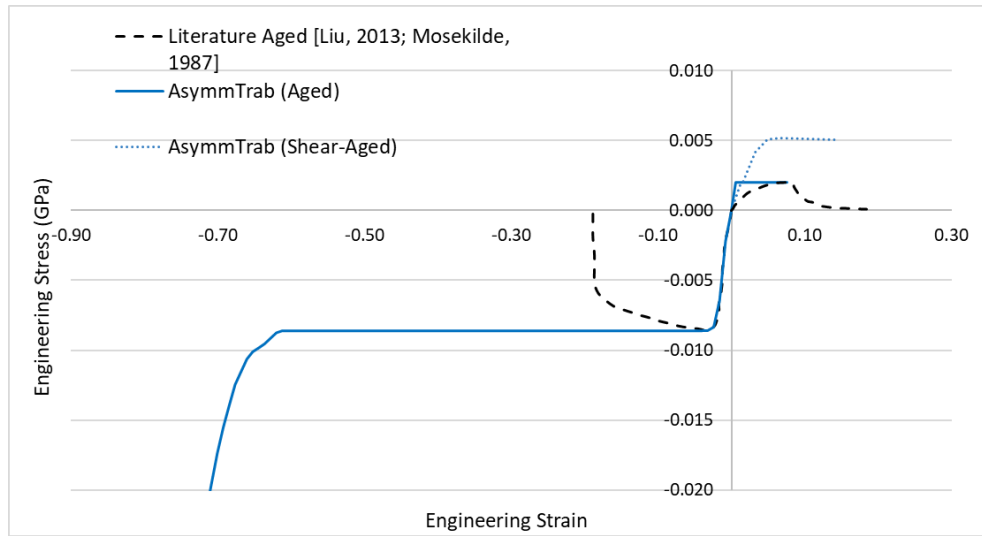
Figure 72: Tension (solid blue), compression (solid blue) and shear (dotted blue) stress-strain curves of the AsymmTrab model compared against experimental data (dotted black) for aged specimens

4.2. Centric Compression

4.2.1. Loading on the Endplate

Kinetic and Kinematic Results

The results of the centric compression loading case with loading on the C5 superior endplate were shown in Figure 73 and Figure 74 whereas the normalized results for the young models with the young experimental values was shown in Figure 75 and the normalized results for the aged models with the aged experimental values was shown in Figure 76. The failure force and displacement results for the young specimen models were depicted in Figure 73 and the aged in Figure 74. The average failure force of the young specimens was based on two C57 segments of male subjects of age 30 and of age 41 (specimen #10 and #40) [Carter, 2002]. The aged specimen failure force and displacement were only based on one C57 segment of a male specimen of age 80. The experimental data were chosen from specifically male subjects at the C57 segmental level as the computation model utilized was of a male C57 segment. However, due to the lack of experimental tests on C57 specimens of male subjects, the average and standard deviation of all failure forces and displacements of all subjects were plotted as well.

The SymIsoCort_SymIsoTrab model utilized in general, predicted the average failure displacement. The model with the young sample boundary condition was approximately 19% higher (3.89 kN) than the average failure force (3.26 kN) of all specimens in the experiment and 24% higher (4.04 kN) for with aged sample boundary condition (Figure 73 and Figure 74). The only difference between the boundary conditions of the young and aged SymIsoCort_SymIsoTrab model were the ram displacement values (typical young specimen (highest displacement: ~14 mm) and aged specimen (highest displacement: ~8mm)). Comparing

with the average failure force of the young specimens (4.43 kN) and displacement (3.05 mm) (average of the two young experimental data points in Figure 73), the SymIsoCort_SymIsoTrab model under predicted the force by 12.2% (3.89 kN) and the displacement by 34.9% (2.88 mm). As seen in Figure 73 and Figure 75 below, the young constitutive models all predicted higher failure forces and displacements closer to the forces and displacements of the young specimens than the average force and displacement of all specimens. The AsymmCort_AnisoTrab model over predicted the average force of the two young specimens by 3.0% (4.57 kN) and the displacement by 4.4% (3.19 mm) whereas the AnisoCort_AnisoTrab model under predicted the force by 1.4% (4.37 kN) and over predicted the displacement by 1.4% (3.08 mm). The most accurate constitutive model was the AnisoCort_AnisoTrab models based on kinetic and kinematic values.
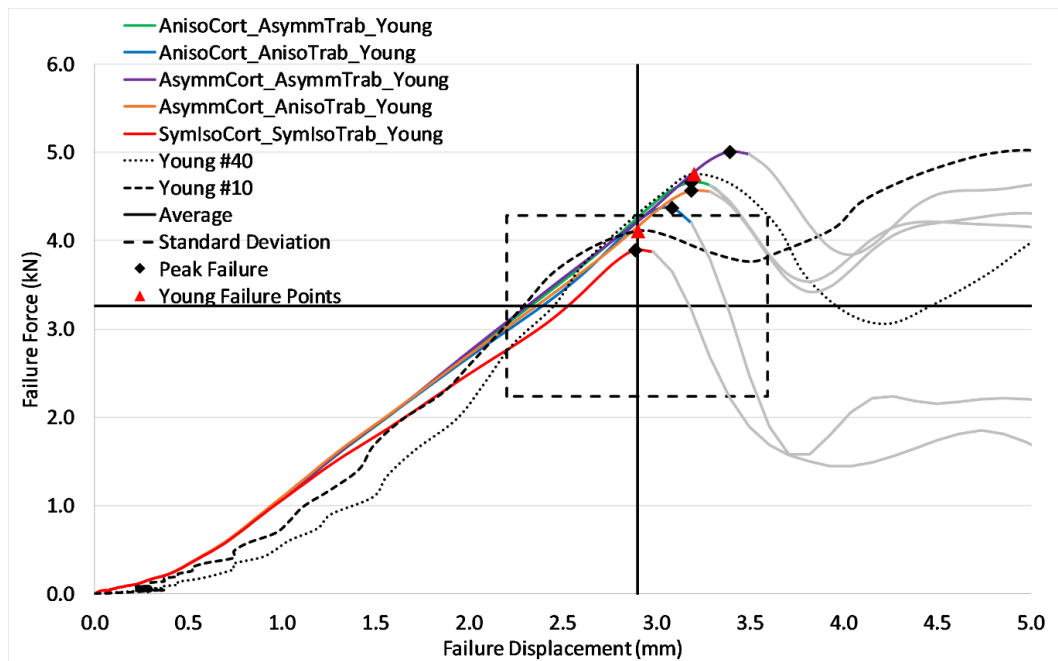
Figure 73: Force-displacement curves of the 5 model configurations against young experimental data (dotted and dashed black) and average data (solid black)

As seen in Figure 74 and Figure 76, the aged constitutive models predicted the aged experimental force (2.8k N) and displacement (2.9 mm) better than the SymIsoCort_SymIsoTrab model which over predicted aged experimental force by 45.8% (4.04 kN) and displacement by 3.4% (3.00 mm) (Table 18). The AsymmCort_AnisoTrab model was 30.3% higher in force (3.61kN) and 0.6% lower in displacement (2.88 mm) than the failure force and displacement of the aged specimens. The AnisoCort_AnisoTrab model on the other hand was 20.4% higher in force (3.33kN) and 10.5% lower in displacement (2.59mm). The most accurate aged constitutive model was the AnisoCort_AnisoTrab model, similar to the young constitutive model based on kinetic and kinematic values.

However as there was only one data point of an aged male specimen at the C57 segment level, the values were compared with the average failure force and displacement as well. The model that represented the average failure force and displacement the closest was the AnisoCort_AnisoTrab model, which over predicted the failure force by 2.2% and under predicted the displacement by 10.5%. Although the aged AsymmCort_AnisoTrab model better predicted the failure displacement of the aged specimen than the AnisoCort_AnisoTrab model, the failure force was more important than the displacement as the scale of the displacement was in millimeters whereas the scale of the failure force was in kiloNewton which represented a larger influence.
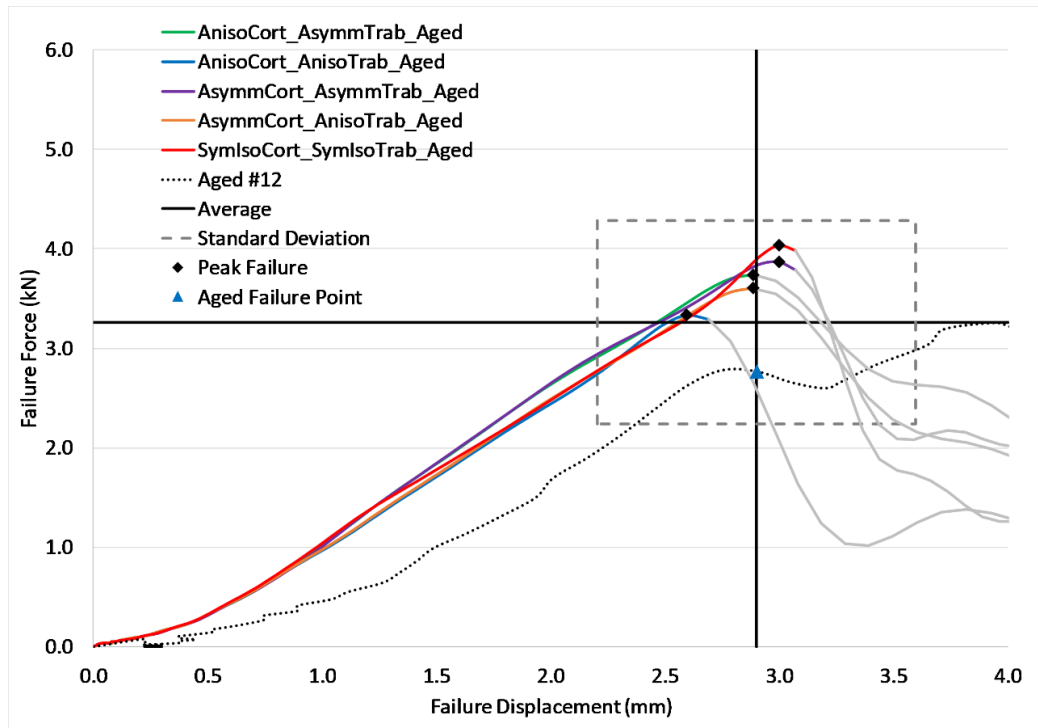
Figure 74: Force-displacement curves of the 5 model configurations against aged experimental data (dotted black) and average data (solid black)
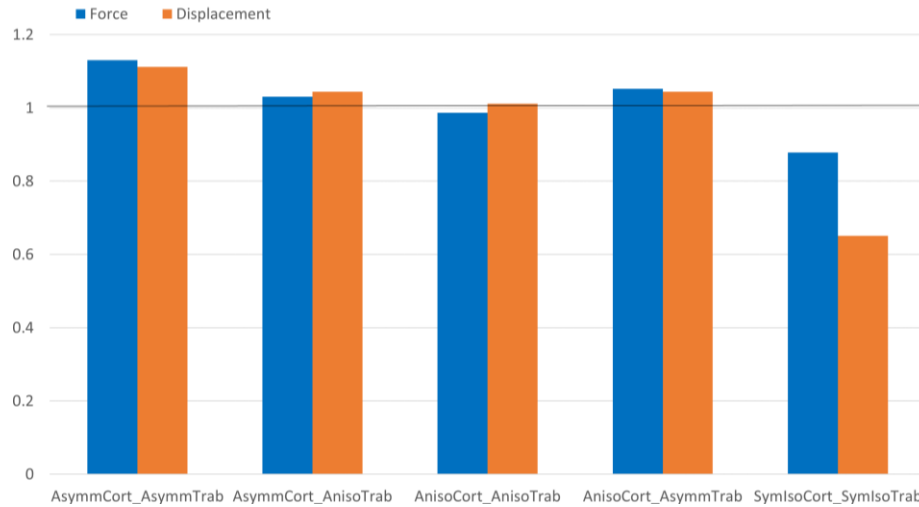
Figure 75: Normalized force (blue) and displacement (orange) results of the four young model configurations and the original symmetric isotropic model
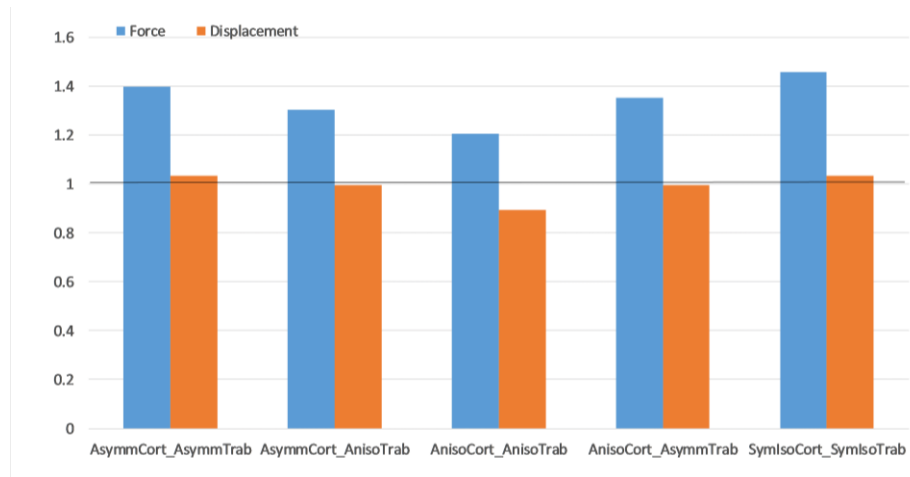
Figure 76: Normalized force (blue) and displacement (orange) results of the four aged model configurations and original symmetric isotropic model

Table 18: Percentage difference of the models compared against the young and aged experimental data

Young	AsymmCort_AsymmTrab	AsymmCort_AnisoTrab	AnisoCort_AnisoTrab	AnisoCort_AsymmTrab	SymIsoCort_SymIsoTrab
Force	13.0%	3.0%	-1.4%	5.2%	-12.2%
Displacement	11.2%	4.4%	1.1%	4.4%	-34.9%
Aged					
Force	39.7%	30.3%	20.4%	35.2%	45.8%
Displacement	3.4%	-0.6%	-10.5%	-0.6%	3.4%

In conclusion, in terms of both young and aged models, the AnisoCort_AnisoTrab model predicted failure forces and displacements closest to the experimental value.

4.2.1.2 Fracture Pattern Results

The fracture patterns from the CT scans from the experiment [Carter, 2002] were analyzed and obtained using 3D Slicer as mentioned in Section 3.6 (Figure 77). From all the specimens in the experiment, C57 segments of a young and an aged male specimen (age 41 (#40) and 80 (#12)) were chosen to depict typical fracture patterns that were found in the experiment. The young specimen showed burst fracture of the superior C5 vertebral body and inferior posterior fracture of the vertebral body that led to spinal cord occlusion (Figure 77).

The fracture patterns for each constitutive model configuration for both young and aged were compiled below (Figure 78 and Figure 79). For the young constitutive model, in comparison with the SymIsoCort_SymIsoTrab model, the fracture onset location for all models except the AnisoCort_AnisoTrab model was at the articular pillars (Figure 78). The fracture pattern then progressed into the pedicles and the posterior inferior region of the vertebral body. Later in time, the fracture was seen in the entire vertebral body, the pedicles, and the articular pillars in all model configurations.

Young Specimen (#10-Male, 30 yo, C57)
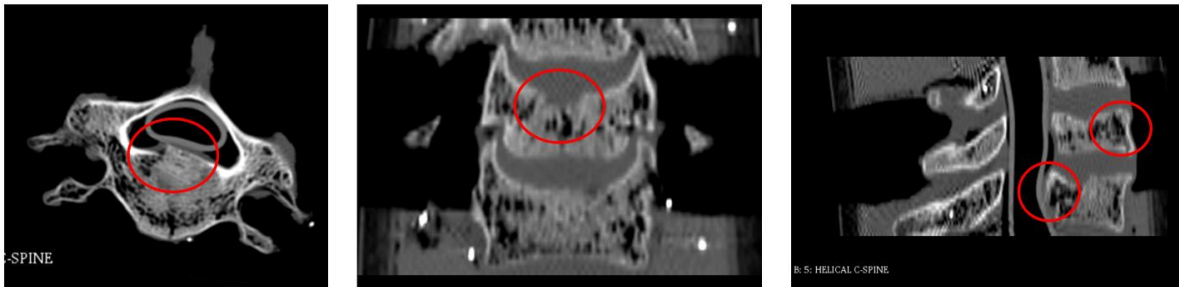
Aged Specimen (#12- Male, 80 yo, C57)
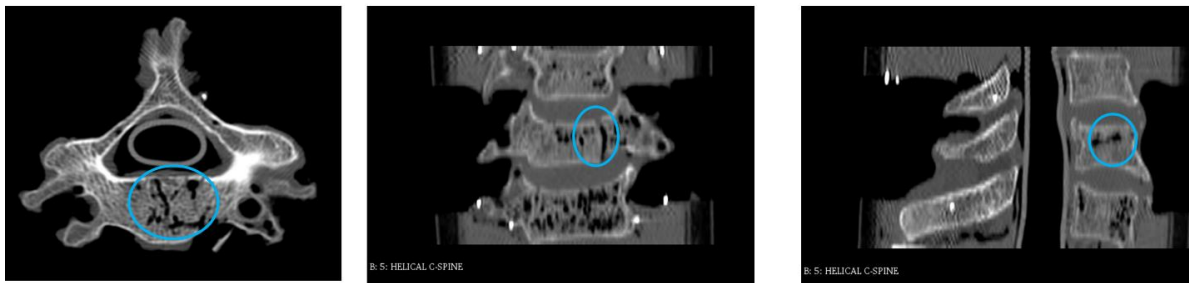
Figure 77: Typical young (#10) and aged (#12) experimental specimens fracture locations on X-ray [Carter, 2002]
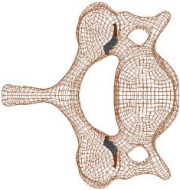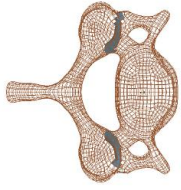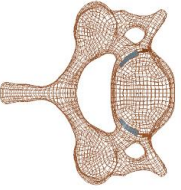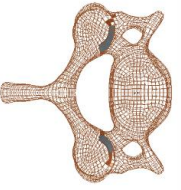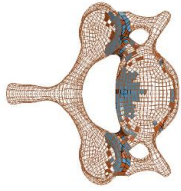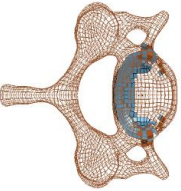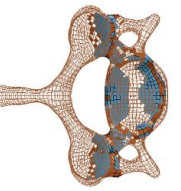
Young	AsymmCort_AsymmTrab	AsymmCort_AnisoTrab	AnisoCort_AnisoTrab	AnisoCort_AsymmTrab	SymmIsoCort_SymmIsoTrab
Onset					
Progression					

Figure 78: Fracture initiation and progression for young simulation models
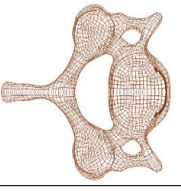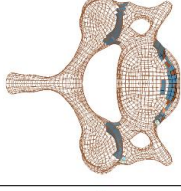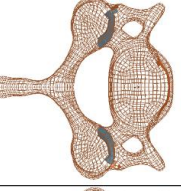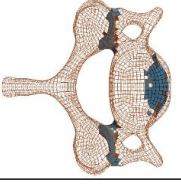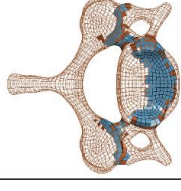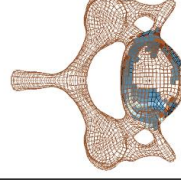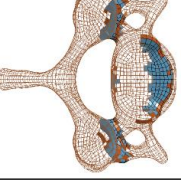
Aged	AsymmCort_AsymmTrab	AsymmCort_AnisoTrab	AnisoCort_AnisoTrab	AnisoCort_AsymmTrab	SymmIsoCort_SymmIsoTrab
Onset					
Progression					

Figure 79: Fracture initiation and progression of aged simulation models

For the aged constitutive models, the fracture onset began at the anterior superior region of the vertebral body for all models except the AnisoCort_AsymmTrab model, which began at the articular pillar, and the AnisoCort_AnisoTrab model, which began at the sides of the vertebral body (Figure 79). In general, however, the fracture progression led to similar results amongst all models in which fracture was seen at the articular pillar, pedicles and the vertebral body. Fracture was also seen in the lamina and spinous process later in time for the AnisoCort_AnisoTrab and AsymmCort_AnisoTrab models. The AnisoCort_AsymmTrab and AsymmCort_Asymm Trab models did not show this, likely due to the simulation terminating early due to the large deformation in the disc. The young and aged SymIsoCort_SymIsoTrab model predicted similar results in which fracture occurred in the center of the vertebral body and progressed within. This was expected, as there were no changes in the material property in this model as it was based on a prior study [De Wit et al., 2012] and the only changes were the boundary conditions as explained in earlier sections.

In general, all the models predicted results that would agree with the experimental fracture locations (Table 16) that mostly occurred in the vertebral body although 88% of the specimens also showed fractures in other locations. Both the AnisoCort_AsymmTrab and AnisoCort_AnisoTrab models had very similar results in terms of kinetic and kinematic responses and fracture locations. The AnisoCort_AnisoTrab model was the only one that depicted fracture initiation here similar to the original SymIsoCort_SymIsoTrab model and unlike the SymIsoCort_SymIsoTrab model, fracture progression into other areas of the cervical spine was also predicted. Besides that, anisotropy in cortical bone seemed to be an important factor in predicting failure in different loading modes [Khor et al.,2018]. Therefore, AnisoCort_AnisoTrab model was chosen out of all the constitutive model configurations.

Table 19: Summary of failure locations for all experimental specimens, AnisoCort_AnisoTrab, and SymIsoCort_SymIsoTrab models

Centric Compression	Soft Tissue											Hard Tissue					
Spec #	ALL	AVD	PVD	PLL	AFC	MFC	LFC	PFC	LF	ISL	SSL	AVB	PVB	PED	AP	LAM	SP
2	X	X	X					X				X					
10		X	X									X			X		
12		X										X				X	
23		X	X				X					X					
28	X	X	X		X		X					X		X			
40		X	X									X				X	
44	X	X	X		X		X			X		X			X		
46		X	X									X					X
SymIsoCort_SymIsoTrab												X	X				
AnisoCort_AnisoTrab (Young)		X	X									X	X	X	X		
AnisoCort_AnisoTrab (Aged)		X	X									X	X	X	X	X	X

Soft tissue and disc failure were compared between AnisoCort_AnisoTrab and SymIsoCort_SymIsoTrab models (Figure 80). In the SymIsoCort_SymIsoTrab model, no ligament and disc failure were seen. In the young and aged AnisoCort_AnisoTrab models, no ligament failure was seen but the C56 and C67 discs showed failure as nodes in that region were released due to failure in the tiebreak contact from element erosion in the hard tissues (Figure 80) as the normal stresses were exceeded.
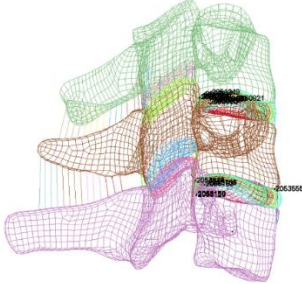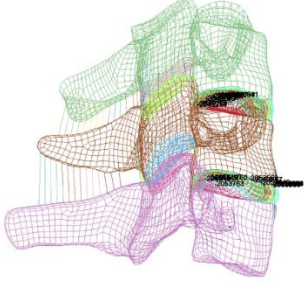
SymIsoCort_SymIsoTrab	
No ligament and disc failure	
Young (AnisoCort_AnisoTrab)	Aged (AnisoCort_AnisoTrab)
No ligament failure. Anterior and posterior C67 disc failure and posterior C56 disc failure.	No ligament failure. Anterior and posterior C67 disc failure and posterior C56 disc failure.

Figure 80: Soft tissue failure comparison between the young and aged AnisoCort_AnisoTrab and SymIsoCort_SymIsoTrab models

In general, hard tissue failure was seen mostly in the vertebral body, the pedicle, articular pillars, lamina, and spinous process and soft tissue failure in the anterior longitudinal ligament and anterior and posterior discs [Table 19]. In comparison with the simulated models, the SymIsoCort and SymIsoTrab model predicted hard tissue failure only in the vertebral body. On the other hand, the AnisoCort_AnisoTrab model predicted disc failure and hard tissue failure in the vertebral body, pedicle, and articular pillar in both young and aged models with the young model exhibiting additional fracture in the spinous process and lamina.

4.2.2. Loading on the Superior Potting

For the young AnisoCort_AnisoTrab model in the potting configuration of the centric compression case (Figure 48), the failure force and displacement (4.04 kN and 2.59 mm) were approximately 7.54% and 15.86% lower respectively than the endplate configuration (4.37 kN and 3.08 mm) of the centric compression case (Figure 81). This is due to the potting model representing a better load distribution on the vertebral segment. The displacement shift to a lower value was a better approximation of the peak displacement curve of specimen #10 of which the young simulation boundary condition ram displacement was based on. For the aged AnisoCort_AnisoTrab model, the failure force is 5.28% lower and the displacement is 9.26% lower (3.16 kN and 2.35 mm) than the endplate configuration (3.33 kN and 2.59 mm) (Figure 82). Unlike the young model, the displacement shift in the aged model was a worse approximation of the peak displacement curve of specimen #12 of which the aged simulation boundary condition was based on.
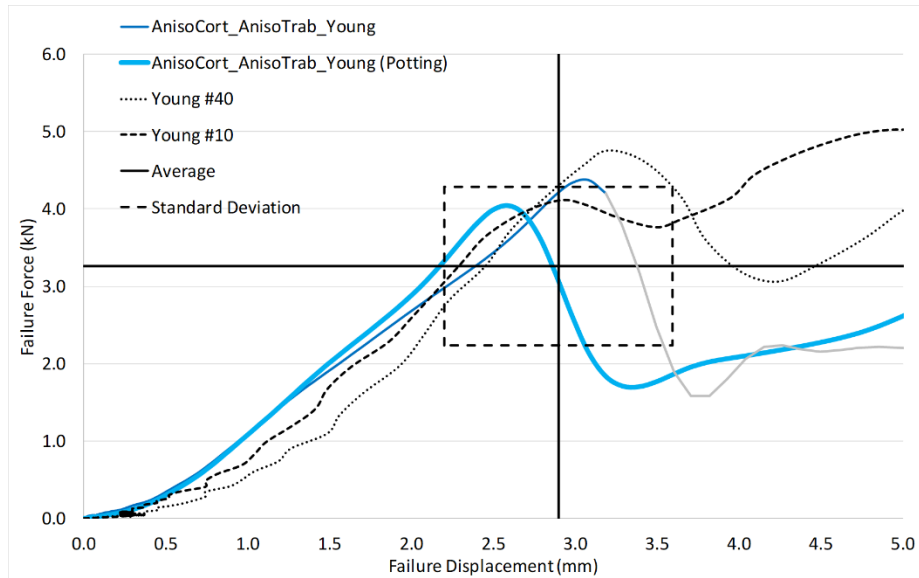
Figure 81: Comparison of endplate loading configuration (thin solid blue) and superior potting loading configuration (thick solid blue) for the young and aged AnisoCort_AnisoTrab models in the centric compression case
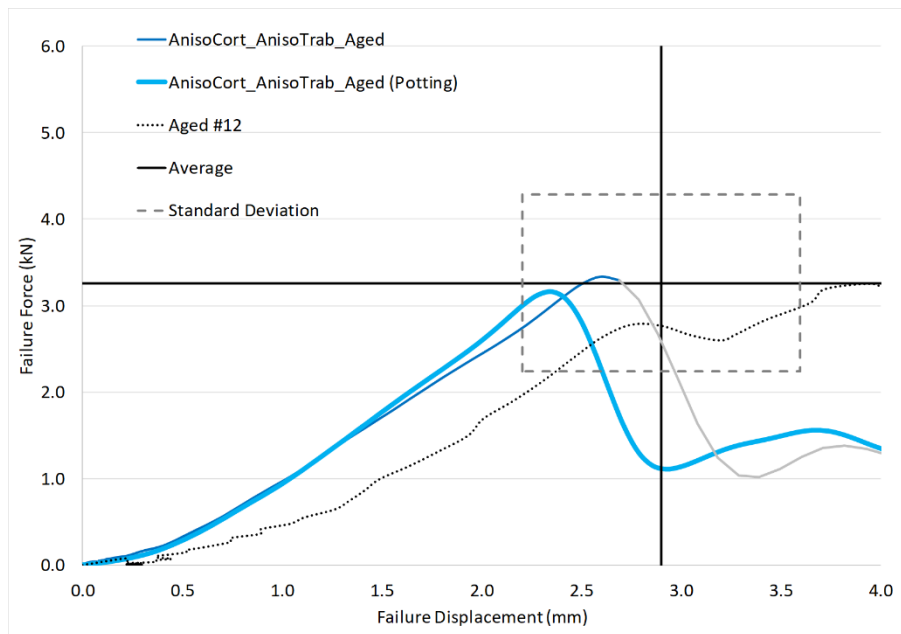
Figure 82: Fracture location comparison between the potting (solid thick blue) and endplate (solid thin blue) loading configuration for the aged AnisoCort_AnisoTrab models
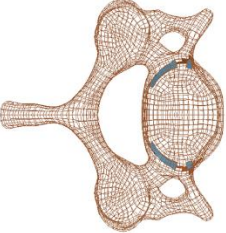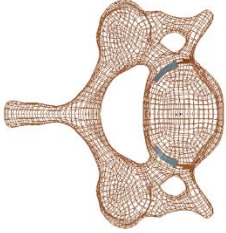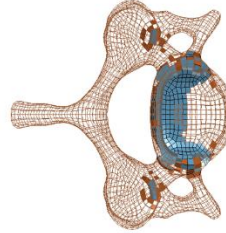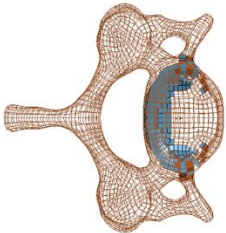
Loading Method	With Potting (Young)	With Endplate (Young)
Fracture Onset		
Fracture Propagation		

Figure 83: Fracture location comparison between the potting and endplate loading configuration for the young AnisoCort_AnisoTrab models
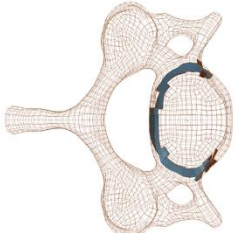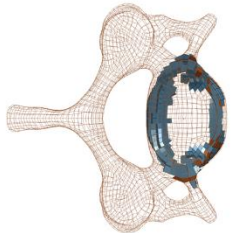
Loading Method	With Potting (Aged)	With Endplate (Aged)
Fracture Onset		
Fracture Propagation		

Figure 84: Fracture location comparison between the potting and endplate loading configuration for the aged AnisoCort_AnisoTrab models

Table 20: Summary of failure locations for both the endplate and potting loading configuration young and aged AnisoCort_AnisoTrab models (ALL: Anterior longitudinal ligament, AVD: anterior vertebral disc, PVD: posterior vertebral disc, PLL: posterior longitudinal ligament, AFC: anterior facet capsular ligament, MFC: medial facet capsular ligament, LFC: lateral facet capsular ligament, PFC: posterior facet capsular ligament, LF: ligamentum flavum, ISL: intraspinal ligament, SSL: supraspinal ligament, AVB: anterior

Centric Compression				Soft Tissue								Hard Tissue					
Spec #	ALL	AVD	PVD	PLL	AFC	MFC	LFC	PFC	LF	ISL	SSL	AVB	PVB	PED	AP	LAM	SP
AnisoCort_AnisoTrab_Young (Endplate)		X	X									X	X	X	X		
AnisoCort_AnisoTrab_Young (Potting)		X	X									X	X	X	X	X	X
AnisoCort_AnisoTrab_Aged (Endplate)		X	X									X	X	X	X	X	X
AnisoCort_AnisoTrab_Aged (Potting)		X	X									X	X	X	X		

As for the fracture locations, they were comparable to the endplate configuration. With the young AnisoCort_AnisoTrab constitutive model, fracture initiated in the sides of the vertebral body and then progressed within the vertebral body (Figure 83) in both the potting and endplate configuration. At the end of the simulation, fractures were seen in the vertebral body, articular pillars, and pedicles for both endplate and potting configuration with additional fractures in the spinous process and lamina in the potting configuration. With the aged AnisoCort_AnisoTrab constitutive model, both endplate and potting configurations had fracture initiated in the sides of the vertebral body and then progressed around the vertebral body (Figure 84). The potting configuration only predicted fractures in the vertebral body, pedicle, and articular pillars whereas additional fracture was seen in the spinous process and lamina in the endplate configuration (Table 20). As for soft tissue failure, only disc failure was seen, similar to the endplate configuration case (Table 20).

4.3. Posterior Eccentricity

4.3.1. Failure Force and Moment Results

In the posterior eccentricity case (Figure 50), there was only one data point for a C57 segment of the male specimen. Due to the lack of data points, the average of all specimens was considered. The SymIsoCort_SymIsoTrab model over-predicted the average failure force (3.47 kN) by 23% (4.29 kN) and the moment (47.8 Nm) by 149% (119 Nm) (Figure 85). The predicted force was still within the standard deviation of the average failure force (0.99 kN) but not the moment (19.7 Nm). As seen in Figure 85 below, the AnisoCort_AnisoTrab model was able to predict both failure force and moment well (under-predicted failure force by 12% (3.06 kN) and over-predicted failure moment by 36% (65.Nm)) and was within the standard deviation of the average experimental data. In terms of comparing with the only aged male C57 segment in the experiment (specimen #47) (3.54 kN and 58.8 Nm), the AnisoCort_AnisoTrab model under-predicted the failure force by 14% and the moment by 11% whereas the SymIsoCort_SymIsoTrab model over-predicted the failure force by 21% and the moment by 102%.

Figure 85: Comparison of failure forces and moments between the SymIsoCort_SymIsoTrab model, aged AnisoCort_AnisoTrab model, aged experimental C57 specimen (#47) and the average experimental value for the posterior eccentricity compression case [Carter, 2002]

4.3.2. Hard Tissue, Soft Tissue and Disc Failure Results

Figure 86 depicted the fracture locations in a C57 segment of an aged male specimen (Specimen #47) [Carter,2002]. For the SymIsoCort_SymIsoTrab model, fracture initiated in the spinous process and progressed further within the spinous process only (Figure 87). The fracture progression of the posterior eccentricity simulation with AnisoCort_AnisoTrab from the top view is shown in Figure 87 below. Fracture was initiated in the articular pillar, and then progresses to the pedicles, lamina and spinous process.
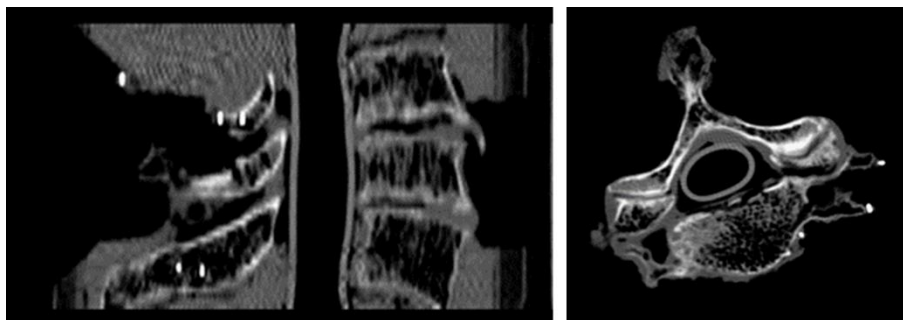
Figure 86: X-ray of fracture locations in a typical aged specimen under posterior eccentricity compression (right: lateral view, left: top view) [Carter, 2002]

Figure 87: Fracture progression in the SymIsoCort_SymIsoTrab and aged AnisoCort_AnisoTrab models in the posterior eccentricity compression simulation

In the SymIsoCort_SymIsoTrab model, no ligament failure was seen (Figure 88). There was disc failure in the C56 and C67. For the AnisoCort_AnisoTrab model, no ligament failure was seen but there was failure seen in the tiebreak contact of the C67 disc (Figure 88). Figure 88 below shows a few of the nodes that were released indicating failure of the tiebreak contact between the bone and the disc as the nodes exceeded the normal stress of 0.01 GPa. Failure was seen in both the anterior and posterior regions of the disc.
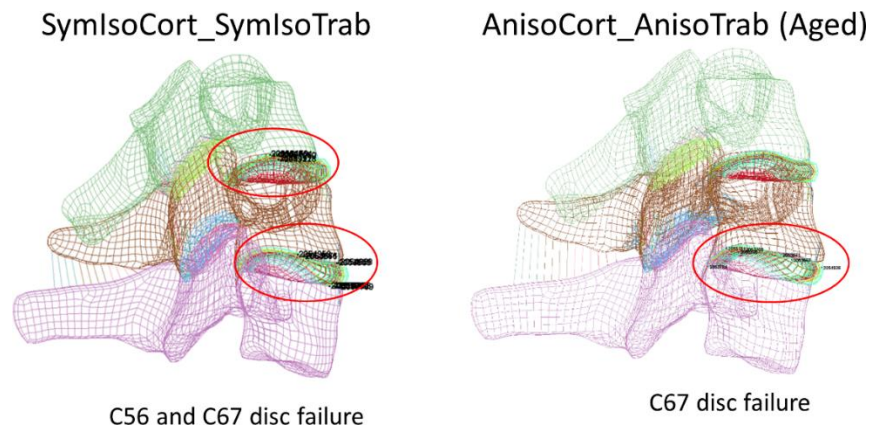
Figure 88: Soft tissue failure in the SymIsoCort_SymIsoTrab and the aged AnisoCort_AnisoTrab models in the posterior eccentricity compression simulation

93

Table 21: Summary of failure locations of all experimental specimens and the SymIsoCort_SymIsoTrab and aged AnisoCort_AnisoTrab models in the posterior eccentricity compression case

Posterior Eccentricity	Soft Tissue											Hard Tissue					
Spec #	ALL	AVD	PVD	PLL	AFC	MFC	LFC	PFC	LF	ISL	SSL	AVB	PVB	PED	AP	LAM	SP
14		X									X						X
29		X	X								X					X	X
39											X					X	X
41		X									X					X	X
43		X	X					X			X					X	X
45								X		X	X					X	X
47		X									X			X		X	X
49		X	X								X						X
SymIsoCort_SymIsoTrab		X															X
AnisoCort_AnisoTrab_Aged		X	X											X	X	X	X

For hard tissue failure in the experiment, the fracture was mostly found in the vertebral body, pedicles and spinous process (Table 21). The SymIsoCort_SymIsoTrab model predicted fracture only in the spinous process whereas the AnisoCort_AnisoTrab model predicted fracture in the pedicles, articular pillar, lamina, and spinous process. For soft tissue failure in the experiment, failure was seen in the anterior longitudinal ligament, discs, posterior longitudinal ligament, facet ligaments, ligament flavum, interspinous ligament, and supraspinous ligament. Although no ligament failure was seen in both the SymIsoCort_SymIsoTrab and AnisoCort_AnisoTrab models, failure was seen in the disc (anterior for SymIsoCort_SymIsoTrab model and both anterior and posterior for AnisoCort_AnisoTrab models) (Table 21).

4.4. Anterior Eccentricity

4.4.1. Failure Force and Moment Results

The anterior eccentricity simulation set up was shown in Figure 50. The SymIsoCort_SymIsoTrab model over-predicted both average experimental failure force (0.77 kN) and moment (21.4 Nm) by 181% (2.15 kN) and 48% (31.7 Nm) respectively (Figure 89). Both force (0.35 kN) and moment (9.9 Nm) fell outside the standard deviation range. In comparison to the one aged male, C57 segment specimen's data point (failure force: 0.49 kN, failure displacement: 37.40 Nm), the SymIsoCort_SymIsoTrab model over-predicted the failure force by 343% and under-predicted the failure displacement by 15%.

For the AnisoCort_AnisoTrab model on the other hand, the failure force (2.14 kN) predicted was similar to the SymIsoCort_SymIsoTrab model (2.15 kN) whereas the failure moment (25.59 Nm) predicted was slightly lower in comparison to the SymIsoCort_SymIsoTrab model (31.73 Nm). The average failure force and moment (0.77 kN and 21.4 Nm) were however still over-predicted by the AnisoCort_AnisoTrab model by 179% and 20% respectively (Figure 89). The failure moment fell within the standard deviation of the average experimental moment. The failure force, on the other hand, was out of the standard deviation range. In comparison to the aged male C57 segment (specimen #17), the force and displacement predicted by the AnisoCort_AnisoTrab model was 340% higher than the experimental failure force and 32% lower than the experimental failure displacement (Figure 89). The SymIsoCort_SymIsoTrab model over-predicted the force

similarly by 340% and under-predicted the displacement by 15%. The failure forces for both the constitutive models were too high even when the aged AnisoCort_AnisoTrab model was utilized.
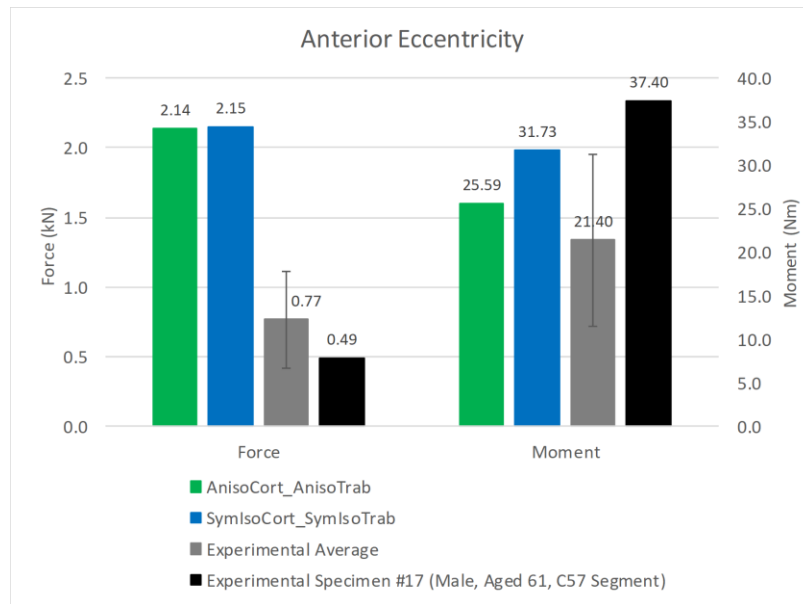
Figure 89: Comparison of failure forces and moments between the SymIsoCort_SymIsoTrab model, aged AnisoCort_AnisoTrab model, aged experimental C57 specimen (#17) and the average experimental value for the anterior eccentricity compression case [Carter, 2002]

4.4.2. Hard Tissue, Soft Tissue and Disc Failure Results

Based on an X-ray image of a C57 segment of the aged male specimen (Age 61, #17), the fracture was seen in the anterior region of the vertebral body (Figure 90). Based on Table 19, hard tissue fractures were not dominant in comparison to soft tissue failure in this eccentricity case. A few specimens showed fractures in the anterior region of the vertebral body or anterior and posterior. The SymIsoCort_SymIsoTrab model did not predict any hard tissue failure (Figure 91). The AnisoCort_AnisoTrab model, on the other hand, showed fracture initiating at the pedicles, and then the anterior superior region of the vertebral body (Figure 91).
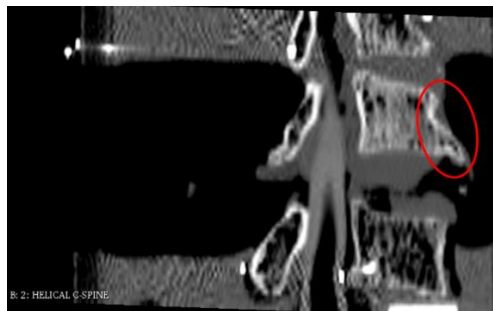
Figure 90: X-ray of anterior fracture in specimen #17 of the anterior eccentricity compression case [Carter, 2002]

95

SymIsoCort_SymIsoTrab
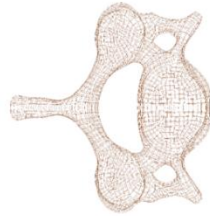
No hard tissue failure is seen.

AnisoCort_AnisoTrab (Aged)

396.7 ms   396.8 ms   400.0 ms   450.0 ms
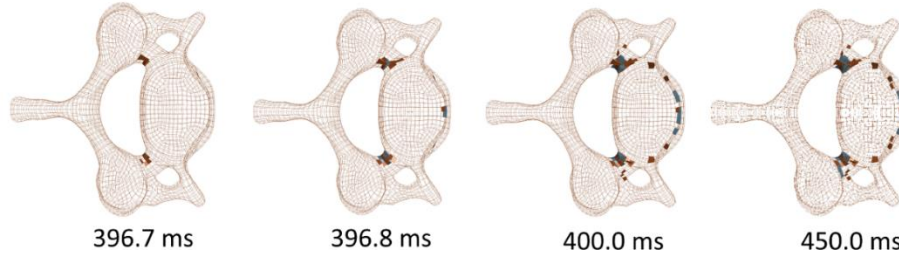
Figure 91: Fracture progression in the SymIsoCort_SymIsoTrab model and aged AnisoCort_AnisoTrab model in the anterior eccentricity compression simulation

In both the SymIsoCort_SymIsoTrab and the AnisoCort_AnisoTrab models, posterior interspinous ligament (ISL) failure was shown in the red and black circles (Figure 92). Both models also showed disc failure in the posterior region (Figure 92) with a few of the released nodes due to the tiebreak contact failure, exceeding the normal stress of 0.01 GPa.

SymIsoCort_SymIsoTrab   AnisoCort_AnisoTrab (Aged)
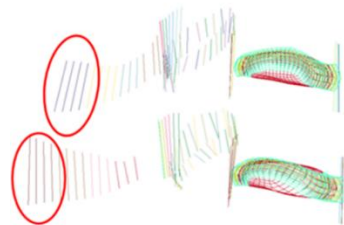
Interspinous ligament failure   Interspinous ligament failure
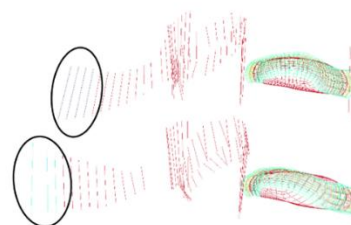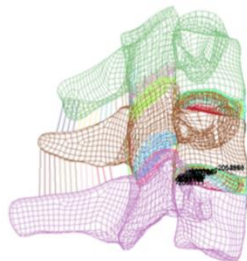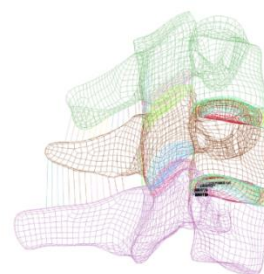
C67 disc failure   C67 disc failure

Figure 92: Soft tissue failure comparison between the SymIsoCort_SymIsoTrab model and the aged AnisoCort_AnisoTrab model in the anterior eccentricity compression case

Table 22: Summary of soft and hard tissue failure in all experimental specimens, SymIsoCort_SymIsoTrab model and the aged AnisoCort_AnisoTrab model in the anterior eccentricity compression case

Anterior Eccentricity	Soft Tissue											Hard Tissue					
Spec #	ALL	AVD	PVD	PLL	AFC	MFC	LFC	PFC	LF	ISL	SSL	AVB	PVB	PED	AP	LAM	SP
3								■	■	■							
5			■			■	■	■	■	■	■	■					
7					■			■	■	■	■	■					
8		■			■	■		■	■	■	■	■					
15					■	■		■	■	■	■	■					
17	■				■			■	■	■	■	■					
27								■	■	■	■						
48		■			■	■		■	■	■	■	■					
SymIsoCort_SymIsoTrab			■							■							
AnisoCort_AnisoTrab_Aged			■							■			■	■			

For all the experimental failure results, only vertebral body fractures were seen in a few specimens for hard tissue failure whereas most injuries occurred in the soft tissues like facet capsules, ligamentum flavum, interspinous ligaments and supraspinous ligaments (Table 22). Some disc avulsion was seen in some specimens. In comparison with the simulated models, the SymIsoCort_SymIsoTrab model did not predict any hard tissue failure whereas the AnisoCort_AnisoTrab predicted failure in the vertebral body and the pedicles (Table 22). As for soft tissue failure, both models predicted posterior disc avulsion and interspinous ligament failure.

4.5. Lateral Eccentricity

4.5.1. Low Lateral Eccentricity

4.5.1.1. Failure Force and Moment Results

The low lateral eccentricity set up was shown in Figure 51. The only C57 sample in the experiment was from an aged female specimen (72 YO) with a failure force of 2.0 kN similar to the average experimental failure force (2.7 kN). Therefore, the results were compared with the average experimental failure values. The SymIsoCort_SymIsoTrab model over-predicted the average experimental failure force (2.7 kN) by 71% (4.61 kN) and under-predicted the average experimental failure moment (2 Nm) by 73% (0.55 Nm) (Figure 93). The failure force was over the standard deviation range (1.24 kN), but the failure moment still fell within (9 Nm). In comparison with the aged AnisoCort_AnisoTrab model, the predicted failure force (3.53 kN) and failure moment (0.19 Nm) were lower than the SymIsoCort_SymIsoTrab values (4.61 kN, 0.55 Nm). The AnisoCort_AnisoTrab model over-predicted the average experimental failure force by 20% and under-predicted the failure moment by 77% (Figure 93). However, both still fell within the standard deviation range.
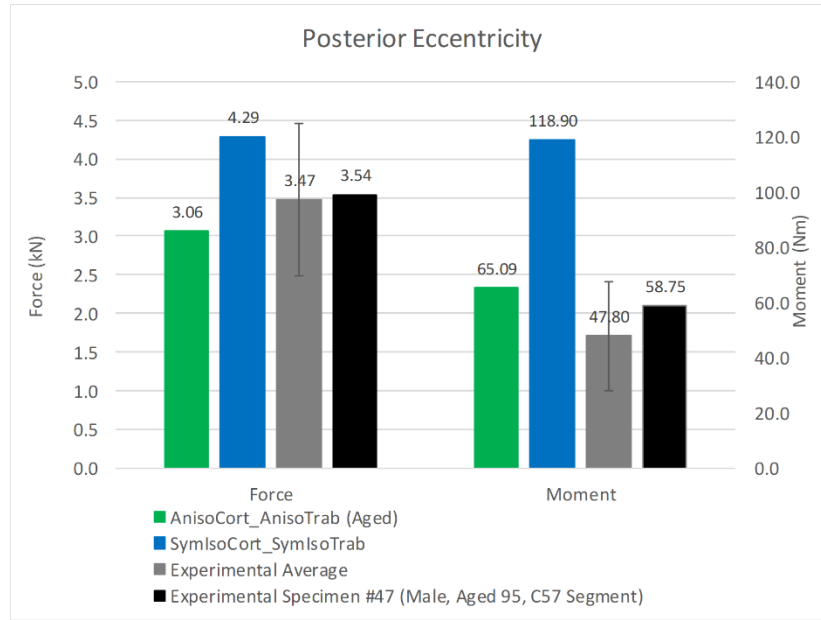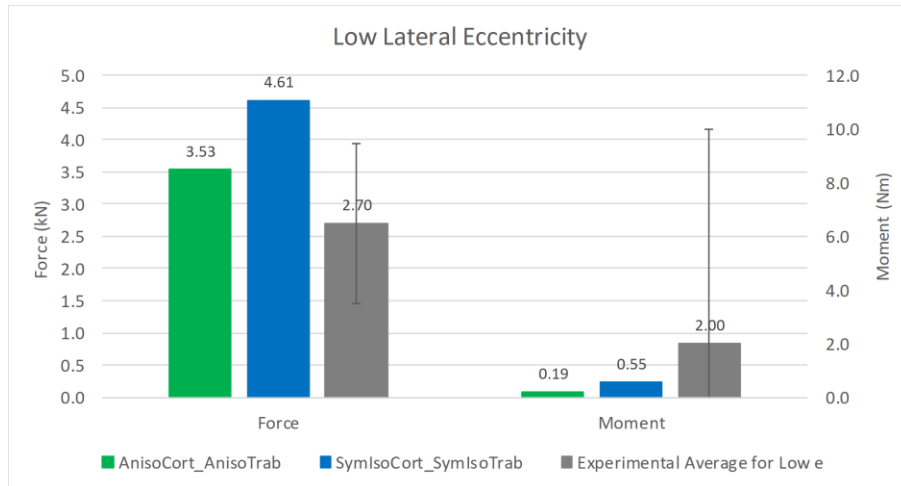
Figure 93: Comparison of failure forces and moments between the SymIsoCort_SymIsoTrab and aged AnisoCort_AnisoTrab model against the average experimental value for the lateral eccentricity compression case [Van Toen, 2014]

4.5.2.1. Hard Tissue, Soft Tissue and Disc Failure Results

Figure 94 depicted the fracture in the low lateral eccentricity case in the vertebral body [Van Toen, 2014]. In the low lateral eccentricity experiment, majority of the specimens showed fractures in the vertebral body (83%) with some specimens obtaining additional fractures in the articular pillar and the lamina (Table 23). In the SymIsoCort_SymIsoTrab model, fracture initiated in the vertebral body and progressed within (Figure 95). The fracture then developed in the pedicles and then the lamina. In the AnisoCort_AnisoTrab model, on the other hand, fracture initiated in the vertebral body and the articular pillars and then progressed into the pedicles, lamina, and spinous process (Figure 95).
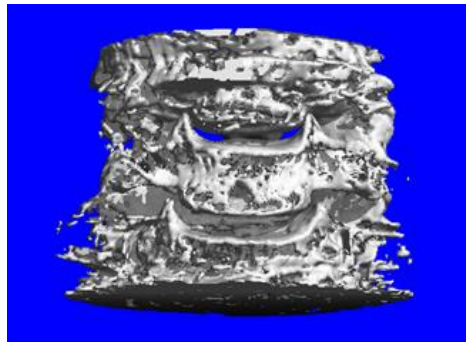
Figure 94: CT scan image of fracture in the low lateral eccentricity compression case (specimen #H1318) [Van Toen, 2014]

SymIsoCort_SymIsoTrab

257.7 ms 259.7 ms 260.7 ms 275.0 ms

AnisoCort_AnisoTrab (Aged)

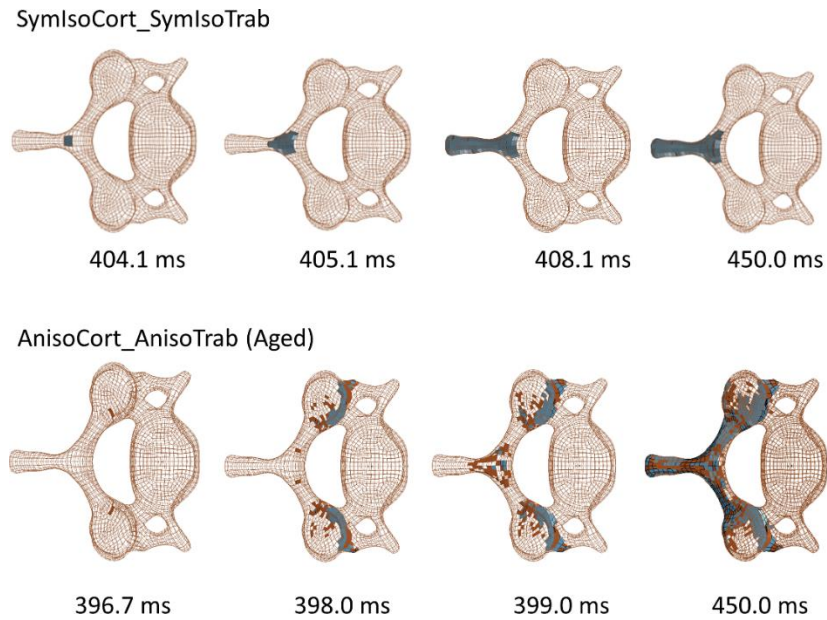256.5 ms 257.0 ms 259.0 ms 275.0 ms
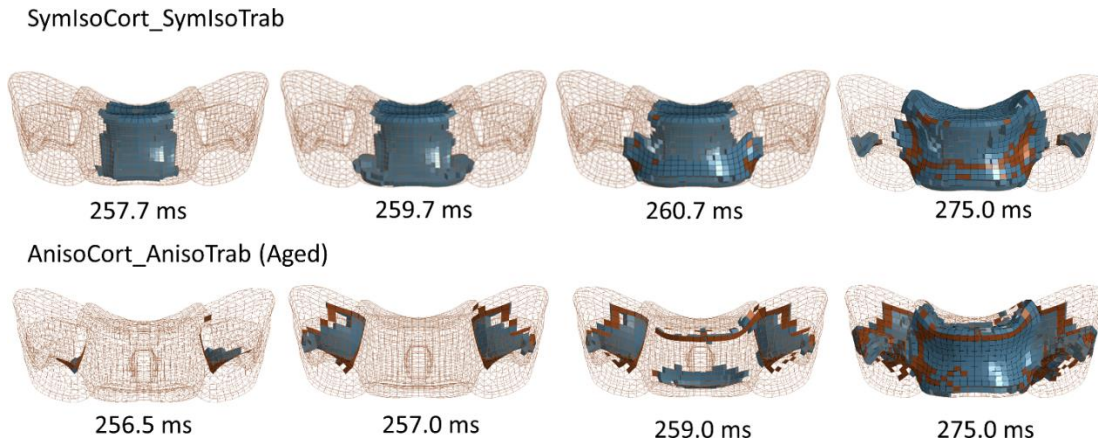
Figure 95: Fracture progression in the SymIsoCort_SymIsoTrab model and aged AnisoCort_AnisoTrab model in the lateral eccentricity compression simulation

Failure was seen in the C67 capsular ligaments in the SymIsoCort_SymIsoTrab model (Figure 96). There was also a failure in the C67 disc in the posterior region based on the released nodes due to the failure of the tiebreak contact highlighted (Figure 96). In the AnisoCort_AnisoTrab model, failure was also seen in the C67 facet capsular ligaments (Figure 96). There was also a failure in the C67 disc and based on the highlighted nodes that were released from the tiebreak contact (Figure 96). No soft tissue failure was reported in the experimental specimens.

SymIsoCort_SymIsoTrab

AnisoCort_AnisoTrab (Aged)

C67 capsular ligament failure

C67 capsular ligament failure

C67 disc failure

C67 disc failure
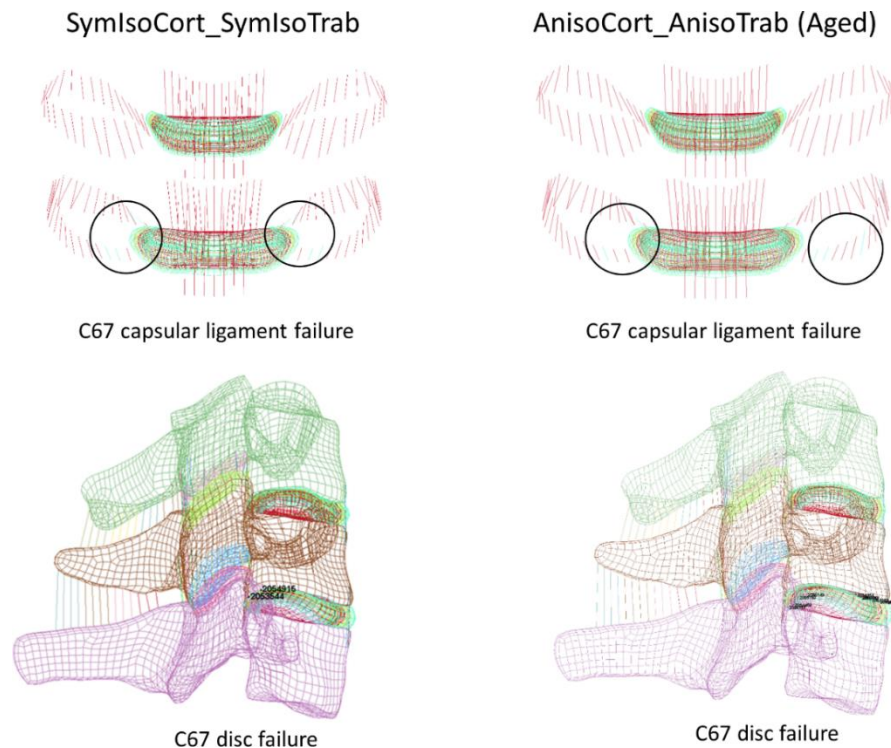
Figure 96: Soft tissue failure comparison between the SymIsoCort_SymIsoTrab and the aged AnisoCort_AnisoTrab models in the low lateral eccentricity compression case

Table 23: Summary of soft and hard tissue failure in all experimental specimens, SymIsoCort_SymIsoTrab and AnisoCort_AnisoTrab constitutive models in the lateral eccentricity compression case

Lateral Compression (Low e)	Endplate (inferior)	Endplate (superior)	Articular Pillar	Vertebral Body	Lamina	Pedicles	Spinous Process
H1318	V1			V1			
H1323		V2		V2	V2		
H1321		V2		V2			
H1298		V2			V2		
H1975	V2	V2		V2			
H1274			V2	V1			
SymIsoCort_SymIsoTrab				V2	V2	V2	
AnisoCort_AnisoTrab_Aged			V2	V2	V2	V2	V2

V1= Superior Vertebra, V2= Middle Vertebra

It was noted that the specimens in the experiment mostly have disc degeneration and facet osteoarthritis joint failure, which could lead to the differences seen in the failure values and patterns. The experiment showed endplate, articular facet or pillar, vertebral body, and lamina failure in hard tissue (Table 23). For hard tissue failure, the fracture was predicted in the vertebral body, pedicles and lamina in the both the SymIsoCort_SymIsoTrab and AnisoCort_AnisoTrab models. Additional fractures in the articular pillar and the spinous process were predicted by the AnisoCort_AnisoTrab model (Table 23).

4.5.2. High Lateral Eccentricity

4.5.1.1. Failure Force and Moment Results

The high lateral eccentricity simulation set up was shown in Figure 51. Similar to the low eccentricity case, the only C57 sample was from a male specimen with undefined age that resulted in a failure force of approximately 1.0 kN which was close to the average experimental failure force (0.78 kN). Therefore, the results were compared with the average experimental failure values. In general, the SymIsoCort_SymIsoTrab model predicted a failure force (0.67 kN) that was 14% lower and a failure moment (24.7 Nm) that was 12% lower than the average experimental values (0.78 kN and 28 Nm) and fell within the standard deviation range (0.30 kN and 10 Nm) (Figure 97). The AnisoCort_AnisoTrab model, on the other hand, predicted a failure force (0.56 kN) that was 28% lower and moment (21.15 Nm) that is 24% lower than the average experimental values (Figure 97). The SymIsoCort_SymIsoTrab model predicted the failure force and displacement better than the AnisoCort_AnisoTrab model in this case but both constitutive models predicted results that fell within the standard deviation range.
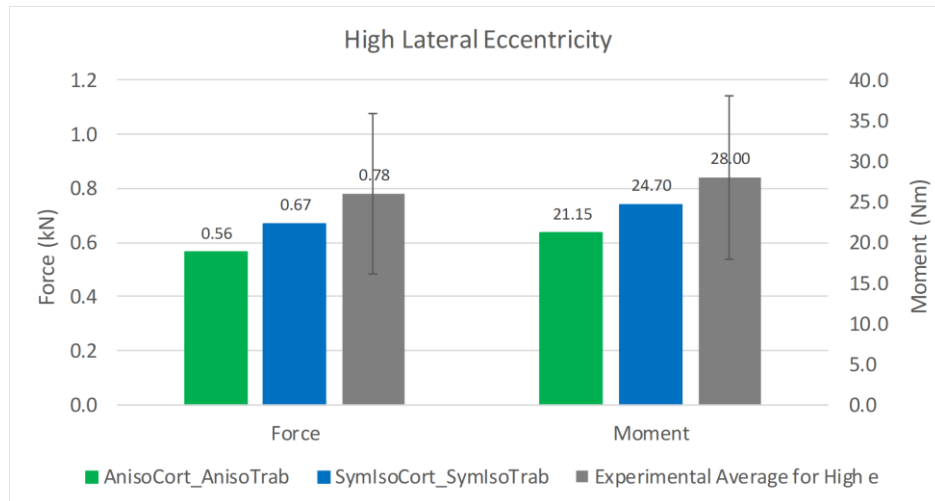
Figure 97: High lateral eccentricity failure force and moment results of the aged AnisoCort_AnisoTrab and SymIsoCort_SymIsoTrab models compared against the experimental average

4.5.2.1. Hard Tissue, Soft Tissue and Disc Failure Results
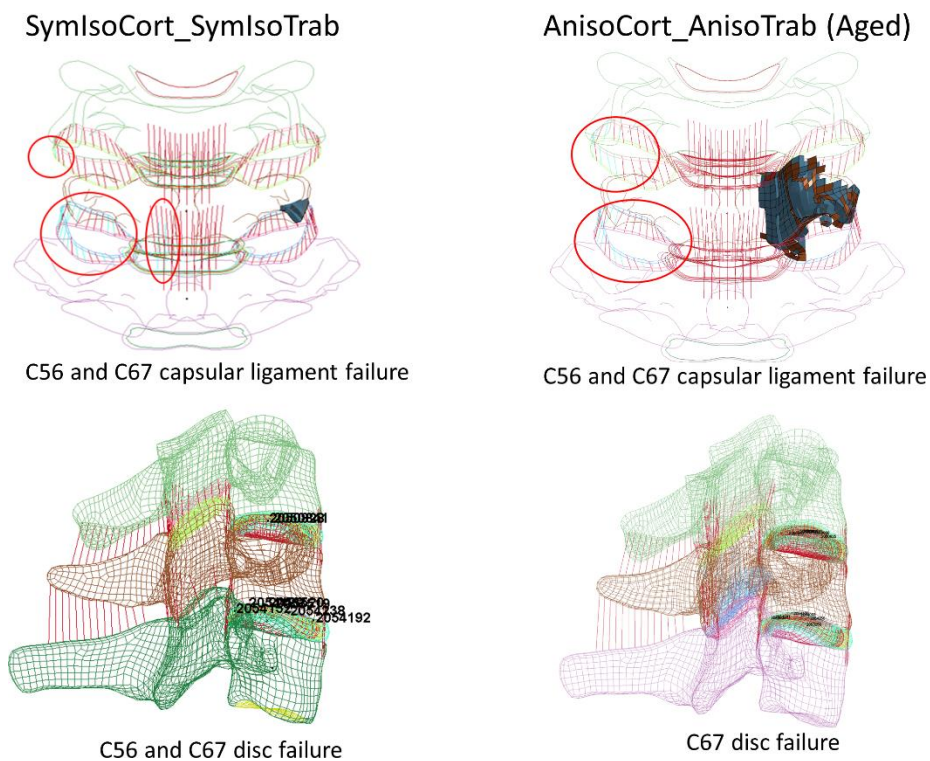
Figure 98: Hard tissue and soft tissue failure of the aged AnisoCort_AnisoTrab and SymIsoCort_SymIsoTrab models

In the high lateral eccentricity experiment, only one specimen showed hard tissue fracture in the vertebral body. The SymIsoCort_SymIsoTrab model predicted fracture in the pedicles and the

101

capsular ligaments between the C56 and C67 facet joints (Figure 98). Later in time, failure was seen in the C67 posterior longitudinal ligament and disc. In the AnisoCort_AnisoTrab model, hard tissue fracture was seen in the articular pillar, the pedicles, and the lamina (Figure 98). The fracture occurred first at the right articular pillar and pedicles before the facet capsule ligaments on the left failed. Both the C56 and C67 showed some disc failure as well due to tiebreak contact failure as the nodes exceeded the normal stress of 0.01 GPa. In general, as shown in Table 24 below, none of the hard tissue fractures predicted by either model were seen in experiment whereas facet capsular ligament and disc failure was predicted by both models and seen in experiment. The SymIsoCort_SymIsoTrab model predicted an additional posterior longitudinal ligament failure that was not seen in the experiment.

Table 24: Summary of soft and hard tissue failure in all experimental specimens, SymIsoCort_SymIsoTrab and the aged AnisoCort_AnisoTrab models in the lateral eccentricity compression case

Lateral Compression (High e)	Endplate (inferior)	Endplate (superior)	Vertebral Body	Articular Pillar	Lamina	Pedicles	Facet Capsule	Anterior longitudinal Ligament	Posterior Longitudinal Ligament	Intervertebral Disc	Ligamentum Flavum	Interspinous Ligament
H1125							V2/3	V2/3		V2/3	V2/3	
H1329							V2/3	V2/3	V2/3	V2/3	V2/3	V2/3
H1275			V2				V2/3	V2/3	V2/3	V2/3	V2/3	V2/3
H1286		V2					V1/2	V1/2	V1/2	V1/2	V1/2	V1/2
H1998	V2	V3					V2/3	V2/3		V2/3	V2/3	V2/3
H1292	V2	V3					V2/3	V2/3	V2/3	V2/3	V2/3	V2/3
SymIsoCort_SymIsoTrab						V2	V1/2/3		V2/3	V1/2/3		
AnisoCort_AnisoTrab_Aged				V2	V2	V2	V1/2/3			V1/2/3		

V1= Superior Vertebra, V2= Middle Vertebra, V3= Inferior Vertebra

4.6. Mesh Refinement Analysis Results

The medium (single split) and fine (double split) mesh computational models both yielded similar failure forces to one another (Figure 99: original mesh: 3.08 mm, 4.37 kN; medium mesh: 3.08 mm, 3.98 kN; fine mesh: 3.50 mm, 3.94 kN).
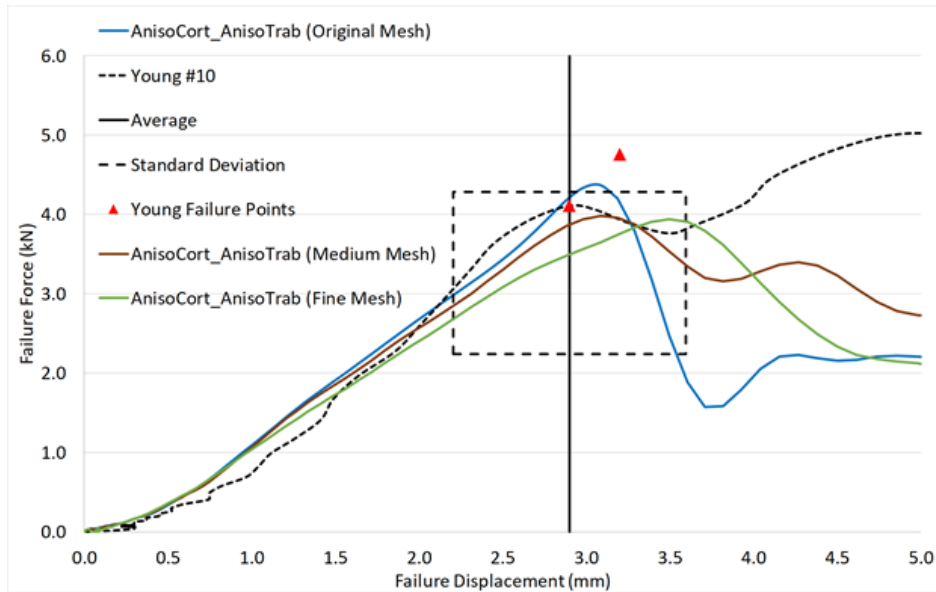
Figure 99: Force-displacement curve of the original mesh computational model (blue), medium mesh model (brown), and fine mesh model (green) in the centric compression case with young AnisoCort_AnisoTrab constitutive model

The medium mesh computational model with the young AnisoCort_AnisoTrab constitutive model predicted similar failure displacement (3.08 mm) to the original mesh computational model but predicted the failure force by approximately 9% lower (3.98 kN). The fine mesh computational model with the young AnisoCort_AnisoTrab constitutive model on the other hand, predicted a failure displacement that was 14% (3.50 mm) higher than the failure displacement of the original mesh computational model (3.08 mm). The fine mesh computational model predicted similar failure force as the medium mesh model, which was 9% higher than the failure force predicted in the original mesh computational model (4.37 kN). The reduction of failure force seen was expected as the failure strain was not recalibrated for the refined mesh models. In terms of mesh convergence, with failure based on element erosion, it is often difficult to achieve full convergence as mass is deleted from the calculations.

103
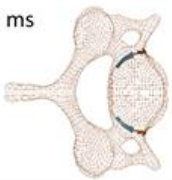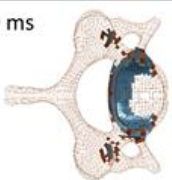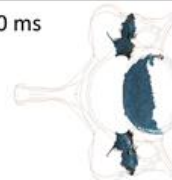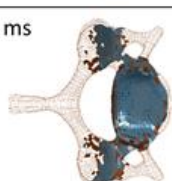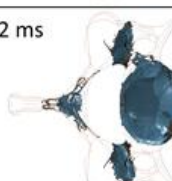
Original Mesh	Medium Mesh	Fine Mesh
401.7 ms	401.5 ms	401.5 ms
403.0 ms	404.0 ms	404.0 ms
450.0 ms	407.0 ms	449.2 ms

Figure 100: Fracture progression in the original mesh, medium mesh, and fine mesh computational models with time (ms)

The fracture patterns in the medium and fine mesh computational models were similar such that fracture initiated at the articular pillars and progressed to the vertebral body and finally spinous process in the fine mesh computational model (Figure 100). The spinous process fracture in the medium mesh computational model was not predicted as the simulation terminated early (407.0 ms). In comparison to the original mesh computational model, fracture initiated at the sides of the vertebral body and progressed into the articular pillars. In general, all these models still predicted the experimental fracture location.

Chapter 5: Discussion

5.1. Comparison between SymIsoCort_SymIsoTrab and AnisoCort_AnisoTrab Models

5.1.1. Constitutive Model Comparisons

The young and aged AnisoCort_AnisoTrab models were compared against the SymIsoCort_SymIsoTrab model that were ran using the ram displacement curve (Figure 102) used for a young specimen and aged specimen respectively (Figure 101). The SymIsoCort_SymIsoTrab model resulted in a higher peak force when ran using the ram displacement curve that was used for the aged specimen (Figure 101). Based on the ram displacement curve between the young and aged specimens, the ram displacement curve of the aged specimen had a lower rate, which would lead to a higher peak force (Figure 101).
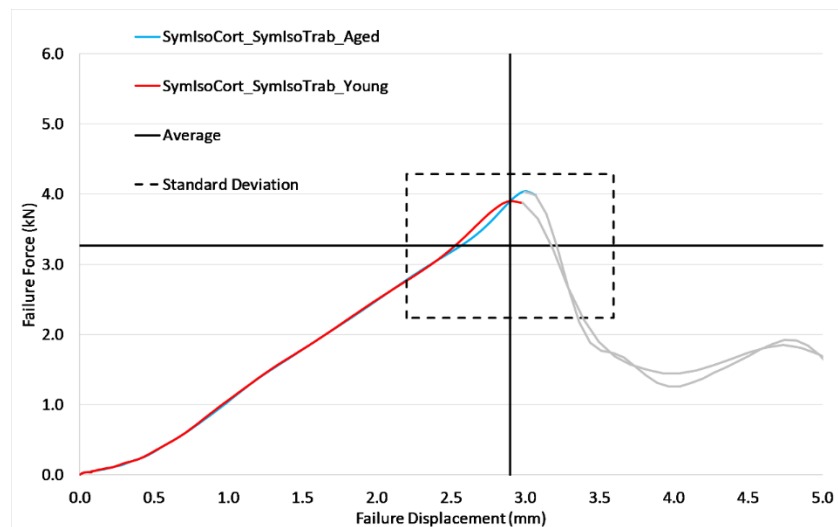
Figure 101: Comparison of the force-displacement curves of the symmetric (GHBMC) model with the young (red) and aged (blue) specimen loading curve inputs
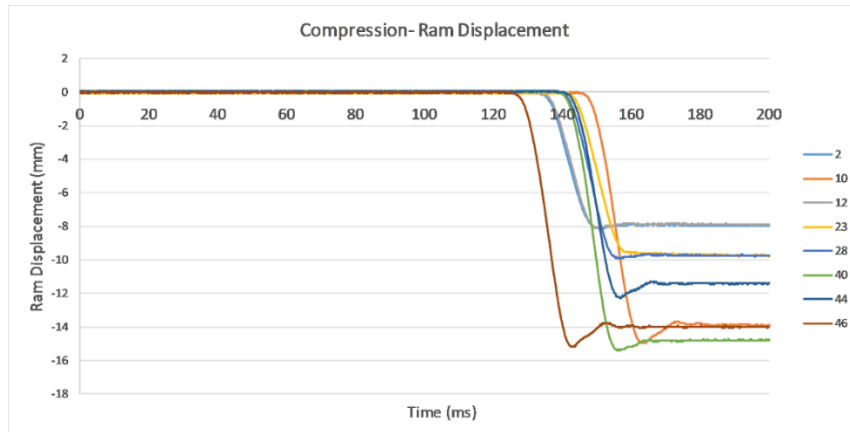
Figure 102: Ram displacement input of all the experimental specimens in the centric compression case [Carter, 2002]

In general, in all cases, the SymIsoCort_SymIsoTrab model predicted a higher failure force than the aged AnisoCort_AnisoTrab model but a lower failure force than the young AnisoCort_AnisoTrab model. Although the properties of the trabecular bone in the SymIsoCort_SymIsoTrab constitutive model were more compliant than the aged trabecular bone properties in the aged model, the combination with the stronger cortical bone properties that were similar to the young longitudinal compressive properties increased the overall strength. In addition, in the AnisoCort_AnisoTrab model, the failure values in the transverse direction were weaker than the SymIsoCort_SymIsoTrab failure values and the onset of failure due to the failure of elements in the transverse direction could potentially cause the AnisoCort_AnisoTrab model to be more compliant.

The key difference between the SymIsoCort_SymIsoTrab model and the AnisoCort_AnisoTrab model would be the tissue failure and predicted fracture patterns. In the centric compression loading case, the young and aged versions of the AnisoCort_AnisoTrab model were able to predict the fracture patterns in the young and aged specimens (posterior vertebral body and burst fracture for the young specimen and posterior and anterior region of the vertebral body for the aged specimen). The SymIsoCort_SymIsoTrab model predicted fracture just within the vertebral body whereas fracture was also seen in the pedicles and articular pillars in the AnisoCort_AnisoTrab model with the endplate configuration and including the spinous process and lamina in the young potting configuration and aged endplate configuration. The additional failure location was due to the potting boundary condition that had the entire cervical spine from anterior to posterior region confined and compressed. The lower strength aged material properties would also make model more susceptible to fracture. The decreased failure displacements in the potting configuration would be due to the additional confined region, which would cause failure at an earlier time.

In the posterior eccentricity case, the predicted force and moment were higher than the average experimental failure force and moment (higher than 1SD for failure moment) in the

SymIsoCort_SymIsoTrab model whereas the aged AnisoCort_AnisoTrab model was able to predict the average experimental failure forces and moments within the standard deviation range. The aged AnisoCort_AnisoTrab model was a better predictor of the average failure force and moment because the specimens in this loading case were all aged specimens above the age of 50 as shown in Table 25 below. However, as the SymIsoTrab model utilized mechanical properties that were compliant that the aged trabecular bone properties utilized in the AnisoTrab model, the high moment value could be due to the absence of anisotropy effect in which the weaker transverse mechanical properties in the AnisoTrab model predicted the lower moment value that agreed with experimental data.

Table 25: Failure force and moments of all experimental specimens in the posterior eccentricity case [Carter, 2002]

Gender, Aged, Segment	F,55,C 6T1	M,88, C24	F,76,C 6T1	M,91, C35	F,87,C 57	F,88,C 57	M,94, C57	F,86,C 46	SD	Avera ge
Failure Moment	13.70	80.90	51.60	45.60	40.80	34.30	58.80	56.90	19. 69	47.83
Failure Force	2.63	5.68	3.09	3.43	3.04	2.57	3.54	3.80	0.9 9	3.47
Specimen #	14	29	39	41	43	45	47	49		

In terms of fracture patterns, however, the SymIsoCort_SymIsoTrab model only predicted fracture at the spinous process whereas the aged AnisoCort_AnisoTrab model was able to predict fracture in the pedicles, articular pillars, lamina, and spinous process. Spinous process fracture occurred in all cases as shown in Table 21 (Section 4.3.2.) but not alone. This indicated that the spinous process fracture was due to failure in other regions, which would compromise the spinous process upon further compression as shown in Table 21 (Section 4.3.2.). In unrestrained whole cadaver studies [Yoganandan et al., 1986] with preserved lordosis of the spine, compression of the C3 vertebra and upper cervical spine fractures were seen. In his subsequent isolated head study [Yoganandan et al., 1991], no comminuted spinous process fractures were seen. In the posterior eccentricity experiment [Carter, 2002] and simulation results in this thesis, spinous process fractures were seen in all specimens. This could be due to the experimental set up, which created a confined loading whereas in the whole neck experiment, the neck was subjected to flexion in the C67 segment and extension in the C25 segments [Nightingale et al., 1997].

For the anterior eccentricity case, both the SymIsoCort_SymIsoTrab model and the aged AnisoCort_AnisoTrab model over-predicted the average failure force (higher than 1SD of average experimental force) and moments although the failure moment predicted by the aged AnisoCort_AnisoTrab model was within the standard deviation range of the average failure moment. This was likely due to the higher number of female specimens (Table 26) in which there would be a geometric difference as female vertebral segments are generally smaller. Therefore, at a similar eccentricity value, due to the smaller size of the vertebral segments, the

female specimen samples would be subjected to more flexion than a larger male specimen sample would. However, a few female specimens did result in higher failure forces than the two male specimens, which represented the amount of scatter present in biological data due to various reasons like quality and size of specimens and curvature of the spine. The location of the load vector could also contribute to the lower failure force. If the load vector was further more anterior, more flexion would be incurred which would cause more soft tissue injuries, failing the specimen at an earlier stage. The predicted failure moment by the SymIsoCort_SymIsoTrab model was closer to the failure moments predicted by the two aged male specimens (~30 Nm).

Table 26: Failure force and moments of all experimental specimens in the anterior eccentricity case [Carter, 2002]

Gender, Age, Segment	F,70,C5-7	F,90,C57	F,53,C57	F.34.C57	M.50.C57	M,61,C57	F,77,C57	F,72,C57	SD	Average
Failure Moment	18.10	7.00	22.60	23.90	32.20	37.40	13.80	15.90	9.90	21.36
Failure Force	0.33	0.93	1.07	0.54	0.46	0.49	1.21	1.09	0.35	0.77
#	3	5	7	8	15	17	27	48		

In the posterior eccentricity case, fractures were seen in the vertebral body in a few experimental specimens whereas in the computational models (SymIsoCort_SymIsoTrab and AnisoCort_AnisoTrab constitutive models), fractures were only seen in the posterior elements of the vertebra. This could be due to the specimens being in extension prior to loading due to the weight of the test set up (Figure 103). The failure forces predicted by the models were within the standard deviation range of the average experimental failure force and this could be because the preload was considered prior to the compression loading. This preload however was applied such that the model specimen was rotationally constrained and only moved downwards. Similarly, the anterior eccentricity case was already in flexion prior to loading due to the weight of the test set up which probably compromised the specimen and caused an earlier failure, explaining the lower experimental failure force. The pre-flexed state in the anterior eccentricity case seemed to have a larger effect on the failure values compared to the pre-extended state probably due to the angle of which the specimen was pre-flexed in the anterior eccentricity case (Figure 104).
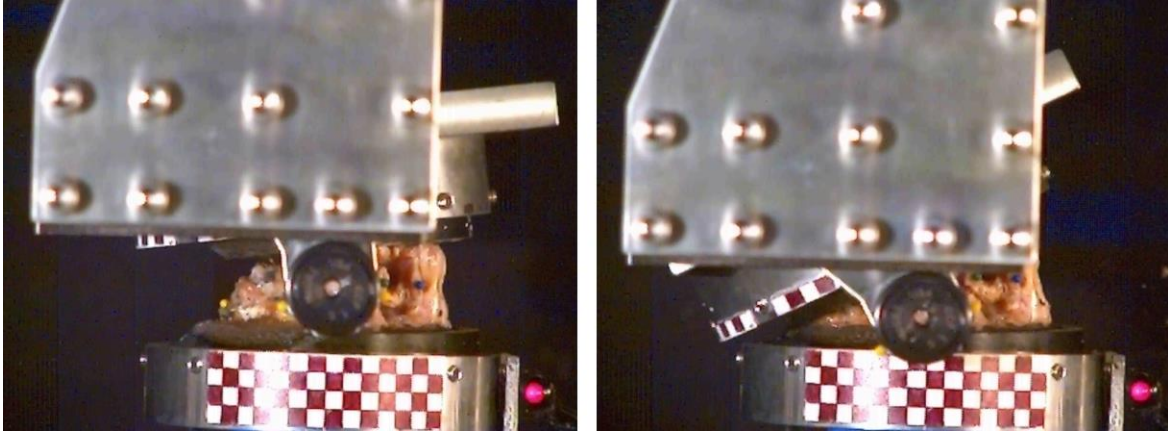
Figure 103: Posterior eccentricity experiment (left: at the start of the experiment, right: during loading) [Carter, 2002]
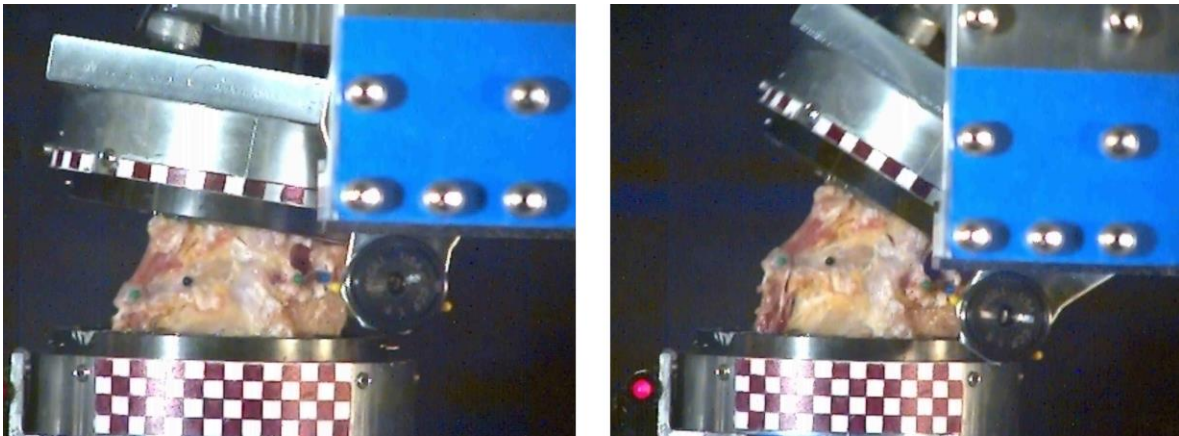
Figure 104: Anterior eccentricity experiment (left: at the start of the experiment, right: during loading) [Carter, 2002]

The SymIsoCort_SymIsoTrab model did not predict any hard tissue fracture and some specimens did not show any hard tissue failure as well (Table 22) (Section 4.4.2). The AnisoCort_AnisoTrab model predicted fracture in the anterior region of the vertebral body and the pedicle. This was also seen in a few specimens although none occurred at the pedicles. Supraspinous ligaments do not exist in the model but interspinous ligaments failure was seen in both models.

In the low lateral eccentricity case, the SymIsoCort_SymIsoTrab model over-predicted the failure force compared to the average failure force whereas the aged AnisoCort_AnisoTrab model was able to predict both failure force and moment well within the standard deviation range. This was because most specimens in the experiment were female or aged specimens (Table 27). However, in the high lateral eccentricity case, the SymIsoCort_SymIsoTrab model predicted the failure force and moment in better agreement than the aged AnisoCort_AnisoTrab model, which predicted lower failure force and moment values although they were both within the standard deviation range. The aged AnisoCort_AnisoTrab model predicted lower failure

values as hard tissue failure was seen in regions (articular pillars, pedicles, and lamina) where transverse failure occurred (lower ultimate strength and strain than longitudinal direction).

Table 27: Experimental specimens segment, age and gender information in the low and high lateral eccentricity case [Van Toen, 2014]

Low Eccentricity Specimens	H1318	H1323	H1321	H1298	H1975	H1274
Segment	C57	C35	C46	C35	C6T1	C35
Age, gender	72, F	NA, M	72, M	68, F	79, M	78, M
High Eccentricity Specimens	H1125	H1329	H1275	H1286	H1998	H1292
Segment	C46	C57	C35	C46	C6T1	C35
Age, gender	NA,M	NA, M	79, M	66, F	68, F	67, M

In terms of fracture pattern, in the low lateral eccentricity case, the fracture was seen in the vertebral body in both models (Table 23, Section 4.5.2). The fracture was seen in the articular pillar as well in the AnisoCort_AnisoTrab model. It was noticed that the fracture occurred in a more progressive manner in the AnisoCort_AnisoTrab model than the SymIsoCort_SymIsoTrab model. In the high lateral eccentricity case, on the other hand, the fracture was seen in the articular pillar, lamina, and pedicles in the AnisoCort_AnisoTrab model whereas only in the pedicles in the SymIsoCort_SymIsoTrab model. In general, none of these fractures were seen in the experimental specimens but the failure in the facet capsular ligament and disc were seen in both computational models and experiment. The SymIsoCort_SymIsoTrab model did also predict failure in the posterior longitudinal ligament, which was not seen in experiment. The differences seen could be due to the average experimental specimens from various segment levels whereas only the C57 segment model was utilized in this study. Vertebrae from different levels have different sizes and they increase going down in level towards the lumbar section. In addition, geometry differences such as facet gap and facet angles between the experimental specimens and model could cause this disparity in results.

The AnisoCort_AnisoTrab model predicted more fractures than the SymIsoCort_SymIsoTrab model as well probably due to it having weaker and more compliant mechanical properties in general. The additional hard tissue fracture in the AnisoCort_AnisoTrab model possibly led to the lower failure forces and moments predicted in general. Besides that, the aged transverse properties were weaker by almost twice the SymIsoCort_SymIsoTrab trabecular bone properties. The high failure in hard tissue in the aged anisotropic model in the high lateral eccentricity case could mean that the transverse properties were too weak which is possible as due to lack of experimental data, the transverse properties were scaled from the longitudinal properties [Mosekilde et al., 1985; Sanyal et al., 2012; Augat et al., 1998]

In general, the young and aged model of the AnisoCort_AnisoTrab model was able to predict kinetic and kinematic values better than the SymIsoCort_SymIsoTrab model. This indicated the importance of age effect in mechanical properties that represented the age of the experimental samples as the mechanical properties of hard tissue decline with age (Section 2.4.2.). The AnisoCort_AnisoTrab model was also able to predict the fracture patterns in a more progressive

manner and not as concentrated in one location as the SymIsoCort_SymIsoTrab model did. In both SymIsoCort_SymIsoTrab and anisotropic models in the anterior eccentricity and posterior eccentricity compression cases, the disc avulsion was predicted by the model but most of the ligament failure was not predicted except the interspinous ligaments in the anterior eccentricity compression case probably due to the simulation terminating before further compression that could possibly fail these other ligaments.

Time of Failure Definition in Experiments and Simulation

In the experiments (centric, posterior and anterior eccentricities) performed by Carter (2002), the time at failure was defined by examining both axial load and moment about the y-axis together. In the study by Carter (2002), the peak axial load prior to a reversal (decrease in load) was assumed to represent the onset of failure but after examining all of the load data, it was suggested that failure could have occurred at the peak moment prior to a reversal instead of at the force reversal [Carter, 2002]. In the experiments (lateral and high lateral eccentricities) performed by Van Toen (2014), acoustic emission (AE) signals were utilized to predict the time of failure or 'injury'. This methodology was more objective in determining the time of failure compared to using the force or moment response. Based on the load history, the time of injury when the AE signal reached 40% of the peak signal for low lateral eccentricity and 5% of the peak signal for high lateral eccentricity was close to the local force peak. Although it was mentioned that there was no available gold standard to evaluate the accuracy of this method and that the selection of the threshold value was subjective, the study by Van Toen (2014) showed that using AE signal was better compared to the moment or force reversal method in determining the time at injury. In comparison to traditional methods, high-speed video evidence in the study by Van Toen (2014) was only able to show failure later in time (relatively close to local force peak in low eccentricity case in which hard tissue failure was dominant but further away in the high eccentricity case in which majority of failure was seen in the soft tissue).

In the simulation work, failure was defined as the first occurrence of element erosion. When comparing the results of the experiments, in general, all the force and moment results predicted by the model were comparable to the force-moment results predicted by Van Toen (2014) for the low lateral eccentricity and high lateral eccentricity cases. This was because the methodology in determining the time of failure by Van Toen (2014) was similar to the methodology utilized in the simulation in which the time of failure was the time of the first tissue or element failure. When comparing with the results of the experiment by Carter (2002), in general, most of the failure forces and moments in all the cases were comparable except the anterior eccentricity case. In the anterior eccentricity case, the failure force was approximately 4 times higher than the C57 experimental specimen (#17- male, 61 years old) and also approximately 3 times higher than the average failure forces of all specimens. It was mentioned that the differences seen with the average failure force of all the specimens was due to the geometrical differences as 75% of the experimental specimens were from female subjects [Carter, 2002]. However, when compared against the failure force of the aged male specimen (#17), the failure force was still low at

0.49 kN while the aged AnisoCort_AnisoTrab model predicted a failure force of 2.1 kN. The geometrical differences were insignificant except for some curvature differences when the X-ray of the specimen was compared against the geometry of the finite element model (Appendix A).

More importantly, the method proposed by Carter (2002) was more subjective compared to the AE method. As shown in Figure 105, the time of injury in the anterior eccentricity experimental specimen (#17) was determined as the time of the second local peak moment instead of the time of the first local peak force or first local peak moment which differed from the definition of time of failure described by Carter (2002). The peak force of 1.6 kN was actually observed before the local peak moment. The peak force shown in the experiment could be due to hard tissue failure. In the simulation on the other hand, the time of first element erosion approximately corresponded to the time at global peak force, which also happened to be the time at global peak moment in many cases. The peak force and peak moment occurred simultaneously in the simulation. If the experimental force-moment curve was analyzed such that the first local peak of either force or moment was the time of failure, the failure force would be 1.6 kN, which would be more comparable to the failure force of 2.1 kN predicted by the model. However, the failure moment would then be 5.15 Nm, which then would be further away from the model prediction of 25.6 Nm. The simulation time at failure occurred approximately 3.5 ms before the experimental time at failure.

In the posterior eccentricity simulation, the measured experimental failure force and moment (3.54 kN and 58.75 Nm) of specimen #47 (male, 94 years old) was similar to the predicted aged AnisoCort_AnisoTrab model (3.06 kN, 65.09 Nm). In the anterior eccentricity case, the time at failure was defined as the time of the second local peak moment (Figure 105) which differed from the general methodology applied as shown in Figure 106 in which the experimental time at failure was determined as the time of the first local peak moment. The experimental time at failure occurred earlier by 3.5 ms than the model time at failure. The model time at failure on the other hand correlated to the time of global peak force. In Figure 105 and Figure 106, a thing to note was that the force and moment history from the simulation model were recorded starting only from 0.14 s onwards to save data space and prior to this time, nothing crucial occurred.

In general, the failure detection techniques in experiments such as high-speed video evidence or by load-moment history analysis were more subjective and could cause the differences in definition of failure points. The AE signal technique proved to be a more consistent technique in failure definition and also predicted values closer to the simulation model as the methodology of defining time of failure was similar (time of first tissue failure or element failure).
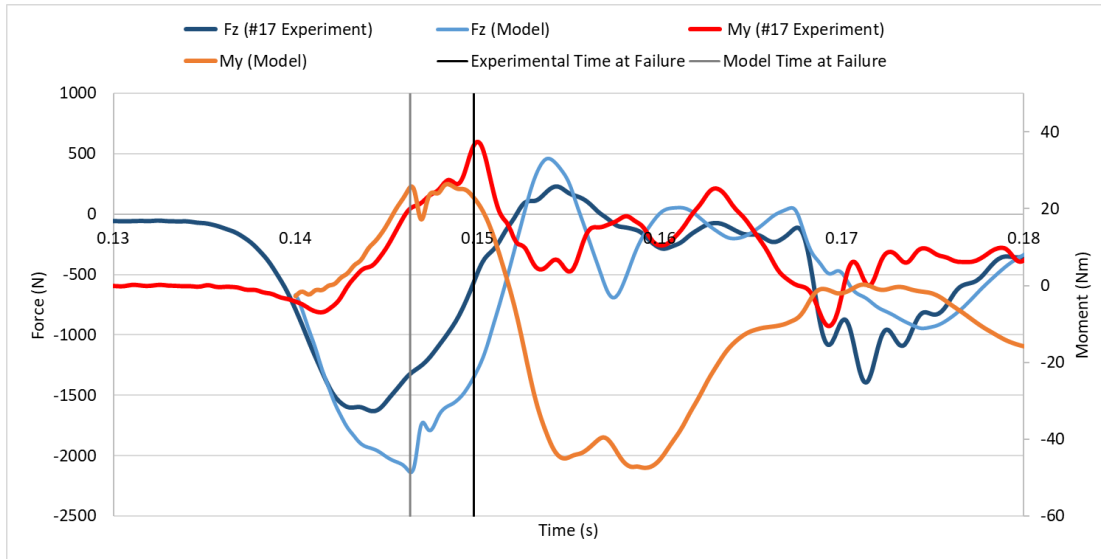
Figure 105: Anterior eccentricity force-moment curve comparison between experimental (#17) and model
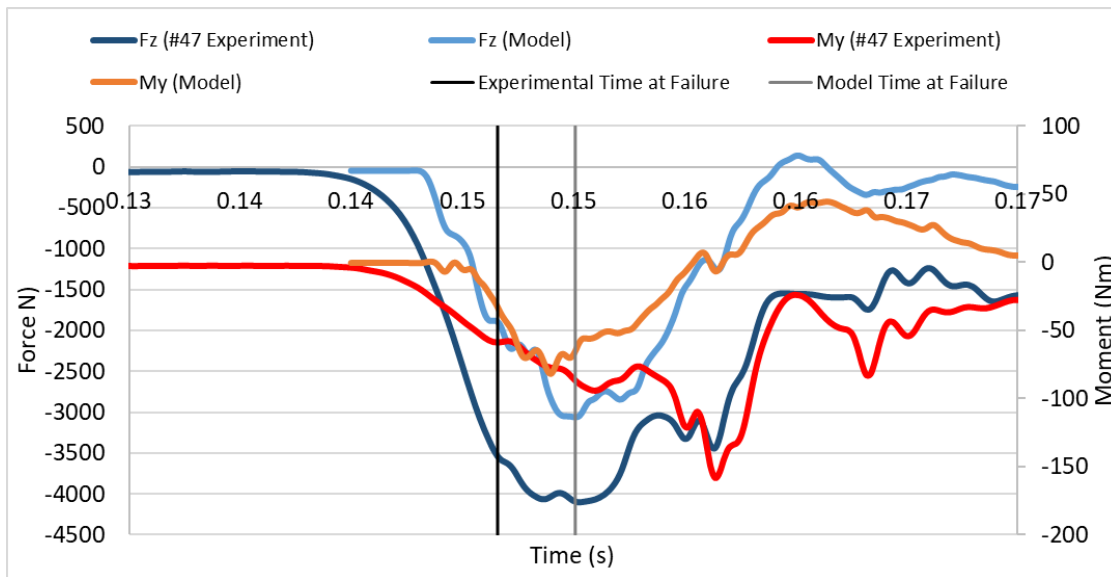
Figure 106: Posterior eccentricity force-moment curve comparison between experimental (#47) and model

5.1.2. Fracture Analysis with High-Speed Video Data

As seen in Section 4.2.1, anterior longitudinal ligament failure was seen in some specimens in the centric compression case but none in the simulation. Based on the high-speed video for specimen #10, which was the aged specimen in which anterior longitudinal ligament (ALL) failure was seen, there was anterior shearing upon crushing (Figure 107). This probably led to the ALL failure seen.
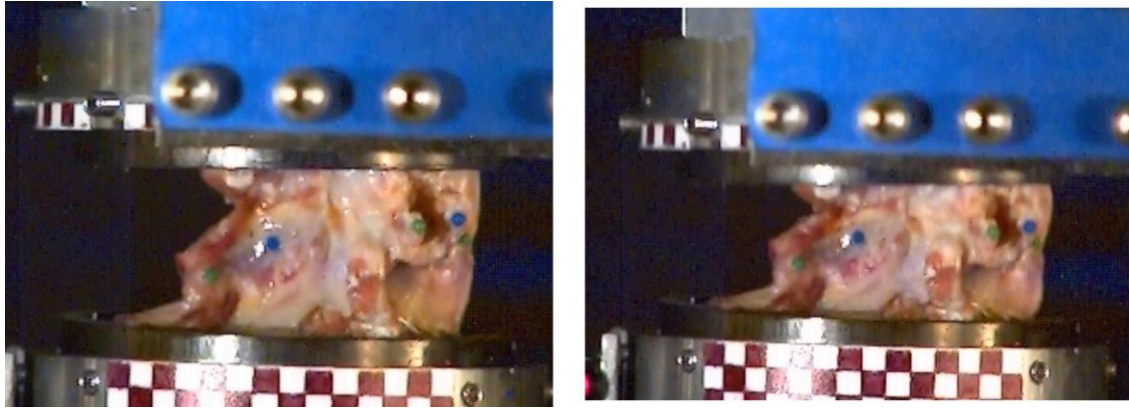
Figure 107: Aged specimen in the centric compression case (specimen #17) (left: at the start of the experiment, right: during compression) [Carter, 2002]

Besides that, specimen #28 (female, age 85, segment C35) was recorded to have several soft tissues like facet capsular ligaments and spinous process failure. The soft tissue failure and spinous process fracture seemed to occur post-hard tissue failure due to deformation later upon further crushing (Figure 108).

Figure 108: Specimen #28 in centric compression case (left: at the start of the experiment, right: during compression) [Carter, 2002]

As noticed in the simulations, no spinous process fracture or soft tissue failure (except the disc) was predicted. The example of specimen #28 that showed spinous process fracture was a different segment level and the curvature of the segment could be important in determining failure locations and onset. Based on the simulations, however, it was found that failure was usually seen in the hard tissue first before the soft tissue. This may be difficult to capture in actual dynamic experiments or high-speed video.

5.1.4. Effects of Filtering

The simulation numerical results were filtered with a SAE filtering of CFC600 based on experiments performed by Dr. Carter [Carter, 2002] and a SAE filtering of CFC1000 for those that were based on experiments by Dr. Van Toen [Van Toen et al., 2014]. One of the limitations of filtering was the decrease in failure force and displacement as for example the CFC1000 filter

class filters at 1650 Hz and removes the 10,000 Hz component in the curve, which would alter the actual failure force and displacement. However, the filters were applied to replicate the filters applied in the experiments. In the centric compression simulation model with the SymIsoCort_SymIso_Trab constitutive model, filtered results (CFC 600) predicted failure displacement (3.19 mm) and force (4.11 kN) that were 9.46% (2.88 mm) and 5.28% (3.89 kN) lower respectively than the unfiltered results as seen in Figure 109 below.
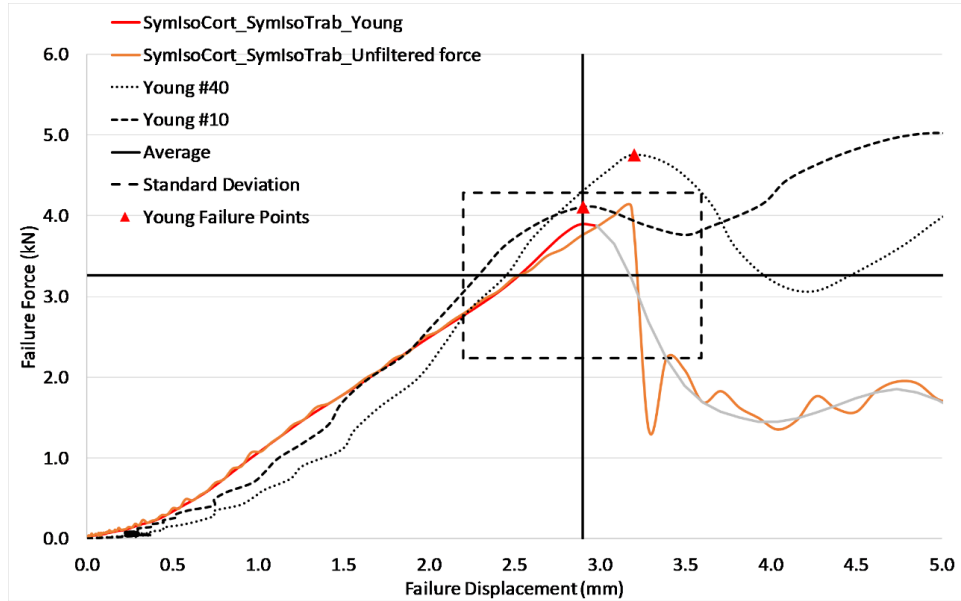
Figure 109: Comparison between the filtered force-displacement symmetric (GHBMC) curve (red) and the unfiltered curve (yellow)

5.2. Centric Compression Case Boundary Conditions

In terms of the centric compression case, the entire test set up was not modeled. Rather, the boundary condition was simplified such that the load was applied at the superior C5 endplate. To investigate any differences that might be caused with the absence of the test set up, the test set up that was used in the compression with eccentricity simulations was used with the load bearing moved to the center of gravity of the endplate (Figure 110) to simulate a centric compression case.
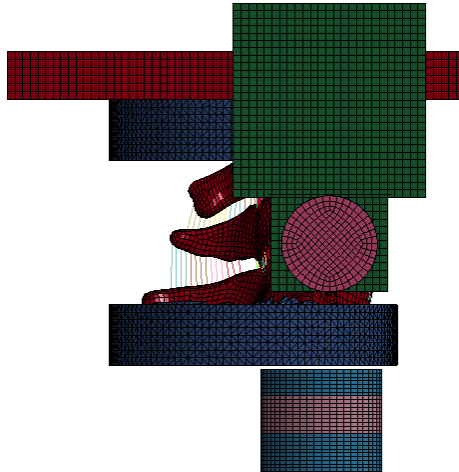
Figure 110: Centric compression set up utilizing the eccentricity compression test set up
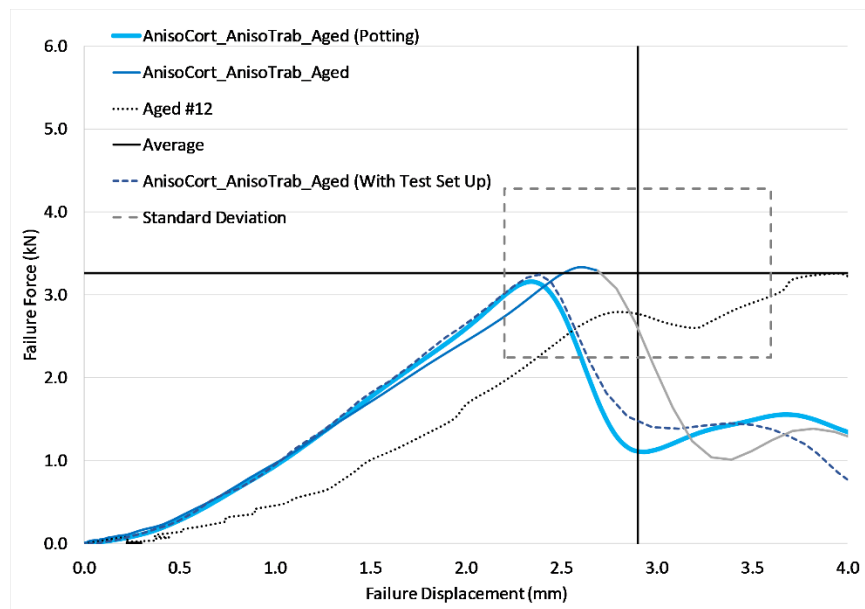
Figure 111: Force-displacement curves comparison between the aged anisotropic model with endplate (solid thin blue), with potting (solid thick blue) and with the eccentricity test set up (dotted blue) boundary condition

The failure force predicted by the potting (Section 4.2.2) and test set up simulation models were similar to force predicted by the endplate simulation model whereas the failure displacement predicted by the potting and test set up models were lower than the displacement predicted by the endplate simulation model. As seen in Figure 111 above, the failure forces in general between the potting (3.16 kN) and the test set up (3.24 kN) were approximately 9% and 8% lower than the endplate (3.33 kN) case. The failure displacement between the potting (2.35 mm) and the test set up (2.39 mm) were approximately 5% and 3% lower than the endplate case (2.59 mm).
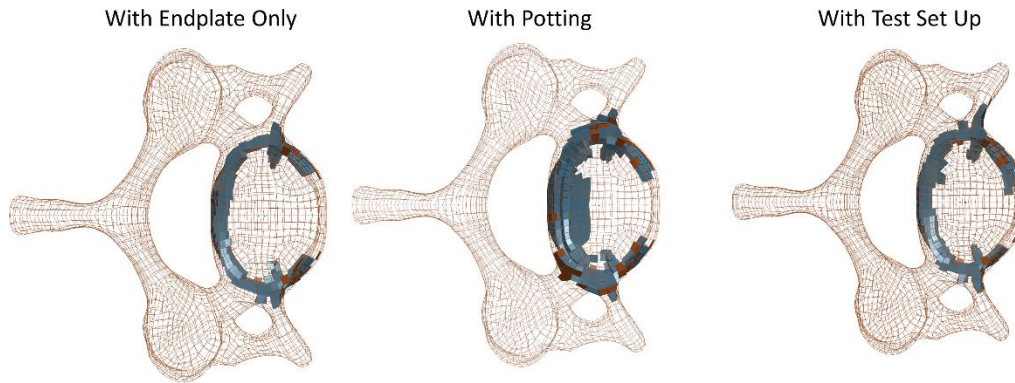
Figure 112: Fracture location comparison between the centric compression cases with the endplate, with the potting and with the eccentricity test set up boundary conditions

As for fracture patterns, similar fracture patterns were seen in all cases such that failure was seen and progressed from the edge of the vertebral body (Figure 112). The lower failure forces and displacements utilizing the potting and the test set up were reasonable as the specimen was more constrained in both these two cases and was subjected to earlier failure. Therefore, for the centric compression case, it was not necessary to model the entire test set up and modeling the potting, or applying the boundary conditions directly on the C5 superior endplate were sufficient to produce reasonable results.

5.3. Model Sensitivity

5.3.1. Orientation of Specimen

The differences seen in the failure values and the fracture patterns may be attributed to the differences in the orientation of the specimen. Figure 113 below showed one of the X-ray scans of the specimen with the computational model displayed in colored lines. It could be seen that in this specimen, the size of the vertebrae was similar but the angle of the posterior element of the C7 segment was different.

Figure 113: The simulated model (colored lines) overlapped on an X-ray scan to show differences in geometry and orientation

The computational model was reoriented from its original position by rotating around the y-axis such that the line connecting the two center of the vertebral segment C6 and C7 were parallel (Figure 114). The rotation was 6.17 degrees. This reorientation method was similar to the method in Van Toen's study [Van Toen, 2014].
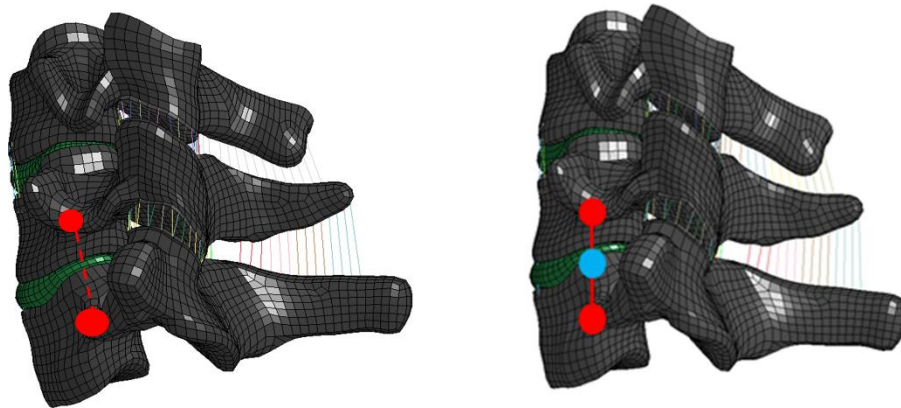
Figure 114: Re-orientation method (left: before, right: after)

It was noted that this approach did not change the failure results significantly (Figure 115 and Figure 116). More fracture was seen in the articular pillar but did not represent a significant increase.
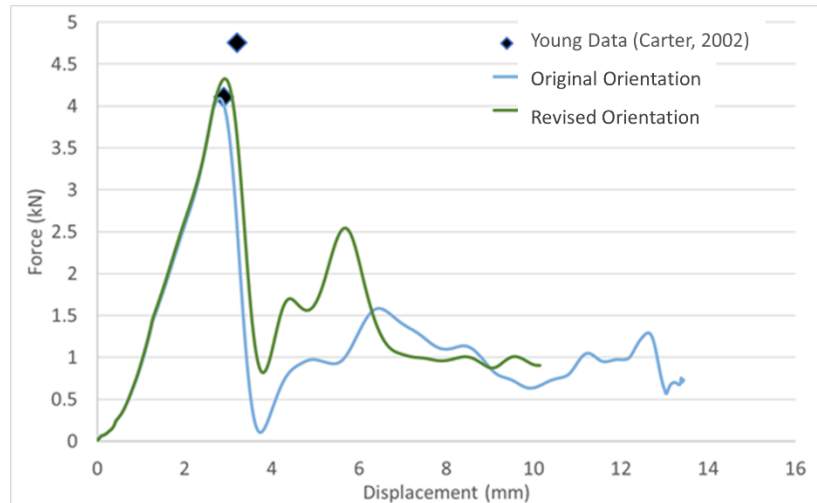
Figure 115: Force-displacement curves between the asymmetric model with original and revised orientation
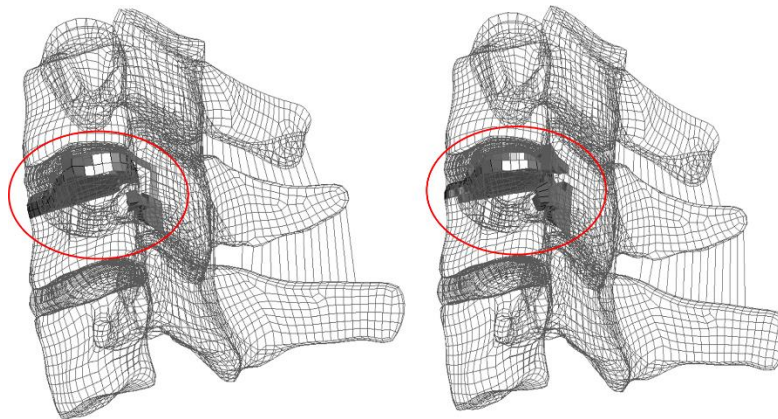
Figure 116: Fracture locations of the original orientation model (left) and the reoriented model (right)

For the anterior eccentricity case, the experimental specimen had a higher flexion in both superior vertebra and inferior vertebra (6.8 degrees, 2.4 degrees) than the GHBMC computational C57 model (2 degrees, 2 degrees) (Appendix A) which may attribute to the higher failure force (higher than 1SD of average experimental failure force) predicted by the SymIsoCort_SymIsoTrab and AnisoCort_AnisoTrab models. In addition, fracture was seen in the pedicles in the computational models but not in the experiment, which may be attributed to the orientation.

5.3.2. Load Vector Position

5.3.2.1. Antero-Posterior Eccentricity
To test the sensitivity of the load vector position, the load vector was varied 10 mm in the anterior and posterior direction from the original 18 mm eccentricity (Figure 117).

Anterior   Posterior
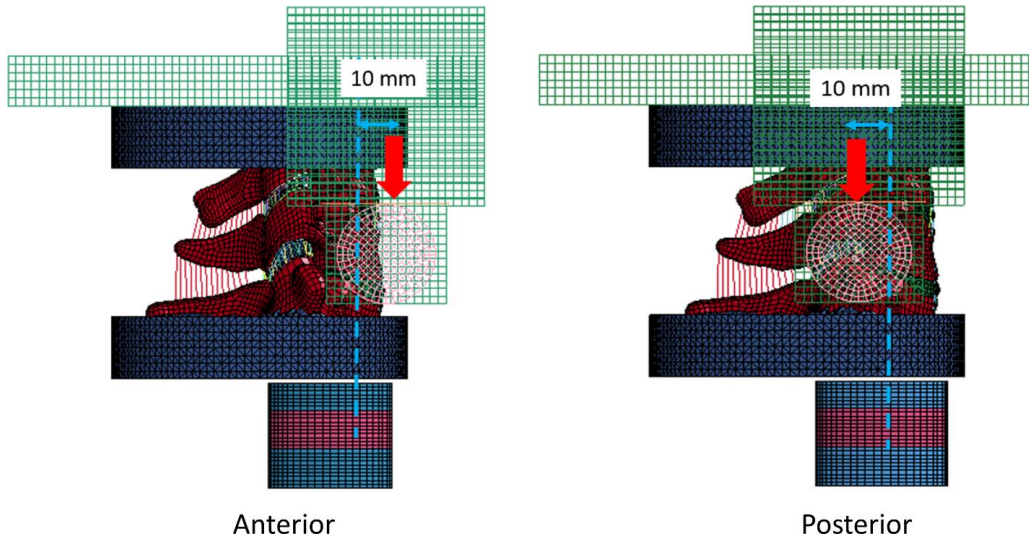
Figure 117: Anterior vs. Posterior 10 mm Eccentricity Set Up

Based on Figure 118 the failure force increased by 34% (2.87 kN) in comparison to the failure force (2.14 kN) when the eccentricity was 18 mm anteriorly. The failure moment on the other hand decreased by 93% (1.83 Nm) in comparison to the moment predicted when the eccentricity was 18 mm anteriorly (25.59 Nm). The results achieved were reasonable in which the failure force increased and the moment decreased when the eccentricity was closer to the center of gravity as there was more vertebral body support with a reduction in the moment arm distance. More fracture was seen in the vertebral body in comparison to when the eccentricity was further away from the center of gravity (Figure 119).
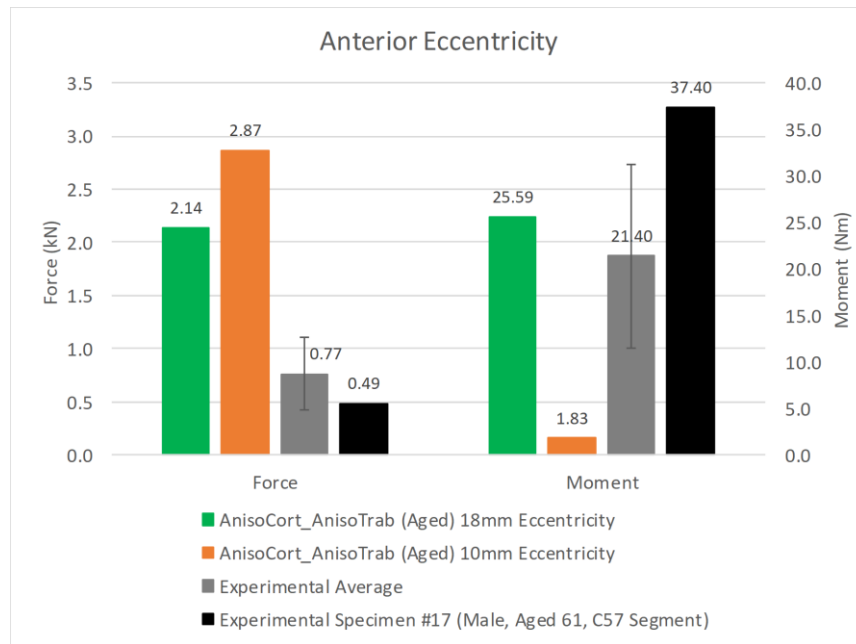
Figure 118: Failure force and moment comparison in anterior eccentricity case (18mm (Original): Green, 10mm: Orange)

120

393.6 ms   393.8 ms   394.5 ms   397.0 ms   450.0 ms
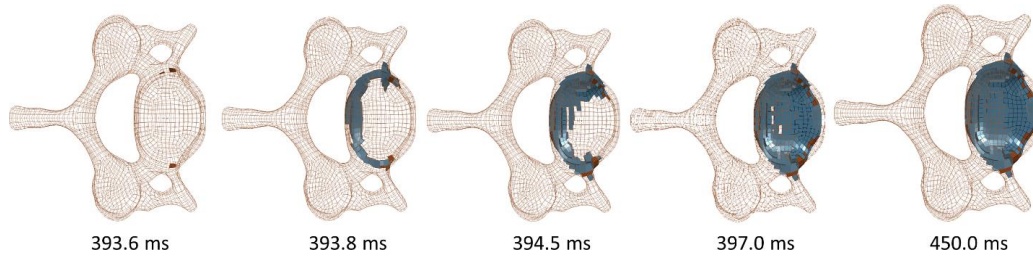
Figure 119: Fracture Pattern in 10mm Anterior Eccentricity Case

In the posterior eccentricity case, the failure force increased by 31% (4.0 kN) and the failure moment by 46% (95 Nm) in comparison to the failure values (3.06 kN and 65 Nm) predicted when the eccentricity was 18 mm posteriorly (Figure 120). The increase in failure force was expected as mentioned earlier the eccentricity was closer to the center of gravity of the vertebrae and thus, there was more support from the vertebral bodies. In terms of the increasing moment, the reason could be because the facet joints were engaged more resulting in more resistance and a higher failure moment. The fracture patterns were reasonable as well and more failure was seen in the posterior vertebral body whereas, in a larger eccentricity, most of the failure occurred in the posterior elements (Figure 121).
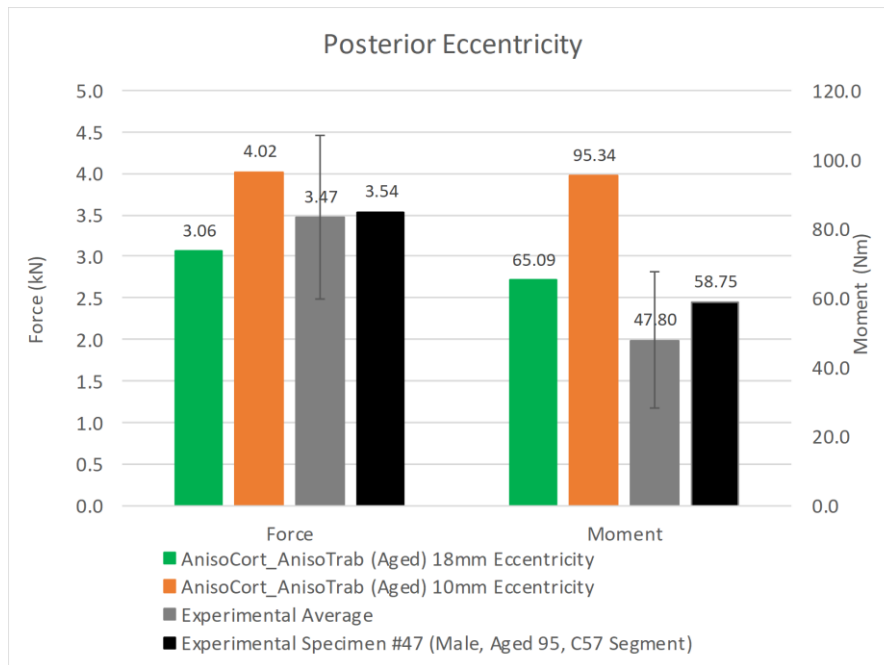
Figure 120: Failure force and moment comparisons in posterior eccentricity case (18mm (Original): Green, 10mm: Orange)

396.8 ms   398.0 ms   399.0 ms   400.0 ms   450.0 ms
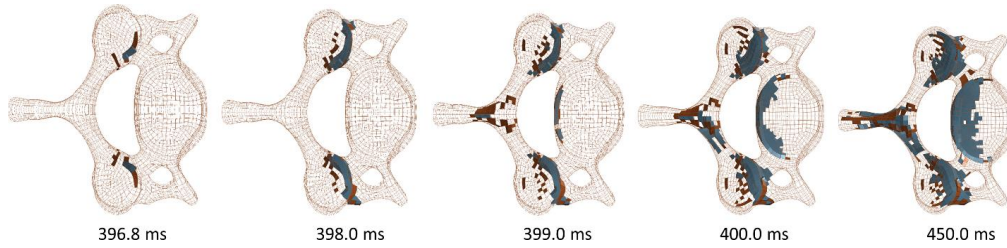
Figure 121: Fracture Pattern in 10mm Posterior Eccentricity Case

This study showed how the anterior eccentricity was a lot more sensitive than the posterior eccentricity. One reason might be that posteriorly, the cervical spine has posterior elements, which would provide further support under posterior eccentricity. Anteriorly however, the cervical spine has nothing pass the vertebral body. This resulted in higher flexion and lower failure forces and moments. This showed that the range of failure forces and moments vary depending on the eccentricity value. This could also cause the large differences in failure values seen between the model and experimental results.

5.3.2.2. 1 mm eccentricity sensitivity

The anterior, posterior, and lateral compressive simulations were ran with 1 mm eccentricity to study the sensitivity of the model. The lateral compressive simulations were performed by having the load vector in the test set up to be positioned 1 mm from the inferior C67 IVD center of gravity in the positive y-direction and negative y-direction. Similarly, the anterior compressive simulation was performed with the load vector in the test set up to be positioned 1 mm from the inferior C67 IVD center of gravity in the positive x-direction and negative x-direction for the posterior case. The results shown in Figure 122 were compared against the centric compression case where the test set up was positioned such that the load vector was aligned with the center of gravity of the C67 IVD.
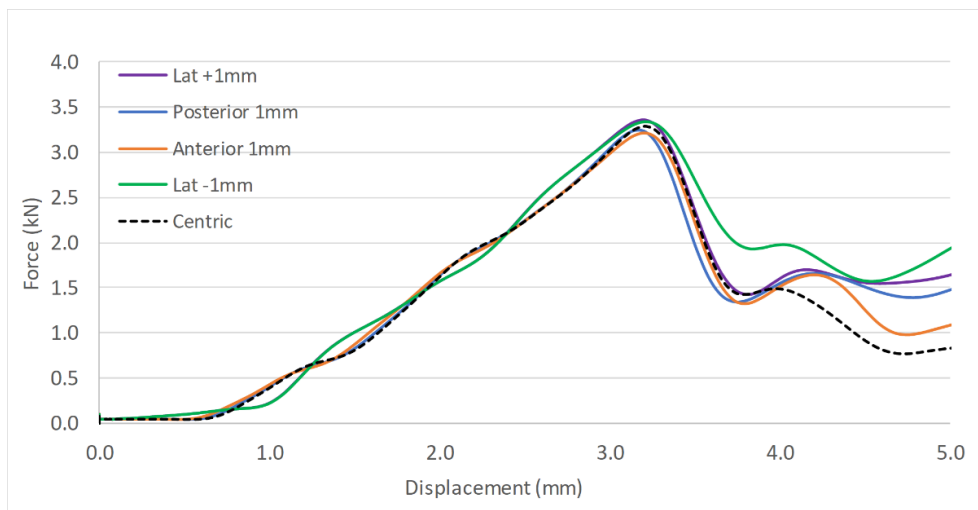
Figure 122: Force-displacement curves for sensitivity analysis

122
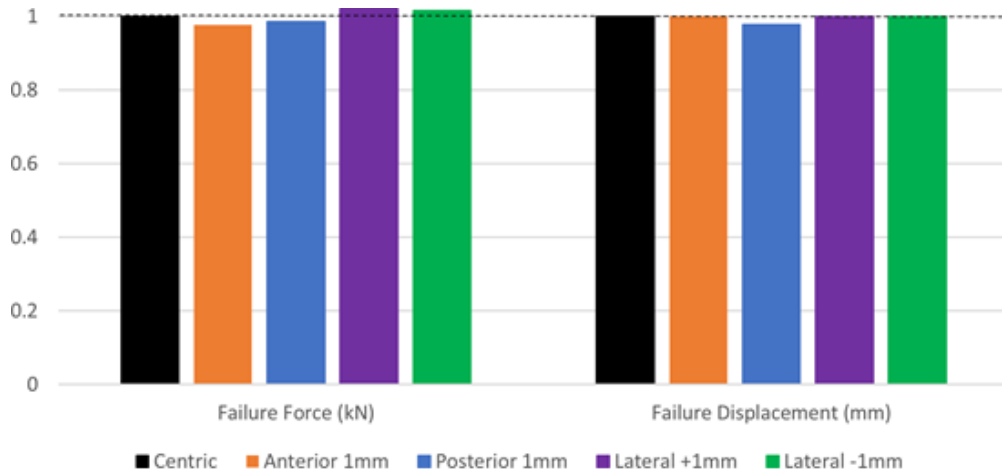
Figure 123: Standardized failure force-displacement bar graphs with the centric case (black)

In general, in terms of failure forces, the anterior case was approximately 2.3% lower (3.21 kN) and the posterior 1.4% lower (3.24 kN) than the failure force of the centric case (3.29 kN) (Figure 122 and Figure 123). The lateral +1 mm was approximately 2% higher (3.36 kN) and the lateral -1 mm 1.6% higher (3.34 kN) (Figure 123). In terms of failure displacements, the anterior, lateral +1 mm, and lateral -1 mm were all similar to the centric case displacement (3.22 mm) (Figure 123). Only the posterior case predicted a failure displacement that was approximately 2.3% lower (3.14 mm) (Figure 123).
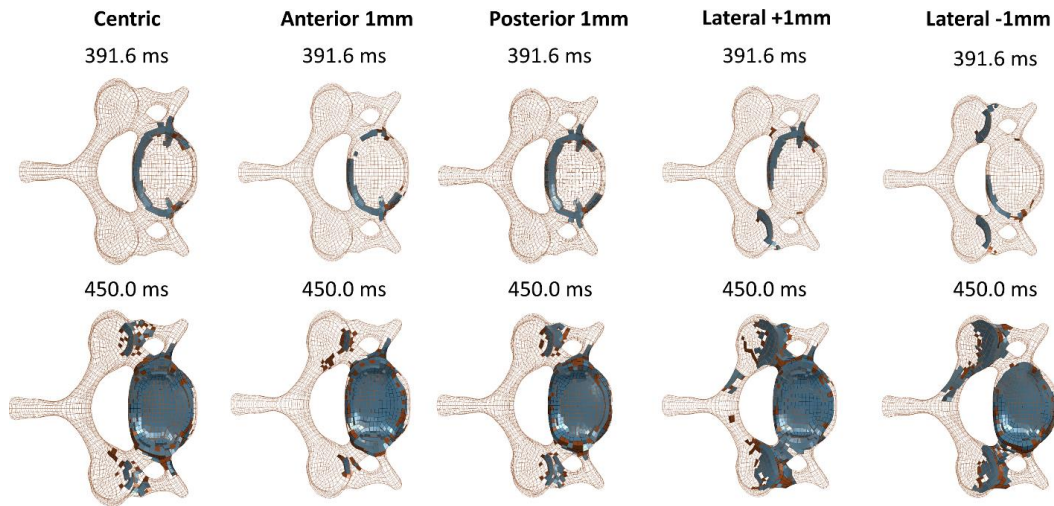
Figure 124: Fracture patterns for sensitivity analysis

In terms of fracture pattern, the fracture at 391.6ms was similar between the centric and posterior case in which failure was seen around the posterior and side edges of the vertebral body (Figure 124). In the anterior case, failure was predominantly seen on one side of the edge of the vertebral body (Figure 124). For the lateral +1 mm case, failure was initiated in the right articular pillar and then the left edge of the vertebral body whereas in the lateral -1 mm, failure was initiated in the left articular pillar and then the right edge of the vertebral body and articular pillar (Figure

123

124). In terms of final fracture pattern at 450 ms, the posterior case was similar to the centric case in which failure was seen in the vertebral body and a little at the transition region from the articular pillars to the pedicles (Figure 124). There was slightly more failure however at the posterior region of the vertebral body and the pedicles in the posterior case compared to the centric case, which was expected. For the anterior case, failure was seen in similar locations as the centric case but predominantly more in the vertebral body, which was also, expected (Figure 124). For the lateral +1 mm and -1 mm cases, additional failure was seen in the articular pillar and lamina. Although the fracture initiation location was different due to the location of the load vector, the final fractures were similar.

This study showed that there was more sensitivity between the anterior and posterior direction than the lateral direction. This was reasonable as the geometry differences laterally were similar but the geometry differences between the anterior and posterior regions were substantially different. Besides that, this study also showed that the model was more compliant in the anterior-posterior regions than the lateral regions.

5.4. Element Erosion Approach and Mesh Refinement

One of the pros of the element erosion approach is it takes less computational time and is a relatively stable method. The element erosion approach in this work utilized a strain-based criterion such that when the failure strain was reached, the element was eroded. The disadvantage of this methodology is that once an element erodes, the surrounding elements follow as the model loses its compliance and structural integrity. In the actual bone of the cervical spine, the trabecular bone gets crushed and densifies, filling in the pores of its structure. One of the methods to address this would be to incorporate damage modeling. With damage modeling, damage will be applied to the elements and only once reaching full damage will the elements be eroded. In this way, the fracture pattern can be captured more precisely as the elements will not immediately erode at a set strain and invoke erosion of the elements around it and thus, preventing a fracture path or crack to be formed. With the strain-based element erosion approach as well, if the mesh of the computational model is refined, the failure strain must be recalibrated to a larger value, as the smaller element will reach the set failure strain faster than a larger element (Figure 125). The medium and fine mesh models experienced earlier failure (401.5 ms versus 401.7 ms) than the original mesh model and this was because the smaller elements used in these cases were a better representation of the strain gradient in the model (Figure 100). As shown in Figure 125, the critical strain occurred at the sides of the vertebral body for the original mesh and in the articular pillars in the medium and fine mesh computational models, which would be the location of the fracture initiation. Therefore, to achieve similar failure force and displacement, the failure strain had to be adjusted to a larger value to consider the size of the element (mesh regularization study). Although the refined meshes had earlier failure time, the failure displacement was higher (Figure 99) and this is because fracture initiated in the articular pillars in the refined models that would give the vertebra a higher range of motion upon being crushed than when fracture initiated in the vertebral body.
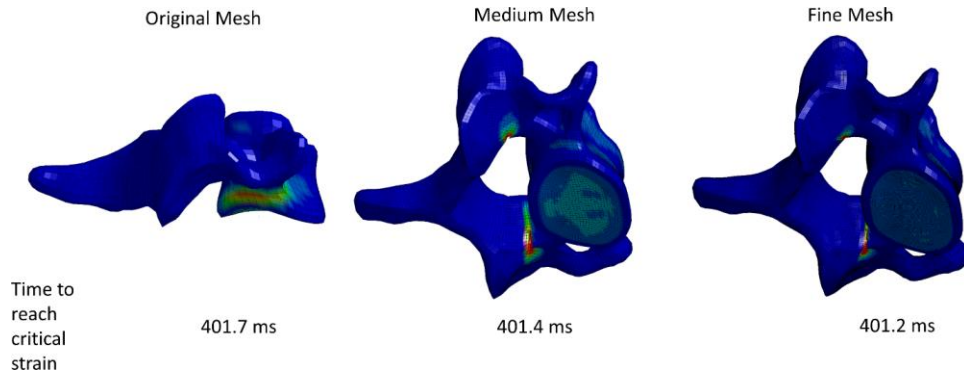
Figure 125: Strain gradient in original, medium, and fine mesh computational models and the time taken to reach the critical strain

A lower failure force (9% lower) was seen in both medium and fine mesh computational models compared to the original mesh model. The failure displacement was similar in the medium but approximately 14% higher in the fine mesh computational model. In general, the differences were not large (within 10-15%) and the differences were expected as the failure strain had not been calibrated for the refined computational models. The element size dependency is the one disadvantage of the strain-based element erosion approach. One of the possibilities that cause the differences in failure location would be the disc behavior that affected the kinematic motion Figure 126). This, however, may be attributed as well to the time the elements took to reach the failure strain and the state the computational model was in at that time. Although mesh convergence was not achieved as it could be difficult to with a failure based on element erosion due to the removal of mass from calculations, this study gauged the amount of differences seen with a refined mesh model. In this work, the differences were approximately 10% with the medium and fine mesh models.
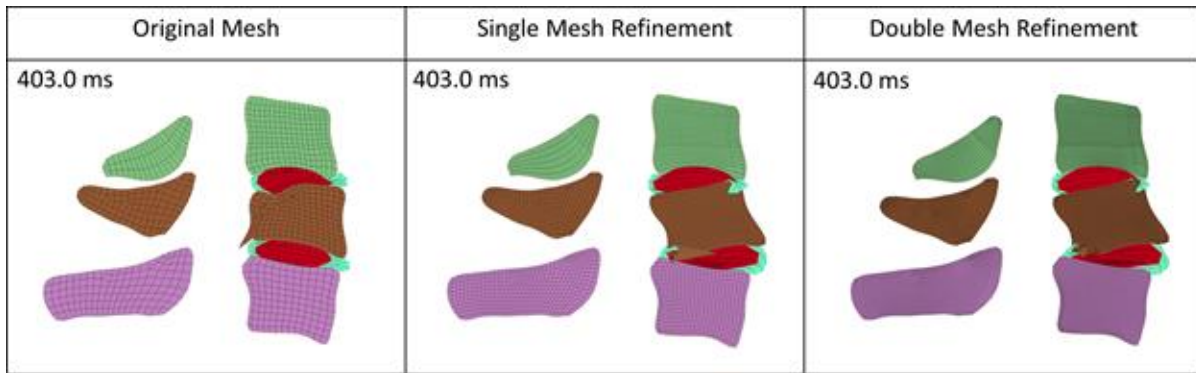
Figure 126: Lateral view of the fracture in the original mesh, medium mesh, and fine mesh computational models in the centric compression case

125

Chapter 6: Summary and Conclusion

The objective of this thesis was to investigate constitutive models to predict the response and failure for both cortical and trabecular bone using a detailed finite element neck model. In current human body models, trabecular and cortical bones are often modeled using linear isotropic material properties. One of the critical requirements that denote the accuracy and fidelity of computational models is having accurate material properties and tissue level failure criteria. As there is no single constitutive model currently that incorporates all the mechanical properties of hard tissues such as anisotropy, asymmetry, strain rate dependency, and damage, this study analyzed the importance of anisotropy and asymmetry in the constitutive models for bones. In addition, this study also investigated the importance of aging effects on material properties and failure results. The constitutive models were evaluated using a lower cervical spine motion segment extracted from the full neck model, specifically the C5-C6-C7 segment.

In terms of methods of modeling fracture, the element erosion technique was employed in this study. Several studies had performed bone fracture modeling technique and the more novice methods are the cohesive element approach or the X-FEM analysis method. The main limitation for the cohesive element approach is that the fracture path has to be pre-defined for the analysis and for the X-FEM approach, it is computationally costly and is still at early stages in 3D models. In terms of the most cost-efficient method, the element deletion approach is utilized although this method has its own limitations as well such as that the crack initiation and propagation occur together. This is because the element erosion method is usually based on a failure strain criterion and once an element reaches the failure strain value, it is removed from the model. Therefore, it is not possible to "weaken" the element for crack initiation and then deletion of the element for the path of the crack. Despite its limitation, this method is numerically stable and has shown accurate fracture locations and values.

The experiments that were simulated in this study all predicted hard tissue failure. The experimental test data utilized in the study corresponded to different ages and gender. The Global Human Body Models Consortium (GHBMC) model was utilized in this study which is a representative of a 26 YO 50th percentile male. The GHBMC model was compared with C5-C6-C7 segments from male specimens in the centric compression, compression with posterior, anterior, and lateral eccentricity load cases. Unfortunately, none of the specimens were in the 20 YO age range (centric: 20-84 YO; posterior: 55-94 YO; anterior: 34-90 YO; low lateral: 68-79; high lateral: 66-79). Therefore, for better comparison with experimental data, two sets of mechanical properties were determined corresponding to the age of the experimental subjects. The "young" set of properties corresponded to subjects that were younger than 50 YO while the aged data corresponded to subjects that were greater than 70 YO. In general, it is understood that biological data is variable and the differences in the geometry and curvature of the specimens and the model may result in a difference in the predicted failure responses.

The constitutive models that were analyzed for the cortical bone included an asymmetric elastic-plastic model (AsymmCort) and an orthotropic elastic-plastic model (AnisoCort). For the trabecular bone, a low-density crushable foam model (AsymmTrab) and a transversely isotropic density crushable foam (AnisoTrab) model were evaluated. The GHBMC model, which utilized a symmetric model for both cortical (SymIsoCort) and trabecular (SymIsoTrab) bones, incorporated compressive properties. The AsymmCort model was able to predict both tensile and compressive response whereas the SymIsoCort model only predicted the compressive response. On the other hand, the AnisoCort model predicted both longitudinal and transverse response for compression loading. The AnisoCort model was also able to predict the ultimate shear value whereas the other models over-predicted the shear strength of the material.

For the trabecular bone model, the SymIsoTrab model was based on a symmetric isotropic elastic-plastic model and therefore did not predict the atypical foam stress-strain curve consisting of the plateau and densification region. The AnisoTrab model was able to predict the compression response in the longitudinal and transverse directions. This model also predicted the tensile and shear response and was able to predict the ultimate tensile stress and strain. The AsymmTrab model on the other hand was able to predict the longitudinal compressive and the tensile responses. This model, however, did not allow definition of shear properties and therefore over-predicted the shear values.

For the centric compression simulation, five configurations of the constitutive models for the trabecular and cortical bones (SymIsoCort_SymIsoTrab, AnisoCort_AsymmTrab, AnisoCort_AnisoTrab, AsymmCort_AsymmTrab, AsymmCort_AnisoTrab) were evaluated. The SymIsoCort_SymIsoTrab model was able to predict the average failure displacement of the specimens but over-predicted the failure force. In general, all the model configurations with young mechanical properties were able to predict the young failure values. With aged mechanical properties, all the models over-predicted the aged failure forces but predicted the aged failure displacement well. In terms of fracture patterns, all the models predicted dominant fracture in the vertebral body, which agreed with the experimental results. The SymIsoCort_SymIsoTrab and AnisoCort_AnisoTrab models only predicted fracture in the vertebral body whereas all other model configurations for the young model predicted fracture initiating at the articular pillar, towards the pedicle and then the posterior region of the vertebral body. For the aged models, fracture initiated at the anterior region of the vertebral body for models with the AsymmCort constitutive model whereas fracture initiated at the sides of the vertebral body when both the cortical bone and trabecular bone were anisotropic (AnisoCort_AnisoTrab) and at the articular pillars in the AnisoCort_AsymmTrab model. The fracture location of the AnisoCort_AnisoTrab model was in better agreement with the experimental fracture locations compared to the GHBMC model as this model was able to predict fractures in other locations as well other than the vertebral body, which was also seen in majority of the experimental samples (88%). The AnisoCort_AnisoTrab was selected out of the other model configurations as it agreed well in both failure values and location. Disc failure was

also seen in this model, agreeing with the experimental results but the important finding was that failure of the disc was due to hard tissue failure that compromised the soft tissue structures later in time. This highlights the importance of simulation studies to provide additional insight on the failure initiation and progression.

The following eccentricity cases utilized the identified AnisoCort_AnisoTrab model. For the posterior eccentricity case, as there was only one data point for a C57 segment specimen (aged male) with a failure force and moment of 3.54 kN and 58.75 Nm, an aged model was utilized. However, since it was only one data point, the results were also compared with the average of all specimens which had a slightly lower failure force (3.47 kN) and moment (47.80 Nm). In general, the SymIsoCort_SymIsoTrab over-predicted the failure moment (average and individual aged male C57 sample), whereas the aged AnisoCort_AnisoTrab model was able to predict both failure force and moment (average and individual aged male C57 sample), falling within the one standard deviation range of the average experimental failure vales. In terms of fracture locations, the SymIsoCort_SymIsoTrab model was only predicted fracture in the spinous process whereas the AnisoCort_AnisoTrab predicted fracture initiating in the articular pillar, towards the lamina and then the spinous process, which agreed better with experimental results as majority of the samples (88%), showed fracture in other locations as well other than the spinous process. It was noted that some experimental specimens experienced failure in the soft tissue and vertebral body. This could be due to the differences in the geometry, the curvature and the location of the load vector. Apart from that, by analyzing the high-speed video, it seemed that the specimens were already in extension prior to loading due to the weight of the experimental setup.

For the anterior eccentricity case, an aged model was utilized to compare with the aged male C57 segment. Again, as there was only one data point relevant to a C57 male specimen, the failure values (0.49 kN and 37.40 Nm)were also compared with the average values which had a higher overall failure force (0.77 kN) and lower overall failure moment (21.40Nm) . The SymIsoCort_SymIsoTrab and AnisoCort_AnisoTrab models over-predicted the individual aged male C57 failure force and average failure forces and were within the SD of the average failure moment. Similarly, from the high-speed video, the specimen was already in flexion prior to loading due to the weight of the experimental test setup, which may have led to a lower failure force. Besides that, a high percentage of the test samples were from female subjects, which had geometry differences compared to male specimens. In terms of fracture patterns, 63% of the experimental specimens showed no hard tissue fractures whereas the remaining showed fracture in the vertebral body. No hard tissue failure was seen in the SymIsoCort_SymIsoTrab model, whereas fracture was seen in the vertebral body and pedicles in the AnisoCort_AnisoTrab model. Experimentally, failures were identified in the soft tissue and only a few specimens exhibited failure in the vertebral body. These differences in fracture pattern might be due to the load vector location sensitivity as well as the pre-flexed state that the specimens in the experiment were in.

For the low lateral eccentricity case, an aged AnisoCort_AnisoTrab model was utilized as the only C57 segment was from an aged female specimen. The SymIsoCort_SymIsoTrab model

over-predicted the average failure force (similar to the failure force of the one aged C57 female sample) whereas the AnisoCort_AnisoTrab model was able to predict both the average experimental failure and moment. The over-prediction in force by the SymIsoCort_SymIsoTrab model could be due to the fact some transverse failure in certain regions occurred in the AnisoCort_AnisoTrab model in which the SymIsoCort_SymIsoTrab model would not predict. In terms of fracture location, similar to the experiments, the SymIsoCort_SymIsoTrab model predicted fracture in the vertebral body, lamina, and pedicles whereas the AnisoCort_AnisoTrab model predicted additional fractures in the articular pillar and spinous process. In comparison to the experimental test, majority of the fracture was in the vertebral body with a few specimens showing fractures in the articular pillar and lamina as well. In the high lateral eccentricity case, the experimental C57 segment was from a male specimen with undefined age, however the failure force of this sample was similar to the average failure force and therefore, the results in this study were compared with the average experimental results. The SymIsoCort_SymIsoTrab model predicted average failure values in better agreement than the AnisoCort_AnisoTrab model, which predicted values too low. This could be due to the variability in experimental subjects such as geometry, age, segment levels, and curvature. Facet capsular ligament and disc failure were identified in both finite element models agreeing with experimental data, but the hard tissue failure predicted that was not seen in the experiment could be due to the actual amount of eccentricity utilized in the experiment.

For the mesh refinement study, the medium and fine mesh computational models predicted failure forces that were approximately 9% lower than the original mesh failure force. The medium mesh model predicted similar failure displacement to the original mesh but the finer mesh model predicted a failure displacement that was 14% higher than the value predicted by the original mesh computational model. The fracture initiation location changed from the sides of the vertebral body to the articular pillars with mesh refinement. The differences were expected as the element erosion method is known to be dependent on the finite element size. Decreasing the element size without modifying the failure criterion (failure strain) for element deletion would result in lower failure force values.

In conclusion, the AnisoCort_AnisoTrab model was important in predicting fracture locations in better agreement with experimental results than the SymIsoCort_SymIsoTrab model as well as failure values, especially in the posterior eccentricity case in which the transverse failure values allowed accurate prediction of the failure moment. Including age effects on the mechanical properties, corresponding to the subject age, was identified as important. This study also showed the importance of simulation studies in terms of determining the fracture initiation location and propagation of failure that would be challenging to measure in a dynamic experiment. One of the limitations in this study was that the material models did not consider strain rate and damage definitions and were also missing strain rate, gender and level effects. Further research is required to consider the significance of these effects. In addition, another limitation in this study was the lack of human cervical spine experimental data to characterize especially the trabecular

bone properties as well as data for comparison of the compression results. One of the key achievements in this study was utilizing published material properties from experiment studies on bone in the constitutive models, corresponding to the subject age, and achieving comparable results in the compression simulations. Future research will investigate hard tissue fracture at the full neck level.

Letter of Copyright Permission

<div align="center">

SPRINGER NATURE LICENSE
TERMS AND CONDITIONS

</div>

<div align="right">May 18, 2018</div>

This Agreement between University of Waterloo -- Fiona Khor ("You") and Springer Nature ("Springer Nature") consists of your license details and the terms and conditions provided by Springer Nature and Copyright Clearance Center.

License Number	4351930176585
License date	May 18, 2018
Licensed Content Publisher	Springer Nature
Licensed Content Publication	European Journal of Orthopaedic Surgery & Traumatology
Licensed Content Title	Classification of lower cervical spine injuries
Licensed Content Author	C. Argenson, F. de Peretti, A. Ghabris et al
Licensed Content Date	Jan 1, 1997
Licensed Content Volume	7
Licensed Content Issue	4
Type of Use	Thesis/Dissertation
Requestor type	academic/university or research institute
Format	print and electronic
Portion	figures/tables/illustrations
Number of figures/tables/illustrations	2
Will you be translating?	no
Circulation/distribution	<501
Author of this Springer Nature content	no
Title	Computational Modeling of Hard Tissue Response and Fracture in the Lower Cervical Spine under Compression Including Age Effects
Instructor name	Dr. Duane Cronin
Institution name	University of Waterloo
Expected presentation date	Aug 2018
Portions	Figure 2, Figure 4
Requestor Location	University of Waterloo 200 University Ave W
	Waterloo, ON N2L3G1 Canada Attn: Fiona Khor

Billing Type	Invoice
Billing Address	University of Waterloo
	200 University Ave W
	Waterloo, ON N2L3G1
	Canada
	Attn: Fiona Khor
Total	**0.00 USD**

OXFORD UNIVERSITY PRESS LICENSE
TERMS AND CONDITIONS

May 18, 2018

This Agreement between University of Waterloo -- Fiona Khor ("You") and Oxford University Press ("Oxford University Press") consists of your license details and the terms and conditions provided by Oxford University Press and Copyright Clearance Center.

License Number	4351921482543
License date	May 18, 2018
Licensed Content Publisher	Oxford University Press
Licensed Content Publication	Neurosurgery
Licensed Content Title	Subaxial Cervical Spine Injury Classification Systems
Licensed Content Author	Aarabi, Bizhan; Walters, Beverly C.
Licensed Content Date	Mar 1, 2013
Type of Use	Thesis/Dissertation
Institution name	
Title of your work	Computational Modeling of Hard Tissue Response and Fracture in the Lower Cervical Spine under Compression Including Age Effects
Publisher of your work	University of Waterloo
Expected publication date	Aug 2018
Permissions cost	0.00 USD
Value added tax	0.00 USD
Total	**0.00 USD**
Title	Computational Modeling of Hard Tissue Response and Fracture in the Lower Cervical Spine under Compression Including Age Effects
Instructor name	Dr. Duane Cronin
Institution name	University of Waterloo
Expected presentation date	Aug 2018
Portions	Figure 3
Requestor Location	University of Waterloo 200 University Ave W

Waterloo, ON N2L3G1
Canada
Attn: Fiona Khor

Publisher Tax ID	GB125506730
Billing Type	Invoice
Billing Address	University of Waterloo 200 University Ave W
	Waterloo, ON N2L3G1 Canada Attn: Fiona Khor
Total	**0.00 USD**
Terms and Conditions	

ELSEVIER LICENSE
TERMS AND CONDITIONS

May 18, 2018

This Agreement between University of Waterloo -- Fiona Khor ("You") and Elsevier ("Elsevier") consists of your license details and the terms and conditions provided by Elsevier and Copyright Clearance Center.

License Number	4351921456444
License date	May 18, 2018
Licensed Content Publisher	Elsevier
Licensed Content Publication	Journal of the Mechanical Behavior of Biomedical Materials
Licensed Content Title	On the effect of marrow in the mechanical behavior and crush response of trabecular bone
Licensed Content Author	J. Halgrin,F. Chaari,É. Markiewicz
Licensed Content Date	Jan 1, 2012
Licensed Content Volume	5
Licensed Content Issue	1
Licensed Content Pages	7
Start Page	231
End Page	237
Type of Use	reuse in a thesis/dissertation
Intended publisher of new work	other
Portion	figures/tables/illustrations
Number of figures/tables/illustrations	1
Format	both print and electronic
Are you the author of this Elsevier article?	No
Will you be translating?	No
Original figure numbers	Figure 2
Title of your thesis/dissertation	Computational Modeling of Hard Tissue Response and Fracture in the Lower Cervical Spine under Compression Including Age Effects
Publisher of new work	University of Waterloo
Author of new work	Dr. Duane Cronin
Expected completion date	Aug 2018
Estimated size (number of pages)	1
Requestor Location	University of Waterloo 200 University Ave W

136

Waterloo, ON N2L3G1
Canada
Attn: Fiona Khor

Publisher Tax ID   GB 494 6272 12

Total   **0.00 USD**

Terms and Conditions

JOHN WILEY AND SONS LICENSE
TERMS AND CONDITIONS

May 18, 2018

This Agreement between University of Waterloo -- Fiona Khor ("You") and John Wiley and Sons ("John Wiley and Sons") consists of your license details and the terms and conditions provided by John Wiley and Sons and Copyright Clearance Center.

License Number	4351921420283
License date	May 18, 2018
Licensed Content Publisher	John Wiley and Sons
Licensed Content Publication	Journal of Orthopaedic Research
Licensed Content Title	Systematic and random errors in compression testing of trabecular bone
Licensed Content Author	Tony M. Keaveny, Tania P. Pinilla, R. Paul Crawford, et al
Licensed Content Date	Feb 18, 2005
Licensed Content Volume	15
Licensed Content Issue	1
Licensed Content Pages	10
Type of Use	Dissertation/Thesis
Requestor type	University/Academic
Format	Print and electronic
Portion	Figure/table
Number of figures/tables	1
Original Wiley figure/table number(s)	Figure 1
Will you be translating?	No
Title of your thesis / dissertation	Computational Modeling of Hard Tissue Response and Fracture in the Lower Cervical Spine under Compression Including Age Effects
Expected completion date	Aug 2018
Expected size (number of pages)	1
Requestor Location	University of Waterloo 200 University Ave W
	Waterloo, ON N2L3G1 Canada Attn: Fiona Khor
Publisher Tax ID	EU826007151
Total	**0.00 USD**

ELSEVIER LICENSE
TERMS AND CONDITIONS

This Agreement between University of Waterloo -- Fiona Khor ("You") and Elsevier ("Elsevier") consists of your license details and the terms and conditions provided by Elsevier and Copyright Clearance Center.

License Number	4351921384000
License date	May 18, 2018
Licensed Content Publisher	Elsevier
Licensed Content Publication	Seminars in Spine Surgery
Licensed Content Title	Fractures of the C1 and C2 Vertebrae
Licensed Content Author	S. Babak Kalantar
Licensed Content Date	Mar 1, 2013
Licensed Content Volume	25
Licensed Content Issue	1
Licensed Content Pages	13
Start Page	23
End Page	35
Type of Use	reuse in a thesis/dissertation
Intended publisher of new work	other
Portion	figures/tables/illustrations
Number of figures/tables/illustrations	2
Format	both print and electronic
Are you the author of this Elsevier article?	No
Will you be translating?	No
Original figure numbers	Figure 6 (A) and (B)
Title of your thesis/dissertation	Computational Modeling of Hard Tissue Response and Fracture in the Lower Cervical Spine under Compression Including Age Effects
Publisher of new work	University of Waterloo
Author of new work	Dr. Duane Cronin
Expected completion date	Aug 2018
Estimated size (number of pages)	1
Requestor Location	University of Waterloo 200 University Ave W
	Waterloo, ON N2L3G1

Canada
Attn: Fiona Khor

Publisher Tax ID   GB 494 6272 12

Total   **0.00 CAD**

ELSEVIER LICENSE
TERMS AND CONDITIONS

This Agreement between University of Waterloo -- Fiona Khor ("You") and Elsevier ("Elsevier") consists of your license details and the terms and conditions provided by Elsevier and Copyright Clearance Center.

License Number	4351921292403
License date	May 18, 2018
Licensed Content Publisher	Elsevier
Licensed Content Publication	Journal of Biomechanics
Licensed Content Title	A continuous wave technique for the measurement of the elastic properties of cortical bone
Licensed Content Author	R.B. Ashman,S.C. Cowin,W.C. Van Buskirk,J.C. Rice
Licensed Content Date	Jan 1, 1984
Licensed Content Volume	17
Licensed Content Issue	5
Licensed Content Pages	13
Start Page	349
End Page	361
Type of Use	reuse in a thesis/dissertation
Intended publisher of new work	other
Portion	figures/tables/illustrations
Number of figures/tables/illustrations	1
Format	both print and electronic
Are you the author of this Elsevier article?	No
Will you be translating?	No
Original figure numbers	Figure 2(a) and (b)
Title of your thesis/dissertation	Computational Modeling of Hard Tissue Response and Fracture in the Lower Cervical Spine under Compression Including Age Effects
Publisher of new work	University of Waterloo
Author of new work	Dr. Duane Cronin
Expected completion date	Aug 2018
Estimated size (number of pages)	1
Requestor Location	University of Waterloo 200 University Ave W

Waterloo, ON N2L3G1
Canada
Attn: Fiona Khor

Publisher Tax ID   GB 494 6272 12

Total   **0.00 CAD**

<div align="center">

ELSEVIER LICENSE
TERMS AND CONDITIONS

</div>

This Agreement between University of Waterloo -- Fiona Khor ("You") and Elsevier ("Elsevier") consists of your license details and the terms and conditions provided by Elsevier and Copyright Clearance Center.

License Number	4351941128333
License date	May 18, 2018
Licensed Content Publisher	Elsevier
Licensed Content Publication	Journal of Biomechanics
Licensed Content Title	The mechanical behaviour of cancellous bone
Licensed Content Author	L.J. Gibson
Licensed Content Date	Jan 1, 1985
Licensed Content Volume	18
Licensed Content Issue	5
Licensed Content Pages	12
Start Page	317
End Page	328
Type of Use	reuse in a thesis/dissertation
Intended publisher of new work	other
Portion	figures/tables/illustrations
Number of figures/tables/illustrations	1
Format	both print and electronic
Are you the author of this Elsevier article?	No
Will you be translating?	No
Original figure numbers	Figure 1
Title of your thesis/dissertation	Computational Modeling of Hard Tissue Response and Fracture in the Lower Cervical Spine under Compression Including Age Effects
Publisher of new work	University of Waterloo
Author of new work	Dr. Duane Cronin
Expected completion date	Aug 2018
Estimated size (number of pages)	1
Requestor Location	University of Waterloo 200 University Ave W
	Waterloo, ON N2L3G1

<div align="center">

143

</div>

Canada
Attn: Fiona Khor

Publisher Tax ID   GB 494 6272 12

Total   **0.00 USD**

Terms and Conditions

145

Waterloo, ON N2L3G1
Canada
Attn: Fiona Khor

Publisher Tax ID	GB125506730
Billing Type	Invoice
Billing Address	University of Waterloo 200 University Ave W

Waterloo, ON N2L3G1
Canada
Attn: Fiona Khor

Total	**0.00 USD**

Terms and Conditions

References

Aarabi, B., Walters, B. C., Dhall, S. S., Gelb, D. E., Hurlbert, R. J., Rozzelle, C. J., et al. (2013). Subaxial cervical spine injury classification systems. *Neurosurgery, 72*(3)

Abdel-Wahab, A. A., Alam, K., & Silverschmidt, V. V. (2011). Analysis of anisotropic viscoelastoplastic properties of cortical bone tissues. *Journal of the Mechanical Behavior of Biomedical Materials, 4*, 807-820.

Abdel-Wahab, A. A., Maligno A.R., & Silberschmidt, V. V. (2012). Micro-scale modelling of bovine cortical bone fracture: Analysis of crack propagation and microstructure using X-FEM. *Computational Materials Science, 52*, 128.

Acaroglu, E. R., Iatridis, J. C., Setton, L. A., Mow, V. C., & Weidenbaum, M. (1995). Degeneration and aging affect the tensile behavior of human lumbar anulus fibrosus.. *Spine, 20*(24), 2690.

Adams, M. A., McNally, D. S., & Dolan, P. (1996). 'Stress' distributions inside invertebral discs the effects of age and degeneration. *Journal of Bone & Joint Surgery, 78*

Ali, A. A., Cristofolini, L., Schileo, E., Hu, H., Taddei, F., K., R.H., R., P.J., et al. (2014). Specimen-specific modeling of hip fracture pattern and repair. *Journal of Biomechanics, 47*, 536.

Allen, B. L., Jr., Ferguson, R. L., Lehmann, T. R., & O'Brien, R. P. (1982). A mechanistic classification of closed, indirect fractures and dislocations of the lower cervical spine. *Spine, 7*(1), 1.

Amling, M., Posl, M., Ritzel, H., Hahn, M., Vogel, M., Wening, V. J., et al. (1996). Architecture and distribution of cancellous bone yield vertebral fracture clues : A histomorphometric analysis of the complete spinal column from 40 autopsy specimens . *Archives of Orthopaedic and Trauma Surgery, 115*, 262-269.

Antonio, T. S., Ciaccia, M., Muller-Karger, C., & Casanova, E. (2012). Orientation of orthotropic material properties in a femur FE model: A method based on the principal stresses directions. *Medical Engineering & Physics, 34*, 914-919.

Argenson, C., de Peretti, F., Ghabris, A., Lovet, E. J., & Hovorka, I. (1997). Classification of lower cervical spine injuries. *European Journal of Orthopaedic Surgery & Traumatology, 7*, 215-229.

Ariza, O., Gilchrist, S., Widmer, R. P., Guy, P., Ferguson, S. J., Cripton, P. A., et al. (2015). Comparison of explicit finite element and mechanical simulation of the proximal femur during dynamic drop-tower testing. *Journal of Biomechanics, 48*, 224-232.

Arnold, J. S. (1970). External and trabecular morphologic changes in lumbar vertebrae in aging. In G. D. Whedon, & J. R. Cameron (Eds.), *Progress in methods of bone mineral measurement* () U.S. Department of Health, Education and Welfare.

Asgharpour, Z., Zioupos, P., Graw, M., & Peldschus, S. (2014). Development of a strain rate dependent material model of human cortical bone for computer-aided reconstruction of injury mechanisms. *Forensic Science International, 236*, 109-116.

Ashman, R. B., Cowin, S., Van Buskirk, W. C., & Rice, J. C. (1984). A continuous wave technique for the measurement of the elastic properties of cortical bone. *Journal of Biomechanics, 17*(5), 349.

Ashman, R. B., & Rho, J. Y. (1988). Elastic modulus of trabecular bone material. *Journal of Biomechanics, 21*, 177-188.

Ashman, R. B., Rho, J. Y., & Turner, C. H. (1989). Anatomical variation of orthotropic elastic moduli of the proximal human tibia. *Journal of Biomechanics, 22*(8-9), 895-900.

Augat, P., & Schorlemmer, S. (2006). The role of cortical bone and its microstructure in bone strength. *Age and Ageing, 35*(Supplementary 2), ii27.

Augat, P., Link, T., Lang, T. F., Lin, J. C., Majumdar, S., & Genant, H. K. (1998). Anisotropy of the elastic modulus of trabecular bone specimens from different anatomical locations. *Medical Engineering & Physics, 20*(124), 131.

Babcock, J. L. (1976). Cervical spine injuries: Diagnosis and classfication. *Archives of Surgery, 111*, 646.

Barker, J. B., Cronin, D. S., & Nightingale, R. W. (2017). Lower cervical spine motion segment computational model validation: Kinematic and kinetic response for quasi-static and dynamic loading. *Journal of Biomechanical Engineering, 139*(6)

Bayraktar, H. H., Morgan, E. F., Niebur, G. L., Morris, G. E., Wong, E. K., & Keaveny, T. M. (2004). Comparison of the elastic and yield properties of human femoral trabecular and cortical bone tissue. *Journal of Biomechanics, 37*(1), 27.

Bouxsein, M. L., Melton, L. J., III, Riggs, B. L., Muller, J., Atkinson, E. J. L., et al. (2006). Age- and sex-specific differences in the factor of risk for vertebral fracture: A population-based study using QCT*. *Journal of Bone and Mineral Research, 21*(9), 1475-1482.

Buckley, J. M., Loo, K., & Motherway, J. (2007). Comparison of quantitative computed tomography-based measures in predicting vertebral compressive strength. *Bone, 40*, 767-774.

Burr, D. B., & Akkus, O. (2013). Bone morphology and organization. In D. B. Burr, & M. R. Allen (Eds.), *Basic and applied bone biology* (1st ed., pp. 3) Academic Press.

Burstein, A. H., Reilly, D. T., & Martens, M. (1976). Aging of bone tissue: Mechanical properties*. *The Journal of Bone and Joint Surgery, 58*(1), 82-86.

Cao, K. D., Grimm, M. J., & Yang, K. H. (2001). Load sharing within a human lumbar vertebral body using the finite element method. *Spine, 26*(12), 253-260.

Carter, D. R., & Hayes, W. C. (1977). The compressive behavior of bone as a two-phase porous structure. *The Journal of Bone and Joint Surgery, 59*, 954-962.

Carter, J. W. (2002). Compressive cervical spine injury: The effect of injury mechanism on structural injury pattern and neurologic injury potential. (Doctor of Philosophy, University of Washington).

Carter, J. W., K, M., S.K., Tencer, A. F., & Ching, R. P. (2000). Canal geometry changes associated with axial compressive cervical spine fracture. *Spine, 25*(1), 46.

Carter, J. W., Ku, G. S., Nuckley, D. J., & Ching, R. P. (2002). Tolerance of the cervical spine to eccentric axial compression. *Stapp Car Crash Journal, 46*, 441-459.

Chaari, F., Markiewic, É., & Drazetic, P. (2007). Identification of the spongy bone mechanical behaviour under compression loads: Numerical simulation versus experimental results. *International Journal of Crashworthiness, 12*(3), 247.

Charlebois, M., Pretterklieber, M., & Zysset, P. K. (2010). The role of fabric in the large strain compressive behavior of human trabecular bone. *Journal of Biomechanical Engineering, 132*

Chen, Y., He, Y., & DeVivo, M. J. (2016). Changing demographics and injury profile of new traumatic spinal cord injuries in the united states, 1972-2014. *Archives of Physical Medicine and Rehabilitation, 97*, 1610-1619.

Choi, K., Kuhn, J. L., Ciarelli, M. J., & Goldstein, S. A. (1990). The elastic moduli of human subchondral, trabecular and cortical bone tissue and the size-dependency of cortical bone modulus*. *Journal of Biomechanics, 23*(11), 1103.

Cowin, S. (1985). The relationship between the elasticity tensor and the fabric tensor. *Mechanics of Materials, 4*(2), 137-147.

Cowin, S. (2001). In Cowin S. (Ed.), *Bone mechanics handbook* (2nd ed.). Boca Raton, Florida: CRC Press.

Cowin, S., & Yang, G. (1997). Averaging anisotropic elastic constant data. *Journal of Elasticity, 46*, 151-180.

Cramer, G. D., & Darby, S. A. (2014). *Clinical anatomy of the spine, spinal cord, and ANS* (3rd ed.). St Louis, MO: Elsevier Mosby.

Crawford, R. P., Cann, C. E., & Keaveny, T. M. (2003). Finite element models predict in vitro vertebral body compressive strength better than quantitative computed tomography. *Bone, 33*, 744-750.

Currey, J. D. (1984). *The mechanical adaptations of bones*. Princeton, New Jersey: Princeton University Press.

David, K. S., & Krishnan, V. (2013). Extension injuries of the cervical spine. *Seminars in Spine Surgery, 25*, 57.

Demetriades, D., Charalambides, K., Chahwan, S., Hanpeter, D., Alo, K., Velmahos, G., et al. (2000). Nonskeletal cervical spine injuries: Epidemiology and diagnostic pitfalls. *The Journal of Trauma: Injury, Infection and Clinical Care, 48*(4), 724.

Denis, F. (1983). The three column spine and its significance in the classification of acute thoracolumbar spinal injuries.. *Spine, 8*(8), 817-831.

De Wit, J. A., & Cronin, D. S. (2012). Cervical spine segment finite element model for traumatic injury prediction.. *Journal of the Mechanical Behavior of Biomedical Materials, 10*, 138-150.

Digges, K. H. (2002). Summary report of rollover crashes. *FHWA/NHTSA National Crash Analysis Center,*

Dong, X. N., Lui, Q., & Wang, X. (2013). Progressive post-yield behavior of human cortical bone in shear. *Bone, 53*, 1-5.

Ebara, S., Iatridis, J. C., Setton, L. A., Foster, R. J., Mow, V. C., & Weidenbaum, M. (1996). Tensile properties of nondegenerate human lumbar anulus fibrosus. *Spine, 21*(4), 452.

Edeiken-Monroe, B., Wagner, L. K., & Harris, J. H. J. (1986). Hyperextension dislocation of the cervical spine. *American Journal of Neuroradiology,*

El-Hennaway, H., El-Menyar, A., Al-Thani, H., Tuma, M., Parchani, A., Abdulrahman, H., et al. (2014). Epidemiology, causes and prevention of car rollover crashes with ejection. *Annals of Medical and Health Sciences Research, 4*(4), 495-502.

El-Rich, M., Arnoux, P., Wagnac, E., Brunet, C., & Aubin, C. (2009). Finite element investigation of the loading rate effect on the spinal load-sharing changes under impact conditions. *Journal of Biomechanics, 42*, 1252-1262.

Erbulut, D. U., Zafarparandeh, I., Lazoglu, I., & Ozer, A. F. (2014). Application of an asymmetric finite element model of the C2-T1 cervical spine for evaluating the role of soft tissues in stability. *Medical Engineering & Physics, 36*, 915-921.

Eswaran, S. K., Gupta, A., Adams, M. F., & Keaveny, T. M. (2006). Cortical and trabecular load sharing in the human vertebral body. *Journal of Bone and Mineral Research, 21*(2), 307.

Feerick, E. M., Liu, X., & McGarry, P. (2013). Anisotropic mode-dependent damage of cortical bone using the extended finite element method (XFEM). *Journal of the Mechanical Behavior of Biomedical Materials, 20*, 77.

Ford, C. M., & Keaveny, T. M. (1996). The dependence of shear failure properties of trabecular bone on apparent density and trabecular orientation. *Journal of Biomechanics, 29*(10), 1309-1317.

Ford, C. M., Keaveny, T. M., & Hayes, W. C. (1996). The effect of impact direction on the structural capacity of the proximal femur during falls. *Journal of Bone and Mineral Research, 11*, 377.

Forsyth, H. F. (1964). Extension injuries of the cervical spine. *Journal of Bone & Joint Surgery, 46*(8), 1792.

Foster, J. (2013). Injury mechanisms and priorities for cervical spine trauma mitigation in rollover crashes: The development and analysis of in vitro testing of axial compressive cervical spine impacts. (Masters of Science in Mechanical and Aerospace Engineering, University of Virginia).

Fyhrie, D. P., & Schaffler, M. B. (1994). Failure mechanisms in human vertebral cancellous bone. *Bone, 15*(1), 105-109.

Garcia, D., Zysset, P., Charlebois, M., & Curnier, A. (2009). A three-dimensional elastic plastic damage constitutive law for bone tissue. *Biomechanics and Modeling in Mechanobiology, ,* 149-165.

Gayzik, F. S., Moreno, D. P., Vavalle, N. A., Rhyne, A., & Stitzel, J. D. (2011). Development of the global human body models consortium MidSized male full body model. *Injury Biomechanics Research, Proceedings of the 39th International Workshop,*

Ge, L., Arul, K., Ikpeze, T., Baldwin, A., Nickels, J. L., & Mesfin, A. (2018). Traumatic and nontraumatic spinal cord injuries. *World Neurosurgery, 111*, e142.

Giambini, H., Qin, X., Dragomir-Daescu, D., An, K., & Nassr, A. (2016). Specimen-specific vertebral fracture modeling: A feasibility study using the extended finite element method. *Medical & Biological Engineering & Computing, 54*(4), 583-593.

Gibson, L. J. (1985). The mechanical behavior of cancellous bone. *Journal of Biomechanics, 18*(5), 317-328.

Gibson, L. J. (2005). Biomechanics of cellular solids. *Journal of Biomechanics, 38*, 377-399.

Gibson, L. J., & Ashby, M. F. (1988). *Cellular solids: Structure & properties* (1st ed.). Oxford, England: Pergamon Press.

Gibson, L. J., & Ashby, M. F. (1997). *Cellular solids: Structure & properties* (2nd ed.). Cambridge: Cambridge University Press.

Go, B. K., DeVivo, M. J., & Richards, J. S. (1995). The epidemiology of spinal cord injury. In S. L. Stover, J. A. DeLisa & G. G. Whiteneck (Eds.), *Spinal cord injury* (pp. 21-55). Gaithersberg, Maryland: Aspen Publishers.

Goldstein, S. A., Wilson, D. L., Sonstegard, D. A., & Matthews, L. S. (1983). The mechanical properties of human tibial trabecular bone as A function of metaphyseal location. *Journal of Biomechanics, 16*(12), 965.

Gray, H. *Anatomy of the human body.* Retrieved January, 2018, from http://www.bartleby.com/107/

Grote, H. J., Amling, M., Vogel, M., Hahn, M., Posl, M., & Delling, G. (1995). Intervertebral variation in trabecular microarchitecture throughout the normal spine in relation to age. *Bone, 16*(3), 301-308.

Halgrin, J., Chaari, F., & Markiewic, É. (2012). On the effect of marrow in the mechanical behavior and crush response of trabecular bone. *Journal of the Mechanical Behavior of Biomedical Materials, 5*, 231-237.

Hambli, R., Bettamer, A., & Allaoui, S. (2012). Finite element prediction of proximal femur fracture pattern based on orthotropic behaviour law coupled to quasi-brittle damage. *Medical Engineering & Physics, 34*, 202.

Hambli, R., & Thurner, P. J. (2013). Finite element prediction with experimental validation of damage distribution in single trabeculae during three-point bending tests. *Journal of the Mechanical Behavior of Biomedical Materials, 27*, 94.

Hansen, U., Zioupos, P., Simpson, R., Currey, J. D., & Hynd, D. (2008). The effect of strain rate on the mechanical properties of human cortical bone. *Journal of Biomechanical Engineering, 130*

Harrison, N. M., McDonnell, P., Mullins, L., Wilson, N., O'Mahoney, D., & McHugh, P. (2013). Failure modelling of trabecular bone using a non-linear combined damage and fracture voxel finite element approach. *Biomechanics and Modeling in Mechanobiology, 12*, 225.

Hasler, R. M., Exadaktylos, A. K., Bouamra, O., Benneker, L. M., Sieber, R., Zimmermann, H., et al. (2012). Epidemiology and predictors of cervical spine injury in adult major trauma patients: A multicenter cohort study. *Journal of Trauma and Acute Care Surgery, 72*(4), 975.

Hayes, W. C., & Carter, D. R. (1976). Postyield behavior of subchondral trabecular bone. *Journal of Biomedical Materials Research Symposium, 7*, 537-544.

Hayes, W. C., & Carter, D. R. (1979). Biomechanics of bone. In D. J. Simmons, & A. S. Kunin (Eds.), *Skeletal research: An experimental approach* (pp. 263). New York: Academic Press.

Hernandez, C. J. (2016). Cancellous bone. In W. Murphy (Ed.), *Handbook of biomaterial properties* (pp. 15) Springer Science+Business Media.

Hoffler, C. E., Moore, K. E., Kozloff, K., Zysset, P. K., Brown, M. B., & Goldstein, S. A. (2000). Heterogeneity of bone lamellar-level elastic moduli. *Bone, 26*(6)

Hoffmeister, B. K., Smith, S. R., Handley, S. M., & Rho, J. Y. (2000). Anisotropy of young's modulus of human tibial cortical bone. *Medical and Biological Engineering and Computing, 38*(3), 333.

Holzapfel, G. A., Schulze-Bauer, C. A. J., Feigl, G., & Regitnig, P. (2005). Single lamellar mechanics of the human lumbar anulus fibrosus. *Biomechanics and Modeling in Mechanobiology, 3*, 125.

Hong, J., Cha, H., Park, Y., Lee, S., Khang, G., & Kim, Y. (2007). Elastic moduli and poisson's ratios of microscopic human femoral trabeculae. In T. Jarm, P. Kramar & A. Županič (Eds.), *Medicon 2007, IFMBE proceedings 16* (pp. 274-277) Springer-Verlag Berlin Heidelberg.

Hong-Wan, N., & Teo, E. C. (2001). Nonlinear Finite=Element analysis of the lower cervical spine (C4-C6) under axial loading. *Journal of Spinal Disorders, 14*(3), 201-210.

Hulme, P. A., Boyd, S. K., & Ferguson, S. J. (2007). Regional variation in vertebral bone morphology and its contribution to vertebral fracture strength. *Bone, 41*, 946-957.

Iatridis, J. C., Setton, L. A., Weidenbaum, M., & Mow, V. C. (1997). Alterations in the mechanical behavior of the human lumbar nucleus pulposus with degeneration and aging. *Journal of Orthopaedic Research, 15*, 318.

Iatridis, J. C., Weidenbaum, M., Setton, L. A., & Mow, V. C. (1996). Is the nucleus pulposus a solid or a fluid? mechanical behaviors of the nucleus pulposus of the human intervertebral disc. *Spine, 21*(10), 1174.

Idkaidek, A., & Jasiuk, I. (2016). Cortical bone fracture analysis using XFEM- case study. *International Journal for Numerical Methods in Biomedical Engineering,*

Ioannidis, G., Papaioannou, A., Hopman, W. M., Akhtar-Danesh, D., Anastassiades, T., Pickard, L., et al. (2009). Relation between fractures and mortality: Results from the canadian multicentre osteoporosis study.. *Canadian Medical Association Journal, 181*(5), 265.

Iwamoto, M., Miki, K., & Tanaka, E. (2005). Ankle skeletal injury predictions using anisotropic inelastic constitutive model of cortical bone taking into account damage evolution. *Stapp Car Crash Journal, 49*, 133-156.

Jaasma, M. J., Bayraktar, H. H., Niebur, G. L., & Keaveny, T. M. (2002). Biomechanical effects of intraspecimen variations in tissue modulus for trabecular bone. *Journal of Biomechanics, 35*, 237.

Jones, A. C., & Wilcox, R. K. (2008). Finite element analysis of the spine: Towards a framework of verification, validation and sensitivity analysis. *Medical Engineering & Physics, 30*, 1287-1304.

Kabel, J., van Rietbergen, B., Odgaard, A., & Huiskes, R. (1999). Constitutive relationships of fabric, density, and elastic properties in cancellous bone architecture. *Bone, 25*(4), 481-486.

Kalantar, S. B. (2013). Fractures of the C1 and C2 vertebrae. *Seminars in Spine Surgery, 25*(1), 23.

Kallemeyen, N., Gandhi, A., Kode, S., Shivanna, K., Smucker, J., & Grosland, N. (2010). Validation of a C2–C7 cervical spine finite element model using specimen-specific flexibility data. *Medical Engineering & Physics, 32*(5), 482-489.

Kanis, J. A., Melton, L. J., Christiansen, C., Johnston, C. C., & Khaltaev, N. (1994). Perspective: The diagnosis of osteoporosis. *Journal of Bone and Mineral Research, 9*(8)

Kazarian, L. (1981). Injuries to the human cervical column: Biomechanics and injury classification. *Exercise & Sport Sciences Reviews, 9*(1), 297.

Keaveny, T. M., & Hayes, W. C. (1993). A 20-year old perspective on the mechanical properties of trabecular bone. *Journal of Biomechanical Engineering, 115*(4B), 534.

Keaveny, T. M., Morgan, E. F., Niebur, G. L., & Yeh, O. C. (2001). Biomechanics of trabecular bone. *Annual Review of Biomedical Engineering, 3*, 307-333.

Keaveny, T. M., Pinilla, T. P., Crawford, R. P., Kopperdahl, D. L., & Lou, A. (1997). Systematic and random errors in compression testing of trabecular bone . *Journal of Orthopaedic Research, 15*, 101.

Keaveny, T. M., Wachtel, E. F., Ford, C. M., & Hayes, W. C. (1994). Differences between the tensile and compressive strengths of bovine tibial trabecular bone depends on modulus. . *Journal of Biomechanics, 27*(9), 1137-1146.

Khor, F., Cronin, D. S., Watson, B., Gierczycka, D., & Malcolm, S. (2018). Importance of asymmetry and anisotropy in predicting cortical bone response and fracture using human body model femur in three-point bending and axial rotation . *Journal of the Mechanical Behavior of Biomedical Materials, In Review*

Kim, H. S., & Al-Hassani, S. T. S. (2002). A morphological model of vertebral trabecular bone. *Journal of Biomechanics, 35*(8), 1101-1114.

Klinich, K. D., Ebert, S. M., Van Ee, C. A., Flannagan, C. A. C., Prasad, M., Leed, M. P., et al. (2004). Cervical spine geometry in the automotive seated posture: Variations with age, stature and gender. *Stapp Car Crash Journal, 48*

Kopperdahl, D. L., & Keaveny, T. M. (1998). Yield strain behavior of trabecular bone. *Journal of Biomechanics, 31*, 601-608.

Kumaresan, S., Yoganandan, N., Pintar, F. A., & Maiman, D. J. (1999). Finite element modeling of the cervical spine: Role of intervertebral disc under axial and eccentric loads. *Medical Engineering & Physics, 21*, 689.

Laville, A., Laporte, S., & Skalli, W. (2009). Parametric and subject-specific finite element modelling of the lower cervical spine. Influence of geometrical parameters on the motion patterns. *Journal of Biomechanics, 42*, 1409-1415.

LeBoff, M. S., & Glowacki, J. (1999). Sex steroids, bone, and aging. In C. J. Rosen, J. Glowacki & J. P. Bilezikian (Eds.), *The aging skeleton* (pp. 159). San Diego, California, USA: Academic Press.

Li, S., Abdel-Wahab, A., & Silberschmidt, V. V. (2013). Analysis of fracture processes in cortical bone tissue. *Engineering Fracture Mechanics, (448)*

Li, S., Abdel-Wahab, A., & Silberschmidt, V. V. (2013). Analysis of fracture processes in cortical bone tissue. *Engineering Fracture Mechanics, 110*, 448-458.

Li, S., Demirci, E., & Silverschmidt, V. V. (2013). Variability and anisotropy of mechanical behavior of cortical bone in tension and compression. *Journal of the Mechanical Behavior of Biomedical Materials, 21*, 109-120.

Liebschner, M. A., Kopperdahl, D. L., Rosenberg, W. S., & Keaveny, T. M. (2003). Finite element modeleing of the human thoracolumbar spine. *Spine, 28*(6), 559-565.

Lim, T. H., & Hong, J. H. (2000). Poroelastic properties of bovine vertebral trabecular bone. *Journal of Orthopaedic Research, 18*, 671.

Lindahl, O. (1976). Mechanical properties of dried defatted spongy bone. *Acta Orthopaedica Scandinavica, 47*(1), 11-19.

Linde, F., Norgaard, P., Hvid, I., Odgaard, A., & Soballe, K. (1991). Mechanical properties of trabecular bone. dependency on strain rate. *Journal of Biomechanics, 24*(9), 803-809.

Liu, J. F., Shim, V. P. W., & Lee, P. V. S. (2013). Chapter 16: Quasi-static compressive and tensile tests on cancellous bone in human cervical spine. In B. C. Prorok, et al. (Eds.), *Mechanics of biological systems and materials, volume 5: Proceedings of the 2012 annual conference on experimental and applied mechanics* (1st ed., pp. 109) Springer.

Maiman, D. J., Sances, A., Myklebust, J. B., Larson, S. J., Houterman, C., Chilbert, M., et al. (1983). Compression injuries of the cervical spine: A biomechanical analysis. *Neurosurgery, 13*(3), 254.

Marta, K. (2010). Finite element modeleing of human lumbar spine. In D. Moratal (Ed.), *Finite element analysis* (pp. 123) InTech.

Martin, R. B., Burr, D. B., & Sharkey, N. A. (1998). *Skeletal tissue mechanics* Springer.

Mattucci, S. (2011). Strain rate dependent properties of younger human cervical spine ligaments. (Masters of Applied Science, University of Waterloo).

Mattucci, S., Speidel, J., Liu, J., Kwon, B. K., Tetzlaff, W., & Oxland, T. R. (2018). Basic biomechanics of spinal cord injury — how injuries happen in people and how animal models have informed our understanding. *Clinical Biomechanics,*

Mattucci, S. F. E., Moulton, J. A., Chandrashekar, N., & Cronin, D. S. (2012). Strain rate dependent properties of younger human cervical spine ligaments. *Journal of the Mechanical Behavior of Biomedical Materials, 10*, 216.

McCalden, R. W., McGeough, J. A., Barker, M. B., & Court-Brown, C. M. (1993). Age-related changesin the tensile properties of cortical bone: The relative importance of changes in porosity, mineralization and microstructure*. *The Journal of Bone and Joint Surgery, 75-A*(8), 1193.

McCalden, R. W., McGeough, J. A., & Court-Brown, C. M. (1997). Age-related changes in the compressive strength of cancellous bone: The relative importance of changes in density and trabecular architecture*. *The Journal of Bone and Joint Surgery, 79-A*(3), 421.

McElhaney, J. H. (1966). Dynamic response of bone and muscle tissue. *Journal of Applied Physiology, 21*(4), 1231.

McElhaney, J. H., Alem, N., & Roberts, V. (1970). A porous block model for cancellous bones. *ASME Publication, #70=WA/BHF-2*, 1.

McElhaney, J. H., Paver, J. G., McCrackin, H. J., & Maxwell, G. M. (1983). Cervical spine compression responses. *Proceedings of the 27th Stapp Car Crash Conference, SAE Paper #831615*

Melnis, A. E., & Knets, I. V. (1982). Effect of the rate of deformation on the mechanical properties of compact bone tissue. *Mechanics of Composite Materials, 18*(3), 358.

Moore, K. L., & Dalley, A. F. (1999). *Clinically oriented anatomy* (4th ed.) Lippincott Williams and Wilkins.

Moore, K. L., Dalley, A. F., & Agur, A. M. R. (2018). *Clinically oriented anatomy* (8th ed.). Philadelphia: Wolters Kluwer.

Morgan, E. F., Bayraktar, H. H., & Keaveny, T. M. (2003). Trabecular bone modulus–density relationships depend on anatomic site. *Journal of Biomechanics, 36*, 897-904.

Mosekilde, L. (1993). Vertebral structure and strength in vivo and in vitro. *Calcified Tissue International, 53*(Suppl 1), S121-S126.

Mosekilde, L., & Mosekilde, L., Danielsen, C.C. (1987). Biomechanical competence of vertebral trabecular bone in relation to ash density and age in normal individuals . *Bone, 8*, 79-85.

Mosekilde, L., Viidik, A., & Mosekilde, L. (1985). Correlation between the compressive strength of iliac and vertebral trabecular bone in normal individuals. *Bone, 6*, 291-295.

Myers, B. S., McElhaney, J. H., Richardson, W. J., Nightingale, R. W., & Doherty, B. J. (1991). The influence of end condition on human cervical spine injury mechanisms. *Proceedings of the 35th Stapp Car Crash Conference, 912915*, 391.

Myers, B. S., & Winkelstein, B. A. (1995). Epidemiology, classification, mechanism, and tolerance of human cervical spine injuries. *Critical Reviews in Biomedical Engineering, 23*(5&6), 307.

Nalla, R. K., Kinney, J. H., & Ritchie, R. O. (2003). Mechanistic fracture criteria for the failure of human cortical bone. *Nature Materials, 2*, 164.

Newell, N., Little, J. P., Christou, A., Adams, M. A., Adams, C. J., & Masouros, S. D. (2017). Biomechanics of the human intervertebral disc: A review of testing techniques and results. *Journal of the Mechanical Behavior of Biomedical Materials, 69*, 420.

Ng, H., & Teo, E. (2001). Nonlinear finite-element analysis of the lower cervical spine (C4–C6) under axial loading. *Journal of Spinal Disorders, 14*(3), 201-210.

Niebur, G. L., Feldstein, M. J., Yuen, J. C., Chen, T. J., & Keaveny, T. M. (2000). High-resolution finite element models with tissue strength asymmetry accurately predict failure of trabecular bone. *Journal of Biomechanics, 33*, 1575.

Nightingale, R. W., McElhaney, J. H., Camacho, D. L., Kleinberger, M., Winkelstein, B. A., & Myers, B. S. (1997). The dynamic responses of the cervical spine: Buckling, end conditions, and tolerance in compressive impacts. *SAE Technical Paper 973344,*

Nightingale, R. W., Sganga, J., Cutcliffe, H., & Bass, C. R. (2016). Impact responses of the cervical spine: A computational study of the effects of muscle activity, torso constraint, and pre-flexion. *Journal of Biomechanics, 49*, 558-564.

O' Connor, P. (2002). Injury to the spinal cord in motor vehicle traffic crashes. *Accident Analysis and Prevention, 34*, 477-485.

O'Connor, P. J., & Brown, D. (2006). Relative risk of spinal cord injury in road crashes involving seriously injured occupants of light passenger vehicles. *Accident Analysis and Prevention, 38*(6), 1081.

Odgaard, A., & Linde, F. (1991). The underestimation of young's modulus in compressive testing of cancellous bone specimens. *Journal of Biomechanics, 24*(8), 691.

Ohman, C., Dall' Ara, E., Baleani, M., Van Sint, J. S., & Viceconti, M. (2008). The effects of embalming using a 4 % formalin solution on the compressive mechanical properties of human cortical bone. *Clinical Biomechanics, 23*, 1294.

Öhman, C., Dall'Ara, E., Baleani, M., Van Sint Jan, S., & Viceconti, M. (2008). The effects of embalming using a 4% formalin solution on the compressive mechanical properties of human cortical bone. *Clinical Biomechanics, 23*(10), 1294-1298.

Oschia, R. S., Tencer, A. F., & Ching, R. P. (2003). Effect of loading rate on endplate and vertebral body strength in human lumbar vertebrae. *Journal of Biomechanics, 36*, 1875-1881.

Oxland, T. R. (2016). Fundamental biomechanics of the spine—What we have learned in the past 25 years and future directions. *Journal of Biomechanics, 49*, 817-832.

Panjabi, M. M., Chen, N. C., Shin, E. K., & Wang, J. (2001). The cortical shell architecture of human cervical vertebral bodies. *Spine, 26*, 2478-2484.

Pankaj, P., & Donaldson, F. E. (2012). Algorithms for a strain-based plasticity criterion for bone. *International Journal for Numerical Methods in Biomedical Engineering, 29*(1), 40-61.

Panzer, M. B. (2006). Numerical modelling of the human cervical spine in frontal impact. (Master of Applied Science, University of Waterloo).

Panzer, M. B., & Cronin, D. S. (2009). C4-C5 segment finite element model development, validation, and load-sharing investigation. *Journal of Biomechanics, 42*(4), 480.

Pickett, G. E., Campos-Benitez, M., Keller, J. L., & Duggal, N. (2006). Epidemiology of traumatic spinal cord injury in canada. *Spine, 31*(7), 799-805.

Pintar, F. A., Sances, A., Yoganandan, N., Reinartz, J., Maiman, D. J., Suh, J. K., et al. (1990). Biodynamics of the total human cadaveric cervical spine. *SAE Technical Paper 902309,*

Pintar, F. A., Yoganandan, N., Pesigan, M., Voo, L., Cusick, J. F., Maiman, D., et al. (1995). Dynamic characteristics of the human cervical spine. *Proceedings of the 39th Stapp Car Crash Conference, 95722*, 195.

Pintar, F. A., Yoganandan, N., & Voo, L. (1998). Effect of age and loading rate on human cervical spine injury threshold. *Spine, 23*(18), 1957.

Qiu, T. X., Tan, K. W., Lee, V. S., & Teo, E. C. (2006). Investigation of thoracolumbar T12–L1 burst fracture mechanism using finite element method. *Medical Engineering & Physics, 28*(7), 656-664.

Raddin, J., Cormier, J., Smyth, B., Croteau, J., & Cooper, E. (2009). Compressive neck injury and its relationship to head contact and torso motion during vehicle rollovers. *Society of Automotive Engineers,*

Reilly, D. T., & Burstein, A. H. (1975). The elastic and ultimate properties of compact bone tissue. *Journal of Biomechanics, 8*(6), 393-396.

Reilly, D. T., Burstein, A. H., & Frankel, V. H. (1974). The elastic modulus for bone. *Journal of Biomechanics, 7*, 271-275.

Rho, J. Y. (1996). An ultrasonic method for measuring the elastic properties of human tibial cortical and cancellous bone. *Ultrasonics, 34*, 777.

Rho, J. Y., Tsui, T. Y., & Pharr, G. M. (1997). Elastic properties of human cortical and trabecular lamellar bone measured by nanoindentation. *Biomaterials, 18*(20), 1325-1330.

Ritzel, H., Amling, M., Posl, M., Hahn, M., & Delling, G. (1997). The thickness of human vertebral cortical bone and its changes in aging and osteoporosis: A histomorphometric analysis of the complete spinal column from thirty-seven autopsy specimens. *Journal of Bone and Mineral Research, 12*(1), 89.

Roy, M. E., Rho, J. Y., Tsui, T. Y., Evans, N. D., & Pharr, G. M. (1999). Mechanical and morphological variation of the human lumbar vertebral cortical and trabecular bone. *Journal of Biomedical Materials Research, 44*(2), 191.

Runkle, J. C., & Pugh, J. (1975). The micromechanics of cancellous bone. *Bulletin of the Hospital for Joint Diseases, 36*, 2-10.

Saha, S., & Hayes, W. C. (1976). Tensile impact properties of human compact bone. *Journal of Biomechanics, 9*(4), 243.

Sanborn, B., Gunnarsson, C. A., Foster, M., & Weerasooriya, T. (2016). Quantitative visualization of human cortical bone mechanical response: Studies on the anisotropic compressive response and fracture behavior as a function of loading rate. *Experimental Mechanics, 56*, 81-95.

Sanyal, A., Gupta, A., Bayraktar, H. H., Kwon, R. Y., & Keaveny, T. M. (2012). Shear strength behavior of human trabecular bone. *Journal of Biomechanics, 45*, 2513-2519.

Schileo, E., Taddei, F., Schileo, E., & Viceconti, M. (41). Subject-specific finite element models implementing a maximum principal strain criterion are able to estimate failure risk and fracture location on human femurs tested in vitro. *Journal of Biomechanics, ,* 356.

Schmitz, B., Pitzen, T., Beuter, T., Steudel, W. I., & Reith, W. (2004). Regional variations in the thickness of cervical spine endplates as measured by computed tomography. *Acta Radiologica, 45*(1), 53-58.

Shan, Z., Li, S., Liu, J., Mamuti, M., Wang, C., & Zhao, F. (2015). Correlation between biomechanical properties of the annulus fibrosus and magnetic resonance imaging (MRI) findings. *European Spine Journal, 24*, 1909.

Shim, V. P. W., Yang, L. M., Liu, J. F., & Lee, V. S. (2005). Characterisation of the dynamic compressive mechanical properties of cancellous bone from the human cervical spine. *International Journal of Impact Engineering, 32*, 525.

Shore, S. W., Unnikrishnan, G. U., Hussein, A. I., & Morgan, E. F. (2013). Bone biomechanics. In B. A. Winkelstein (Ed.), *Orthopaedic biomechanics* (1st ed., pp. 3). Boca Raton, FL: CRC Press.

Silva, M. J., Wang, C., Keaveny, T. M., & Hayes, W. C. (1994). Direct and computer tomography thickness measurements of the human, lumbar vertebral shell and endplate. *Bone, 15*(4), 409-414.

Singh, A. P. *Anatomy of cervical spine.* Retrieved February, 2017, from http://boneandspine.com/anatomy-cervical-spine/

Skaggs, D. L., Weidenbaum, M., Iatridis, J. C., Ratcliffe, A., & Mow, V. C. (1994). Regional variation in tensile properties and biochemical composition of the human lumbar anulus fibrosus. *Spine, 19*(12), 1310.

Smit, T. H., Odgaard, A., & Schneider, E. (1997). Structure and function of vertebral trabecular bone. *Spine, 22*(24), 2823-2833.

Teo, E., & Ng, H. (2001). Evaluation of the role of ligaments, facets and disc nucleus in lower cervical spine under compression and sagittal moments using finite element method. *Medical Engineering & Physics, 23*, 155-164.

Tang, T., Ebacher, V., Cripton, P., Guy, P., McKay, H., & Wang, R. (2015). Shear deformation and fracture of human cortical bone.. *Bone, 71*, 25-35.

Thurman, D. J., Burnett, C. L., Beaudoin, D. E., Jeppson, L., & Sniezek, J. E. (1995). Risk factors and mechanism of occurrence in motorvehicle-related spinal cord injuries: Utah. *Proceedings of the 37th Annual Conference Association for the Advancement of Automotive Medicine,* San Antonio, Texas.

Turner, C. H., & Cowin, S. (1988). Errors induced by off-axis measurement of the elastic properties of bone. *Journal of Biomechanical Engineering, 110*(3), 213-215.

Turner, C. H., Rho, J. Y., Takano, Y., Tsui, T. Y., & Pharr, G. M. (1999). The elastic properties of trabecular and cortical bone tissues are similar: Results from two microscopic measurement techniques. *Journal of Biomechanics, 32*, 437.

Ural, A., & Vashishth, D. (2006). Cohesive finite element modeling of age-related toughness loss in human cortical bone. *Journal of Biomechanics, 39*(16), 2974.

Ural, A., Zioupos, P., Buchanan, D., & Vashishth, D. (2011). The effect of strain rate on fracture toughness of human cortical bone: A finite element study. *Journal of the Mechanical Behavior of Biomedical Materials, 4*, 1021.

Van Buskirk, W. C., & Ashman, R. B. (1981). The elastic moduli of bone. *Mechanical Properties of Bone, 45*, 131-143.

Van Toen, C., Melnyk, A. D., Street, J., Oxland, T. R., & Cripton, P. A. (2014). The effect of lateral eccentricity on failure loads, kinematics, and canal occlusions of the cervical spine in axial loading. *Journal of Biomechanics, 47*, 1164-1172.

Van Toen, C., Street, J., Oxland, T. R., & Cripton, P. A. (2012). Acoustic emission signals can discriminate between compressive bone fractures and tensile ligament injuries in the spine during dynamic loading. *Journal of Biomechanics, 45*, 1643-1649.

Van Toen, C., Street, J., Oxland, T. R., & Cripton, P. A. (2015). Cervical spine injuries and flexibilities following axial impact with lateral eccentricity. *European Spine Journal, 24*, 136-147.

Vernon-Roberts, B., & Pirie, C. J. (1973). Healing trabecular microfractures in the bodies of lumbar vertebrae. *Annals of the Rheumatic Disease, 32*(5)

White, A. A., & Panjabi, M. M. (1990). *Clinical biomechanics of the spine* (2nd ed.). Philadephia: Lippincott Company.

Whitehouse, W. J. (1974). The quantitative morphology of anisotropic trabecular bone. *Journal of Microscopy, 101*, 153-168.

Whyne, C. M., Hu, S. S., & Lotz, J. C. (2001). Parametric finite element analysis of verterbral bodies affected by tumors. *Journal of Biomechanics, 34*(10), 1317-1324.

Wigglesworth, E. C. (1991). Motor vehicle rollovers and spinal cord injury. *International Journal of Vehicle Design, 12*(5), 609-617.

Wishart, J. M., Need, A. G., Horowitz, M., Morris, H. A., & Nordin, B. E. C. (1995). Effect of age on bone density and bone turnover in men. *Clinical Endocrinology, 42*, 141-146.

Wolfram, U., Wilke, H. J., & Zysset, P. K. (2010). Valid micro finite element models of vertebral trabecular bone can be obtained using tissue properties measured with nanoindentation under wet conditions. *Journal of Biomechanics, 43*(9), 1731-1737.

World Health Organization. (2017). *Global health observatory (GHO) data.* Retrieved January, 3, 2017, from http://www.who.int/gho/mortality_burden_disease/daly_rates/text/en/

Xie, S., Wallace, R. J., Callanan, A., & Pankaj, P. (2018). From tension to compression: Asymmetric mechanical behaviour of trabecular bone's organic phase. *Annals of Biomedical Engineering, 46*(6)

Yamada, H. (1970). In Evans F. G. (Ed.), *Strength of biological materials*. Baltimore, Maryland, U.S.A.: The Williams & Wilkins Company.

Yamashita, J., Furman, B. R., Rawls, H. R., Wang, X., & Agrawat, C. M. (2001). The use of dynamic mechanical analysis to assess viscoelastic properties of human cortical bone. *Journal of Biomedical Materials Research, 58*, 47.

Yang, G., Kabel, J., Rietbergen, B. V., Odgaard, A., Huiskes, R., & Cowin, S. (1999). The anisotropic Hooke's law for cancellous bone and wood. . *Journal of Elasticity, 53*, 125-146.

Yanson, K. A., Knets, I. V., & Saulgozis, Y. Z. (1974). Physiological significance of changes in bone volume associated with deformation. *Polymer Mechanics (Translation of Mekhanika Polimerer), 4*, 695.

Yeni, Y. Y., Zinno, M. J., Yerramshetty, J. S., Zauel, R., & Fyhrie, D. P. (2011). Variability of trabecular microstructure is age-, gender-, race- and anatomic site-dependent and affects stiffness and stress distribution properties of human vertebral cancellous bone   . *Bone, 49*, 886-894.

Yoganandan, N., Sances, A. J., Maiman, D. J., Myklebust, J. B., Pech, P., & Larson, S. J. (1986). Experimental spinal injuries with vertical impact. *Spine, 11*(9), 855.

Yoganandan, N., Chirvi, S., Voo, L., Pintar, F. A., & Banerjee, A. (2017). Role of age and injury mechanism on cervical spine injury tolerance from head contact loading. *Traffic Injury Prevention,*

Yoganandan, N., Haffner, M., Maiman, D., & Nichols, H. e. a. (1989). Epidemiology and injury biomechanics of motor vehicle related trauma to the human spine. *SAE Technical Paper 892438,*

Yoganandan, N., Kumaresan, S., Voo, L., Pintar, F. A., & Larson, S. J. (1996). Finite element modeling of the C4-C6 cervical spine unit . *Medical Engineering & Physics, 18*(7), 569-574.

Yoganandan, N., Pintar, F. A., Stemper, B. D., Baisden, J. L., Aktay, R., Shender, B. S., et al. (2006). Trabecular bone density of male human cervical and lumbar vertebrae. *Bone, 36*, 336-344.

Yoganandan, N., Sances, A. J., & Pintar, F. A. (1989). Biomechanical evaluation of the axial compressive responses of the human cadaveric and manikin necks. *Journal of Biomechanical Engineering, 111*(3), 250.
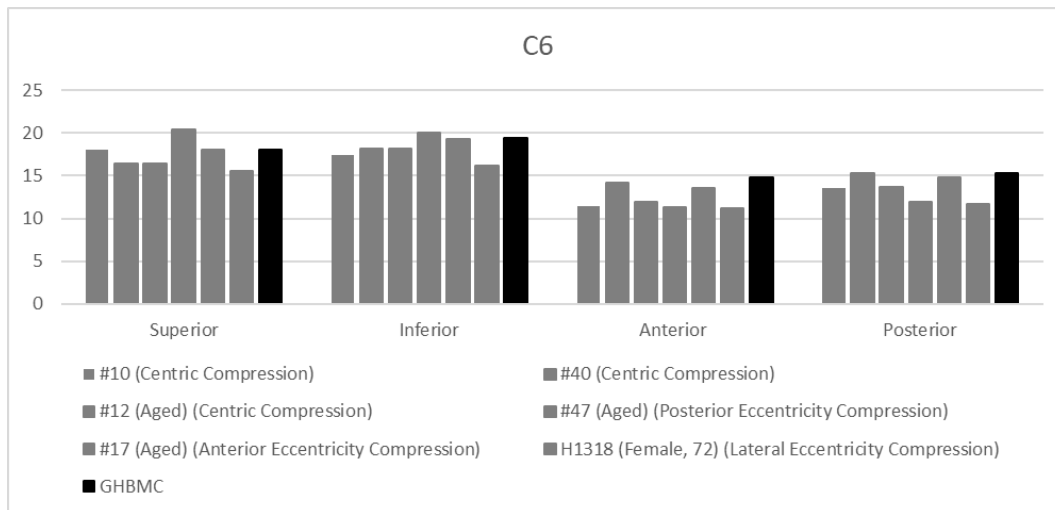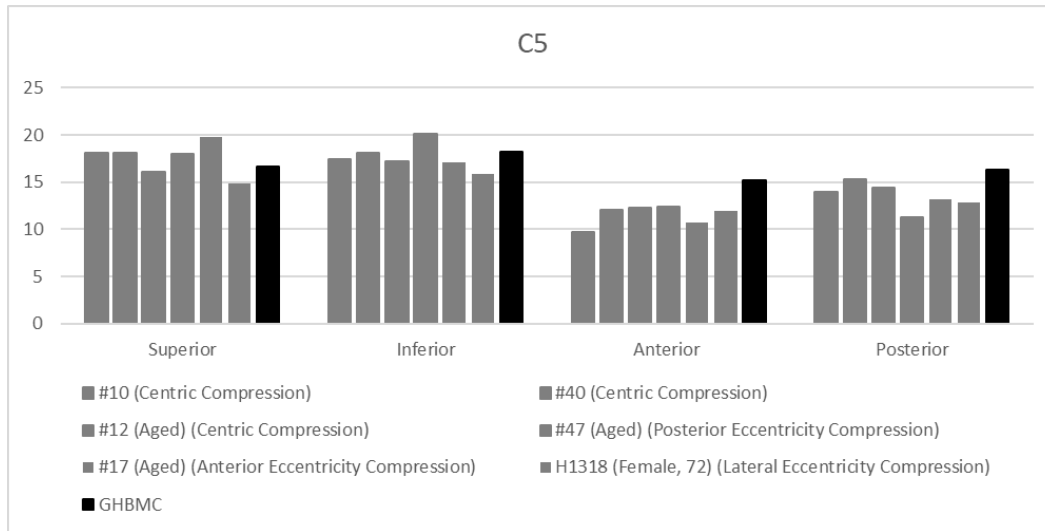
Yoon, H. S., & Katz, J. L. (1976). Ultrasonic wave propagation in human cortical bone—I. theoretical considerations for hexagonal symmetry. *Journal of Biomechanics, 9*(6), 407.

Yoon, Y. J., Yang, G., & Cowin, S. (2002). Estimation of the effective transversely isotropic elastic constants of a material from known values of the material's orthotropic elastic constants. *Biomechanics and Modeling in Mechanobiology, 1*(1), 93-93.

Zeinali, A., Hashemi, B., & Akhlaghpoor, S. (2010). Noninvasive prediction of vertebral body compressive strength using nonlinear finite element method and an image based technique. *Physica Medica, 26*, 88-97.

Zhang, L., Yang, G., Wu, L., & Yu, B. (2010). The biomechanical effects of osteoporosis vertebral augmentation with cancellous bone granules or bone cement on treated and adjacent non-treated vertebral bodies: A finite element evaluation. *Clinical Biomechanics, 25*(2), 166-172.

Zink, P. -., Samii, M., Luedemannm, W., Bellinzona, M., & Prokop, M. (1997). Accuracy of single-energy quantitative computed tomography in the assessment of bone mineral density of cervical vertebrae*. *European Radiology, 7*, 1436.

Zysset, P. K., Dall'Ara, E., Varga, P., & Pahr, D. H. (2013). Finite element analysis for prediction of bone strength. . *BoneKey Reports 2,* (386)

Zysset, P. K., Guo, E., Hoffler, C. E., Moore, K. E., & Goldstein, S. A. (1999). Elastic modulus and hardness of cortical and trabecular bone lamellae measured by nanoindentation in the human femur. *Journal of Biomechanics, 32*, 1005.
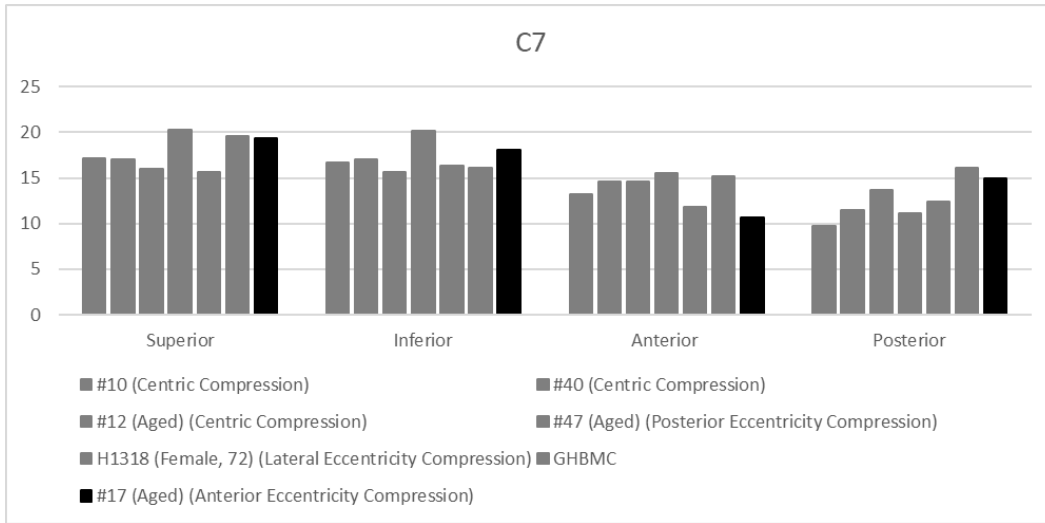
Appendix A: Geometry Measurements of Experimental Specimens and GHBMC Model

Vertebral Body Depth (mm)	Specimen / Loading Mode						
	#10 (Centric Compression)	#40 (Centric Compression)	#12 (Aged) (Centric Compression)	#47 (Aged) (Posterior Eccentricity Compression)	#17 (Aged) (Anterior Eccentricity Compression)	H1318 (Female, 72) (Lateral Eccentricity Compression)	GHBMC Model
	C5						
Superior	18.07	18.09	16.1	17.98	19.74	14.87	16.61
Inferior	17.38	18.09	17.15	20.1	17.07	15.83	18.24
Anterior	9.73	12.06	12.25	12.34	10.69	11.94	15.19
Posterior	13.9	15.25	14.35	11.28	13.14	12.84	16.34
	C6						
Superior	18.07	16.45	16.45	20.45	18.03	15.61	18.1
Inferior	17.38	18.2	18.2	20.1	19.35	16.15	19.44
Anterior	11.47	14.19	11.9	11.28	13.59	11.15	14.87
Posterior	13.55	15.25	13.65	11.99	14.77	11.75	15.37
	C7						
Superior	17.16	17.04	16.04	20.22	19.3	15.66	19.53
Inferior	16.63	17	15.69	20.13	18.06	16.34	16.13
Anterior	13.19	14.55	14.6	15.48	10.65	11.8	15.22
Posterior	9.79	11.53	13.68	11.1	14.93	12.45	16.07

Intervertebral Disc Height (mm)	Specimen / Loading Mode						
	#10 (Centric Compression)	#40 (Centric Compression)	#12 (Aged) (Centric Compression)	#47 (Aged) (Posterior Eccentricity Compression)	#17 (Aged) (Anterior Eccentricity Compression)	H1318 (Female, 72) (Lateral Eccentricity Compression)	GHBMC Model
	C56						
Anterior	6.95	7.45	7.7	3.52	6.49	6.1	5.13
Posterior	4.17	4.26	4.9	2.12	3.86	3.6	4.02
	C67						
Anterior	6.95	7.8	7	4.23	3.92	5.66	5.25
Posterior	5.56	5.32	3.5	1.76	2.3	4.32	4.32

	Specimen / Loading Mode						
	#10 (Centric Compression)	#40 (Centric Compression)	#12 (Aged) (Centric Compression)	#47 (Aged) (Posterior Eccentricity Compression)	#17 (Aged) (Anterior Eccentricity Compression)	H1318 (Female, 72) (Lateral Eccentricity Compression)	GHBMC Model
Bezier Angle (degrees)							
Superior	13.78	5.83	10	0.59	6.8	13.2	2
Inferior	11.07	0.411	5.7	7	2.4	11	2

C5

C6

C5, C6 and C7 Vertebral Body Depths
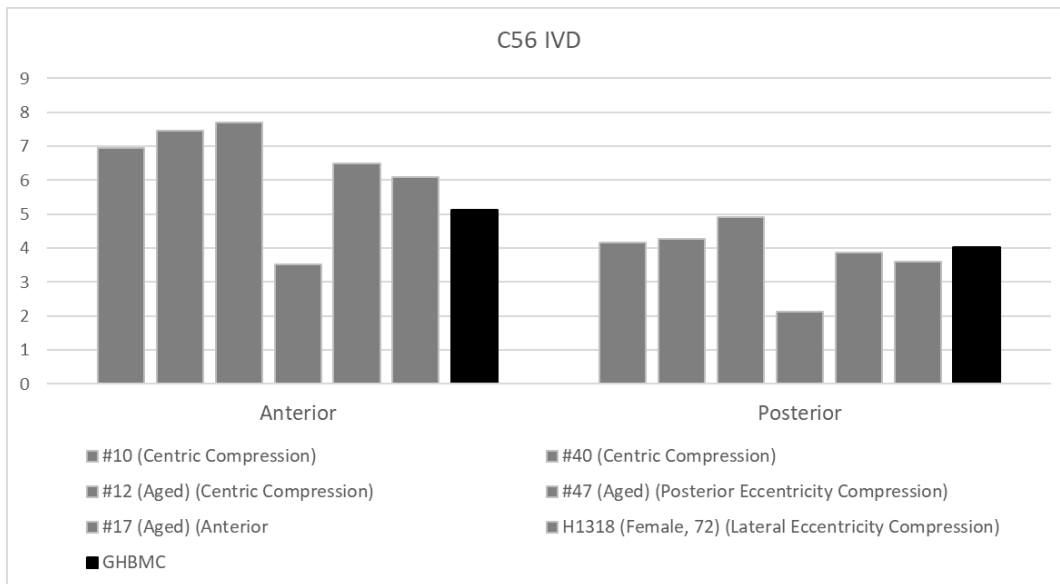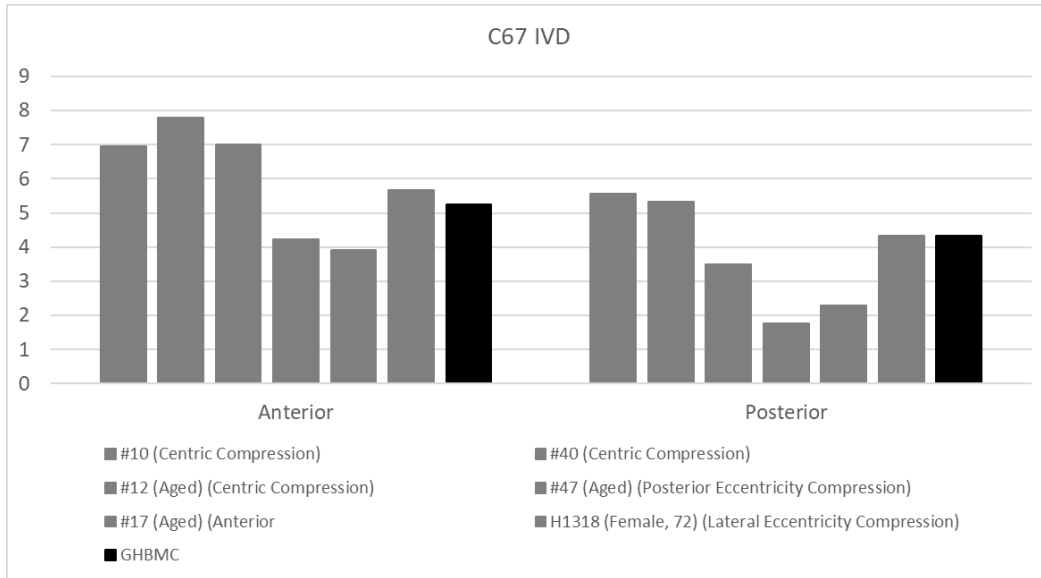
C56 and C67 inferior invertebral disc height

Bezier Angle

Appendix B: Compressive and Tension Mechanical Properties of Cortical Bone [Reilly and Burstein, 1974]

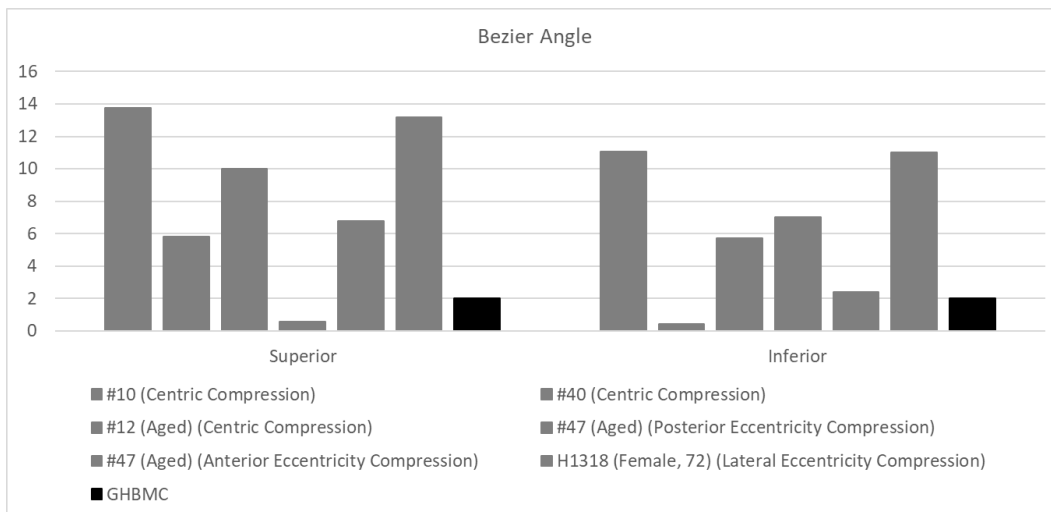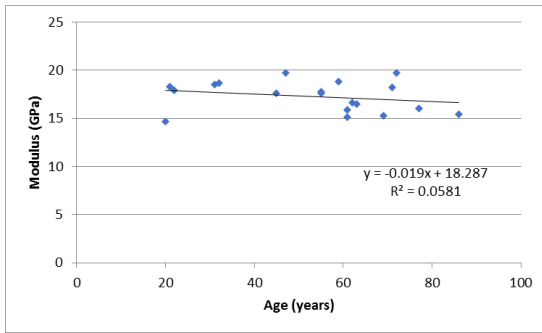| Compression	Age	E (GPa)	Std dev	UTS (GPa)	Std dev	Ult Strain	Std dev
	20	14.7	2.62	0.171	0.0085	0.022	0.0048
	21	18.3	1.86	0.206	0.01	0.019	0.0029
	22	17.9	0.85	0.211	0.0144	0.018	0.0007
	31	18.5	1.08	0.203	0.0276	0.019	0.0034
	32	18.7	3.44	0.215	0.0221	0.027	0.0047
	45	17.6	0.76	0.212	0.0062	0.022	0.0027
	47	19.7	4.75	0.188	0.0185	0.017	0.0018
	55	17.8	1.88	0.196	0.0222	0.018	0.0032
	55	17.6	3.65	0.167	0.0244	0.025	0.0046
	59	18.8	0.96	0.205	0.0067	0.019	0.0016
	61	15.9	3.3	0.191	0.0107	0.028	0.0041
	61	15.1	1.79	0.156	0.0089	0.023	0.0044
	62	16.6	1.66	0.186	0.0149	0.018	0.0018
	63	16.5	3.57	0.171	0.0095	0.023	0.0058
	69	15.3	0.87	0.189	0.0109	0.021	0.0045
	71	18.2	0.85	0.209	0.0024	0.026	0.0004
	72	19.7	2.43	0.192	0.0169	0.017	0.0014
	77	16	1.25	0.17	0.0118	0.019	0.002
	86	15.4	1.92	0.18	0.0208	0.02	0.0018
Average	53.105	17.279	2.405	0.190	0.016	0.021	0.003

Tension	Age	E (GPa)	Std dev	E hardening (GPa)	Std dev	UTS (GPa)	Std dev	Ult Strain	Std dev
	20	11.4	3.13	0.618	0.1345	0.122	0.0199	0.049	0.0019
	21	18.3	4.57	0.672	0.2498	0.133	0.0186	0.032	0.0073

	22	19.3	5.21	0.755	0.205	0.14	0.0154	0.038	0.012
	31	17.2	3.54	0.598	0.2436	0.132	0.0128	0.036	0.0061
	32	17.8	0.16	0.636	0.1833	0.138	0.0091	0.025	0.0033
	45	14.6	3.5	0.796	0.1501	0.146	0.0107	0.034	0.006
	47	15.8	1.65	1.337	0.3794	0.127	0.012	0.026	0.0078
	55	15.9	0.1	1.12	0.32	0.135	0.0005	0.025	0.0046
	55	14.7	3.65	0.971	0.2984	0.107	0.0167	0.025	0.0051
	59	18.2	1.78	0.802	0.3002	0.132	0.0157	0.02	0.0054
	61	18.6	3.3	1.063	0.1844	0.121	0.0046	0.017	0.0038
	61	14.2	0.69	0.198	0.1287	0.131	0.0086	0.029	0.006
	62	17.8	4.61	1.137	0.3903	0.127	0.0068	0.021	0.0033
	63	19.1	5.71	1.068	0.0392	0.125	0.0031	0.022	0.0044
	69	17.4	3.48	0.912	0.169	0.127	0.0068	0.029	0.0026
	71	17.1	3.01	1.049	0.043	0.12	0.0104	0.015	0.0046
	72	15.6	1.59	1.213	0.1193	0.128	0.004	0.024	0.0045
	77	13.6	2.3	1.247	0.3975	0.131	0.0039	0.029	0.0046
	86	15.1	2.58	0.845	0.1197	0.115	0.0234	0.025	0.0086
Average	53.105	16.405	3.385	0.897	0.250	0.128	0.013	0.027	0.006

Compression   Tension